CPPM-T-2010-08

UNIVERSITÉ DE LA MÉDITERRANÉE
AIX-MARSEILLE II
FACULTÉ DES SCIENCES DE LUMINY
163 avenue de Luminy
13288 MARSEILLE Cedex 09

TYPE DE DOCUMENT

Spécialité : *Physique et Sciences de la Matière*

Mention : *Physique des Particules et Astroparticules*

présentée par

Garabed HALLADJIAN

en vue d'obtenir le grade de docteur de l'Université de la Méditerranée

Recherche de neutrinos cosmiques de haute-énergie émis par des sources ponctuelles avec ANTARES

soutenue le 9 Décembre 2010 devant le jury composé de :

M.	Vincent	BERTIN	Co-Directeur de thèse
M.	José	BUSTO	Examinateur
M.	Paschal	COYLE	Directeur de thèse
M.	Eric	KAJFASZ	Président du jury
M.	Jürgen	KNÖDLSEDER	Examinateur
Mme.	Annarita	MARGIOTTA	Rapporteur
M.	Santiago	PITA	Rapporteur

Remerciements

Tout d'abord, je remercie Paschal Coyle, mon directeur de thèse et le porte-parole de la Collaboration ANTARES, pour le temps qui m'a consacré pour encadrer mon travail, pour les discussions et les conseils précieux. Je remercie aussi Vincent Bertin, mon co-directeur de thèse et le chef du groupe ANTARES au CPPM, pour ses explications claires, son support et les soutiens pendant les difficultés. Je remercie Eric kajfasz, le président du jury de thèse et le directeur du CPPM, pour l'ambiance de travail idéale qu'il a créé au sein du laboratoire. Je remercie le chef de département de physique José Busto non seulement pour son support sur le plan scientifique mais aussi sur le plan humain. Je remercie mes rapporteurs de thèse Santiago Pita et Annarita Margiotta pour leurs suggestions importantes à l'amélioration de manuscrit de ma thèse. Je remercie Jurgen Knodlseder pour avoir accepté l'invitation à être membre du jury.

Je remercie les membres de groupe ANTARES du CPPM pour les discutions fructueuses qu'on a eu pendant et en dehors des réunions de groupe qui m'ont servi d'élargir mes connaissances. Merci pour Jurgen, Damien, Jean-Pierre et Stéphanie. Je remercie aussi tous les physiciens de la Collaboration ANTARES en général et ceux du groupe de point-source avec qui j'ai eu le plaisir de travailler. Merci Juanjo, Antoine, Aart, Juan-Pablo, Juande, Fabian et Paco.

Durant les trois ans de thèse, j'ai vécu des moments heureux avec une deuxième famille constituée de la personnelle du CPPM. Merci profondément pour tous les physiciens, les ingénieurs, le personnel d'administrations, le personnel de communication et le personnel des services généraux pour leurs amitiés et leurs aides. Dans cette famille, je me suis trouvé avec des collègues de qualité scientifique et humaine fine. Des amis qui m'ont aidé chacun à sa façon: Ma copine Houry pour partager avec moi le bonheur et surtout les difficultés durant la thèse, Rémi pour la sincère amitié et les discutions scientifiques fructueuses, Georges, Cécile, Stéphane et Bassem pour les services nombreuses. Merci Sahar, Nancy, Emilie, Cosmé, Ziad, Nicolas, Marine, Davide, Guillaume, Imen, Salvatore, Maximilian et Gabrielle pour leur sympathie.

Je remercie l'Université de la Méditerranée en général et le chef de département de physique José Busto en particulier de m'avoir permis d'enseigner durant la deuxième et la troisième année de thèse. Ces heures d'enseignements m'ont permis de découvrir ma passion à l'enseignement de tous les sujets physiques et mathématiques en général et la Théorie de la Relativité, la probabilité et la statistique en particulier. Ma conclusion après deux ans d'enseignement c'est que la recherche et l'enseignement, en même temps, équilibrent l'esprit scientifique.

Je remercie mes parents pour leurs sacrifices et la consécration de leur vie à ma sœur adorable Maral et moi. Ils nous ont assuré le bonheur pendant des moments très difficile de notre vie. Je remercie ma sœur pour la croyance à mes capacités. Je remercie aussi tous les membres de deux familles Halladjian et Boghossian pour leur support moral.

A cette occasion, je tiens à remercier le CNRS, l'IN2P3 et l'Université de la Méditerranée de m'avoir accueilli.

Finalement, je vous remercie cher lecteur.

Contents

Introduction

Starting with the first intelligent spark of Homo sapiens, about 200 000 years ago, the human mind has searched for the secrets of the Universe. Over time, some of these secrets have been revealed and formulated within the laws of nature to constitute "The Physics" (meaning The Nature in Ancient Greek). Cosmic phenomena have drawn attention for thousands of years. Human beings have used their naked eyes to observe, to analyse, and then to conclude. Civilizations, most notably in Mesopotamia, China, Egypt, Greece, India, and Central America, developed ideas about the nature of the Cosmos. The first revolution in the history of astronomical observation was with the invention of the refracting telescope in about 1608. Since that date, and for almost three centuries, astronomical observations were limited to visible light.

In 1909, Theodor Wulf measured the radiation rate at different altitudes, on the top and the base of the Eiffel Tour. He found that the radiation rate at the top relatively to the base is too high to be due to terrestrial radioactivity. Between 1911 and 1913, Victor Francis Hess repeated the measurement on several free balloon flights. He concluded that the radiation is produced by down-going particles with, most probably, extraterrestrial nature. In 1938, Pierre Auger observed the simultaneous signalisation of two particle detectors separated horizontally by several meters and he discovered the atmospheric showers [1]. With these discoveries science acquired a new astronomical messenger, the cosmic rays. Recently, the Pierre Auger Observatory [2] collected 69 ultra high energy cosmic rays (E $>$ 55 EeV) during the period early 2004 until December 31$^{\text{th}}$ of 2009 [3]. The sources of these cosmic rays remain mysterious since their correlation with the known sources is not established. Their chemical composition is still unknown as well.

The discovery of cosmic radio waves in the early thirties and cosmic γ-rays at the end of sixties enabled physicists to enlarge their observations using a wider electromagnetic spectrum than just visible photons. Recently, experiments such as HESS [4] and the Fermi satellite [5] have probed the Cosmos with large sam-

ples of γ-rays determining their origins and energy spectra. However, the γ-ray astronomy have not brought answers on the nature of cosmic ray sources and a clear understanding of the cosmic rays emission processes.

In addition to cosmic rays and γ-ray astronomy, astronomical observations have made use of another particle to open a new window on the Universe; the neutrino. Neutrino astronomy began in the sixties, with the observation of solar neutrinos in the MeV energy range [6] and later with the observation of a small number of neutrinos coming from the supernova SN1987A on February 23^{th} of 1987 [7].

During the nineties, high energy neutrinos (> 1 TeV) became a new field of research in astroparticles. The detection of these neutrinos will enable physicists to lift the curtain on the mystery of the origin of cosmic rays and understand the acceleration processes in which they are produced. The flux of cosmic neutrinos is expected to be "small" and as yet none has been observed.

The aim of this thesis is the search for high energy cosmic neutrinos emitted by point sources with the first data of the ANTARES neutrino telescope. The thesis is composed of the following parts:

Chapter 1 presents a general introduction to astroparticle physics discussing cosmic rays, the γ-ray astronomy, and the neutrino astronomy. The various galactic (supernova remnants, pulsar wind nebulae, γ-ray binaries ...) and extragalactic (AGN, GRB ...) neutrino potential sources are discussed. In Chapter 2, a study of the γ-ray absorption by the extragalactic background light and the estimation of the neutrino flux from some sources that can be observed by neutrino telescopes such as ANTARES are presented.

Chapter 3 presents the ANTARES telescope. Firstly, the detection of high energy cosmic neutrinos is explained including their interactions with Earth, the Cherenkov effect, and the detection principle. Then, the ANTARES telescope is described, including the ANTARES site, the main detector components, the data acquisition system, the trigger, the time calibration, the atmospheric and the optical backgrounds. The Monte-Carlo simulations of the signal, the background, the detector and its environment are presented. The muon track reconstruction algorithms, BBfit and AAfit, are explained. Finally, future neutrino experiments with km^3 volumes are discussed.

Chapter 4 describes a study of the absolute pointing of the ANTARES telescope and its uncertainty. The acoustic positioning system with its two subsys-

tems (High and Low BaseLine acoustic systems) that are used for this study are presented. The estimation of the sound velocity and the triangulation algorithm used in the acoustic positioning system are discussed. The calculation of the absolute pointing and its uncertainty by both acoustic subsystems are evaluated with and without the systematic uncertainties on the acoustic time measurements and the sound velocity. The errors on the positions of the acoustic devices are also studied.

Chapter 5 presents a search for high energy cosmic neutrinos emitted by the point sources in the 2007 data, acquired by the ANTARES detector in its 5-line configuration, using the BBfit reconstruction algorithm. Comparisons for the main analysis parameters are made between data and Monte-Carlo in order to validate the functioning of the detector and the simulations. The two main characteristics of the telescope, the effective area and the angular resolution, are evaluated for different quality cuts. The likelihood ratio method is explained and then search strategies are developed. The quality cuts are optimized in order to have the best discovery potential. Various systematic uncertainties are discussed and taken into account for the final sensitivity and discovery potential. Finally, the data results are presented and several skymaps are produced. In Chapter 6, the point source analysis is repeated for 2007 + 2008 data using the AAfit reconstruction strategy and with the unbinned search method.

Chapter 1

Astroparticle physics and high energy cosmic neutrinos

In this chapter, a general overview of astroparticle physics is given presenting the cosmic rays, the γ-ray and the neutrino astronomies. Some of the recent results of the experiments of these fields are shown. The unsolved problems and the motivation of neutrino astronomy are discussed. Both galactic and extragalactic potential sources of high energy cosmic neutrinos are presented.

1.1 Cosmic rays

The Earth's atmosphere is bombarded each second by thousands of Cosmic Rays (CR)s per meter square. For energies higher than 10^{19} eV and 10^{20} eV, the flux of CRs is ~ 0.6 particle km^{-2}sr^{-1}year^{-1} and ~ 0.6 particle km^{-2}sr^{-1}century^{-1} respectively. The energy spectrum of the CRs is spread over 12 orders of magnitude over the energy and 32 orders of magnitude over the flux [8]. This spectrum follows a power law distribution (Equation 1.1) where the spectrum index, denoted by Γ, has different values for three different domains of energies as it is shown in Equation 1.2 (Figure 1.1). The CRs are composed $\sim 90\%$ of protons, $\sim 9\%$ of Helium nuclei and $\sim 1\%$ of other atomic nuclei and electrons. The chemical composition of the Ultra-High Energy Cosmic Rays (UHECR)s ($E > 10^{18}$ eV) is still unclear and it is discussed in Section 1.1.3. An explanation to the mechanism of the acceleration process of CRs was given by Enrico Fermi in 1949 [9], it is briefly presented in Appendix A.

$$\frac{\mathrm{d}N}{\mathrm{d}E} \propto E^{-\Gamma} \tag{1.1}$$

where

$$\Gamma = \begin{cases} 2.7 & \text{for} \quad E < E_1 \\ 3.0 \text{ to } 3.3 & \text{for} \quad E_1 < E < E_2 \\ 2.6 & \text{for} \quad E > E_2 \end{cases} \tag{1.2}$$

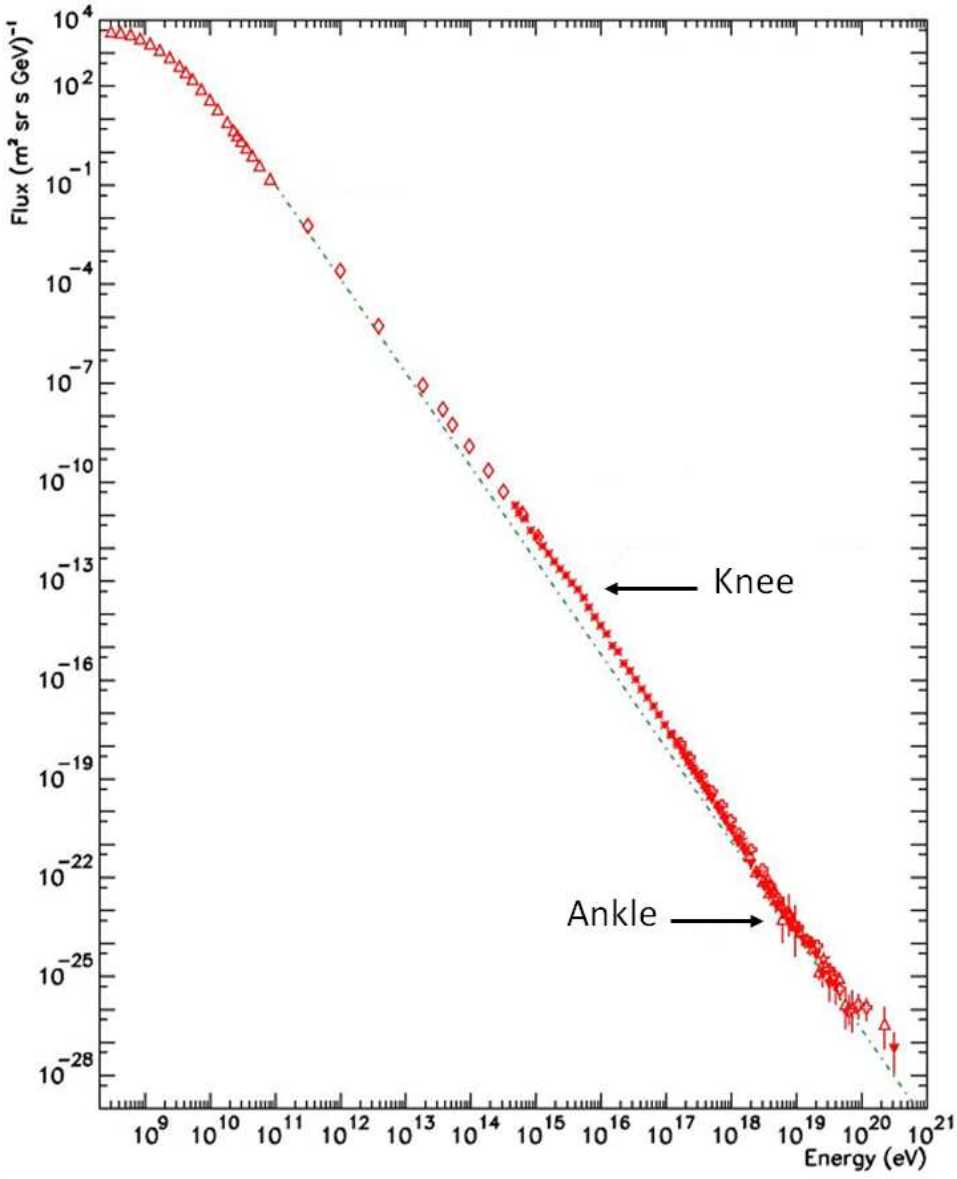

Figure 1.1: The energy spectrum of the cosmic rays [10]. The data is taken by the following experiments: LEAP, Proton, Akeno, AGASA, Fly's Eye, Haverah Park, Yakutsk.

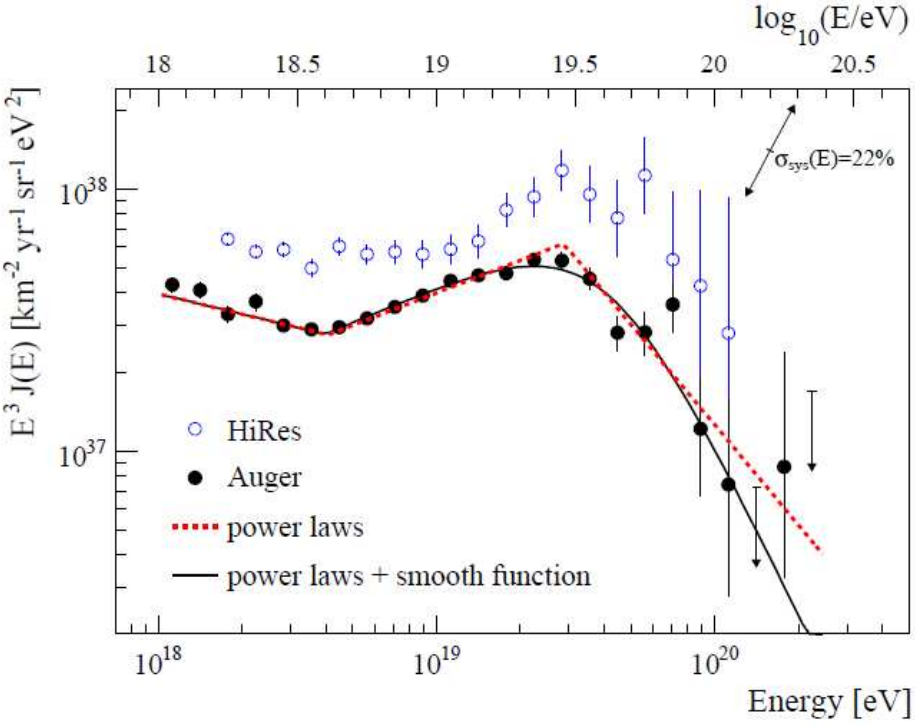

Figure 1.2: The energy spectrum of UHECRs measured by PAO (Section 1.1.1.1) and HiRes (Section 1.1.1.2) [12].

E_1 is equal to $\sim 10^{15}$ eV and it is called "the knee". The flux of the cosmic rays at this region is ~ 1 particle $m^{-2}sr^{-1}year^{-1}$. It can be explained as a modification of the propagation conditions of the cosmic rays due to the presence of a close by source. Another possibility is new physics. A second knee may exist at $\sim 10^{18}$ eV and several explanations are proposed [11]. E_2 is equal to $\sim 10^{19}$ eV and it is known as "the ankle". The particles with energies above E_2 have an extragalactic nature since their radius of gyration is bigger than the radius of the galaxy.

The rapid decrease of the flux at $E = 10^{19.5}$ to 10^{20} eV (figures 1.1 and 1.2) can be explained by acceleration limitations in the sources or by the Greisen-Zatsepin-Kuz'min (GZK) cut-off in case the UHECRs are protons [13, 14]. The latter is due to the interaction of the UHECRs with the Cosmic Microwave Background[1]

[1]The largest quantity of particles in the Universe (411 photons per cm^3) are the cosmic microwave background photons. They have a temperature of 2.725 K ($E_\gamma = 2.35 \times 10^{-4}$ eV) [15] and they are created at about 379 000 years after the Big Bang with the transition of the Universe from the plasma state to hydrogen atoms. At that time, the temperature of the Universe was about 3000 K.

(CMB) photons producing pions via the delta resonance as it is shown in the following equation:

$$p^+ + \gamma_{\text{CMB}} \rightarrow \Delta^+ \rightarrow \pi^+ + n \tag{1.3}$$

A third explanation for this cut-off is the photodisintegration of Fe nuclei in case the UHECRs are iron nuclei [16, 17, 18].

1.1.1 Detection principle and UHECR detectors

The cosmic rays are electrically charged, therefore, the trajectories of these particles are deviated by the interstellar and intergalactic magnetic fields. This fact makes the localization of the sources positions difficult. The higher the energy of the CRs the lower the deviation is.

The detection principle of the UHECRs is based on two techniques: a Surface Detector (SD) array and a Fluorescence Detector (FD). The SD array consists of a surface array installed on a wide horizontal plane to detect the secondary cosmic particles. The direction of the primary cosmic radiation can be reconstructed from the measured arrival time of these particles. The FD detects the fluorescent light emitted by excited atmospheric nitrogen molecules and the Cherenkov photons induced by the secondary particles [19, 20, 21]. This technique was first used in 1976, four decades after the former, by physicists from the University of Utah detecting fluorescent light from cosmic ray air showers in New Mexico.

Since the first detection of UHECRs with energies around 10^{20} eV in 1963 [22], many experiments have studied the properties of the UHECRs (the energy spectrum, the chemical composition, ...) and attempted to establish their origin. The recent results from two UHECR experiments; the Pierre Auger Observatory (PAO) and the High Resolution Fly's Eye Cosmic Ray Observatory (HiRes) are discussed in the next sections.

1.1.1.1 Pierre Auger Observatory (PAO)

Located in Argentina, PAO [2] is composed of 1600 SDs distributed on a triangular grid over 3000 km^2 and 24 FDs grouped in four buildings. The SDs detect electrons, photons and muons almost 100% of time whereas the FDs are only operational during dark nights. The energy threshold of PAO is $\sim$ 1 EeV. For hybrid events, the angular resolution is $\sim 0.6^\circ$ [23].

1.1.1.2 High Resolution Fly's Eye Cosmic Ray Observatory (HiRes)

HiRes [24] is composed of air FDs that operate in stereo mode and detect UHECRs ($E > 10^{18}$ eV). It is installed on Dugway Proving Grounds in Utah, USA, on two sites (HiRes 1 and 2) separated by 12.6 km. It operated for nine years, from

June 1997 to April 2006 [25, 26]. HiRes 1 (2) consists from 22 (42) telescopes with 256 photomultiplier tubes each covering $[3^\circ, 16.5^\circ]$ ($[3^\circ, 30^\circ]$) in elevation above the horizon [27]. It is characterized by an angular resolution of $\sim 0.6^\circ$.

1.1.2 UHECR sources

In this section, the potential sources of UHECRs and the recent results of PAO are discussed.

1.1.2.1 Potential cosmic rays acceleration sites

Using the Fermi mechanism and based on the estimation of the magnetic field intensity B in some cosmic bodies, the classification of potential regions to accelerate particles up to an energy E was proposed by Hillas in 1984 [28]. This classification is a general approach that ignores the energy loss. The condition for this proposal to be applicable is that the size of these bodies should surpass the gyration radius in order that the particles remain confined in the magnetic field. Therefore, the maximum energy is evaluated as:

$$\frac{E_{\max}}{1\mathrm{EeV}} = Z\left(\frac{L}{1\mathrm{kpc}}\right)\left(\frac{B}{1\mu\mathrm{B}}\right) \tag{1.4}$$

where Z is the charge of the particle and L is the estimated size of the region. Figure 1.3 shows the classification of the astrophysical bodies as a function of their magnetic field, size and their capacity to accelerate particles to a given maximum energy. Active Galactic Nuclei (AGN)s (Section 1.3.2.1) and Gamma Ray Bursts (GRB)s (Section 1.3.2.2) are particularly good candidates.

1.1.2.2 PAO results on the origin of cosmic rays

Using the 69 events observed by FDs in coincidence with at least one SD, the Pierre Auger Collaboration searched for a correlation between these events and the list of AGNs called Véron-Cetty and Véron (VCV) [29]. Figure 1.4 shows the skymap of the 69 UHECR events and the AGNs of VCV catalogue.

Figure 1.5 shows the degree of correlation ($\mathrm{p_{data}}$ = number of correlated events to the sources over the total number of detected events) of the 69 events and the 318 AGNs as a function of the total number of time-ordered events observed during the data taking period. The degree of correlation for all events is $38^{+7}_{-6}\%$, to be compared with the 21% expected to occur by chance if the flux is isotropic [3].

With these results, the sources of the UHECRs remain unknown.

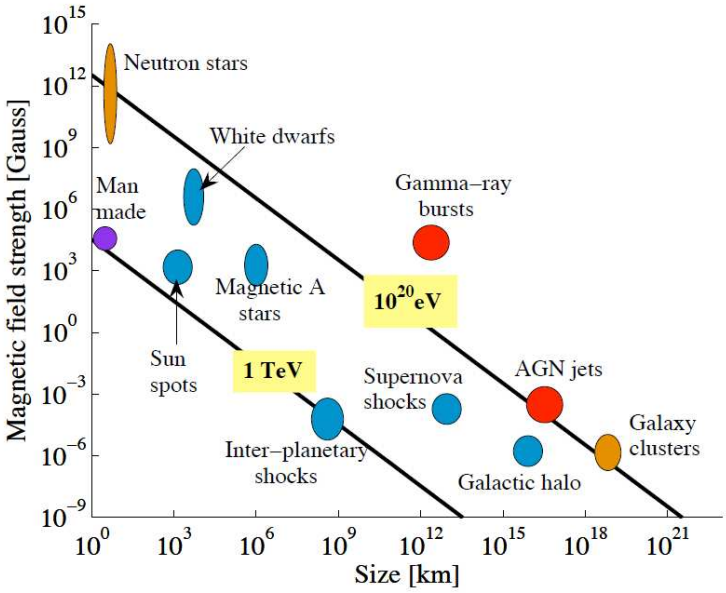

Figure 1.3: Hillas diagram presenting cosmic bodies as a function of their magnetic field, size, and their capacity to accelerate particles to a given maximum energy.

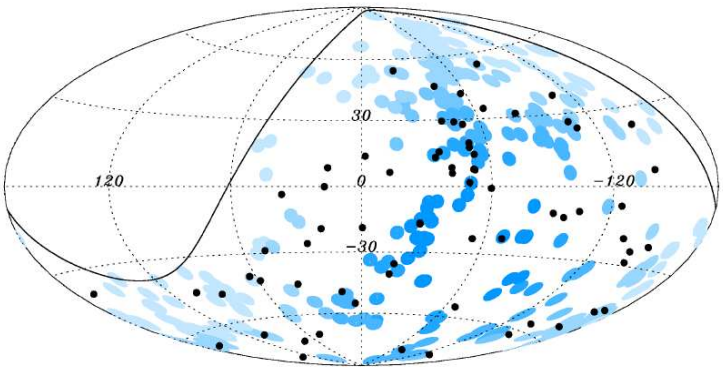

Figure 1.4: The skymap of the PAO 69 events (black points) and the 318 AGNs of VCV catalogue. The solid line represents the visible region of the PAO for zenith smaller than 60°. The blue circles are centered on the AGNs positions, their radius is 3.1°. The intensity of the blue color represents the visibility of the source [3].

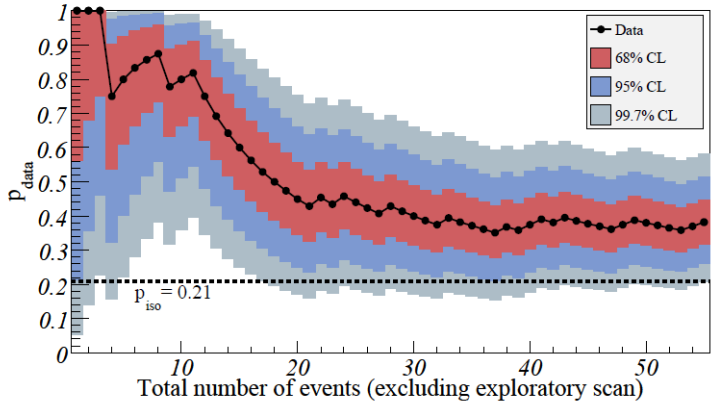

Figure 1.5: The degree of correlation between the 69 events and the 318 AGNs. The 68%, 95% and 99.7% confidence level intervals around the most likely value are plotted. The dashed line at p_{iso} represents the degree of correlation for an isotropic sky [3].

1.1.3 Chemical composition of the ultra high energy cosmic rays

The UHECRs can be protons [13, 14], heavy atomic nuclei (e.g. Fe) [16, 17] or a mixture between them. The understanding of the UHECR composition is one of the main studies of UHECR observatories.

The chemical composition can be extracted from the measurement of the atmospheric depth, $X_{\max}$, where the longitudinal development of CR air shower reaches its maximum[2]. For a data set of detected UHECRs, the mean value $< X_{\max} >$ and the RMS($X_{\max}$) are defined.

References [30, 31] show that $< X_{\max} >$ depends logarithmically on the primary CR energy E and its atomic mass A (Equation 1.5).

$$< X_{\max} >= \alpha\,(\log E - < \log A > + \beta) \tag{1.5}$$

where α and β are the coefficients of the hadronic interaction.

Figures 1.6 and 1.7 indicate a contradiction between the results of both experiments PAO and HiRes. The Former has tendency for the hypothesis of the significant Fe nuclei contribution in the UHECR composition, but the latter supports the protonic nature of UHECRs. Therefore, the measurements of $< X_{\max} >$ and RMS($X_{\max}$) are not conclusive on the chemical composition of UHECRs.

[2] $X_{\max}$ represents the atmospheric depth, given as a column density between P_1 and P_2, where P_1 is the interaction point of the primary particle at the higher level of the atmosphere. P_2 is a point on the primary track where the shower reaches its maximum number of produced secondary particles. $X_{\max}$ is expressed by g.cm^{-2} ($\int \rho \mathrm{d}x$).

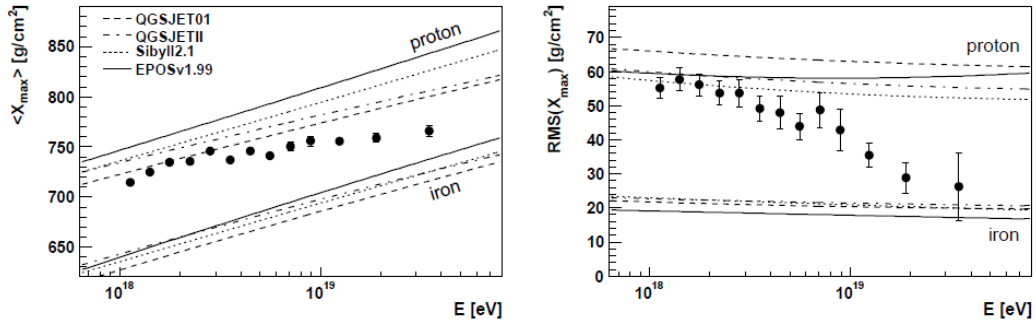

Figure 1.6: PAO's results of $< X_{\max} >$ (left) and RMS($X_{\max}$) (right) [32]. The lines represent the Monte-Carlo simulations results for the protons and Fe nuclei.

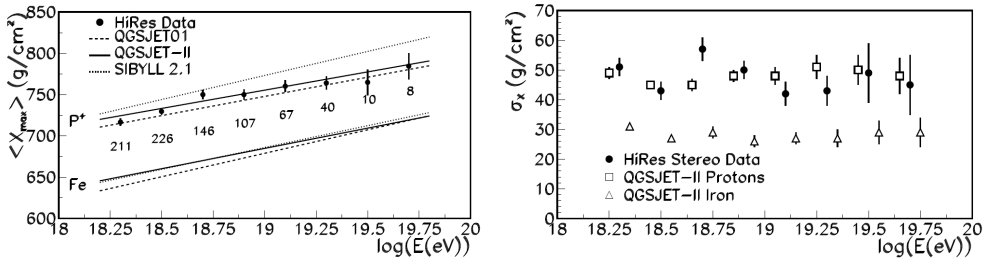

Figure 1.7: $< X_{\max} >$ (left) and RMS($X_{\max}$) (right) published by HiRes [33]. The lines represent the Monte-Carlo simulations results for the protons and Fe nuclei.

The chemical composition cannot be deduced from the cut-off at $\sim 10^{20}$ eV in the CR spectrum. The effective horizon of the protons due to the GZK cut-off and the one of Fe nuclei due to the photodisintegration cut-off [16, 17, 18] are roughly the same. Consequently, the chemical composition of the UHECRs remains to be clarified.

1.2 Cosmic photons and γ-ray astronomy

The recent results of the γ-ray telescopes have identified the nature, the positions and the energy spectra of numerous sources. Figure 1.8 presents some of the detected γ-ray sources. The following lines describe two of the γ-ray telescopes:

- the High Energy Stereoscopic System (HESS) [34]: the HESS telescopes observe the γ-rays with $E > 100$ GeV. HESS is operating since June 2002 in the Khomas highlands of Namibia during dark nights. It detects the Cherenkov light emitted by cascades of particles produced by the interactions of cosmic γ-rays or CRs within the atmosphere. Its angular (energy) resolution is 0.06° (15%) [35].

- the FERMI satellite consists of the Gamma-ray Burst Monitor (GBM) and the Large Area Telescope (LAT). It is operational since 11 August 2008. FERMI is sensitive to γ-rays with energies from 20 MeV up to 300 GeV with an angular resolution of 3° to 6° for $E = 100$ MeV and 0.1° to 0.2° for $E = 10$ GeV [36]. Figure 1.9 shows the catalogue of 1451 γ-ray sources detected by the Fermi Satellite.

The γ-rays can be emitted during the acceleration of cosmic rays or by an inverse Compton interaction with external photons. The process of the electromagnetic emission can be leptonic, hadronic or both of these processes (sections 1.2.1 and 1.2.2). The interaction of the photons with matter limits the γ-rays with energies higher than 10^3 TeV to a horizon of 10 kpc, consequently, the observation of extragalactic phenomena with γ-rays is difficult for energies higher than 100 TeV. Figure 1.10 shows the mean free path of the γ-rays for different energies.

1.2.1 Leptonic processes

In the leptonic processes, the photons can be emitted by electrons (synchrotron radiation) and/or boosted by inverse Compton process. The energy spectrum of these photons is characterized by two bumps (Figure 1.11). The low energy bump

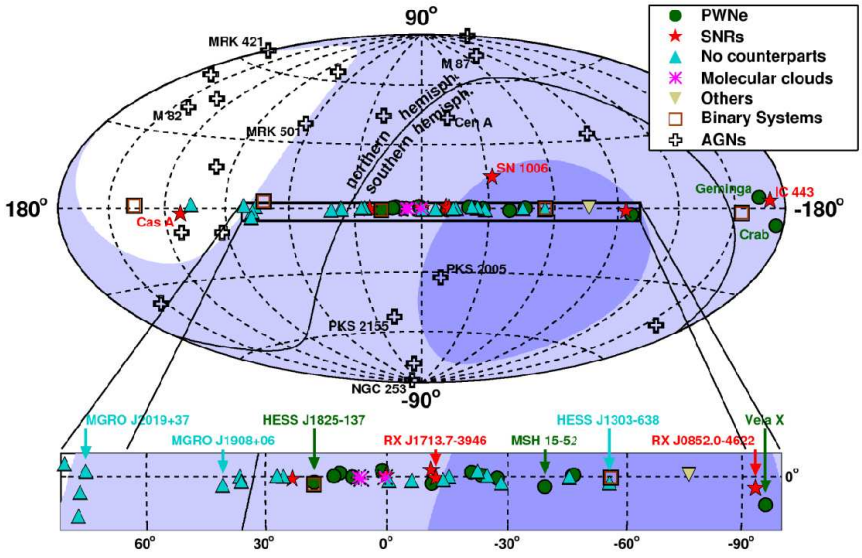

Figure 1.8: γ-ray sources in the galactic coordinates. The visibility of the ANTARES telescope is indicated by violet colors: light indicates a visibility less than 100%, and dark indicates a visibility of 100%. The solid line represents the equator.

is due to the synchrotron radiation of the electrons accelerating in the magnetic fields. Equation 1.6 evaluates the decrease of the energy of these electrons.

$$-\frac{\mathrm{d}\varepsilon}{\mathrm{d}t} = \frac{2}{3}\left(\frac{ev}{mc}\right)4E^2B^2 \tag{1.6}$$

where e, v and m are the electric charge, the velocity and the mass of the electron respectively, c is the speed of light, E and B are the electric and magnetic fields.

The high energy bump can be due to the inverse-Compton scattering of photons produced within the jets (Section 1.3.2.1) [38, 39, 40] or outside the jets [41, 42, 43, 44, 45, 46].

1.2.2 Hadronic processes

In the hadronic processes, within the presence of a high magnetic field ($\sim$ 10 Gauss), the protons exceed the threshold energy of the interaction with γ-rays or other protons to produce π^0 and $\pi^{\pm}$. The photons are emitted by several processes:

- The development of proton synchrotron-supported pair cascades [47, 48].

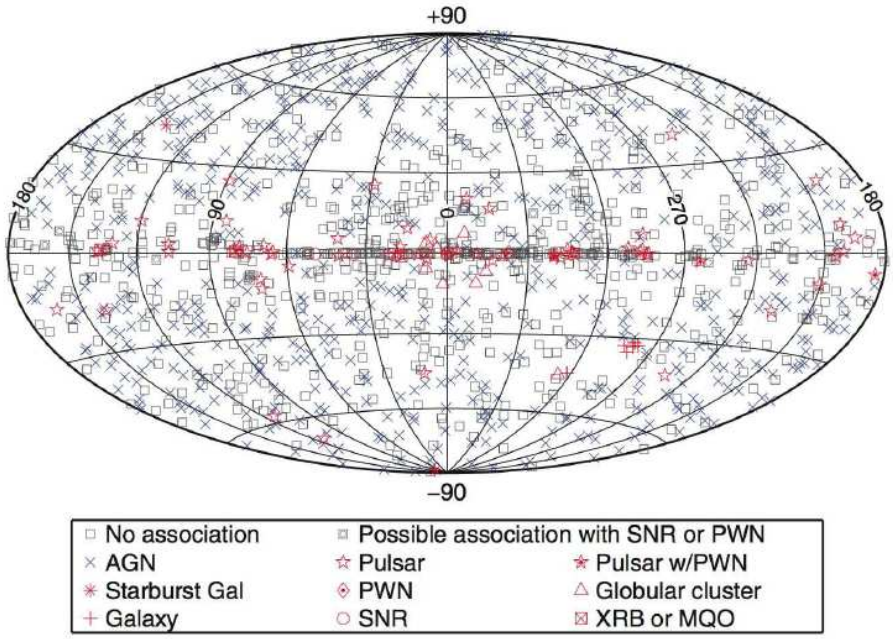

Figure 1.9: Fermi-LAT catalogue of the 1451 γ-ray sources (Galactic coordinates) [37].

- The synchrotron radiation of the primary protons [49, 50] and of the secondary muons and mesons [51, 50, 52, 53].
- The π^0 decay to $\gamma\gamma$.
- The electrons produced by $\pi^{\pm} \rightarrow \mu^{\pm} \rightarrow e^{\pm}$.

1.3 Neutrino astronomy

In 1930, Wolfgang Pauli postulated the existence of neutrinos to preserve the energy conservation of β-decay reaction presented as:

$$n \rightarrow p^{+} + e^{-} + \overline{\nu} \tag{1.7}$$

The neutrinos are elementary particles in the Standard Model of particle physics. They are fermions with a spin of 1/2 and they have three flavours: electronic ν_e, muonic ν_μ, and tauic ν_τ. They interact with other particles only through Gravitational and Weak interactions.

The astronomical use of neutrinos opens a new window to the Universe. The neutrinos cover energies up to twenty orders of magnitude. Some regions of the

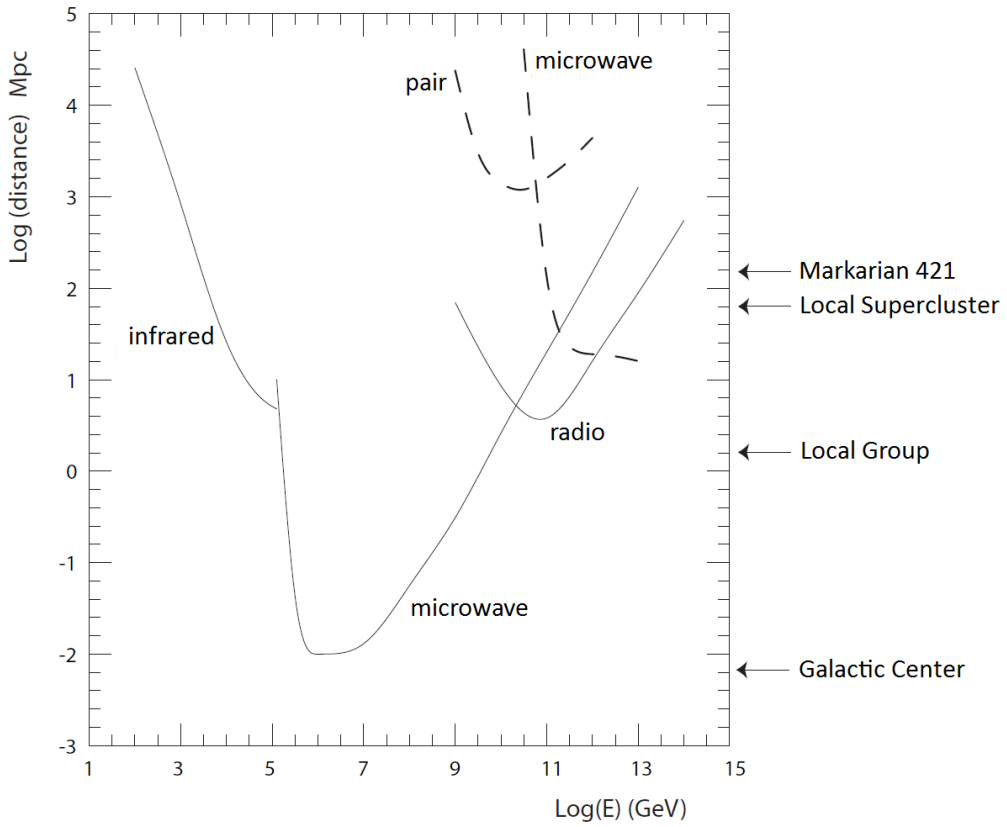

Figure 1.10: The mean free path of the γ-rays due to their interactions with infrared, microwave and radio waves at different energies.

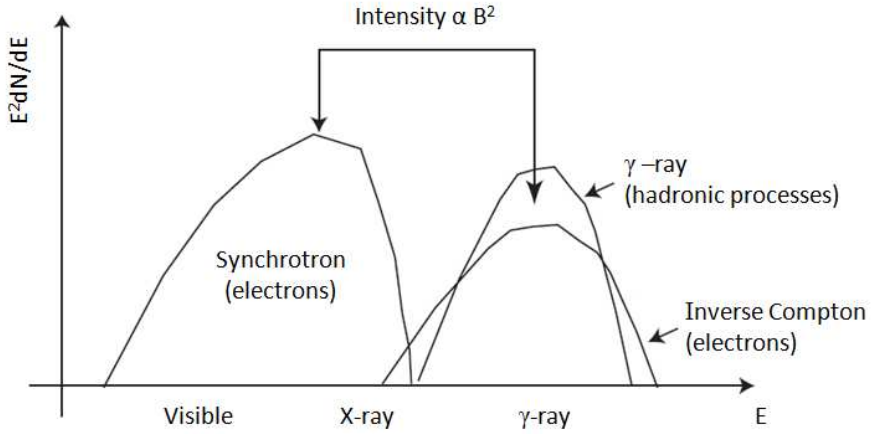

Figure 1.11: The energy spectra of the photons shown for both leptonic and hadronic scenarios.

energy range accessible with neutrinos cannot be explored with electromagnetic radiation or cosmic rays ($\sim 10^5$ to $\sim 10^{10}$ GeV and higher than about 10^{12} GeV) (Figure 1.12).

In Section 1.2, the origin of the high energy γ-rays is discussed. The emission process of the γ-rays (leptonic and/or hadronic) is not completely understood yet. The detection (or the exclusion) of high energy neutrinos will help to reveal the emission process in various sources.

The neutrinos can be produced, through a hadronic process, by $\pi^{\pm}$ decay after the interaction of a proton with a proton/atomic nucleus or with a photon as it is shown in Equation 1.8.

$$\begin{array}{lcccccccc} p(p)+p(\gamma) & \rightarrow & \pi^0 & + & \pi^+ & + & \pi^- & + & \\ & & \downarrow & & \downarrow & & \downarrow & & \\ & & \gamma+\gamma & & \mu^+ + \nu_\mu & & \mu^- + \overline{\nu}_\mu & & \\ & & & & \downarrow & & \downarrow & & \\ & & & & e^+ + \nu_e + \overline{\nu}_\mu & & e^- + \overline{\nu}_e + \nu_\mu & & \end{array} \tag{1.8}$$

The flux of neutrinos generated by these disintegrations is presented by the following equation [54, 55]:

$$\frac{\mathrm{d}N_\nu}{\mathrm{d}E_\nu} = \frac{N(E_\nu)}{1-Z_{NN}} \left(1 + \frac{A_{\pi,\nu}}{1+B_{\pi,\nu}\cos\theta\frac{E_\nu}{\varepsilon_\pi^c}} + 0.635\frac{A_{K,\nu}}{1+B_{K,\nu}\cos\theta\frac{E_\nu}{\varepsilon_K^c}} + X \right) \tag{1.9}$$

where:

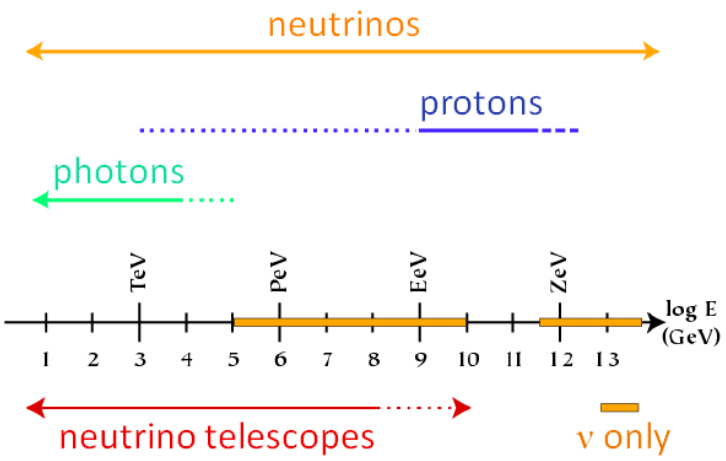

Figure 1.12: The energy range covered by neutrinos, protons and photons.

- I represents the initial flux.
- θ is the angle of incidence with respect to the target.
- A, B, and Z_{NN} are the characteristic constants of the interactions.
- ε_π^c (ε_K^c) is the critical energy of pions (kaons). They give an estimation of the energy below which the probability of the interaction overcomes that of the disintegration.
- X takes into consideration the disintegration of mesons of heavier flavours than pions and kaons.

The first (second) term designates the disintegration of pions (kaons) to neutrinos. The ratio of the flux of neutrinos and anti-neutrinos $\phi_{\upsilon+\overline{\upsilon}}$ to that of photons ϕ_γ depends on the spectral index of the primary particles and the type of interaction.

Figure 1.13 presents the expected fluxes of neutrinos emitted by various sources:

- The cosmological neutrinos CνB created right after the Big Bang by two seconds. Their temperature is estimated to be 1.95 K.
- The solar neutrinos produced by nuclear reactions in the Sun.
- The atmospheric neutrinos created in the Earth's atmosphere by the cosmic rays interactions.

- The neutrinos emitted by the AGNs (Section 1.3.2.1) and the GRBs (Section 1.3.2.2).
- The GZK neutrinos created by the interactions of very high energy cosmic rays with the CMB photons.

1.3.1 Advantages of neutrino astronomy

Neutrino astronomy has many advantages. The neutrinos are stable and their mean free path is much higher than that of the γ-rays. As neutrinos are electrically neutral, galactic and extragalactic magnetic fields have no effect on their trajectory. Therefore, they travel undeviated on their way to the Earth and point back to their origins (Figure 1.14).

The small interaction cross section of the neutrinos with matter allows them to escape from dense sources and pass essentially unhindered through the Universe.

1.3.2 Candidate point sources of cosmic neutrinos

The existence of hadronic processes and the emission of high energy neutrinos are expected from several astrophysical bodies [56, 57, 58]. Some of these sources are of extragalactic nature like the Active Galactic Nuclei, the Gamma Ray Bursts and the Starburst galaxies; others are galactic such as Supernova Remnants, Pulsar Wind Nebulae, Micro Quasars and the Galactic Center. These examples are not the only potential neutrino candidate sources. Recently, the γ-ray telescopes have discovered sources that do not have any counterparts in other astronomical messengers. If these mysterious sources emit neutrinos, they will lead to a better understanding of their origins. The possibility of neutrino-only sources is also an exciting possibility.

1.3.2.1 Active Galactic Nuclei

The Active Galactic Nucleus (AGN) is a compact region, with a volume $<<$ 1 pc^3, at the center of young galaxies called active galaxies (1 to 3 % of galaxies). The AGNs were discovered in 1963 via electromagnetic radio observation and called quasar, which means quasi-stellar object because of its apparition as a star [59]. The luminosity of the AGN can attain 10^{48} erg/s which is higher by four orders of magnitude than the typical luminosities of ordinary galaxies [60]. The energy spectrum of the emitted radiation (from radio to γ-rays) can cover thirteen orders of magnitude for some AGNs. The widths of the observed emission lines indicate particles velocities that reach up to 10^7 m/s. The AGNs are classified as

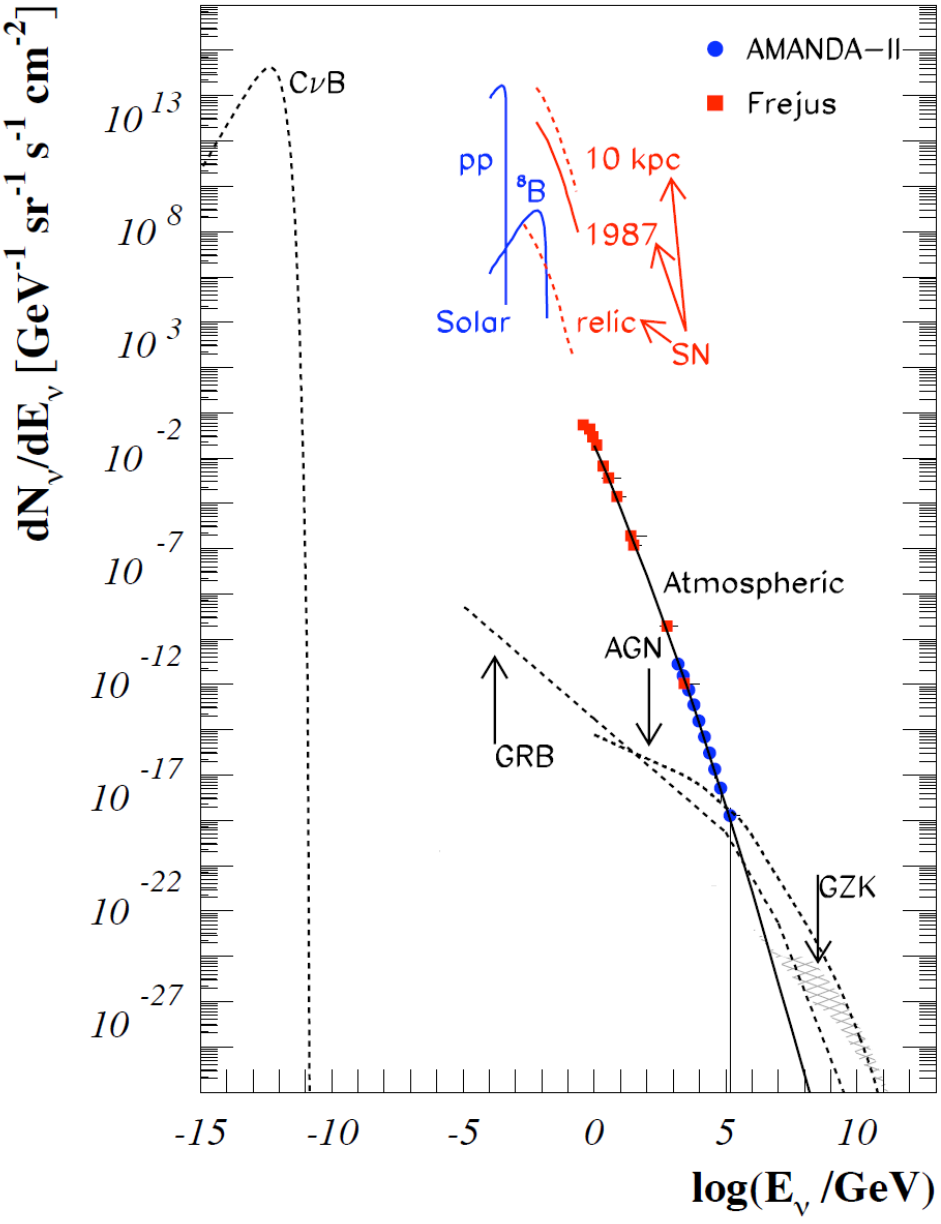

Figure 1.13: The spectra of neutrinos of different sources.

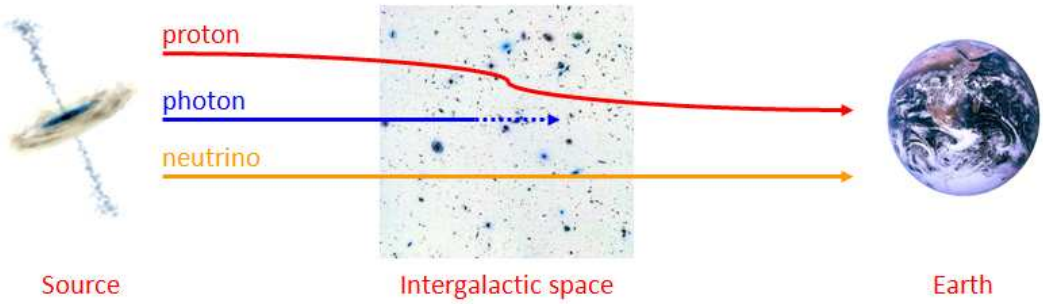

Figure 1.14: Schematic presentation of proton, photon and neutrino traveling through the space between the source and the Earth.

radio-quiet ($\sim$ 90% of AGNs) and radio-loud ($\sim$ 10% of AGNs) according to their radio emission. The radio-quiet AGNs are characterized by thermal like spectrum in contrast to the radio-louds, especially in radio and X-ray ranges.

The central component of the AGN is a super-massive black hole with a mass estimated to be 10^4 to 10^{10} solar mass. The black hole is surrounded by gas, dust and stars composing the accretion disk with a radius of about 10^{-3} pc. This accretion disk is encircled by a large torus containing colder matter. The AGN is powered by the accretion of the material to the black hole by gravitational interaction converting a part of the kinetic energy to radiation. The rotational movement of the plasma creates magnetic fields. Particles with high energies are ejected in the interstellar medium forming two jets perpendicular to the galactic plane.

The AGN is a promising candidate for high energy cosmic ray sources because of the particles acceleration in the jets and their interaction with the interstellar medium.

According to the unified model of AGN, the observation of AGN depends on the angle between the axis of rotation and the observer. Different angular positions lead to different observations (Figure 1.15), therefore subclasses of AGNs are categorized:

- blazar: it is a subclass of AGNs where the rotational axis is pointed in the direction of the observer, the direction of the jets. The characteristics of the blazars are very high luminosity from the radio to γ-ray ranges, very rapid variation and high polarization. The velocity of the plasma in the jets reach 99% of the speed of light. Some examples of blazars are 3C 273, BL Lacertae, PKS 2155-304, Markarian 421, Markarian 501.

- Seyfert galaxy: they were discovered by Carl Keenan Seyfert in 1943 [61]. They are a subclass of AGNs where the observation axis is between the ro-

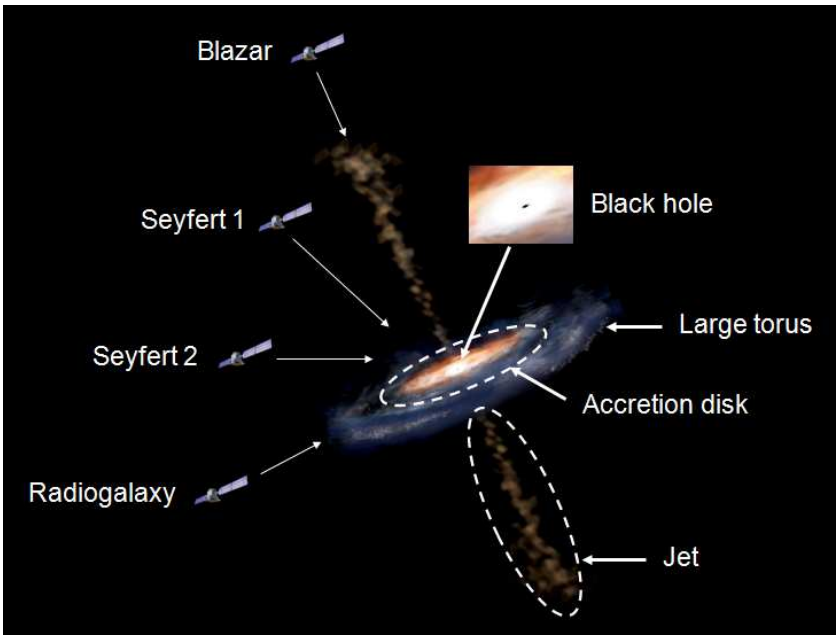

Figure 1.15: Composition of AGN and its appearance from different angular positions.

tational axis of the AGN and the galaxy plane. Their energy spectra contain very bright emission lines of highly ionized gas (hydrogen, helium, nitrogen, and oxygen) [62]. The Seyfert galaxies are classified into two types. Type 1 is characterized by both narrow and broad emission lines emitted by the accretion disk close to the black hole. The broad emission lines indicate high velocities (up to fractions of the speed of light) due to the strong Doppler broadening. Type 2 is characterized by the only narrow emission lines formed in the dust surrounding the accretion disk.

- radio galaxy: it is a very bright source in the radio range (from 10 MHz to 100 GHz up to 10^{38} W). In this case, the observer is located in the galactic plane. The radio waves are emitted by synchrotron processes from relativistic electrons (Lorentz factor $\sim 10^4$).

1.3.2.2 Gamma Ray Burst

The Gamma Ray Bursts (GRB)s last for a few seconds and are one of the most violent phenomena observed in the Universe. They are followed by remnant radiations for the following hours or days. The GRBs were discovered in 1967 by the Vela telescopes [63]. Their isotropic distribution in the sky is an indication of their extragalactic nature (Figure 1.16). This hypothesis was confirmed in the

eighties with simultaneous observations in γ-ray and visible ranges.

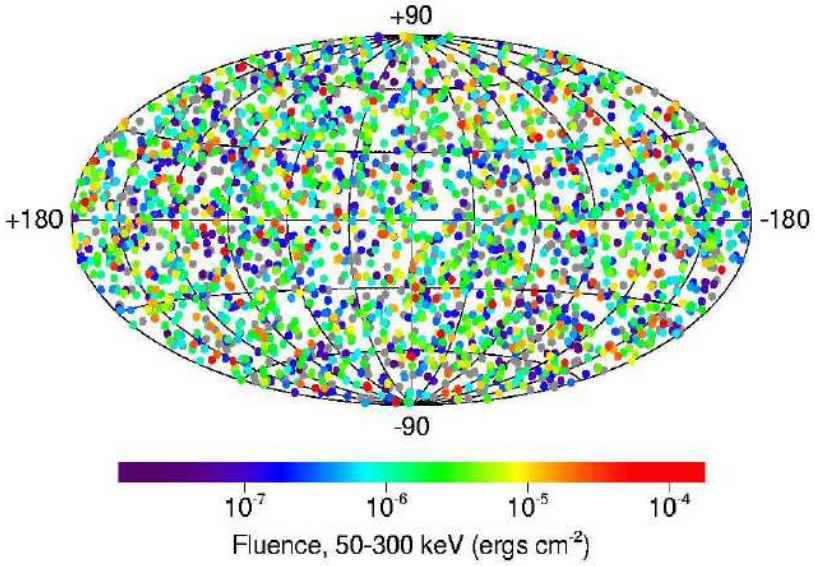

Figure 1.16: The 2704 GRBs detected by BATSE.

The GRBs can be a violent collapse of a massive star to a black hole or a collapse between two massive stars forming a black hole or an accretion of a neutron star by a black hole. As in Figure 1.15 for the AGN, but with a smaller scale, the black hole is surrounded by a plasma disk and two relativistic jets perpendicular to the disk's plane where charged particles are accelerated.

They are classified as long (> 2 s) and short (< 2 s) duration GRBs. The short duration GRBs are more likely to be candidate of cosmic neutrino sources than the others. The emitted energy by a GRB is close to that emitted by the Sun during all its lifetime.

1.3.2.3 Starburst galaxies

The starburst galaxies (M82, NGC 4038/NGC 4039, IC 10, ...) have very high rate of stars formation compared to ordinary galaxies. They are probably created by the collision of two galaxies. A high flux of synchrotron radiation, in the radio range, is observed from the starburst galaxies. These photons are emitted, in the presence of intense magnetic field, by electrons with energies in the order of GeV. The high rate of star formation indicates a dense region of matter which makes these sources opaque to the cosmic rays and the γ-rays. In this dense region, the proton can interact with another proton to produce pions. These interactions

lead to the production of neutrinos with cumulative flux estimated to be $E_\nu^2 \Phi_\nu \approx 10^{-7}$ GeV cm^{-2} s^{-1} sr^{-1}. The detection of these neutrinos may be possible with km-scale neutrino telescopes [64].

1.3.2.4 Supernova Remnants

The Supernova Remnants (SNR)s are the remains of the explosion of a star in a supernova. The SNR SN1987A is the only low energy neutrino source detected outside the solar system. These neutrinos are probably produced by $p^+ + e^- \rightarrow n + \nu$ and $\gamma + \gamma \rightarrow \nu + \overline{\nu}$. The SNRs are potential sources of high energy neutrinos because of the ejection of relativistic particles from the supernova and the shock waves in the surrounded gas. Reference [65] shows the possibility to detect neutrinos with energies above 1 TeV during 1 year of data taking with a kilometer cubic detector from RX J1713.7-3946. Another study estimates the detection of about eleven events from the same source within five years [66].

1.3.2.5 Pulsar Wind Nebulae

A pulsar is a neutron star rotating with a period of $\sim$ 1 ms to $\sim$ 1 s around the rotational axis. It is created at the center of the supernova after the collapse of the star. High energy particles are emitted in the direction of the magnetic axis[3]. The pulsars are surrounded by interstellar cloud of gas called Pulsar Wind Nebulae (PWN)e. The particles are ejected from the inside of the pulsar and interact with the interstellar cloud of gas. The TeV γ-rays are produced by synchrotron and inverse Compton scattering processes.

The most famous PWN is the Crab nebula, used as standard candle for γ-ray astronomy [67]. The PWNe, like the Vela TeV plerion, have a potential to contain hadronic processes [68]. Assuming a 100% hadronic scenarios, the crab nebula can produce 5.8 (1.9) neutrinos with energies higher than 1 TeV (5 TeV) in a km-cube neutrino telescope [66].

1.3.2.6 Micro Quasar

From the point of view of the mechanism, the Micro Quasars are similar to the AGNs but at much smaller scale. Instead of the supermassive black hole (10^4 to 10^{10} solar masses) surrounded by the dust of the young galaxy, the Micro Quasar consists of a compact object like a neutron star or a black hole accreting the matter of a close star. This mechanism produces two jets in the perpendicular direction of the accretion disc containing relativistic hadronic particles ($E \sim 10^{16}$ eV). Therefore, the production of neutrinos with the Micro Quasars is possible. This

[3]The magnetic axis is not necessarily the rotational axis.

hypothesis is supported by the discovery of iron emission lines in the jets of SS 433 [69]. The study of the Micro Quasars like SS 433 and GX339-4 shows the possibility of 5σ neutrino signal detection with kilometer cubic telescopes [70].

1.3.2.7 Galactic Center

The Galactic Center (GC) is the center of the Milky Way Galaxy. The central parsec region, around the black hole, contains thousands of stars (old red main sequence stars, white dwarf stars and neutron stars). It is one of the most important candidate neutrino sources in the galaxy. Very High Energy (VHE) γ-rays (> 100 GeV) are detected from the 200 pc central region of the Milky Way Galaxy correlated with the molecular clouds [71]. The nature of these clouds and the hardness of the γ-ray spectrum make the hadronic scenarios more likely than the leptonic ones. The first TeV γ-rays observed in the direction of GC were from Sagittarius A * (HESS J1745-290) [72], the galactic super massive black hole and the SNR Sgr A East detected by the HESS telescope. Reference [66] estimates the possibility to detect, during five years, about three (two) neutrino events with energies higher than 1 TeV (5 TeV) from the Galactic Center by neutrino telescopes with volume ~ 1 km^3.

1.3.2.8 Fermi Bubbles

Recently, the Fermi satellite showed the evidence of a new feature in the Milky Way Galaxy by detecting γ-rays with a hard and relatively uniform energy spectrum [73]. This feature is presented as two bubbles shaped region centered on the core of Milky Way, perpendicular to the galactic plane, extending 10 kpc from the center of the galaxy (Figure 1.17). Reference [74] shows that the Fermi Bubbles are a promising source of high energy neutrinos.

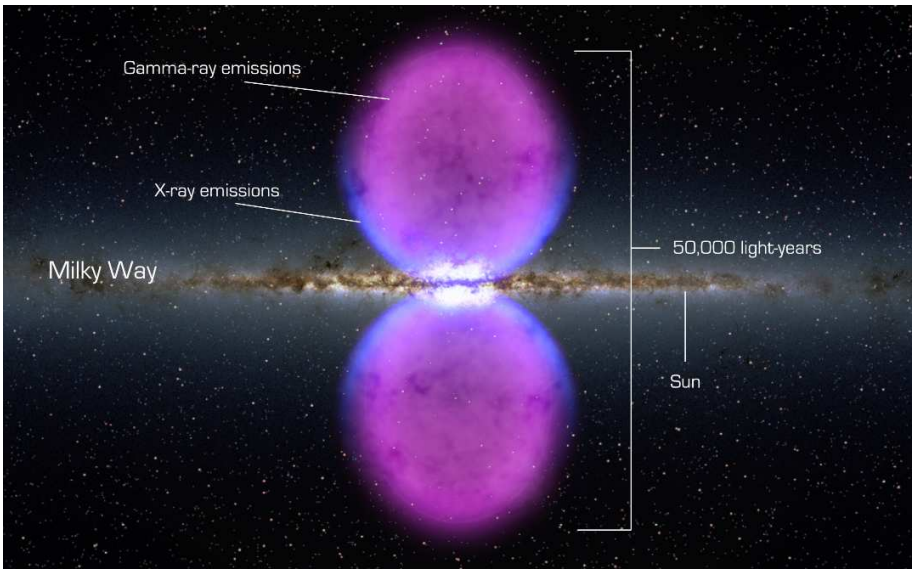

Figure 1.17: The Fermi Bubbles.

Chapter 2

Estimation of the high energy cosmic neutrino flux in ANTARES

In this chapter, the flux of the high energy cosmic neutrinos is estimated in ANTARES. Assuming hadronic scenarios in the galactic and extragalactic sources, the estimated neutrino flux is extracted from the γ-ray astronomy data. In Section 2.1, the various steps of this study are shown. In sections 2.2 and 2.3, the extragalactic background light and the optical depth of the very high energy γ-rays are presented respectively. After their emission, the extragalactic γ-rays are attenuated by this background on their way to Earth. Section 2.4 discusses the conversion from γ-ray energy spectrum to neutrino spectrum at the source. Taking into account the effects of neutrino oscillations, the energy spectrum of the neutrinos at the Earth is deduced. Finally, in Section 2.5, the expected number of neutrino events in ANTARES is calculated. In the following, the word neutrino refers to both neutrino and anti-neutrino.

2.1 Steps of the neutrino flux estimation

The flux of the high energy cosmic neutrinos can be estimated using the CRs or the γ-rays spectra. For the CRs, with the hypothesis that the chemical composition of the UHECRs are protons, Waxman and Bahcall calculated the neutrino production rate as a function of time, volume and energy in the Universe which is equal to [75, 76]:

$$E_p^2 \frac{\mathrm{d}N}{\mathrm{d}E_p \mathrm{d}V \mathrm{d}t} \approx 0.65 \times 10^{44} \phi(z) \text{ erg.Mpc}^{-3}.\text{an}^{-1} \tag{2.1}$$

where $\phi(z)$ is the neutrino production factor as a function of redshift z ($\phi(0) = 1$). In first approximation, this factor can be removed since the free mean path

of the UHECRs is relatively small (GZK cut-off).

Using Equation 2.1, an upper limit of the neutrino flux emitted by the extragalactic sources (AGN, GRB, ...) is deduced (Equation 2.2). The calculation is based on the energy conservation principle where the energy of the produced neutrinos is lower than the energy of the protons.

$$E_\nu^2 \phi_\nu < 2 \times 10^{-8} \xi_z \left[\frac{\left(E_p^2 \frac{\mathrm{d}N}{\mathrm{d}E_p \mathrm{d}V \mathrm{d}t} \right)_{z=0}}{10^{44}\ \mathrm{erg.Mpc^{-3}.an^{-1}}} \right] \ \mathrm{GeV.cm^{-2}.s^{-1}.sr^{-1}} \qquad (2.2)$$

where ξ_z represents the evolution of the neutrino production as a function of the redshift [76].

In this chapter, the Very High Energy (VHE) γ-rays are used to estimate the neutrino flux rather than the CRs. The study consists from the following steps:

1. Using the VHE γ-ray spectrum at the Earth, the VHE γ-ray flux is estimated at the source. For the galactic sources, the attenuation of these γ-rays on their way to Earth is negligible, therefore the energy spectra at the source and at the Earth are considered as identical. However, for the extragalactic sources, the flux of the VHE γ-rays is attenuated by the interaction with the intergalactic photons as illustrated in Figure 2.1.

2. Estimation of the neutrino flux at the source from the estimated γ-ray flux at the source.

3. Estimation of the neutrino flux at the Earth taking in account the oscillation phenomenon of neutrinos.

4. Finally, calculation of the number of neutrino events detected by ANTARES.

2.2 Extragalactic Background Light

The Extragalactic Background Light (EBL) is an intergalactic ocean of photons emitted by the galaxies and accumulated over all the history of the Universe. Based on the cosmological principle[1], the EBL is assumed to be isotropic for a given observer. The precise measurement of the EBL is difficult from the Earth due to the photons emitted by terrestrial, zodiacal and galactic sources which contribute to 99% of night light. The study of the EBL constraints the galaxies formation and the baryonic content of the Universe.

[1]The cosmological principle assumes the homogeneity and the isotropy of the Universe at large scale and the universality of the laws of physics.

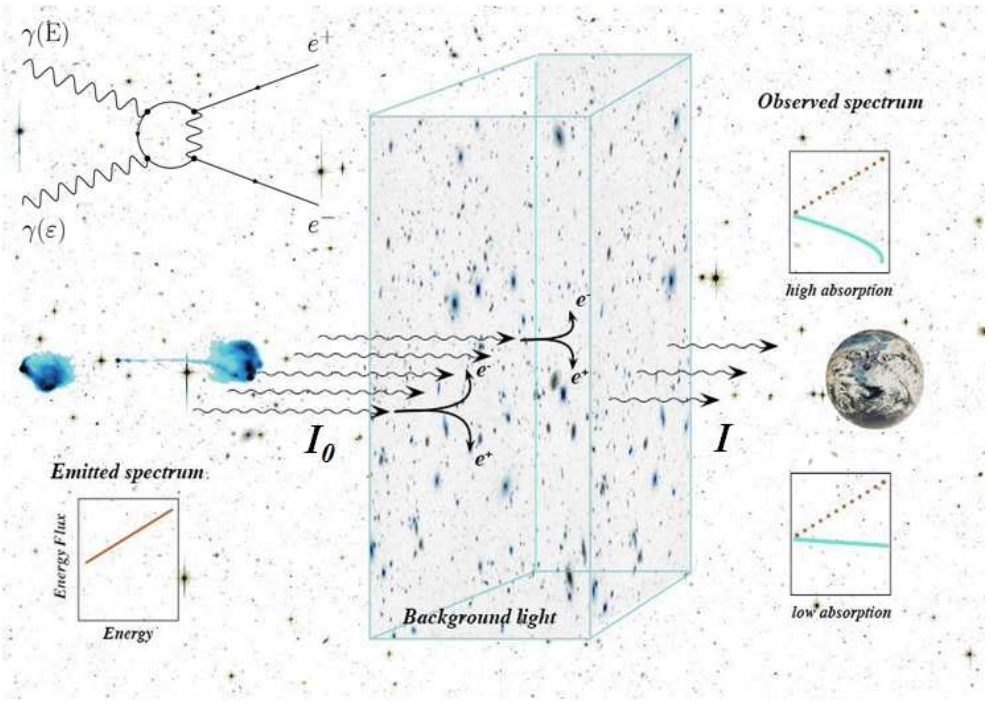

Figure 2.1: Schematic presentation of VHE γ-rays absorption by the extragalactic background light photons. The Feynman diagram of $\gamma(E)\gamma(\varepsilon)$ interaction and γ-rays spectra at the source and at the Earth are shown.

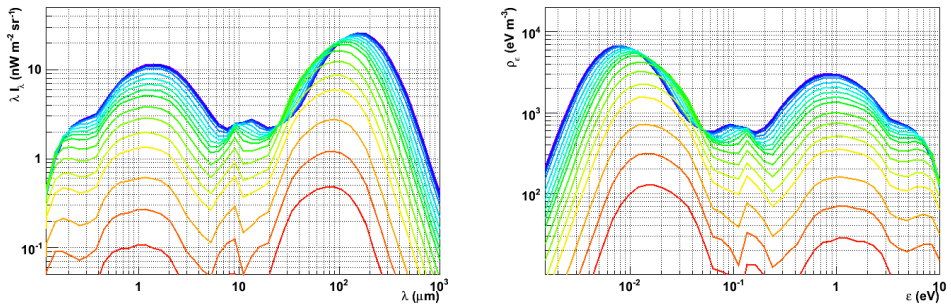

Figure 2.2: The EBL spectrum as a function of EBL photon wave length (left) and the energy density of the EBL as a function of EBL photon energy (right). The colors present the redshift of the source, from blue to red, $z = 0$, 0.01, 0.03, 0.05, 0.1, 0.2, 0.3, 0.4, 0.5, 0.6, 0.8, 1.0, 1.25, 1.5, 2.0, 2.5, 3.0 [77].

Figure 2.2 shows the energy spectrum and the density of the EBL photons [77]. The plot at the right is deduced from the left plot using the following equation:

$$\rho_\varepsilon \text{ (nJ.m}^{-3}) = \frac{4\pi}{c}\lambda I_\lambda \text{ (nW.m}^{-2}\text{.sr}^{-1}) \tag{2.3}$$

The EBL energy spectrum is calculated by counting the galaxies and estimating the flux of their photons emission. Constraints on the EBL flux can also be obtained from γ-rays relying on assumptions of the γ-ray energy spectrum index at the source. Comparing with the measured γ-ray spectrum at the Earth, the absorption of the γ-rays, by the EBL photons, are deduced. At $z = 0$, the EBL energy spectrum consists of two main bumps. The high energy bump (peaked at ~ 0.8 eV) is due to the starlight over all redshifts since the formation of the first star. The low energy bump (peaked at $\sim 8 \times 10^{-3}$ eV) is due to the old population of stars at high redshifts and the re-radiation, as a thermal emission, by the dust of the galaxies after the starlight absorption. Figure 2.2 shows clearly that the EBL density is higher for the local Universe (low z) and it decreases as a function of the redshift.

2.3 Optical depth

A VHE γ-ray with energy E emitted by an extragalactic source at redshift z_s can interact with an EBL photon with energy ε creating an electron and a positron: $\gamma(E)+\gamma(\varepsilon) \rightarrow e^+ + e^-$. The energies E and ε are the redshifted energies observed from the Earth. The intensity of the γ-rays at the source, I_0, is attenuated because of the $\gamma(E)\gamma(\varepsilon)$ interactions to be I at the Earth $(I < I_0)$. This attenuation is quantified by the optical depth τ and defined as in the following equation:

$$I = I_0 \times e^{-\tau} \tag{2.4}$$

The optical depth τ is a function of the energy E and the distance between the source and the Earth (redshift of the source z_s).

The cross-section of the $\gamma(E)\gamma(\varepsilon)$ interaction in the comoving referential frame, with the transformed energies $E' = (1+z)E$ and $\varepsilon' = (1+z)\varepsilon$, is given by [78]:

$$\sigma'_{\gamma\gamma}(E,\varepsilon,\mu,z) = \frac{3\sigma_T}{16}\left(1-\beta^2\right)\left[2\beta\left(\beta^2-2\right)+\left(3-\beta^4\right)\ln\left(\frac{1+\beta}{1-\beta}\right)\right] \tag{2.5}$$

$$\beta \equiv \sqrt{1-\frac{\varepsilon'_{th}(E,\mu,z)}{\varepsilon'}} = \sqrt{1-\frac{\varepsilon'_{th}(E,\mu,z)}{(1+z)\varepsilon}} \tag{2.6}$$

$$\varepsilon'_{th}(E,\mu,z) = \frac{2(m_e c^2)^2}{(1-\mu)E'} = \frac{2(m_e c^2)^2}{(1-\mu)(1+z)E} \tag{2.7}$$

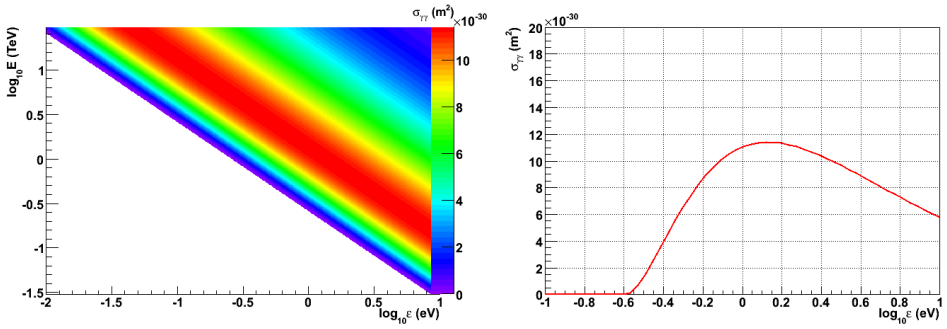

Figure 2.3: The cross section of $\gamma(E)\gamma(\varepsilon)$ interaction as a function of the observed energies E and ε at redshift $z = 0$ (left) and as a function of the observed energy ε at redshift $z = 0$ and with $E = 1$ TeV (right).

where:

- $\sigma_{\rm T} = 6.65 \times 10^{-29}$ m^2 is the Thompson cross section.
- $\varepsilon'_{\rm th}(E,\mu,z)$ is the energy threshold of the $\gamma(E)\gamma(\varepsilon)$ interaction in the comoving referential frame.
- $\mu \equiv \cos\theta'$ where θ' is the interaction angle of both photons in the comoving referential frame.

Figure 2.3 (left) shows that the cross section of $\gamma(E)\gamma(\varepsilon)$ interaction is maximum for $E \times \varepsilon \approx 4(m_{\rm e}c^2)^2 \approx 10^{12}$ eV^2. In the white part of the plot at the left and for $\log_{10}\varepsilon <$ -0.58 in the plot at the right, the cross section is null because the ε is less than the energy threshold of the interaction.

The optical depth is given by the following 3D integral [79]:

$$\tau(E,z_{\rm s}) = \int_0^{z_{\rm s}} {\rm d}z \frac{{\rm d}l}{{\rm d}z} \int_{-1}^{+1} {\rm d}\mu \frac{1-\mu}{2} \int_{\varepsilon'_{\rm th}(E,\mu,z)}^{+\infty} {\rm d}\varepsilon' n'_{\varepsilon}(\varepsilon,z)\sigma'_{\gamma\gamma}(E_\gamma,\varepsilon,\mu,z) \qquad (2.8)$$

where $n'_{\varepsilon}(\varepsilon,z){\rm d}\varepsilon'$ is the comoving number density of EBL photons with energies between ε' and $\varepsilon' + {\rm d}\varepsilon'$ at redshift z. $n'_{\varepsilon}(\varepsilon,z){\rm d}\varepsilon'$ is calculated transforming the observed EBL photons energy ε to the comoving referential frame ($\varepsilon' = (1+z)\varepsilon$). The cosmological distance ${\rm d}l/{\rm d}z$ is given by:

$$\frac{{\rm d}l}{{\rm d}z} = c\frac{{\rm d}t}{{\rm d}z} = \frac{R_H}{(1+z)D(z)} \qquad (2.9)$$

$$D(z) \equiv \{(1+z)^2(\Omega_m z+1) + z(2+z)[(1+z)^2\Omega_r - \Omega_\Lambda]\}^{1/2} \qquad (2.10)$$

where:

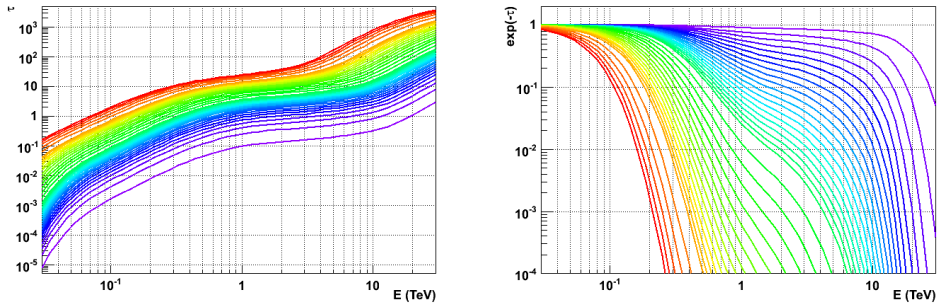

Figure 2.4: The optical depth, τ (left) and $e^{-\tau} = I/I_0$ (right), of the VHE γ-rays emitted by an extragalactic source at different redshifts. The colors present the redshift of the source, from bleu to red, $z = 0.01, 0.025, 0.041, 0.056, 0.071, 0.086, 0.102, 0.117, 0.132, 0.147, 0.163, 0.178, 0.193, 0.208, 0.224, 0.239, 0.254, 0.269, 0.285, 0.3, 0.35, 0.4, 0.45, 0.5, 0.55, 0.6, 0.65, 0.7, 0.75, 0.8, 0.85, 0.9, 0.95, 1.0, 1.2, 1.4, 1.6, 1.8, 2.0$ [77].

- Ω_Λ is the cosmological constant given by $\Omega_\Lambda = \Lambda/3H_0^2$.
- Ω_m and Ω_r are the matter and radiation densities, respectively, normalized to the critical density.
- $R_H \equiv c/H_0$ is Hubble's radius.
- $H_0 = 70$ km.s^{-1}.Mpc^{-1} is Hubble's constant.
- c is the speed of light 299792458 m.s^{-1}.

The 3D integral of Equation 2.8 is computed numerically by Monte-Carlo method where the results are in very good agreement with Reference [77].

Figure 2.4 shows that the attenuation of the γ-rays is more important for the relatively high energy γ-rays than the low energy ones. As it is expected, the attenuation increases with the redshift of the γ-ray sources.

2.4 Neutrino flux estimation at the Earth

Assuming hadronic production of γ-rays by the decay of π^0 only, the neutrino and the γ-ray fluxes are related by the following equation [80]:

$$\int \frac{\mathrm{d}N_\gamma}{\mathrm{d}E_\gamma} E_\gamma \mathrm{d}E_\gamma = \eta \int \frac{\mathrm{d}N_\nu}{\mathrm{d}E_\nu} E_\nu \mathrm{d}E_\nu \tag{2.11}$$

where η depends on the energy distribution of the pions. For pp ($p\gamma$) interaction, η is equal to $1/3$ ($1/4$). Therefore, both interactions provide neutrino

fluxes in the same order of magnitude for the same γ-ray flux. For the rest of this study, pp parameterization is considered [66] since the uncertainty on the emission models are equal or even higher than one order of magnitude. The adopted assumptions are:

- the detected γ-rays are emitted by hadronic processes, more precisely by neutral pion decay only, the synchrotron-proton radiation is considered negligible.
- the absorption of the γ-rays in the source is negligible. This assumption is conservative since any consideration of the source absorption will increase the estimated neutrino flux.
- the pions disintegrate before their interaction with other particles.
- the pp parameterization leads to (ν_e : ν_μ : ν_τ) = (1 : 2 : 0) ratio of neutrino flavour production at the source.
- the distance between the sources in question and the Earth are sufficiently large to have a total neutrino mixing (ν_e : ν_μ : ν_τ) = (1 : 1 : 1) [81].
- the energy spectrum index and the energy cut-off of the primary protons are $1.8 < \Gamma_p < 3.0$ and 10 TeV $< \varepsilon_p <$ 1 PeV respectively.

The energy spectrum of the primary protons is a power-law distribution given by the following equation:

$$\frac{\mathrm{d}N_p}{\mathrm{d}E_p} = k_p \left(\frac{E_p}{1\mathrm{TeV}} \right)^{-\Gamma_p} \exp\left(-\frac{E_p}{\varepsilon_p} \right) \tag{2.12}$$

where k_p is the normalization constant. The energy spectra of γ-rays and the neutrinos are given by:

$$\frac{\mathrm{d}N_{\gamma/\nu}}{\mathrm{d}E_{\gamma/\nu}} = k_{\gamma/\nu} \left(\frac{E_{\gamma/\nu}}{1\mathrm{TeV}} \right)^{-\Gamma_{\gamma/\nu}} \exp\left(-\sqrt{\frac{E_{\gamma/\nu}}{\varepsilon_{\gamma/\nu}}} \right) \tag{2.13}$$

where k_γ (k_ν), Γ_γ (Γ_ν) and ε_γ (ε_ν) are the normalization constant, the spectral index and the energy cut-off respectively for γ-rays (neutrinos). These parameters and those for protons are related by equations 2.14, 2.15 and 2.16 [66].

$$k_\nu \approx (0.71 - 0.16\Gamma_p) k_\gamma \tag{2.14}$$

$$\Gamma_\nu \approx \Gamma_\gamma \approx \Gamma_p - 0.1 \tag{2.15}$$

$$\varepsilon_\nu \approx 0.59\varepsilon_\gamma \approx \varepsilon_p/40 \tag{2.16}$$

2.5 Estimated number of neutrino events detected by ANTARES

Although ANTARES is sensitive to electronic and tauic neutrinos, here, only the muonic neutrino channel is considered (Section 3.1.1). For the rest of this chapter the word neutrino refers to muon neutrino and muon anti-neutrino.

For an estimated neutrino flux $\mathrm{d}N_\nu/\mathrm{d}E_\nu$, the number of neutrino events that can be seen by the ANTARES telescope is given by the following integral:

$$N_\nu = V \int_{\Delta T} \mathrm{d}t \int_{E'}^{+\infty} \mathrm{d}E_\nu A_{\mathrm{eff}}^{\nu} \frac{\mathrm{d}N_\nu}{\mathrm{d}E_\nu} \tag{2.17}$$

where V is the visibility of the source (Section 5.3 and Appendix D), ΔT is the data taking period and A_{eff}^{ν} is the effective area of the telescope (sections 5.3 and 6.2). In this section, the number of neutrinos is estimated for 2007 + 2008 period (ΔT = 295 active days). During this period, the detector knew four different configurations (5-line, 9-line, 10-line and 12-line). The effective area of the combined configuration is calculated in Chapter 6 and it is shown in Figure 2.6 (left).

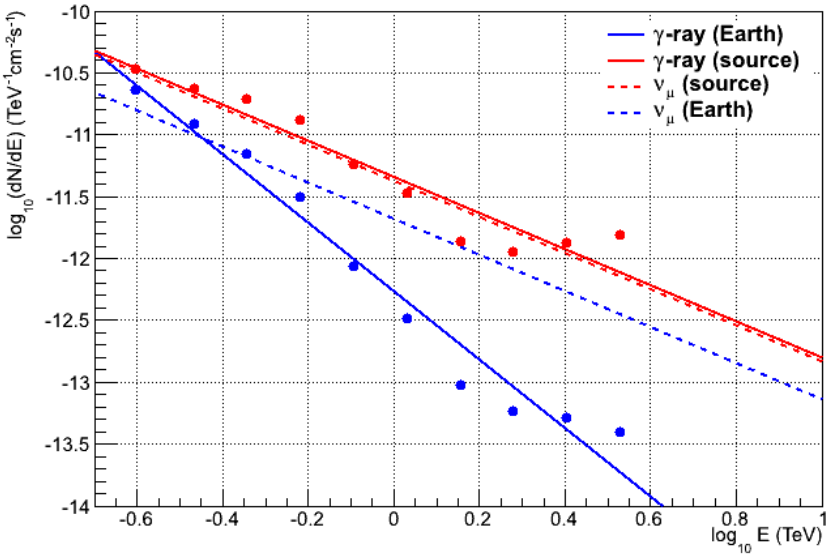

Figure 2.5: The energy spectrum of 1ES 1101-232 at the source and the Earth for both γ-rays and neutrinos.

Figure 2.5 shows the γ-ray energy spectrum (logarithmic fit with a power law function) of the extragalactic source 1ES 1101-232 measured by the HESS tele-

scopes [82]. The γ-ray spectrum at the source is calculated using Equation 2.4 then the neutrino spectra are deduced as it is explained in Section 2.4. The energy cut-off ε_ν is considered 10^7 GeV because of the high opacity of the Earth for the very high energy neutrinos ($E > 10^7$ GeV). The number of neutrinos is calculated integrating the factor $A^\nu_{\text{eff}} \mathrm{d}N_\nu/\mathrm{d}E_\nu$ (Figure 2.6 right), using Equation 2.17 with E' = 1 TeV. The visibility of this source being 0.63, the estimated number of events is equal to $1.08 \times 0.63 = 0.68$ for ΔT = 295 active days. E' is taken 1 TeV to reject a high fraction of atmospheric neutrinos.

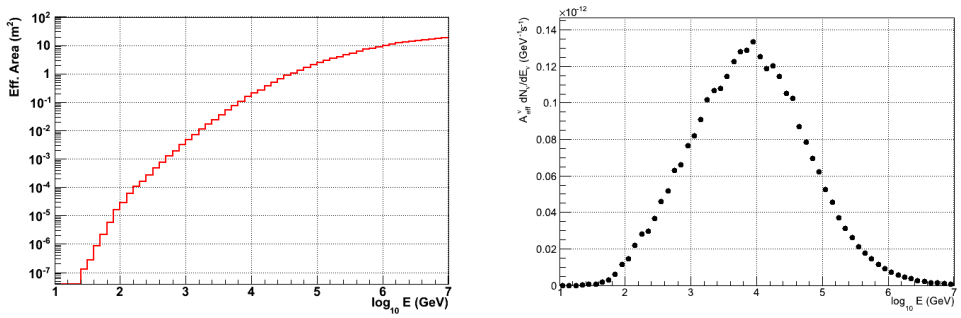

Figure 2.6: The effective area of ANTARES with 5-9-10-12-line combined configuration with AAfit reconstruction strategy (left) and the factor $A^\nu_{\text{eff}} \mathrm{d}N_\nu/\mathrm{d}E_\nu$ (right).

Table 2.1 shows the estimated number of high energy neutrinos for different sources. The expected number for the extragalactic sources is higher than the galactic sources. For about ten years of data taking, it may be possible to detect cosmic neutrinos emitted by extragalactic sources by the ANTARES neutrino telescope.

Name	z	Γ_γ (Earth)	Γ_ν	N_ν (Earth)	Visibility	N_ν (ANTARES)
1ES 1101-232	0.186	2.76	1.46	1.08	0.63	0.68
1ES 0347-121	0.188	2.82	1.50	0.71	0.56	0.40
PKS 0548-322	0.069	2.32	1.86	0.02	0.70	0.014
Centaurus A	0.0009	2.74	2.74	0.0006	0.83	0.0005
RX J1713.7-3946	0	2.25	2.25	0.17	0.78	0.13
RX J0852.0-4622	0	2.30	2.30	0.15	0.92	0.14
HESS J1023-575	0	2.53	2.53	0.017	1.00	0.017
RCW 86	0	2.55	2.55	0.014	1.00	0.014

Table 2.1: The estimated number of high energy cosmic neutrinos ($E_\nu > 1$ TeV) with 5-9-10-12-line combined configuration using AAfit reconstruction strategy for 295 days. The first four sources are extragalactic sources and the others are galactic sources.

Chapter 3

Neutrino detection with ANTARES

In this chapter, the detection of high energy cosmic neutrinos with the ANTARES telescope is discussed. Firstly, the neutrino and the muon interactions with matter, the Cherenkov effect and the detection principle are introduced. The underwater neutrino telescope ANTARES with its different components are described, then the data acquisition, the trigger and the time calibration are presented. The atmospheric and the optical backgrounds are also discussed. The Monte-Carlo simulations and the muon track reconstruction algorithms are discussed as well. Finally, the kilometer cubic (km^3) future detectors like IceCube and KM3NeT are presented. The information given in this chapter is manly based on the references [83, 84].

3.1 High energy cosmic neutrino detection

The weakness of the cross section of the neutrino interaction with matter is an advantage for the neutrino astronomy and a disadvantage at the same time. The detection of neutrinos is a difficult challenge because of this low cross section. In this section, the Cherenkov effect and the kinematics of the neutrino interaction with matter are presented, followed by the detection principle.

3.1.1 High energy neutrino interactions

Neutrinos can interact with matter via Gravitational and Weak interactions only. For the mass scales used in the ANTARES experiment, Gravitational interaction can be neglected. For the Weak interaction, neutrinos interact through Neutral Current (NC) or Charged Current (CC). In the NC, they exchange the gauge boson Z^0 with a nucleon N (proton or neutron) producing a hadronic shower (Equation 3.1).

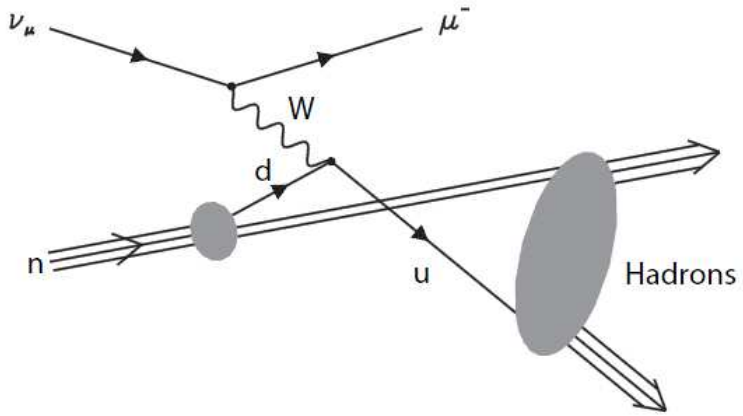

Figure 3.1: The Feynman diagram showing the interaction between a neutrino and a nucleon.

$$\nu_l(\overline{\nu}_l) + N \rightarrow \nu_l(\overline{\nu}_l) + \text{hadronic shower} \tag{3.1}$$

While in the CC, neutrinos exchange the gauge bosons W^+ or W^- producing leptons and hadronic showers as presented in Equation 3.2. The Feynman diagram of Figure 3.1 shows the muon production by the interaction of a muon neutrino with a Down quark.

$$\nu_l(\overline{\nu}_l) + N \rightarrow l(\bar{l}) + \text{hadronic shower} \tag{3.2}$$

For both interactions (neutral and charged) between the neutrino and the nucleon, the cross section is calculated using the Electro-Weak theory and quark-parton's model of Bjorken [85, 86]. It is given by:

$$\frac{\mathrm{d}\sigma^{\mathrm{NC/CC}}}{\mathrm{d}x\,\mathrm{d}y} = \frac{2G_{\mathrm{F}}^2 M E_\nu}{\pi}\left(\frac{M_{Z/W}^2}{Q^2+M_{Z/W}^2}\right)\left[x.q(x,Q^2)+x.\overline{q}(x,Q^2)(1-y^2)\right] \tag{3.3}$$

where G_{F} is the Fermi constant, M the nucleon mass, E_ν the neutrino energy, $M_{Z/W}$ the mass of Z^0 / $W^\pm$ and Q is the parton quadri-momentum.

$$q(x,Q^2) = \frac{u_v(x,Q^2)+d_v(x,Q^2)}{2} + \frac{u_s(x,Q^2)+d_s(x,Q^2)}{2} + s_s(x,Q^2) + b_s(x,Q^2) \tag{3.4}$$

$$\overline{q}(x,Q^2) = \frac{u_s(x,Q^2)+d_s(x,Q^2)}{2} + c_s(x,Q^2) + t_s(x,Q^2) \tag{3.5}$$

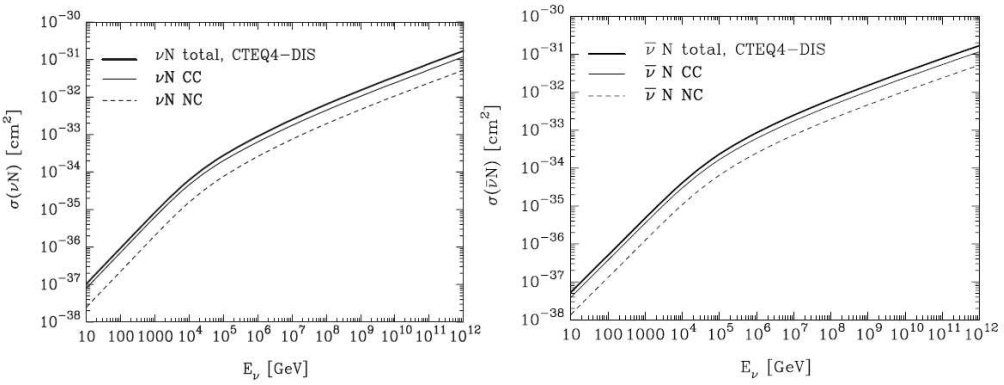

Figure 3.2: The interaction cross section of neutrino (left) and anti-neutrino (right) with the Earth as a function of the (anti-) neutrino energy.

u, d, c, s, t and b represent the distributions of the different quarks in the nucleon (indices v and s refer to valence and sea respectively). The Bjorken variables, x and y, are given by:

$$x = \frac{Q^2}{2M(E_\nu - E_\mu)} \quad \text{and} \quad y = 1 - \frac{E_\mu}{E_\nu} \tag{3.6}$$

Figure 3.2 shows the cross section of the neutrino and anti-neutrino interaction with Earth as a function of the neutrino energy. This cross section increases with the energy. For energies lower than about[1] 3.2 TeV, the cross section of the neutrino interaction is higher than that of the anti-neutrino because of the domination of the valence quark interactions. Once the energy is higher than about 3.2 TeV, both neutrinos and anti-neutrinos have the same cross-section.

For an underwater neutrino telescope such as ANTARES, the detection relies on charged current interactions as shown in Equation 3.2. The neutrinos are indirectly detected by the detection of leptons (electron, muon, and tau). This technique is explained in Section 3.1.3. Among the three lepton flavours, the most important one for an underwater neutrino telescope is the muon. In fact, after the interaction of neutrinos with Earth and the production of leptons, only the muons have a large mean free path. The electrons decelerate rapidly by emission of Bremsstrahlung radiation or/and an electron-positron pair creation. The secondary electrons decelerate the same way as the primary ones and electromagnetic showers are created. The taus disintegrate rapidly due to their short life time ($t_\tau = 290.6 \pm 1.0 \times 10^{-15}$ s) relatively to that of the muons ($t_\mu = 2.197019 \pm 0.000021 \times 10^{-6}$ s) [87]. The muons propagate for a few kilometers

[1] $M_W^2/2m_N \approx 3.2$ TeV

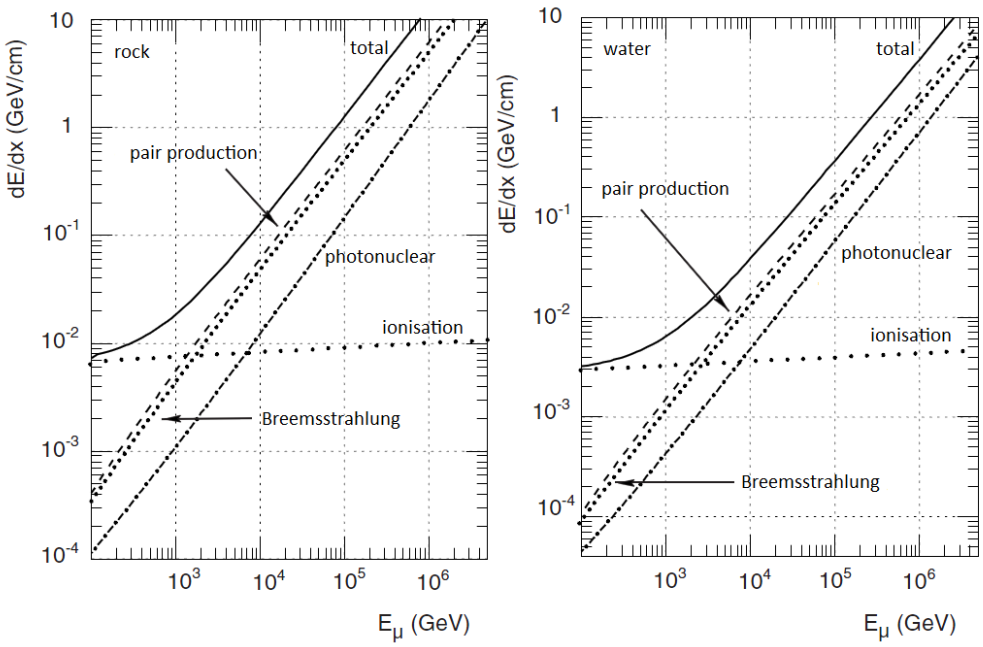

Figure 3.3: The energy loss of the muon in rocks (left) and water (right) as a function of the energy of the muon.

($\sim$ 5 km for $E_\mu = 100$ TeV) [88] before their disintegration losing their energy by four possible processes:

- the ionization of atoms and molecules resulting the emission of δ-rays (relativistic electrons).
- the creation of electron-positron pairs then an electromagnetic shower.
- the emission of Bremsstrahlung radiation while passing nearby atomic nuclei.
- the collision with atomic nuclei. The cross-section of this interaction for $E_\mu \lesssim 10^4$ GeV is much lower than the first three interactions (Figure 3.3).

The Earth's magnetic field effect on the muon trajectory is neglected for the scales used in the ANTARES experiment. The angle between the incident neutrino and the muon is due to the kinematics of the neutrino-nucleon interaction. Figure 3.4 shows the median angular difference between the neutrino and the muon as a function of the neutrino energy. The angle between the neutrino and the muon decreases with the increase of the neutrino energy. For the same neutrino energy,

the median angular difference is smaller for events that respect the quality cuts defined in Chapter 5. This plot is obtained using Monte-Carlo simulation where the neutrino energy spectrum index is 2.

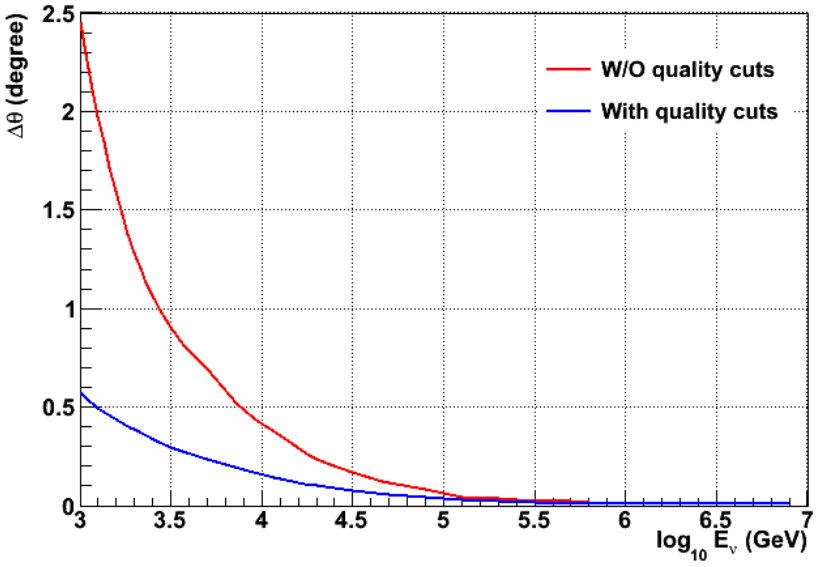

Figure 3.4: Median angular difference between the neutrino and the muon directions as a function of the neutrino energy. The red curve represents the up-going simulated neutrinos (seen by ANTARES) and the blue one represents those which respect the quality cuts optimized in Chapter 5.

In a first approximation, the neutrino-muon angular difference can be given by [89]:

$$\sqrt{\langle \theta^2_{\nu\mu} \rangle} = \sqrt{\frac{m_N}{E_\nu}} \text{ (rad)} \tag{3.7}$$

Figure 3.5 presents the correlation (correlation factor = 0.79) between the energy of the neutrino and the energy of the produced muon for up-going events (the zenith cut is applied on the true zenith of the simulated neutrino). The presented histogram shows that the energy of the incident neutrinos is always higher than the energy of the produced muons.

3.1.2 Cherenkov effect

The displacement of an electrically charged particle, such as the muon, inside a dielectrically transparent medium with a velocity higher than the speed of light in that medium polarizes the local molecules. Returning rapidly to the stable

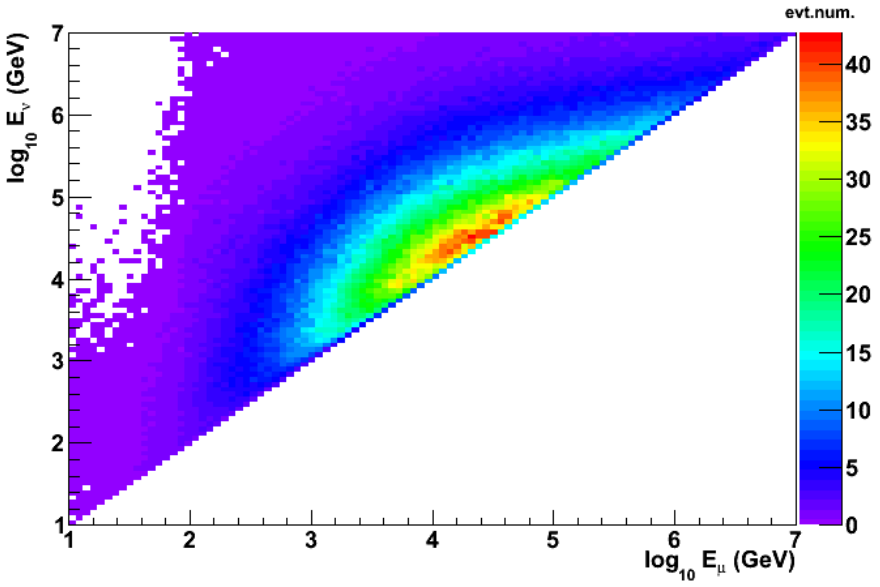

Figure 3.5: The neutrino energy as a function of produced muon energy. The plot presents all up-going simulated neutrinos seen by ANTARES.

state, these molecules emit prompt spherical radiation. The luminous spheres, created faster than the speed of light in the medium all along the muon's trajectory, interfere together and produce a front wave as shown in Figure 3.6. This effect was rigorously characterized by the physicist Pavel Alekseyevich Cherenkov. The threshold energy of the charged particle, to produce Cherenkov light, is given by:

$$E_{\text{th}} = \frac{m_0 c^2}{\sqrt{1 - \frac{v_{ph}^2}{c^2}}} \tag{3.8}$$

where m_0 is the proper mass of the charged particle, v_{ph} is the speed of light in the medium and c is the speed of light in vacuum.

The angle between the muon and the front wave photons, θ_C, shown in Figure 3.6, is given as a function of β (the ratio of the velocity of the muon to the speed of light in vacuum) and the refraction index n of the medium which is, itself, a function of the electric permittivity. θ_C is given by:

$$\cos\theta_C = \frac{1}{\beta \times n} \tag{3.9}$$

In the ANTARES zone, the refraction index of Cherenkov photons is equal to 1.35. For an ultra relativistic muon ($\beta \sim 1$), θ_C is equal to 42.2°. The proper

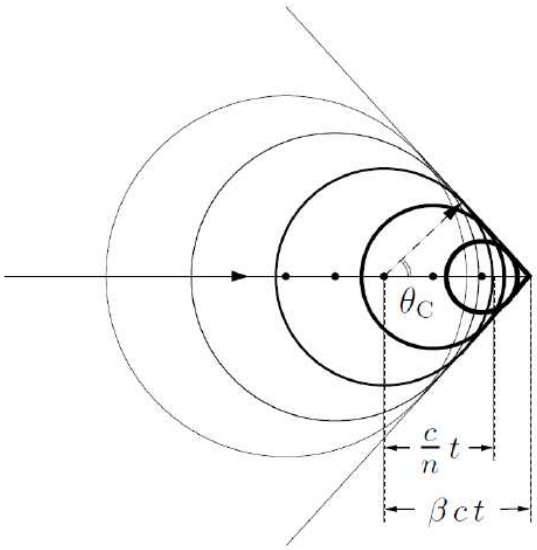

Figure 3.6: The emission of the spherical radiation and the front wave formation.

mass of the muon is equal to 105.658367 ± 0.000004 MeV [87]. Therefore, the threshold energy of the muon is 160 MeV. This value is computed using Equation 3.8.

The spectral distribution of Cherenkov photons is given by [90]:

$$\frac{\mathrm{d}N}{\mathrm{d}x\mathrm{d}\lambda} = \frac{2\pi\alpha}{\lambda^2}\left(1 - \frac{1}{\beta^2 n^2}\right) \tag{3.10}$$

where $\alpha = 1/137$ is the fine-structure constant and λ is the wave length of the emitted photons. The ANTARES optical modules are sensible to $\lambda \in [300;600]$ nm. Using Equation 3.10, the muon emits about 350 photons/cm within the given λ range.

3.1.3 Detection principle

When a high energy cosmic or atmospheric neutrino[2] ($E > 1$TeV) passes through Earth, it has a low probability to interact with a nucleon via Weak interaction and produce a relativistic muon (Equation 3.2 and Figure 3.1). The probability of having a high energy muon increases with the energy of the neutrino (Figure 3.5). If the muon is traveling in a dielectrically transparent medium as water or ice with

[2]The word "cosmic" ("atmospheric") neutrinos refers to the production of neutrinos outside (inside) Earth's atmosphere.

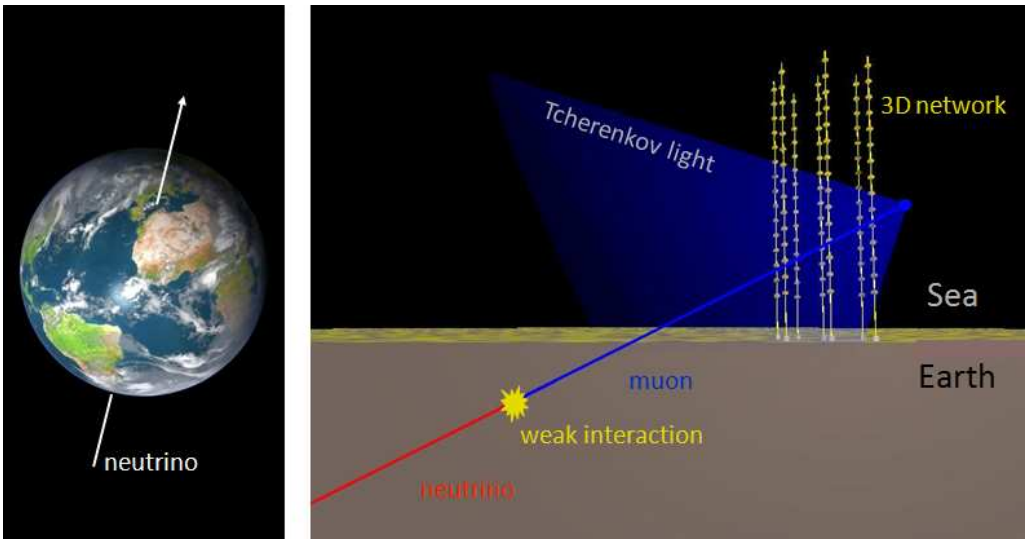

Figure 3.7: The detection of high energy cosmic neutrinos.

an energy higher than the threshold energy (160 MeV) (i.e. if the velocity of the muon is higher than the speed of light in the medium), it emits Cherenkov photons (Section 3.1.2).

In 1960, M. A. Markov proposed an idea to detect high energy neutrinos ($E > 1$TeV) [91]. His idea was based on the installation of a 3 dimensional photo-detector network in the sea water to detect the Cherenkov photons emitted by the relativistic muons. Knowing the positions of the optical modules and measuring the arrival time of the photons, the muon direction can be reconstructed (Figure 3.7). As shown in Figure 3.4, the muon direction is correlated with the neutrino direction and therefore the neutrino source can be located. To reduce the background, consisting of the down-going atmospheric muons, only up-going tracks are studied (Section 3.2.7.1).

3.2 ANTARES neutrino telescope

The ANTARES[3] Collaboration is formed of physicists from 28 institutes in 7 European countries (France, Germany, Italy, Netherlands, Romania, Russia and Spain), who constructed an underwater neutrino telescope in the Mediterranean Sea, 40 km south of Toulon, at 42°48′N, 6°10′E (Figure 3.8), at a depth of 2475 m.

[3]ANTARES is the acronym of "Astronomy with a Neutrino Telescope and Abyss environmental RESearch".

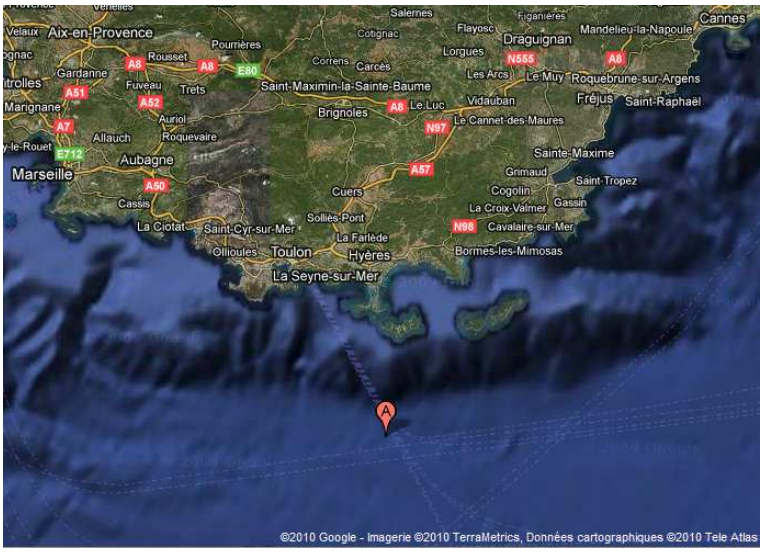

Figure 3.8: The point A indicates the ANTARES site [92].

In 1996, more than 60 deployment operations were done in the sea water in order to install instruments helping the study of the properties of water (light absorption length, salinity, ...) and the environment (bioluminescence, sea current velocity, ...). These operations led to the choice of the ANTARES site location shown in Figure 3.8.

To quantify the water quality, studies were made to calculate the effective attenuation length $L_{\text{eff.att.}}$ defined as follows:

$$I \propto \frac{I_0}{L} \times \exp\left(-\frac{L}{L_{\text{eff.att.}}}\right) \tag{3.11}$$

where I_0 is the light intensity at the source and I the intensity at the distance L from the source. The effective attenuation length $L_{\text{eff.att.}}$ is related to the absorption length $L_{\text{abs.}}$ and the scattering length $L_{\text{sca.}}$ by the following relation:

$$\frac{1}{L_{\text{eff.att.}}} = \frac{1}{L_{\text{abs.}}} + \frac{1}{L_{\text{sca.}}} \tag{3.12}$$

The direct measurement of the effective attenuation length gives $L_{\text{eff.att.}} = 41 \pm 1$ (stat.) ± 1 (syst.) m [93].

Section 3.1.3 explains that ANTARES probes the Universe by looking through Earth. The location of the site in the Mediterranean Sea provides ANTARES a field of view in the sky covering the Southern Hemisphere, a fraction of the Northern Hemisphere and the Galactic Center which is considered as a candidate of

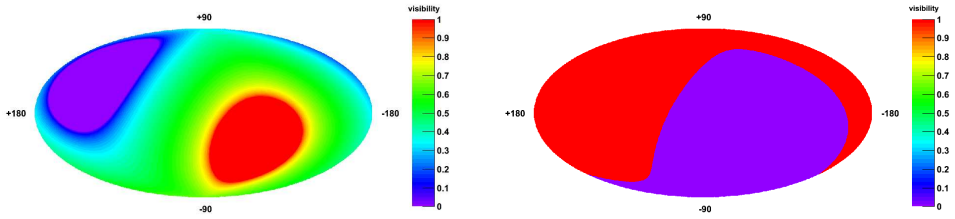

Figure 3.9: The visibility of ANTARES (left) and IceCube (right) in the Galactic Coordinates.

cosmic neutrino sources. The Galactic Center is visible 67% of the time. Thanks to the location of ANTARES and the South Pole neutrino telescope IceCube (Section 3.5.1), together they provide a full sky coverage for cosmic neutrinos search (Figure 3.9).

3.2.1 Final configuration

The ANTARES telescope (Figure 3.10) [94] is composed of 900 optical modules distributed over 12 lines of 450 m length. The lines are separated by about 70 m. Three optical modules are fixed on a storey and inclined downwards with an angle of 45° to the vertical. This angle is optimized for the detection of the upgoing muons. The storeys are separated by 14.5 m and each storey has a Local Control Module (LCM) which contains all the electronic installations. A group of 5 storeys form a sector. One of the five LCMs in the sector is the Master LCM (MLCM). The lines are fixed from the bottom by the Bottom String Socket (BSS) connected with an electro-optical interconnecting link (IL) cable to the Junction Box (JB). The information and the electrical power are transmitted by 40 km electro-optical cable connecting the JB to the control room in La Seyne-sur-Mer (Figure 3.8).

The registration of data started with the connection of Line 1 in March 2006. It was followed by Line 2 in September 2006, lines 3, 4, and 5 in January 2007, then lines 6, 7, 8, 9, and 10 in December 2007 and finally lines 11 and 12 in May 2008.

In addition to the 12 detector lines, the instrumentation line MILOM was installed in ANTARES site to measure and study different parameters [95]. It was operational from March 2005 to June 2007, then it was removed, modified, redeployed and renamed IL-07.

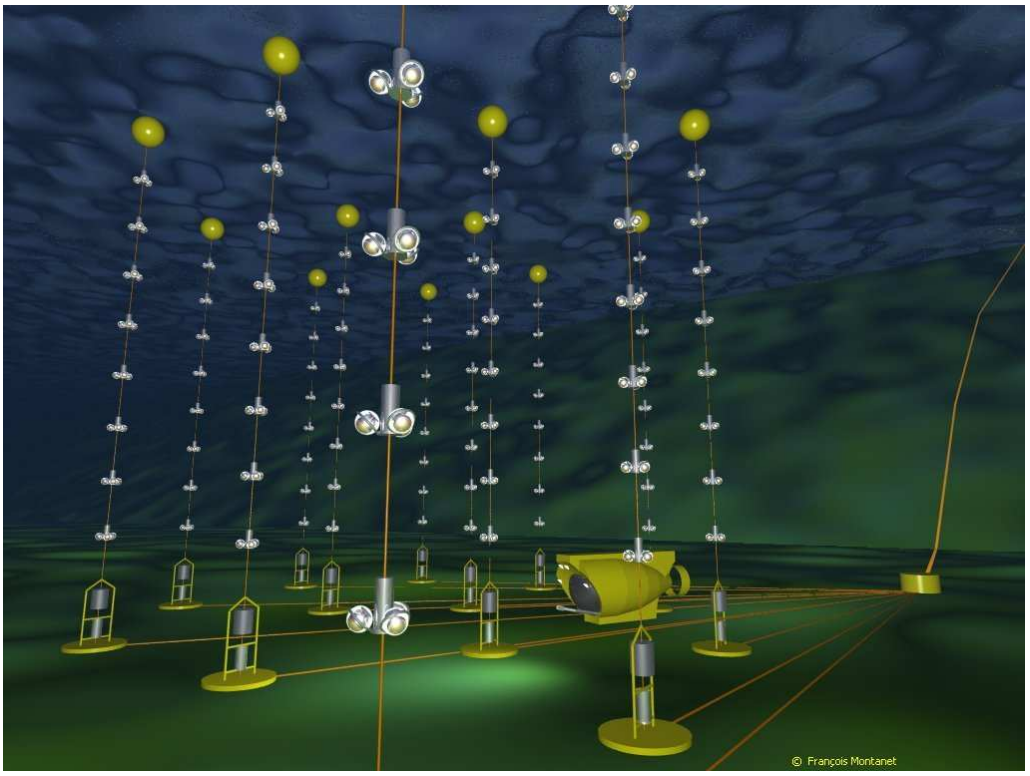

Figure 3.10: Schematic representation of the ANTARES telescope.

3.2.2 Detector storeys

The basic components of the detector storey (Figure 3.11) are:

- Optical Module Frame (OMF): it is the main support frame of the other storey components. The OMF is made from titanium.
- Local Control Module (LCM): it is located at the center of the storey and it contains the electronic installations. The LCM is responsible of the power distribution to the optical modules and the reception of the signal.
- 3 optical modules: they are located in the horizontal plane, forming an angle of 120° between them.
- hydrophone: 5 storeys per line contain a hydrophone used for the acoustic positioning system. A detailed description of the acoustic positioning system is presented in Chapter 4.

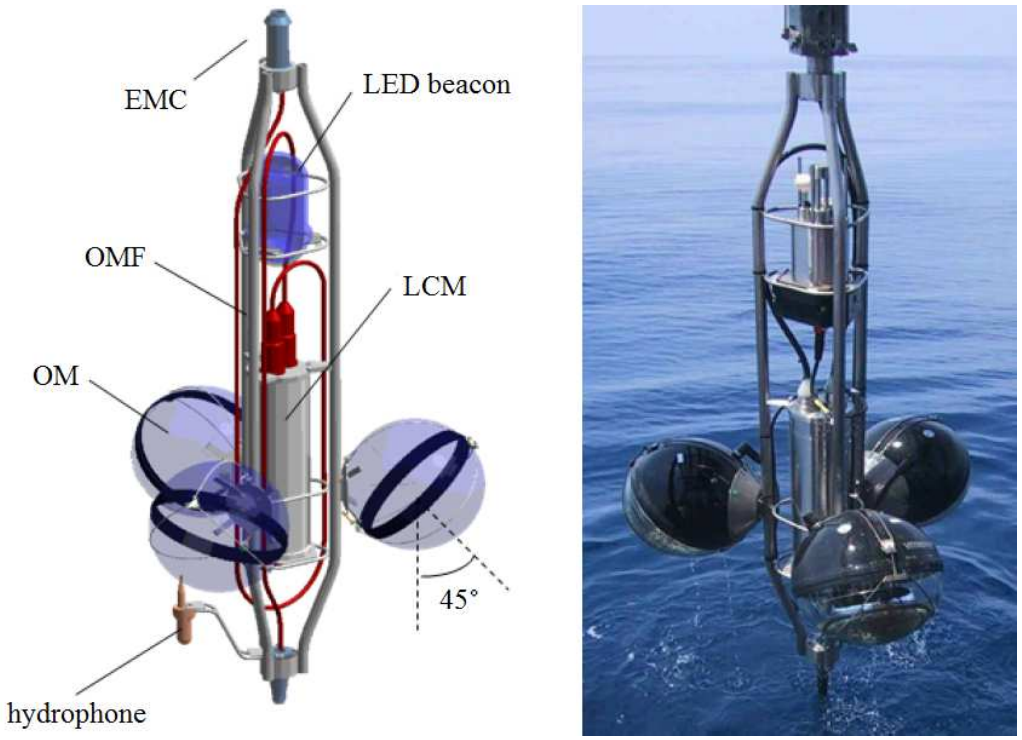

Figure 3.11: Storey of ANTARES detector.

- LED beacon: some storeys have a LED beacon used during the in situ calibrations (Section 3.2.6.2).

3.2.3 Optical modules

The optical modules [96] are the eyes of ANTARES (Figure 3.12). They contain the following components:

- glass sphere: with 43 cm of diameter, it protects the internal elements from surrounding sea water pressure (250 bars).
- photo-multiplier: it has a diameter of 25.4 cm, an area of 440 cm^2 and it contains a 14-stage amplification system. Its role is to convert the luminous signal to electrical signal.
- base: it converts the input low voltage (48 V) to a high voltage (from 800 V to 1200V) serving the photomultiplier.

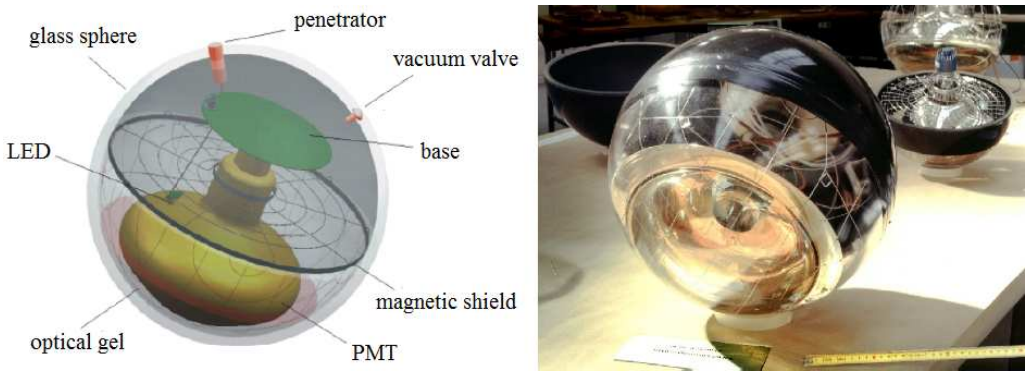

Figure 3.12: Optical module of ANTARES detector.

- OM-LCM link: it is a bi-directional electric link connecting the base and the LCM.
- magnetic shield: it is used to decrease the influence of the Earth's magnetic field on the electrons trajectories between the photocathode and the first dynode. The magnetic shield surrounds the bulb of the photomultiplier.
- LED system: it is used for the in situ calibration (Section 3.2.6.2). It monitors the transit time of the photomultiplier.
- gel: the gel is made of silicon material. It is an optical link between the photomultiplier and the glass and a mechanical link between the sphere, the photomultiplier and the magnetic shield.

3.2.4 Data acquisition

The Cherenkov light, emitted by the muon, is detected by the Photomultipliers (PMT). The PMT converts the optical signal to an electric signal. The electric signal is read by two Analogue Ring Samplers (ARS)s which digitise the signal then send it to the DAQ Board (Data AcQuisition).

3.2.4.1 Hit time and signal digitalisation by the ARS

The hit time is defined as the time when the electric signal, coming from the anode, is higher than the threshold voltage which is equal[4] to 0.3 p.e. (L0 trigger). The charge is integrated within a window of 25 ns after the hit time and 8 ns before

[4]p.e. stands for photoelectron.

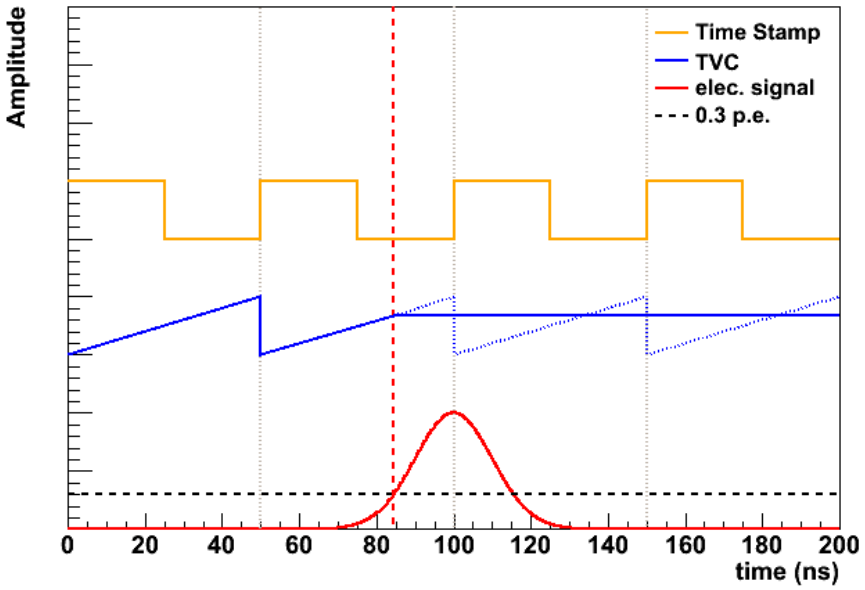

Figure 3.13: Signal arrival time measurement with TVC technique.

the hit time. After 25 ns of the hit time, the first ARS starts to digitise the signal and after 15 ns the relay will be passed to the second ARS.

Figure 3.13 shows the hit time measurement. The Time Stamp with a period of 50 ns, related to an external reference clock, counts the reference clock pulses. Between two pulses, the Time-to-Voltage Converter (TVC) will associate, with a precision of 0.1 ns, the hit time to a given voltage value.

To digitise the signal, the ARS needs 250 ns. This period is known as the ARS dead time. The use of the two ARSs decreases the dead time.

The data is saved on 6 bytes. One byte is for the ARS number and the data mode[5], three bytes are for the hit time, the fifth and the sixth bytes save the TVC and the Analogue to Digital Converter (ADC) values respectively. The data is then sent to the Field Programmable Gate Array (FPGA) in the LCM.

3.2.4.2 Data transmission to the shore

Figure 3.14 shows the data transmission to the shore. Each MLCM collects the data from the sector LCMs at up to 100 Mb/s and sends it to the String Control

[5]The data can be saved by 2 modes: SPE and WE. The first consists of the hit time and the charge. The second takes the information from the waveform of the electric signal in addition. All physical runs use the SPE mode.

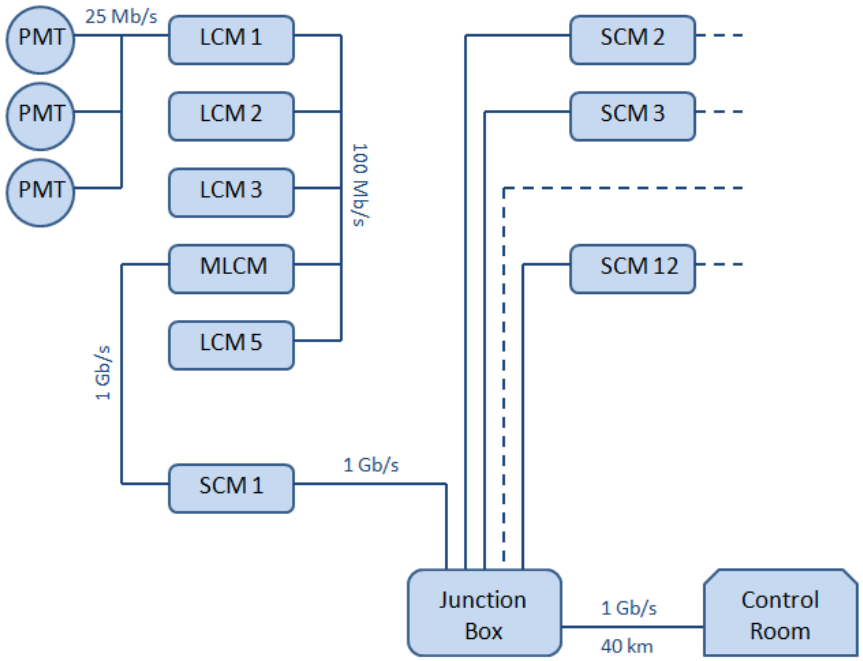

Figure 3.14: Data transmission to the shore.

Module (SCM) located in the BSS, then from the 12 BSSs to the junction box, and finally, with a 40 km cable, to the institute Michel Pacha at La Seyne-sur-Mer at up to 1 Gb/s. All the connections between the MLCMs and the shore are made by electro-optical cables.

3.2.5 Trigger

Various trigger algorithms are applied to data after its transmission to the shore. The triggered data is written on disks. The trigger algorithms rely on three hit types:

- L0: when the electrical signal passes the 0.3 p.e.
- L1: two types of L1 can be distinguished:
  1. when the electrical signal passes the HighThreshold (3 p.e. or 10 p.e. depends from the period of the data taking), the L0 will be L1.
  2. the coincidence of at least two L0 from different OMs inside a 20 ns window of time on the same storey.

- T3: T3 is a cluster of L1. Two types of T3 can be distinguished:
  1. the coincidence of two L1 in 80 ns time window i.e. two L1 on two adjacent storeys.
  2. the coincidence of two L1 in 160 ns time window i.e. two L1 on two next to adjacent storeys.

Six trigger algorithms are currently applied:

- 3N: it requires at least 5 L1 in a time window corresponding to a muon track.
- T3 (2T3): it requires at least one (two) T3.
- GC: The Galactic Center (GC) trigger requires one L1 and four L0 in the direction of the Galactic Center.
- minimum bias: Every second, within a time window of 4 μs, the data is registered without any filter.
- K40: It is used for the in situ calibration explained in Section 3.2.6.2. It requires two L0 on two optical modules of the same storey within a time window of 50 ns. It is downscaled by factor $\sim$ 1000.
- TST: The Transit Sources Trigger is released when an alert is sent by γ-ray satellites (e.g. SWIFT, FERMI, ...). Two minutes of data, around the trigger, will be saved without any filters.

3.2.6 Time Calibration

The time calibration of the ANTARES telescope is mandatory. The time resolution (relative and absolute) has a major contribution on the angular resolution of the telescope.

- The relative time resolution is related to the time offsets between different OMs inside the detector. It affects the reconstruction of the track of the muon which uses the information of the arrival time of Cherenkov photons. The main uncertainties on the relative time are [97]:
  1. the Transit Time Spread (TTS) in the PMT which is equal to 1.3 ns.
  2. the light scattering and the chromatic dispersion in sea water which lead to a smearing of 1.5 ns for 40 m.

3. the residual time offset is estimated to be less than 0.5 ns.

- The absolute time resolution, which is equal to 100 ns, depends on the offset between the UTC time given by the GPS and the master clock. The absolute time of the event is used for the correlation study with transit sources like the AGN flares and the GRBs. It is used also to transform the local referential frame to Equatorial and Galactic coordinates systems.

The time calibration has two phases. First, the on-shore calibration where before the deployment in deep sea water, the devices are tested and calibrated in CPPM (Marseille) and CEA (Saclay) laboratories. Second, in situ calibrations are performed, once the detector is installed, to study the evolution of the properties of the parameters as a function of time. In this section, the on-shore and in situ time calibration are illustrated.

3.2.6.1 On-shore calibration

Before the deployment, every device is checked to insure the good data quality. In the darkroom, the offset of the individual PMT was measured and corrected by sending light pulse, through optical fibres, by a laser of $\lambda = 532$ nm (green light), 1 μJ power and a pulse frequency of 1 kHz. The PMT with the number 0 of the first floor is taken as a reference.

3.2.6.2 In situ calibration

After the deployment, the in situ calibration insures the good functioning of all the devices. Different techniques are used:

1. internal LED: it is situated inside the Optical Module (Figure 3.12) and sends a light pulse of $\lambda = 472$ nm. It measures the transit time of the PMT. The calibration results show that the uncertainty on the transit time is less than 0.5 ns.

2. LED Optical Beacon (LOB): it is constructed from 36 LEDs of $\lambda = 472$ nm. The maximum intensity of the LOB is 160 pJ. Each line has 4 LOBs at storey numbers 2, 9, 15 and 21. This system is used to compute the time offsets between the PMTs of the same storey.

3. Laser Beacon (LB): Two LBs are situated on the BSS of line 7 and line 8. They emit a light pulse of $\lambda = 532$ nm and power = 1 μJ. This system is used to make the interline calibration by measuring the time offsets between the lines ($\delta t \lesssim 5$ ns). It is used also for the calibration of the lower storeys that are not seen with the LOB.

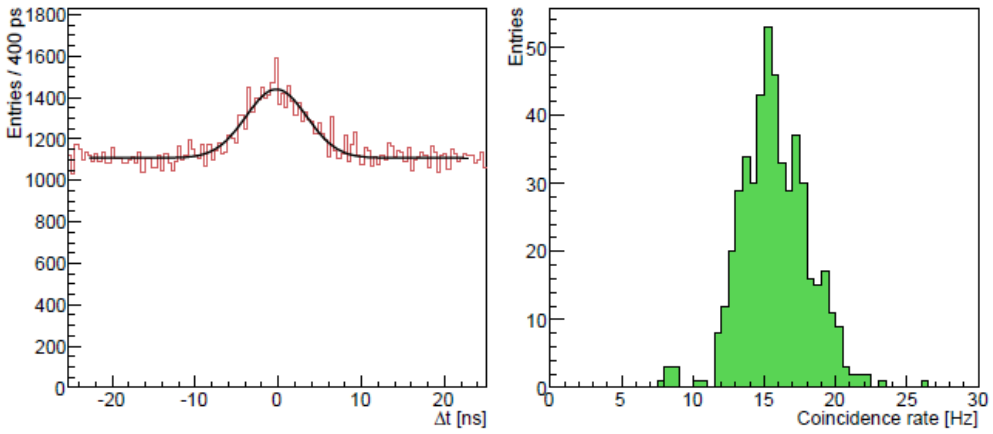

Figure 3.15: The left plot represents the differences of time between hits of two optical modules of the same storey. The right plot illustrates the coincidence rates (the background being subtracted) [98].

4. Potassium 40: The Potassium 40 is a source of optical background in the detector being a radioactive isotope in sea water. It produces photons by two processes:

   - decay of ${}^{40}K \rightarrow {}^{40}Ca + e + \overline{\nu}$. The emitted electrons can attain energies up to 1.3 MeV where the Cherenkov threshold calculated by Equation 3.8 is 0.25 MeV.
   - Compton scattering of photons with energy of 1.46 MeV produced by two consecutive reactions:

$$ {}^{40}K + e \rightarrow {}^{40}Ar^{*} + \nu \quad \text{then} \quad {}^{40}Ar^{*} \rightarrow {}^{40}Ar + \gamma \tag{3.13} $$

The Potassium 40 is used for in situ time calibration studying the coincidence of arrival time of photons, produced by Potassium 40 decay, on two optical modules of the same storey [98]. The left plot of Figure 3.15 shows the time difference between hits of two different optical modules. It is composed by a base line and a Gaussian peak. The base line is the time difference of random hits and the Gaussian peak is due to photons coming from the same decay process. The observed coincidence rates after background subtraction are shown in the right plot of Figure 3.15.

This technique indicates a variation of 15% on the optical modules efficiency due to the different arrival time of photons from the same disintegration and the angular response of the PMT.

3.2.7 Cosmic neutrino search backgrounds

The search of cosmic neutrinos with an underwater telescope like ANTARES has two kinds of backgrounds, the atmospheric background (the down-going atmospheric muons and the atmospheric neutrinos) and the optical background produced inside the detector.

3.2.7.1 Atmospheric background

The interactions of the cosmic rays in Earth's atmosphere produce secondary particles such as protons, neutrons, electrons, pions, muons, neutrinos, and photons (Figure 3.16). Only the muons can reach and interact with the detector. These muons form the atmospheric background and they can be distinguished by two sorts:

- the muons produced by decay of pions (also kaons), known as atmospheric muons.
- the muons produced after the weak interaction of atmospheric neutrinos with the Earth's atmosphere or rocks in Earth.

Figure 3.17 is a schematic presentation of the signal and the background muons, it shows three muons detected by an underwater neutrino telescope. The first (track number 1) presents a muon produced by a cosmic neutrino. This kind of muons represent the signal in the point source analysis and they are up-going events. The second (track number 2) presents a muon produced by an atmospheric neutrino. The third (track number 3) presents the atmospheric down-going muon produced by the decay of a pion. The tracks number 2 and 3 are the atmospheric backgrounds for the point source analysis.

Figure 3.18 presents the flux of atmospheric muons[6] and the flux of muons coming from atmospheric neutrinos as a function of zenith cosine ($\cos\theta$). The up-going muons (-1 $< \cos\theta <$ 0) are the ones produced after the interaction of atmospheric neutrinos with Earth. All the atmospheric up-going muons are absorbed before reaching the detector, while the down-going muons ($0 < \cos\theta < 1$) are atmospheric in majority. Their flux is higher by six orders of magnitude than that of the muons coming from atmospheric neutrinos.

In order to reject a maximum number of atmospheric muons (down-going), one of the solutions is the construction of the detector in sea as deep as possible. Increasing the depth, the absorption of the atmospheric down-going muons will be important. Figure 3.19 shows the flux of an atmospheric muons as a function

[6]The atmospheric muons are produced by the decay of pions (also kaons) in the Earth's atmosphere.

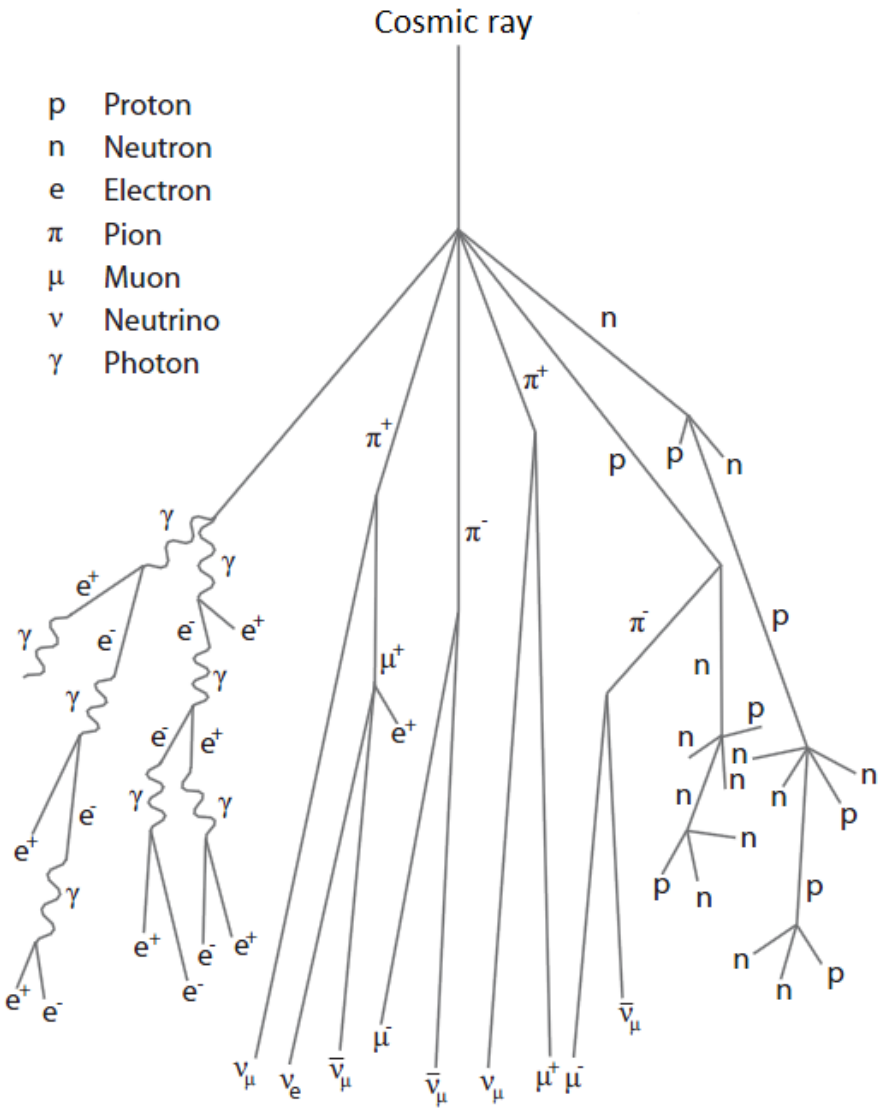

Figure 3.16: Secondary particles production by cosmic ray interactions in the Earth's atmosphere.

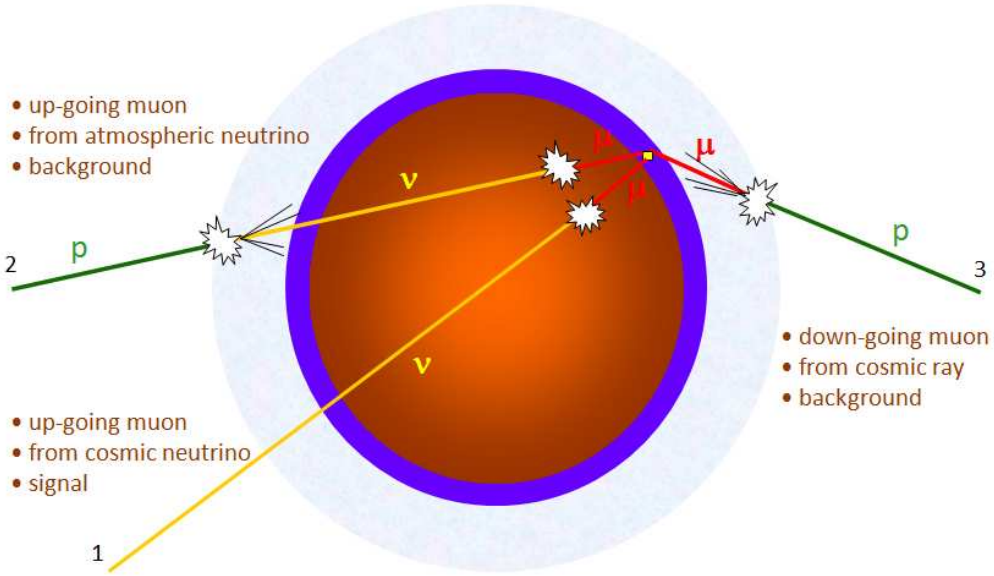

Figure 3.17: The track number 1 represents the signal neutrino produced outside the Earth's atmosphere. The track number 2 represents the muon produced after the interaction of an atmospheric neutrino with Earth. The track number 3 represents an atmospheric muon.

of the depth in the range of the detector. The plot shows that the flux decreases with the increase of the depth [98].

The second way to reject the atmospheric muons is the down-looking orientation design of the optical modules already described in Section 3.2.1.

3.2.7.2 Optical background

The optical background is produced by two sources: the Potassium 40 decay existing naturally in sea water and the bioluminescence.

Figure 3.20 shows the median rate of photons detected by different optical modules. This plot is composed from two components: the base line and the peaks.

- Potassium 40: One of the base line components, with a contribution of ~ 30 kHz on the counting rate, is the Cherenkov light emitted by the relativistic electrons from the Potassium 40 (^{40}K) decay discussed in Section 3.2.6.2.
- Bioluminescence: The majority of the peaks are due to the bioluminescence activities in sea water. These activities have a seasonal variation and they are correlated with the velocity of the sea current. Scientific research groups in

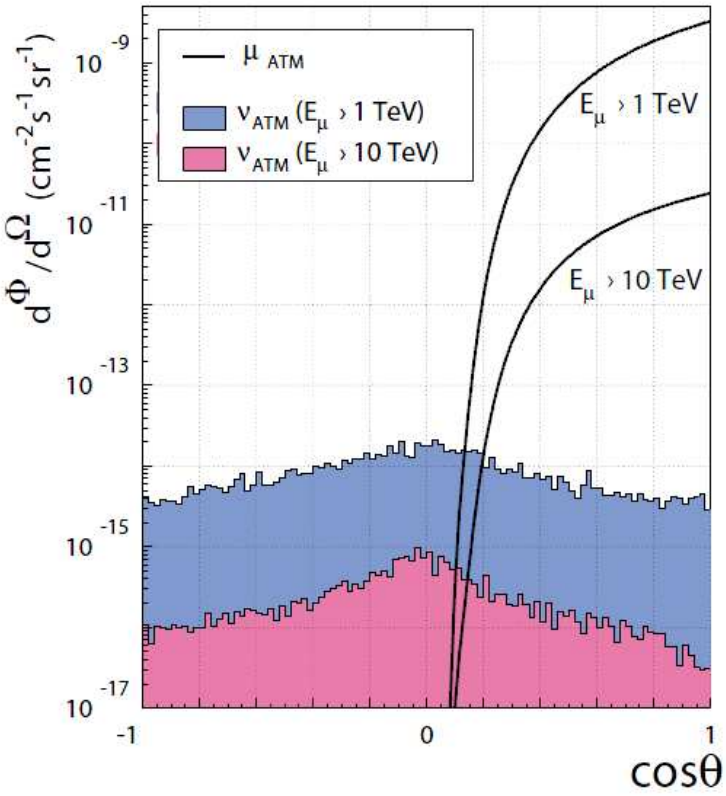

Figure 3.18: Atmospheric neutrino and muon flux as a function of zenith cosine.

ANTARES Collaboration are studying different parameters related to bioluminescence activities like the oxygen consummation by the bacteria, their density and their effects on the environment.

3.3 Monte-Carlo simulations

Monte-Carlo simulations are used to simulate the detector and the behaviour of each particle while passing through it. In order to understand the data behaviour and the performance of the detector, different data to MC comparisons are studied. In this section, the simulations of the detector response to signal and background neutrinos and atmospheric muons are discussed.

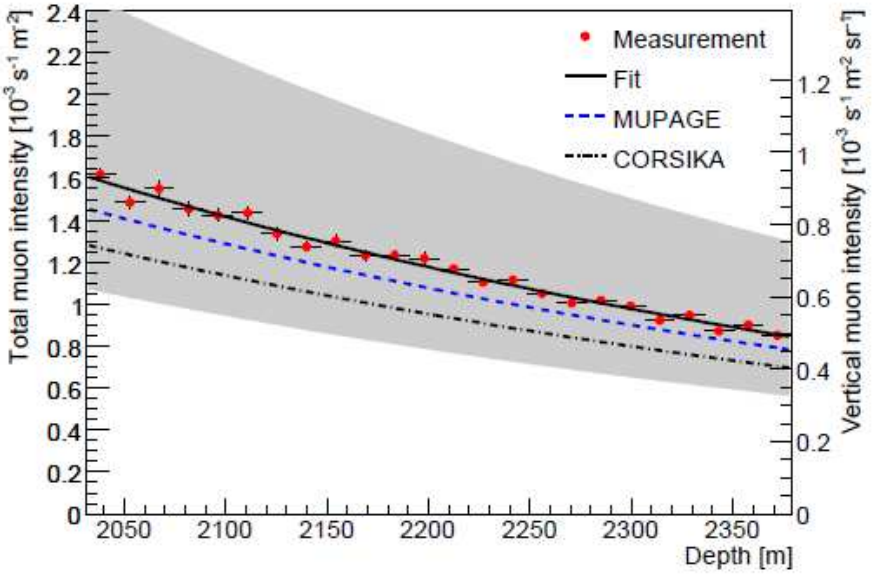

Figure 3.19: The muon flux as a function of depth in the detector range. The left axis represents the total muon intensity and the right axis represents the vertical muon intensity. The grey band shows the normalization uncertainty of the data. The predictions of the Monte-Carlo simulations based on MUPAGE (CORSIKA) are shown by dashed (dash-dotted) lines [98].

3.3.1 Neutrino simulation

The high energy neutrinos, their interactions with matter and the production of the muons, described in Section 3.1.1, are simulated by the GENHEN package [99]. The interaction of the neutrinos with Earth through quasi-elastic and resonance scattering channels are simulated by the RESQUE package [100]. The interactions through the charged current deep inelastic scattering channel are generated using the LEPTO package [101]. The parton distribution functions of the CTEQ collaboration [102] are used in LEPTO. The muon propagation and its energy loss are simulated by the MUSIC[7] package [103].

The neutrinos and their interactions are simulated in a cylindrical volume defined around the detector. To detect all the produced muons, the radius and height (twenties of kilometers) of the cylinder are calculated based on the maximum propagation length of the muons, taking into account the muon interactions with rock and sea water. The muon propagation length is a function of the energy. For the analysis in this thesis, the simulated energy range of neutrinos is 10 GeV to 10^7 GeV. In order to decrease the CPU time of the simulation, the energy range is

[7]MUSIC is the acronym of MUon SImulation Code.

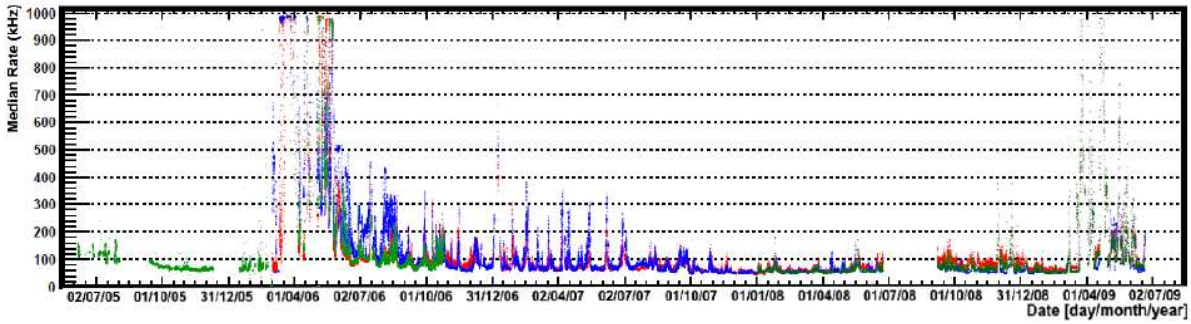

Figure 3.20: The median rate (kHz) of hits measured by the MILOM and storeys 1 and 25 of Line 1 from 2005 to 2009.

divided into 10 logarithmic bins. For each bin, the dimensions of the cylindrical volume are defined.

The flux of the down-going atmospheric muons being six orders of magnitude higher than that of the atmospheric neutrinos, only the up-going atmospheric neutrinos are simulated in 2π srad (i.e. the zenith is between 0° and 90°). The flux of these neutrinos is isotropic and it is given by Equation 3.14. A random time is simulated for each event to apply the transformation from local to Equatorial and Galactic coordinates.

$$\frac{d\Phi(\nu_{\text{atm.}})}{dE\,d\Omega} = 4.9 \left(\frac{E_\nu}{\text{GeV}}\right)^{-3.6} \text{cm}^{-2}.\text{s}^{-1}.\text{sr}^{-1}.\text{GeV}^{-1} \tag{3.14}$$

The simulated atmospheric neutrino events are used to define the Probability Density Functions (PDF)s of the signal neutrinos (Chapter 5). However, they are reweighted to have an energy spectrum index equals[8] to 2 rather than 3.6. The reweighted events are classified by ranges of 10° declination and they are associated to point sources of the same declination range.

3.3.2 Atmospheric muon simulation

The atmospheric muons, described in Section 3.2.7.1, are generated by the CORSIKA[9] package [104]. The interaction of the cosmic rays with the atmosphere and the development of the atmospheric showers are simulated for a wide range of energies up to 10^{20} eV. The secondary particles produced in the atmospheric showers are simulated taking into consideration their energy loss, the decay of

[8]The energy spectrum index of the point sources is assumed to be 2.

[9]CORSIKA is the acronym of COsmic Ray SImulation for KAscade.

unstable particles, the electromagnetic and hadronic interactions and the deviation of the trajectory of electrically charged particles in Earth's magnetic field. The propagation of the muons from the sea level to the detector is simulated using the MUSIC package as in the case of the up-going muons.

To decrease the CPU time of the simulation, the generation process is divided into 3 bins of energy (1 to 10 TeV/nucleon, 10 to 100 TeV/nucleon and 100 to 10^5 TeV/nucleon) and 2 bins for zenith for each atomic nucleus (p, He, N, Mg, Fe). In total, 30 different bins are considered where the simulated numbers of primary cosmic rays are given in Table 3.1.

	$0^\circ < \theta < 60^\circ$			$60^\circ < \theta < 85^\circ$		
Name	h1	h2	h3	v1	v2	v3
Primary nucleus	$1 \rightarrow 10$ TeV/nucleon	$10 \rightarrow 100$ TeV/nucleon	$100 \rightarrow 10^5$ TeV/nucleon	$1 \rightarrow 10$ TeV/nucleon	$10 \rightarrow 100$ TeV/nucleon	$100 \rightarrow 10^5$ TeV/nucleon
P	10^9	10^9	10^8	10^9	10^9	10^8
He	9×10^8	10^8	9×10^7	9×10^8	10^8	9×10^7
N	10^8	10^8	6×10^6	10^8	10^8	$6x10^6$
Mg	10^8	10^8	3×10^6	10^8	10^8	3×10^6
Fe	10^8	3×10^7	10^6	10^8	3×10^7	10^6

Table 3.1: The number of events simulated in CORSIKA bins.

3.3.3 Cherenkov photon simulation and the detector response

To simulate the Cherenkov light discussed in Section 3.1.2, a cylindrical volume, called "can", is defined around the instrumented volume[10]. The radius of the can is equal to few times of the photon absorption length in water which is 69 m for a wave length of 450 nm. The dimensions of the instrumented volume and the can are illustrated in Figure 3.21.

The Cherenkov photons emitted by muons and the secondary particles produced by muons interactions are simulated by the GEASIM and KM3 [105] packages. The former simulates all particles inside the can, as well as, Cherenkov photons produced by the muons and the secondary particles. However, it does not simulate the scattering of photons. The latter simulates all particles including light scattering except hadronic showers. In rare cases, GEASIM is used to simulate hadronic showers when they are produced near to the instrumented volume.

The angular acceptance of the optical modules and the detector are also simulated using the KM3. The simulations take into account the quantum efficiency and the angular acceptance of the PMT, the glass sphere and the gel transparencies, and the effective area of the photocathode.

[10]The instrumented volume presents the detector.

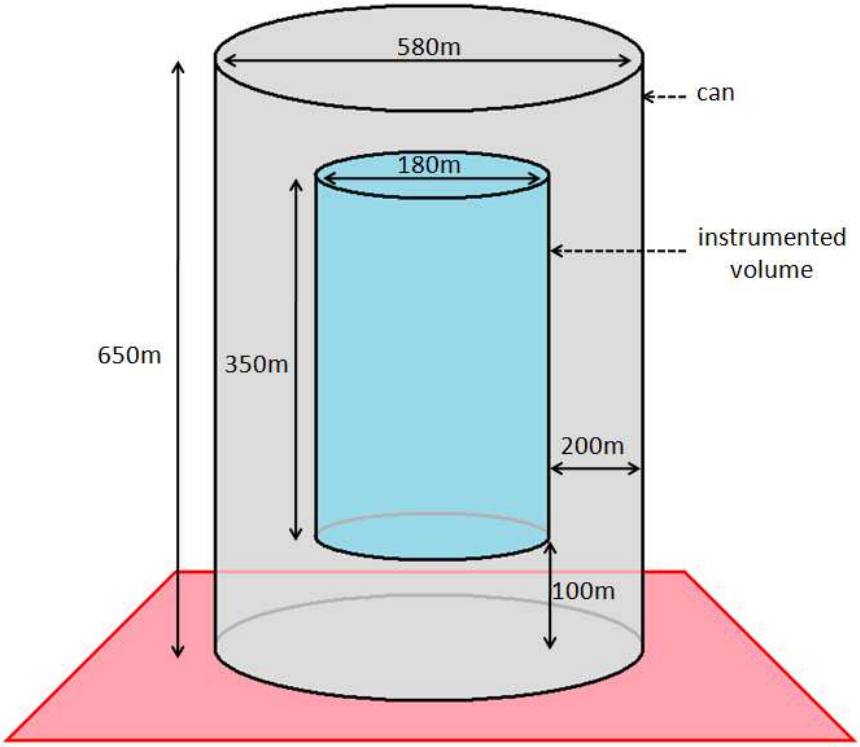

Figure 3.21: The can and the instrumented volume inside it.

3.4 Reconstruction algorithms

Two different track reconstruction algorithms are used in this thesis. The BBfit and AAfit muon track reconstruction algorithms are presented in this section. The former is robust and fast, and the latter is characterized by its accuracy and high effective area.

3.4.1 BBfit muon track reconstruction algorithm

The muon track reconstruction algorithm used in Chapter 5 is the BBfit reconstruction algorithm [106]. It is characterized by robustness and rapidity.

BBfit algorithm uses the following approximations:

- The velocity of the muon is equal to the speed of light in vacuum.
- The muon trajectory is considered as a straight line.

- The lines of the detector are assumed to be vertical i.e. the acoustic positioning system data is not used.
- The distances between the optical modules and the center of the storey (Figure 3.11) are ignored i.e. the positions of the hits are supposed to be at the center of the line.
- The hits recorded in a time interval of 20 ns are merged by adding their amplitudes keeping the time of the earlier hit. If the merged hit consists of hits from different optical modules, it has a bonus charge of 1.5 p.e.
- The Cherenkov photons have the same wave length.
- The refraction index is considered to be 1.38.

The fact that the hits are merged to a single hit, the L1 trigger defined in Section 3.2.5 will have a new threshold on the amplitude. In the algorithm, this threshold amplitude value is taken to be 2.5 p.e.

The pre-selected hits used in the fit consist of all T3 hits. Also, the L0 and L1 hits that are within a narrow time window around the T3 Hits are added.

3.4.1.1 Bright point fit

The bright point fit is used to fit the hits to spherical light waves that are emitted by a fixed geometrical point, propagating with the speed of light in water. It is assumed to be isotropic and it is defined by the four parameters of space-time (3 for space coordinates and 1 for time). It helps to recognize the electromagnetic and hadronic showers. The bright point fit quantity is characterized by the parameter *bchi*2 used as a quality cut.

3.4.1.2 Track fit

The muon track is fitted by the hits corresponding to the wave front of Cherenkov cone based on the closest approach (χ2-like function). The scattered photons and those produced in electromagnetic and hadronic showers are ignored in the fit. The track fit has five free parameters, three for the track coordinates in 3D space and two for the orientation (θ and ϕ). Only the lines that have at least one T3 hit are used in fitting the track in order to avoid, as much as possible, the hits coming from isolated noise.

The χ2-like function, called Q, is given by:

$$Q = \sum_{i=1}^{N_{\text{hit}}} \left[\frac{(t_\gamma - t_i)^2}{\sigma_i^2} + f(a) \right] \tag{3.15}$$

where $f(a)$ is a function of hits amplitude.

The track fit is characterized by the parameter $tchi2$ which is equal to Q divided by the Number of Degrees of Freedom (NDF). The NDF is obtained by subtracting the number of the free parameters (five parameters) from the number of hits used in the track fit.

3.4.2 AAfit muon track reconstruction algorithm

The reconstruction strategy of muon tracks used in Chapter 6 is the AAfit muon track reconstruction algorithm. This algorithm is explained in detail in Reference [107]. It is characterized by the relatively good angular resolution and the effective area. The hits used in the AAfit algorithm use the acoustic positioning (plus compasses) data. This section describes the pre-selection of the hits and the different steps of the fit.

3.4.2.1 Pre-selection of hits

A pre-selection of hits is applied to reduce the optical background hits. Since the hit with the highest amplitude is probably a signal hit, the quantity $\Delta t'$ defined as the time difference between the time of a hit and that of the largest amplitude hit is used for the selection criterion given by the following equation:

$$|\Delta t'| \leq \frac{d}{v} + 100 \text{ ns} \tag{3.16}$$

where d is the distance between the two hits and v_g is the group velocity of light in sea water. The factor 100 ns is a "safety factor" to preserve almost all signal hits.

3.4.2.2 Steps of the fit

The AAfit algorithm consists of four main steps described briefly in the following:

- Linear prefit: The first step of the reconstruction algorithm is the linear prefit. The prefit does not lead to precise track reconstruction but its importance is to give a preliminary reconstructed track from a sub-set of hits. This sub-set consists of hits with amplitude larger than 3 p.e. and hits with local coincidence of less than 25 ns. In this method, no starting point is required and that is taken as an advantage. The track parameters are estimated based on the closest approach (χ^2 minimization).

- M-estimator fit: As a following to the linear prefit that does not give an accurate estimation of the track fit, an M-estimator is chosen in a way to

behave linearly for large time residuals, and quadratic for small ones (Figure 3.22). Equation 3.17 is used in the M-estimator maximization of the time residuals[11] Δt.

$$M(\Delta t) = -2\sqrt{1+\frac{\Delta t^2}{2}}+2 \tag{3.17}$$

The advantage of this fit is the insensitivity to the quality of the starting point. It is used as the second step of the track reconstruction algorithm. At this step, another hit selection is applied. Hits with a time residual between -150 ns and +150 ns and a distance less than 100 m from the reconstruction track in the prefit are selected. Otherwise, hits with amplitude higher than 2.3 p.e. are always selected.

- Maximum likelihood fit: In this step, a maximum likelihood is performed with a Probability Density Function (PDF) free from background hits. The fit results of the M-estimator are used as an input for this fit. The selection consists of choosing hits with residuals in the range $[-0.5\times R, +R]$, R being the root mean square of the time residuals used in the second step. Hits with amplitudes greater than 2.5 p.e. or with a local coincidence are also chosen.

  In order to improve the efficiency of the algorithm, the steps 2 and 3 are repeated several times by using a number of different starting points from that of the prefit. The track with the best maximum likelihood is used as an input for the next step.

- Final maximum likelihood fit: In this last step, the maximum likelihood fit uses a PDF which includes the background hits. The presence of the background hits in the PDF keeps good reconstruction accuracy. Hits with amplitudes greater than 2.5 p.e. or with local coincidences, and time residuals in the range of $[-250, +250]$ ns are used in this fit.

3.5 Km^3 neutrino telescopes

Naturally, neutrino telescopes with a volume of more than km^3 will increase the probability of cosmic neutrinos discovery. For such detectors, the effective area and the angular resolution will be 10 times improved and the sensitivity around 50 times better than ANTARES. Two projects are dedicated to construct km^3 neutrino telescopes: IceCube and KM3NeT.

[11] The time residual is the time difference between the measured time of the hit and the time calculated using the reconstructed track.

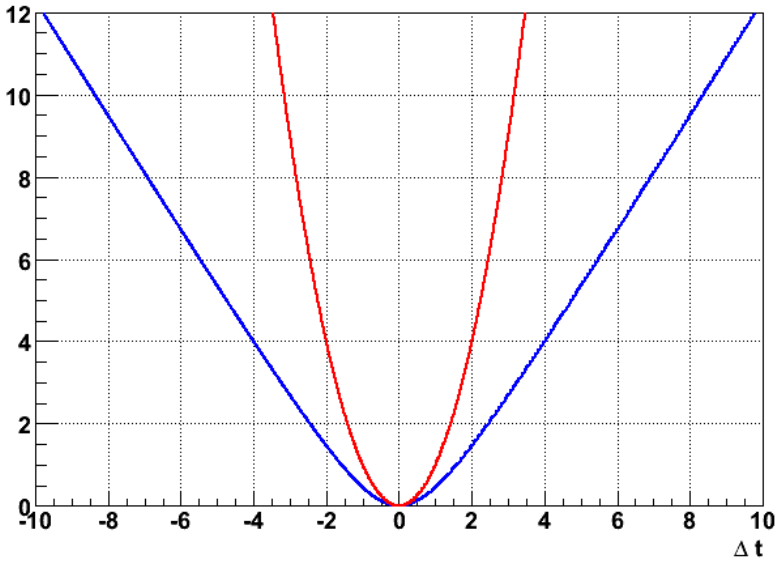

Figure 3.22: The red curve presents the function $\chi 2(\Delta t) = \Delta t^2$ and the blue the M-estimator (the opposite value).

3.5.1 IceCube

The IceCube detector (Figure 3.23), located at the South Pole, is in the construction phase and it will be completed in 2011 [108]. The telescope consists of 5160 optical sensors distributed over 86 strings occupying a volume of 1 km^3 in the Antarctic ice at depths between 1450 m and 2450 m. The optical sensors are spaced constantly over the detector with an exception of the six DeepCore detectors, between 1760 m and 2450 m, where the modules are closer for the low energy particles reconstruction. At the surface, a 1 km^2 air shower array is installed to study the cosmic rays with energies between 300 TeV and 1 EeV. This surface detector, called IceTop, consists of 320 optical sensors in 160 tanks.

Before the construction of the IceCube, a prototype project is made with a smaller detector called AMANDA presented in Figure 3.23. AMANDA contained 677 optical modules at depths between 1500 m and 2000 m.

The IceCube passed through intermediate configurations known as IC22 and IC40 before its final configuration. Figure 3.24 shows the cumulative event fraction of the angular difference between the true neutrino and the reconstructed muon for the different configurations.

The IceCube design permits to study the three neutrino flavours, ν_e, ν_μ and ν_τ, covering a wide energy range (between 100 GeV and 10^9 GeV). It can collect

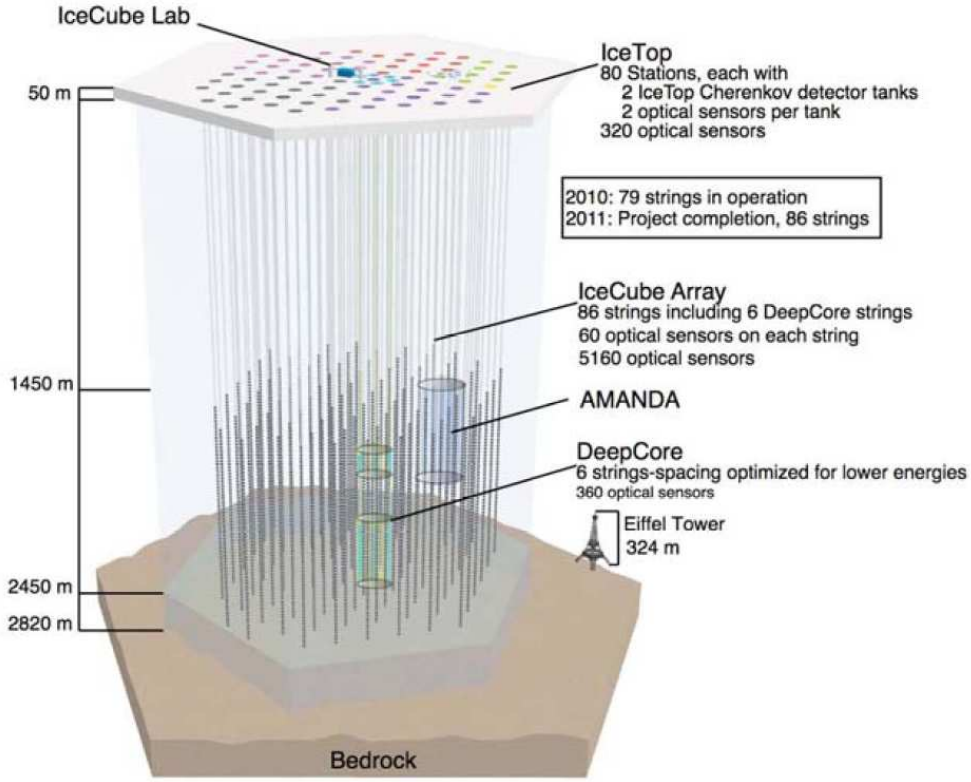

Figure 3.23: The IceCube telescope.

50,000 events per year in an energy range between 500 GeV and 500 TeV.

3.5.2 KM3NeT

In February 2006, the KM3NeT project [110] began to study the technical performance and to build an underwater neutrino telescope in the Mediterranean Sea. In 2010, the Technical Design Report is published. The construction will begin in 2013 and the data taking will start during the construction phase.

Three main configurations are proposed. The design of these configurations is optimized, with Monte-Carlo simulations, to have 0.1° angular resolution for muons with energies above 10 TeV and maximum possible effective area for km^3 volume to study the neutrinos with their three flavours.

Figure 3.25 shows the three different proposed designs for the whole detector. The three designs of the detector lines under study, presented in Figure 3.26, are:

1. NuOne: the main component is 6 m long horizontal bars to support 6 optical

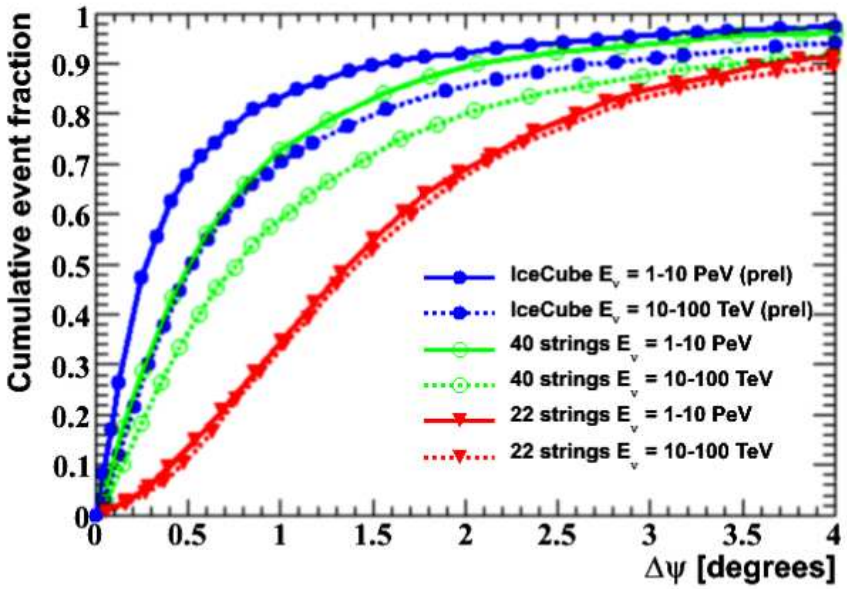

Figure 3.24: The cumulative event fraction of the angular difference between the true neutrino direction and the reconstructed muon direction. The different colors represent 3 different configurations and for each configuration two energy ranges are presented [109].

modules and the electronic container (Figure 3.26 left). Twenty horizontal bars are fixed on a tower and they are separated vertically by 40 m.

2. Seawiet: The multi-PMT optical modules are fixed on string-like mechanical structures (Figure 3.26 center).

3. Medusa: Three pair of optical modules are fixed on a storey forming a horizontal equilateral triangle (Figure 3.26 right).

The KM3NET sensitivity for the neutrino point sources and the neutrino diffuse flux are illustrated in figures 3.27 and 3.28 respectively.

In addition to neutrino astronomy, KM3NeT project will be a deep sea observatory to marine biology research, oceanography, environmental sciences and it is a part of the European Strategic Forum on Research Infrastructures (ESFRI).

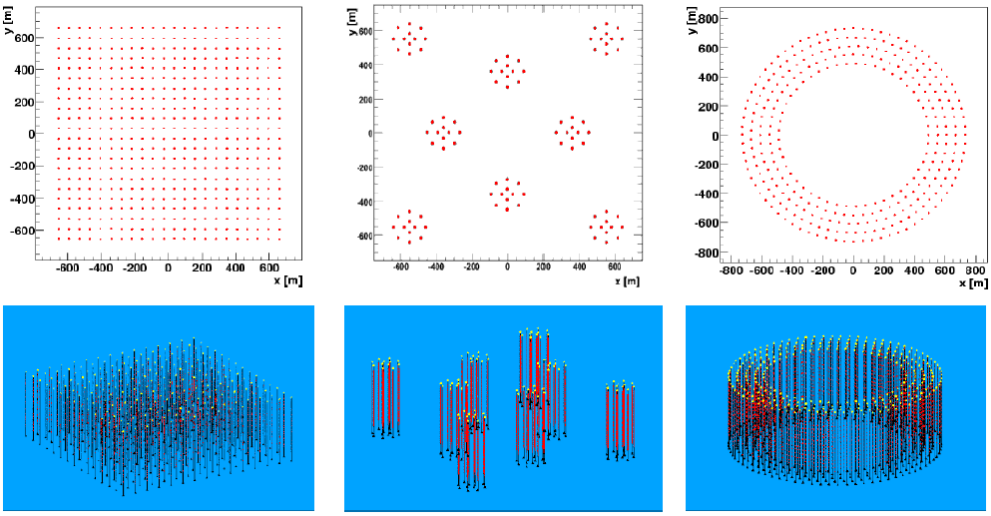

Figure 3.25: kM3NeT detector different designs.

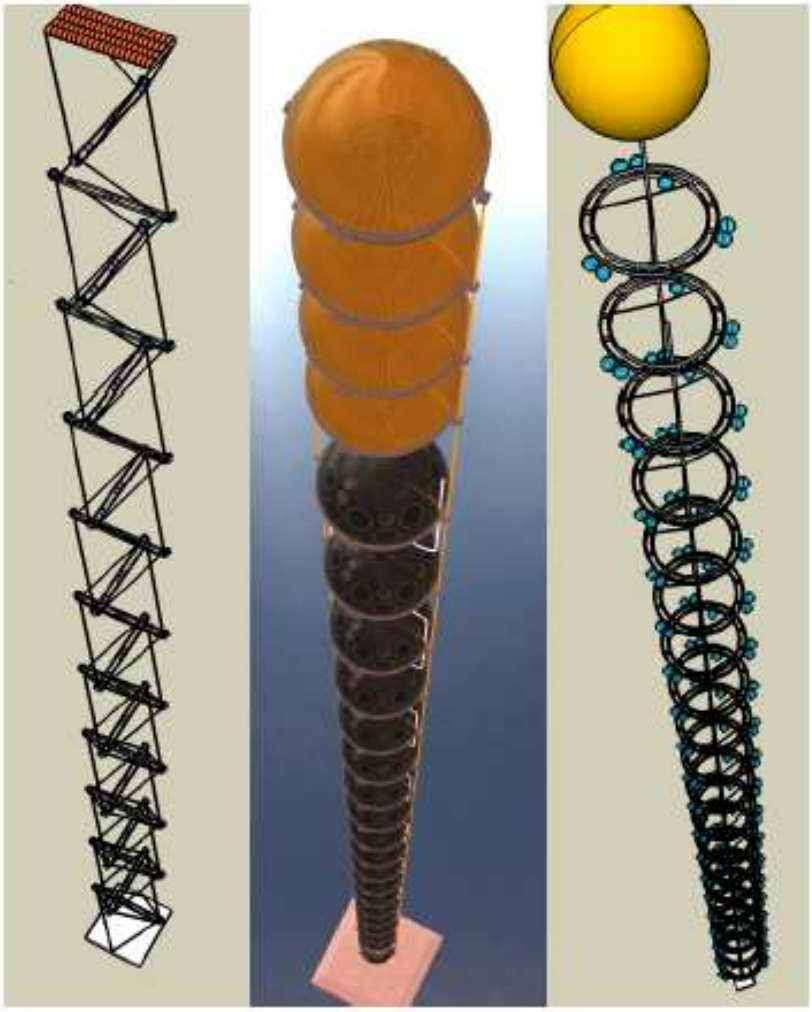

Figure 3.26: The three designs options for KM3NeT lines. Left: The bar has a horizontal extension of 6 m and includes optical modules and an electronics container. Middle: The string has a storey composed of a single multi-PMT optical module. Right: The triangle has 6 optical modules arranged in pairs, placed at a distance of 1.1 m from the center.

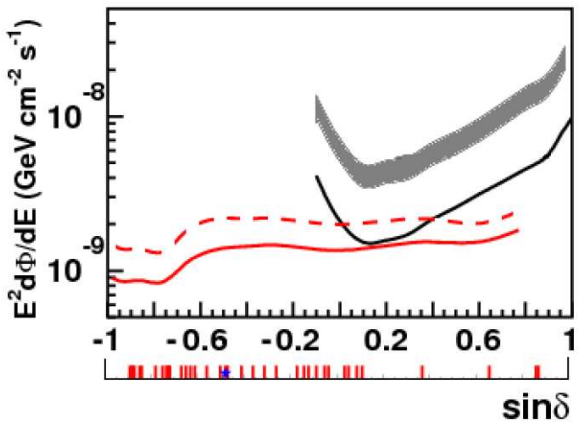

Figure 3.27: KM3NeT sensitivity for the neutrino point sources with an E^{-2} energy spectrum (1 year using binned analysis method). The red solid line indicates the flux sensitivity (90% CL) and the dashed red line shows the discovery flux (5σ with 50% probability). The black solid line is IceCube's flux sensitivity (90% CL for 1 year using unbinned method [111]). The shaded band is IceCube's discovery flux (5σ with 50% probability). The positions of Galactic γ-ray sources [112] are shown by the red thicks below the horizontal axis, where the blue star is the Galactic Center.

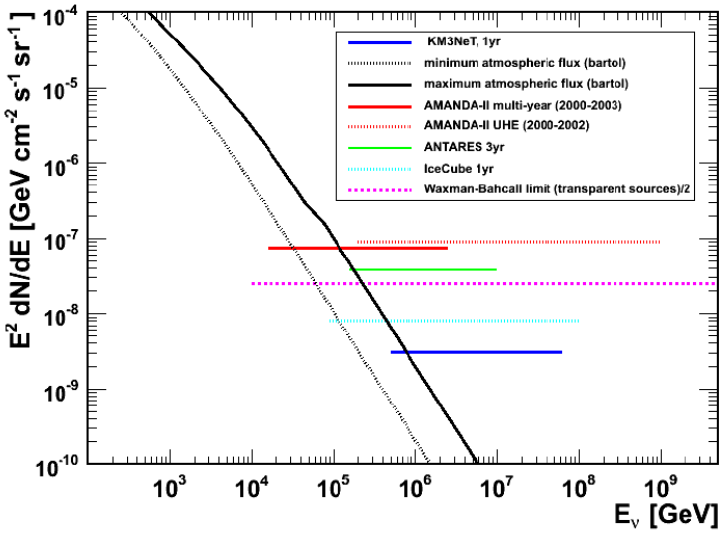

Figure 3.28: The sensitivity of neutrino diffuse flux of the KM3NeT neutrino telescope (1 year), Waxman-Bahcall limit [75], AMANDA [113, 114], ANTARES [115] and IceCube [116].

Chapter 4

Absolute pointing of the ANTARES telescope using the acoustic positioning system

The aim of this chapter is to study the pointing (the orientation) of the ANTARES telescope with respect to the sky using the ANTARES acoustic positioning system, as well as to estimate the uncertainty on the telescope pointing in order to calculate the error on the high energy cosmic neutrinos directions emitted by the point sources and the effect of this uncertainty on the discovery power of cosmic neutrinos.

The acoustic positioning system and the devices used in this analysis are presented in Section 4.1. The absolute referential and the pointing of the telescope are defined in sections 4.2 and 4.3 respectively. One of the main parameters in this study is the sound velocity which is discussed in Section 4.4. It is used to convert the propagation time of acoustic waves to "acoustic distances". The algorithm used to triangulate these distances is detailed in Section 4.5. In sections 4.6 and 4.7, the study of the telescope pointing is illustrated by two acoustic positioning systems evaluating the systematic errors (on the sound velocity, on the acoustic time measurements, ...). In Section 4.8, the uncertainty on the hydrophones relative positions estimated with the acoustic positioning system is shown.

4.1 Acoustic positioning system

The lines of the ANTARES detector are flexible and they are fixed only from the bottom thanks to their anchor bases. Therefore, the shape of these lines and the carried optical modules positions change continuously because of sea current (Figure 4.1). A current velocity of 0.25 m/s can shift horizontally the top storey

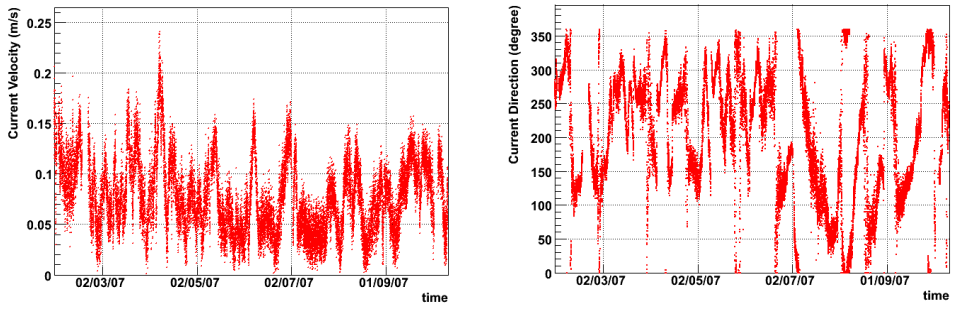

Figure 4.1: Sea current velocity (left) and direction (right) in ANTARES from February to November 2007. The direction is defined from North (0°) to East (90°).

of the line (Storey 25) by $\sim$ 25 m. The precise knowledge of the positions of optical modules is mandatory, because they are used as 3D geometric points in the reconstruction of the muon track. In order to have a good measurement of the detector geometry at any time, an acoustic positioning system is used to determine the geometry of the detector, and therefore the positions of the optical modules as a function of time.

The principle of the acoustic positioning system is illustrated in Figure 4.2. Measuring the emission and the reception time of acoustic waves between emitters attached to every line anchor and receivers distributed all over the detector and knowing the speed of sound in the medium, distances between these devices are computed. These distances are triangulated in order to determine the positions of the acoustic receivers (hydrophones) with respect to the **Relative Referential** which is defined by the relative positions of the lines anchors with respect to each other.

The positions of the optical modules are then derived from the reconstruction of the detector lines shape based on the knowledge of the hydrophones positions as well as local tilts and orientation of the storeys form a set of tiltmeter-compasses[1].

The acoustic positioning system is also used to define the orientation of the telescope (telescope pointing) with respect to the sky i.e. to find the direction of the muon track in the **Absolute Referential** which is the astronomic referential presented by the Equatorial or the Galactic coordinate systems. The lines anchors positions are measured by acoustic waves from a boat which is located by the Differential Global Positioning System[2] (DGPS) network (Section 4.6). This system is used because of the presence of the ANTARES telescope at a depth of 2475 m

[1]The tiltmeter and the compass are devices to measure inclination and orientation respectively.

[2]The Differential GPS network is an improvement of the GPS system. A fixed network of stations on Earth corrects the position of the boat measured by the GPS satellites.

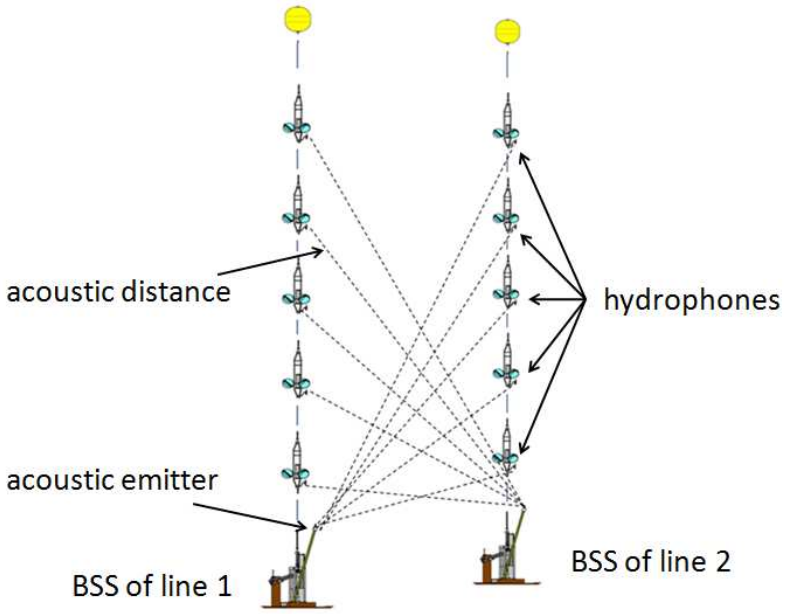

Figure 4.2: Sketch of the acoustic distances measured between the emitters and receivers of two detector lines.

in the seawater which makes ANTARES directly invisible to the DGPS network.

The acoustic positioning system is composed of two subsystems HFLBL and LFLBL presented in sections 4.1.1 and 4.1.3 respectively.

4.1.1 High Frequency Long BaseLine (HFLBL) acoustic positioning system

The High Frequency Long BaseLine (HFLBL) acoustic positioning system uses high frequency devices where the wave band spreads over 40 to 65 kHz. This system is used to measure "short acoustic distances" (up to $\sim$ 700 m) i.e. the distances between different devices in the detector to determine the positions of the optical modules and therefore the muon track direction in the Relative Referential. The functioning of this system is explained in Section 4.1.2. The devices used in this system are:

- Acoustic emitter-receiver module (RxTx): The RxTxs (transducers) are fixed on the top of the Bottom String Socket (BSS) of the 12 lines and on the instrumentation line IL-07. Since the BSS is fixed on Earth, the RxTxs are considered fixed. The altitude of the RxTxs is 3.6 m above the sea bed.

- Acoustic receiver module (Rx): 60 Rxs (hydrophones) are fixed all over the entire detector, five Rxs along one line. The altitude of these Rxs are given in Table 4.1.
- Pyramid: The pyramid is used as an additional fixed high frequency acoustic beacon (transponder) placed on the sea ground near the detector ($\sim$ 200 m from the center of the detector). It sends back an acoustic signal when triggered by a specific frequency. The process of alimentation is autonomous thanks to the presence of a battery that lasts for couple of years. The pyramids are mainly used to position the first lines in the early stage of the construction of the detector. In this study, only one pyramid is used.

Rx	Storey	Altitude (m)
Rx-1	1	100
Rx-2	8	201
Rx-3	14	289
Rx-4	20	376
Rx-5	25	448

Table 4.1: Altitudes of the Rx hydrophones installed on every line.

4.1.2 Functioning of the HFLBL system

The HFLBL is a system that functions by successive emission of acoustic waves between the 12 lines, the IL-07, and the pyramid. This process repeats itself every 2 minutes and it is called "Acoustic Positioning Cycle". The cycle starts by broadcasting a command, from the Master Clock, called "Acoustic Slow Synchronization" which starts the Acoustic Positioning Cycle. The Acoustic Positioning Cycle is split into 14 Acoustic Fast Synchronization signals which trigger the successive emission of all RxTx transducers in turn as well as the measurement of the acoustic signal propagation time by the receivers. The first acoustic signal is emitted by $RxTx$-1 and received by the other RxTxs and Rxs, followed by the second acoustic signal emitted by $RxTx$-2 and so on (Figure 4.3). The consecutive acoustic signals have different frequencies in order to avoid interference between the acoustic waves.

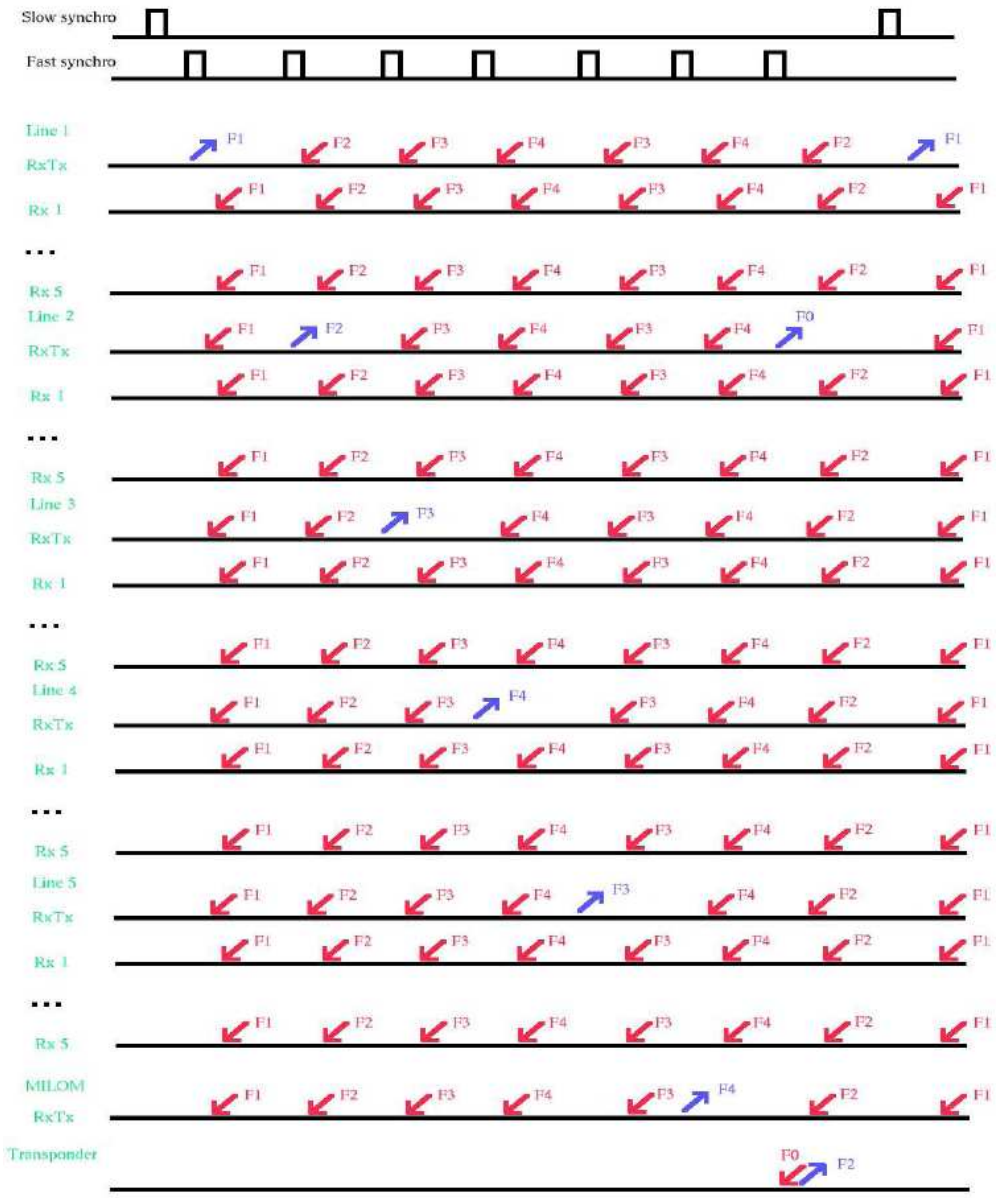

Figure 4.3: Sketch of the HFLBL acoustic positioning system emission cycle. The North-East (South-West) arrows represent the emission (reception) of the acoustic waves. F1, F2, F3 and F4 are different values of acoustic frequencies.

4.1.3 Low Frequency Long BaseLine (LFLBL) acoustic positioning system

The Low Frequency Long BaseLine (LFLBL) acoustic positioning system is used to measure "long acoustic distances" (up to $\sim$ 6000 m) like the distances between the boat from the sea surface and the detector. The LFLBL system devices use an acoustic band between 8.5 to 16 kHz and they are:

- BSS's transponder: Apart of the High Frequency (HF) transducer, a Low Frequency (LF) transponder is fixed on the BSS in order to locate the position of the line anchor from the surface of water. This device, running on battery, is used to position the line during its deployment by the boat.
- Reference Beacon (RB): To measure the absolute positions of the lines anchors from the boat, five transponders *RB-i* ($i = 1, 2, \cdots, 5$) are fixed at distances of several hundreds of meters from the center of the detector (Figure 4.6). Their positions are accurately measured ($\lesssim$ 1 m) by acoustic triangulation from a boat positioned by DGPS network as explained in Section 4.6.1.

The advantage of this system is the capability to perform long distance measurements. However, these measurements are less accurate than the ones of the HFLBL system because of the relatively large wavelengths.

4.2 Absolute referential

The coordinate system used to define the absolute positions of the lines anchors is the geographic coordinate system called "World Geographic System 1984" (WGS84). This system considers the Earth as an ellipsoid (geodesic dome) the center of which is located at the center of mass of the Earth with an error estimated to be less than $\sim$ 2 cm [117]. In addition to the usual coordinates (latitude, longitude), the position of a point P on the Earth's surface can also be defined in the Universal Transverse Mercator (UTM) coordinate system which is a metric coordinate system based on a local projection of the Earth on a cylinder tangential to the globe at the Equator and oriented towards the poles. The x coordinate is the eastward-measured distance on the surface of Earth from the meridian of origin of the zone to the point P, called Easting. The y coordinate, called Northing, is equal to the length of the geodesic[3] going from the Earth's Equator to the point P in the North direction.

[3]The geodesic is the shortest path between two points in a given space.

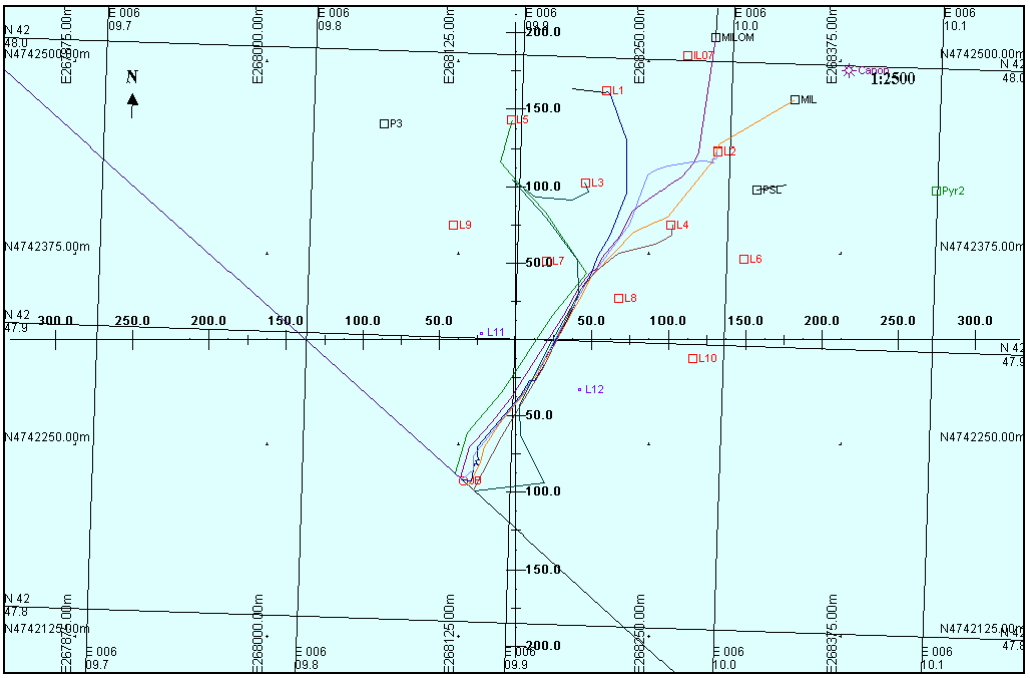

Figure 4.4: The 1.93° angular difference between the Geographic North and the UTM Northing at the ANTARES site [118].

The WGS84 consists from 60 zones of 6° wide centered on each reference meridian. The ANTARES telescope is present in zone 32 of UTM referential with the coordinates $x \approx 260000$ m and $y \approx 4740000$ m. The UTM projection (projection of an ellipsoid on a cylinder) leads to a rotation between the Geographic North and the UTM Northing (Figure 4.4) except on the reference meridian of the UTM zone. In the ANTARES site, this angle is equal to 1.93° [118].

4.3 Pointing of the telescope

Projecting all astrophysical bodies on a spherical surface where the center is the Earth's center, the Universe can be presented by a two dimensional (2D) space. In this chapter, two different spherical spaces are defined: the global and the local spaces. Both spaces are related by a transformation depending on time. The global space is fixed relatively to the astrophysical bodies where their positions are presented in Equatorial and Galactic coordinate systems. The local coordinate system is defined by the fixed components of the telescope with respect to the Earth.

Since both spaces are 2D spherical spaces, at time t, two points (two directions

in 3D space) are needed to define this transformation knowing their coordinates in both spaces; these points are π_{1-2} and π_{1-3}.

- π_{1-2} is defined by the direction of the line going from $RxTx$-1 to $RxTx$-2 projected on the local space.
- π_{1-3} is defined by the direction of the line going from $RxTx$-1 to $RxTx$-3 projected on the local space.

The choice of $RxTx$-1, $RxTx$-2 and $RxTx$-3 are valid since they are not collinear in the 3D space and they are fixed with respect to the Earth.

The pointing of the telescope, at time t, is the calculation of the coordinates of π_{1-2} and π_{1-3} in the global space at t. A specific algorithm is developed for this object and the standard astronomical transformations are used as well.

4.4 Sound velocity

The measured parameter in the acoustic positioning system is the time of emission and reception of acoustic waves. To compute "acoustic distances", a knowledge of the sound velocity in water is mandatory. In this propose, different devices are installed all over the detector in order to measure in direct and in indirect ways the variation of the velocity of sound as a function of time. The direct way is to measure the acoustic signal round-trip time on a distance of 2×20 cm. The indirect way consists of the measurement of the electrical Conductivity (C), the Temperature (T) and the Pressure (P) of sea water to compute the water Salinity (S), which is a function of C, T and P, then the Sound Velocity (SV), which is dependent of P, T and S, using the Chen-Millero empiric equation (Appendix B) commonly used by the oceanographic community [119]. The used devices are:

- SV-01, SV-07, SV-10, SV-13: Sound velocimeters of lines 1, 7, 10 and the MILOM respectively.
- SVCTD-04: Sound velocimeter, electrical conductimeter, thermometer, and pressure sensor of Line 4.
- CT-13 and CT-14: Electrical conductimeter and thermometer of the MILOM and IL-07 respectively.
- CTD-14: Electrical conductimeter, thermometer and pressure sensor of IL-07.

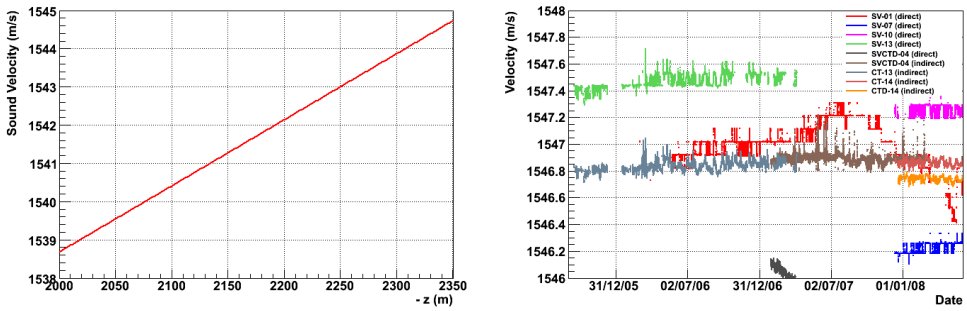

Figure 4.5: Sound velocity in water as a function of depth measured by deploying a CTD sensor from the surface (left). Sound velocity as a function of time at the level of SV-01 given by different devices (right).

In the Mediterranean Sea at a depth more than 200 m ($z <$ -200 m), the T and the S are constant in first order, only the P increases linearly as a function of the depth. The measurements show that also the SV increases linearly with the depth (left plot of Figure 4.5) as it is given by Equation 4.1. At the surface of sea water, the SV variation is not linear because of seasonal temperature variations.

$$v_z = v_0 - K_c \times (z - z_0) \tag{4.1}$$

where:

- v_z is the sound velocity at depth z.
- v_0 is the sound velocity at the depth z_0, the depth of the velocimeter of Line 1, taken as a reference value.
  v_0 = 1547.02 m/s
  z_0 = -2476.57 m
- K_c is a constant computed from the Chen-Millero formula, in agreement with measurement presented in the left plot of Figure 4.5.
  K_c = 0.0171 s^{-1}

The right plot of Figure 4.5 shows the direct and the indirect measurements of the sound velocity obtained with the devices quoted above and translated at the depth of SV-01 by using Formula 4.1 for comparison. These values are in good agreement inside their uncertainty domains, except for few pathological instruments. The error on the SV values computed from C, T and P quantities by the Chen-Millero equation is equal to about 20 cm/s. The precise systematic uncertainty on the direct measurement given by the sound velocimeters is currently under study.

4.5 Triangulation

In the previous section, the sound velocity is computed in order to calculate the acoustic distances using the measured time of emission and reception of acoustic waves. The triangulation of these distances leads to the determination of the acoustic hydrophones positions, consequently, the determination of the positions of the optical modules by the string shape reconstruction. More details about the triangulation can be found in Reference [120].

Let's consider N points P_i $(i = 1,2,\ldots,N)$ in a 3D Euclidean space representing the acoustic emitters and receivers. At a given time t, the positions of these N points is calculated by triangulating the acoustic distances. The distance between P_i and P_j is denoted by $D_{i,j}$. This system of N points provides N^2 distances that are equal to the number of the combinations of the points. However, only $N(N-1)/2$ distances shown in Equation 4.2 are useful for triangulation because of the definition of the metric space which is given by:

- $\forall i \in \mathbb{N}, D_{i,i} = 0$ (identity of indiscernible).
- $\forall i, j \in \mathbb{N}, D_{i,j} = D_{j,i}$ (symmetry).
- $\forall i, j, k \in \mathbb{N}, D_{i,k} \leq D_{i,j} + D_{j,k}$ (triangle inequality).

The first property rejects N null distances that are between the points and themselves, while the second property divides the number of non-null distances by two (Equation 4.2).

$$D = \begin{bmatrix} - & D_{1,2} & \ldots & \ldots & D_{1,N} \\ - & - & D_{2,3} & \ldots & D_{2,N} \\ - & - & - & \ldots & \vdots \\ - & - & - & - & D_{N-1,N} \\ - & - & - & - & - \end{bmatrix} \tag{4.2}$$

Using only information on the distances leads to an infinite number of solutions, therefore an acoustic coordinate system is defined to converge to a unique solution as it is shown in the following section.

4.5.1 Acoustic coordinate system

The acoustic coordinate system is defined by the following three points:

- P_1: P_1 is the origin of the referential frame.
- P_2: $\vec{i} = \lambda \overrightarrow{P_1 P_2}$, $\forall \lambda \in \mathbb{R}^+$. Where $\vec{i}$ is the unity vector of x axis.

- P_3: P_3 is used to define the xP_1y plane ($P_3 \in xP_1y$). It is chosen to be non-linear with P_1 and P_2.

The unit vector $\vec{k}$ is chosen to be vertical and oriented from the bottom to the top ($\vec{k} = \lambda\overrightarrow{P_1z}, \forall\lambda \in \mathbb{R}^+$).

In a 3D Euclidean space, each point P_i is presented by x_i, y_i, z_i, therefore, the system has $3N$ free parameters. However, the definition of the acoustic coordinate system by the three points P_1, P_2 and P_3 leads to six constraints represented in Equation 4.3. Therefore, the number of the unknown parameters is decreased to $3N-6$.

$$\begin{array}{ll} x_1 = 0 & y_2 = 0 \\ y_1 = 0 & z_2 = 0 \\ z_1 = 0 & z_3 = 0 \end{array} \tag{4.3}$$

The coordinates of P_i and P_j are related to the distance $D_{i,j}$ by the following equation:

$$\left(x_i - x_j\right)^2 + \left(y_i - y_j\right)^2 + \left(z_i - z_j\right)^2 = D_{i,j}^2 \tag{4.4}$$

The number of these relations (Equation 4.4) is equal to $N(N-1)/2$ which is the number of the different distances. Therefore, to compute the $3N-6$ unknown parameters at least five points are needed.

In the rest of this chapter, the position vector of the point P_i is denoted by $\vec{P}_i$ instead of $\overrightarrow{P_1P_i}$.

4.5.2 Three main steps for triangulation

The particular subsystem constructed from P_1, P_2 and P_3 has nine parameters (the coordinates of the three points). These nine parameters are defined by the six constraints given in Equation 4.3 and the three distances $D_{1,2}$, $D_{1,3}$ and $D_{2,3}$ relations given by Equation 4.4. For this reason, the triangulation of N points system is done with three main steps:

1. Triangulation of the subsystem by computing the coordinates of P_1, P_2 and P_3 to define the acoustic coordinates system. The solution of this subsystem is given by the following equations:

$$\begin{array}{lll} x_1 = 0 & x_2 = D_{1,2} & x_3 = \left(D_{1,3}^2 + D_{1,2}^2 - D_{2,3}^2\right) / \left(2 \times D_{1,2}\right) \\ y_1 = 0 & y_2 = 0 & y_3 = \varepsilon_3 \sqrt{D_{1,3}^2 - x_3^2} \\ z_1 = 0 & z_2 = 0 & z_3 = 0 \end{array} \tag{4.5}$$

with $\varepsilon_3 = \text{Signe}\left(\left(\vec{P}_2 \wedge \vec{P}_3\right) \cdot \vec{k}\right)$, i.e. $\varepsilon_3 = \pm 1$.

2. Triangulation of the points P_i $(i = 4, \cdots, N)$ based on the coordinates of P_1, P_2 and P_3 and the distances between the point P_i and these three points. At this step, the points are triangulated point by point using the distances $D_{1,i}$, $D_{2,i}$ and $D_{3,i}$ to find x_i, y_i and z_i given by:

$$\begin{aligned} x_i &= \left(D_{1,i}^2 - D_{2,i}^2 + x_2^2\right) / (2 \times x_2) \\ y_i &= \left(D_{1,i}^2 - D_{3,i}^2 + x_3^2 + y_3^2 - 2 \times x_3 \times x_i\right) / (2 \times y_3) \\ z_i &= \varepsilon_i \sqrt{D_{1,i}^2 - x_i^2 - y_i^2} \end{aligned} \tag{4.6}$$

with $\varepsilon_i = \varepsilon_3 \times \text{Signe}\left(\left(\vec{P}_2 \wedge \vec{P}_3\right) \cdot \vec{P}_i\right)$, i.e. $\varepsilon_3 = \pm 1$.

3. In the final step, the positions of the N points are optimized using all the distances and Equation 4.4 by iterative way explained in the next section.

4.5.3 Optimization of points positions

The measured distances having uncertainties, the algorithm finds a pseudo solution computed by recurrence. The fact that the positions found in the iteration number n are a linear combination of the positions obtained in iteration number $n-1$, the recurrence can be represented as a matrix. This algorithm is explained briefly in Section 4.5.3.2 after a mathematical reminder in Section 4.5.3.1. More details can be found in references [121, 122].

4.5.3.1 Singular value decomposition

Let A be a matrix $(n \times m)$ with $n \leq m$. A can be given by a product of three matrices as shown in the following Equation:

$$A = U \cdot W \cdot V^T \tag{4.7}$$

where:

- U is an orthogonal $(n \times n)$ matrix.
- W is a diagonal $(n \times n)$ matrix.
- V is $(m \times n)$ matrix where the column vectors build an orthonormal system.

Let's define the matrix $\widetilde{W}^{-1}$ by:

$$\begin{cases} \widetilde{W}_{ij}^{-1} = 0 & \text{if } i \neq j \text{ or } W_{ij}^{-1} = 0 \\ \widetilde{W}_{ij}^{-1} = W_{ij}^{-1} & \text{otherwise} \end{cases} \tag{4.8}$$

The pseudo-inverse of A, denoted by $\widetilde{A}^{-1}$, is given by the following equation:

$$\widetilde{A}^{-1} = V \cdot \widetilde{W}^{-1} \cdot U^T \tag{4.9}$$

Let's consider the system $A \cdot X = B$ where X is unknown. It is possible that this system does not have a solution. In this case, the singular value decomposition of A can lead to a pseudo-solution $\widetilde{X}$ given by $\widetilde{X} = \widetilde{A}^{-1} \cdot B$ minimizing $|A \cdot X - B|$ by square minimization approach.

4.5.3.2 Definition of the recurrence relation

In iteration number n, the coordinates of P_i are denoted by $(x_i^{(n)}, y_i^{(n)}, z_i^{(n)})$ where the initial iteration $n = 0$ represents the positions given by the step 2 (Section 4.5.2). For each indices (i, j), an equation of the n^{th} iteration is associated. This equation is obtained by linearization of neighbourhood positions of the $(n-1)^{th}$ iteration given by the following equation:

$$\begin{aligned} &\frac{1}{D_{i,j} \times \sigma_{i,j}} \left(\vec{P}_i^{(n)} - \vec{P}_j^{(n)}\right) \left(\vec{P}_i^{(n-1)} - \vec{P}_j^{(n-1)}\right) = \\ &\frac{1}{2 \times D_{i,j} \times \sigma_{i,j}} \left(D_{i,j}^2 + \left(\vec{P}_i^{(n-1)} - \vec{P}_j^{(n-1)}\right)^2\right) \end{aligned} \tag{4.10}$$

The matrices $X^{(n)}$, $A^{(n)}$ and $B^{(n)}$ in equation $A^{(n)} \cdot X^{(n)} = B^{(n)}$ of iteration n are represented by equations 4.11, 4.12 and 4.13 respectively.

$$X^{(n)} = \begin{bmatrix} x_1^{(n)} \\ y_1^{(n)} \\ z_1^{(n)} \\ \vdots \\ x_N^{(n)} \\ y_N^{(n)} \\ z_N^{(n)} \end{bmatrix} \tag{4.11}$$

$$A_{(i,j),k}^{(n)} = \frac{1}{D_{i,j} \times \sigma_{i,j}} \left(\delta_{jk} - \delta_{ik}\right) \left(u_{j,m}^{(n-1)} - u_{i,m}^{(n-1)}\right) \tag{4.12}$$

where:

- $\sigma_{i,j}$ is a weight presenting the reliability of the measured $D_{i,j}$.
- δ_{ij} is the Kröenecker symbol[4].

[4] $\delta_{ij} = 1$ if $i = j$ and $\delta_{ij} = 0$ if $i \neq j$.

- $(u_{i,1}^{(n-1)}, u_{i,2}^{(n-1)} u_{i,3}^{(n-1)})$ corresponds to $(x_i^{(n-1)}, y_i^{(n-1)}, z_i^{(n-1)})$.

The matrix A has $N(N-1)/2$ lines (equations number) and $3N$ columns (parameters number).

$$B_{(i,j)}^{(n)} = \frac{1}{2 \times D_{i,j} \times \sigma_{i,j}} \left(D_{i,j}^2 + \left(\vec{P}_i^{(n-1)} - \vec{P}_j^{(n-1)} \right)^2 \right) \tag{4.13}$$

The pseudo solution is given by the following equation:

$$\widetilde{X}^{(n)} = \widetilde{A}^{-1} \left(X^{(n-1)} \right) \cdot B \left(X^{(n-1)}, D \right) \tag{4.14}$$

The convergence of the algorithm is based on the study of the norm of the vector $|\widetilde{X}^{(n)} - \widetilde{X}^{(n-1)}|$. The pertinence of the solution is evaluated by the $\chi 2^{(n)}$ factor presented in the following equation:

$$\chi 2^{(n)} = |A^{(n)} \cdot \widetilde{X}^{(n)} - B^{(n)}|^2 \tag{4.15}$$

4.6 Absolute pointing by the DGPS network and the LFLBL acoustic positioning system

As mentioned before, ANTARES is directly invisible to the DGPS network being at the depth of 2475 m from the sea level. To point the telescope (to find its orientation) in the sky, the LFLBL acoustic system is used in addition to the DGPS network, a boat, the RBs and the telescope itself.

4.6.1 RB absolute position measurement

The absolute positions of the five RBs are computed using the boat and the DGPS network. The DGPS network is used to determine the position of the boat. The measuring system measures the distances between the boat and each RB by LF acoustic waves. The boat changes its position many times, with every change, the distances between the boat and the RBs are measured. These distances are triangulated to locate the absolute position of each RB (Table 4.2) [123]. Figure 4.6 shows the positions of RBs with respect to the detector lines.

4.6.2 BSS absolute position measurement by the LFLBL system

After the measurement of the RBs absolute positions, the DGPS network is not used anymore. The position of each BSS is measured by two steps:

Name	x RB (m)	y RB (m)	z RB (m)
RB 01	8837	3296	-2460
RB 02	8067	0714	-2454
RB 03	7219	1959	-2439
RB 04	9028	1674	-2465
RB 05	7146	3385	-2456

Table 4.2: The absolute positions of RBs in UTM coordinates. Easting $= x = 26****$ and Northing $= y = 474****$ (where the stars, *, should be replaced by the values of x and y given in the table).

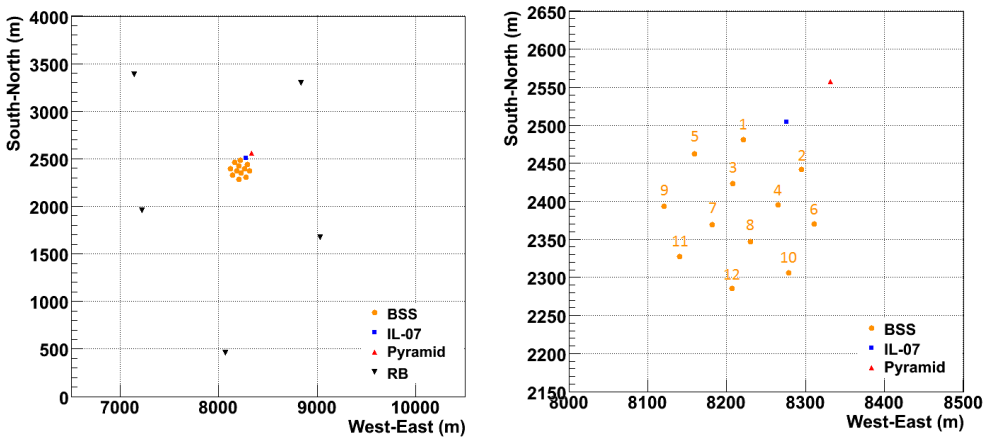

Figure 4.6: The absolute positions of the detector lines, the IL-07, the Pyramid and the RBs in UTM coordinates. Easting $= x = 26****$ m and Northing $= y = 474****$ m (where the stars, *, should be replaced by the values of x and y given in the plots). The right plot is a zoom of the left plot with the lines number.

1. Determination of the position of the boat: The distances between the boat and the five RBs are calculated using LF acoustic waves (Distance 3 in Figure 4.7). Triangulating these distances, the position of the boat is found. A quality check is anyway performed by comparing this acoustic position to the DGPS position of the boat.

2. Determination of the position of each BSS: In order to determine the position of each BSS, five sub-steps are applied:

   (a) LF acoustic signal is emitted by the boat; this signal triggers the transponder of each BSS.

   (b) The transponder responds by emitting LF waves of different frequency which trigger the boat receiver and the RBs. At this point, the distance between the boat and the BSS is calculated (Distance 1 in Figure 4.7).

   (c) The RBs being triggered, in their turn, emit different LF waves and trigger the boat receiver. The reception of these waves by the boat leads to calculate the distance Distance 1 + Distance 2 + Distance 3 (Figure 4.7).

   (d) Knowing the Distance 3 from the Step 1 and Distance 1 from Step 2 (b), Distance 2 is concluded.

   (e) Triangulating distances 1 and 2, the position of each BSS is calculated.

4.6.3 Pointing by the LFLBL system

In the previous section, the measurement of the BSS absolute position by the LFLBL system is explained. To calculate each RxTx transducer position, the geometry of the BSS is used as well as its orientation. The BSS geometry is measured before the lines deployment. The orientation of the BSS on the sea bed is measured during the line connection operation by using the compass of the submarine. The resulting positions of the RxTx transducers given by this system are presented in Table 4.3. As it is explained in Section 4.3, using the positions of $RxTx$-1, $RxTx$-2 and $RxTx$-3, the coordinates of π_{1-2} and π_{1-3} are calculated and they are given in Table 4.4 for January the first, 2007 at $12^h00'00''$. Figures 4.8 and 4.9 show the skymap of both points in the Equatorial and Galactic coordinates systems respectively.

4.6.4 Pointing uncertainty of the LFLBL system

The uncertainty on the pointing is estimated by Monte-Carlo technique simulating N_{sim} = 10000 detectors. Each detector has different positions of transducers and

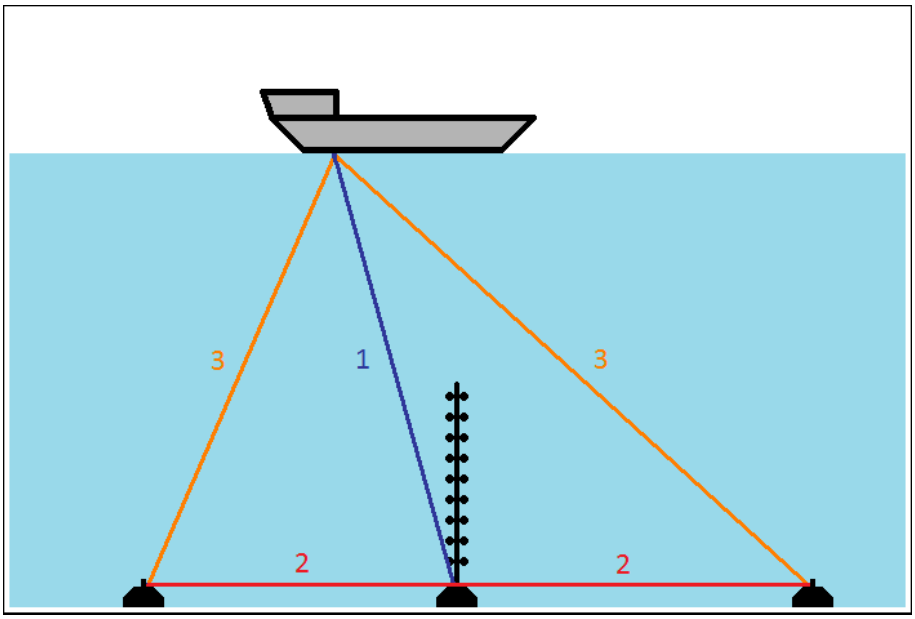

Figure 4.7: Schematic representation of the distances that will lead to the measurement of the absolute positions of the BSSs by LFLBL acoustic positioning system. Distance 1 represents the distance between the boat and the BSS, Distance 2 is the distance between the BSS and the RB and Distance 3 is the distance between the boat and the RB.

Name	x RxTx	y RxTx	z RxTx	σ_x	σ_y	σ_z
Line 01	8221.22	2481.33	-2474.39	1.00	0.80	0.60
Line 02	8294.79	2442.20	-2473.64	0.50	0.70	0.40
Line 03	8207.68	2423.42	-2474.51	0.90	1.00	0.50
Line 04	8264.96	2395.56	-2474.19	0.80	0.60	0.70
Line 05	8159.17	2462.50	-2473.08	0.70	1.00	0.50
Line 06	8311.47	2370.37	-2473.53	0.70	0.70	1.50
Line 07	8182.14	2369.41	-2474.08	0.70	1.00	1.60
Line 08	8230.60	2346.77	-2474.28	0.80	0.70	0.70
Line 09	8120.50	2393.56	-2474.37	0.80	0.60	0.40
Line 10	8279.04	2306.05	-2473.73	0.50	1.10	0.30
Line 11	8140.89	2326.98	-2474.69	0.80	1.10	0.60
Line 12	8206.81	2285.66	-2474.38	0.60	0.70	0.40
MILOM	8275.75	2504.21	-2474.09	0.70	0.70	0.60
Pyramid	8331.90	2557.80	-2473.13	0.60	0.70	0.70

Table 4.3: The positions of the RxTxs measured by LFLBL and the uncertainty of the system.

Point	r.a.	δ	l	b
π_{1-2}	$23^h52'15''$	$-18°29'06''$	$62.239°$	$-73.876°$
π_{1-3}	$18^h01'53''$	$-46°08'33''$	$346.577°$	$-11.333°$

Table 4.4: The coordinates of π_{1-2} and π_{1-3} in the Equatorial and the Galactic coordinates in January first, 2007 at $12^h00'00''$.

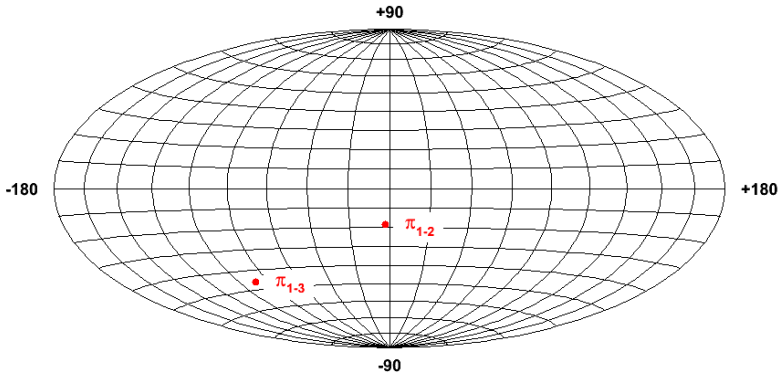

Figure 4.8: π_{1-2} and π_{1-3} in the Equatorial coordinates in January the first, 2007 at $12^h00'00''$.

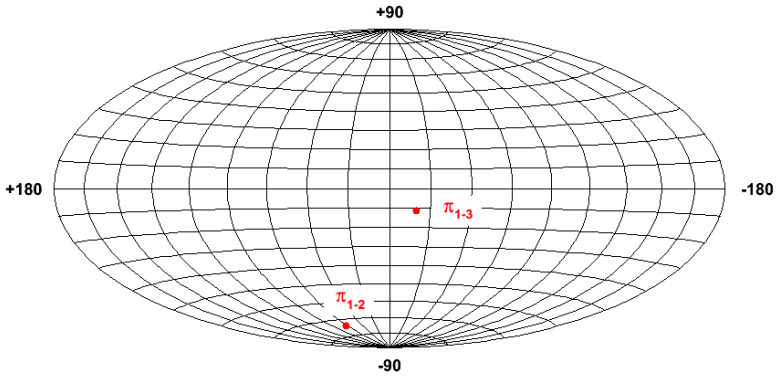

Figure 4.9: π_{1-2} and π_{1-3} in the Galactic coordinates in January the first, 2007 at $12^h00'00''$.

transponder. The generated positions are represented by the matrix P given in the following equation:

$$P = \begin{bmatrix} p_1^1 & p_2^1 & \cdots & p_{N_{\text{sim}}}^1 \\ p_1^2 & p_2^2 & \cdots & p_{N_{\text{sim}}}^2 \\ \vdots & \vdots & \vdots & \vdots \\ p_1^{14} & p_2^{14} & \cdots & p_{N_{\text{sim}}}^{14} \end{bmatrix} \tag{4.16}$$

where the superscript index refers to the 12 lines, the IL-07 and the pyramid respectively. The subscript index refers to the N_{sim} simulated detectors.

These detectors are simulated in a way so they form, for a given transducer (transponder), a 2D Gaussian distribution of N_{sim} simulated transducers (transponders) positions in the horizontal plane and a 1D distribution in the vertical direction. In other words, for a given i, the distribution of the points p_j^i, $j = 1,2,\cdots,N_{\text{sim}}$ is a 2D (1D) horizontal (vertical) Gaussian. The mean values of the Gaussians are the positions measured by the LFLBL system and the RMSs represent their positions uncertainties (Table 4.3).

Fixing both indices m and n, $m \neq n$, m and $n \in \{1,2,\cdots,14\}$, the relative angular distribution of the N_{sim} directions made by the two points p_j^m and p_j^n with $j = 1,2,\cdots,N_{\text{sim}}$ represents the pointing variation in this particular *m-n* direction. This angular distribution is a Gaussian where the RMS is the 3D angular uncertainty on the pointing in the particular *m-n* direction. Figure 4.10 shows the RMSs of the 91 RxTxs combinations (1-2, 1-3, $\cdots$, 2-3, 2-4, $\cdots$, 13-14). For the rest of this chapter, the pointing uncertainty is calculated in the horizontal and vertical directions due the difference of the system feature in both directions (Figure 4.11). These two uncertainties are calculated the same way as the 3D value but with projecting the *m-n* directions in the horizontal plane and the vertical direction. Figure 4.11 shows that in some directions the pointing uncertainty is equal to 1.3° and 1.9° in the horizontal and vertical directions respectively.

For different values of m and n, the uncertainty on the pointing as defined above is not the same (Figure 4.11), the reason for that is the weak "rigidity" of the detector. For a given m and n, the distances between p_j^m and p_j^n for $j = 1,2,\cdots,N_{\text{sim}}$ are different because of the random generation of the p_j^i positions. For the 91 combinations of the RxTxs, Figure 4.12 shows the RMS of the distribution of the distance between p_j^m and p_j^n. It should be stressed that rigidity, in this paragraph, does not refer to the real detector but to the detector reconstructed by the acoustic distances.

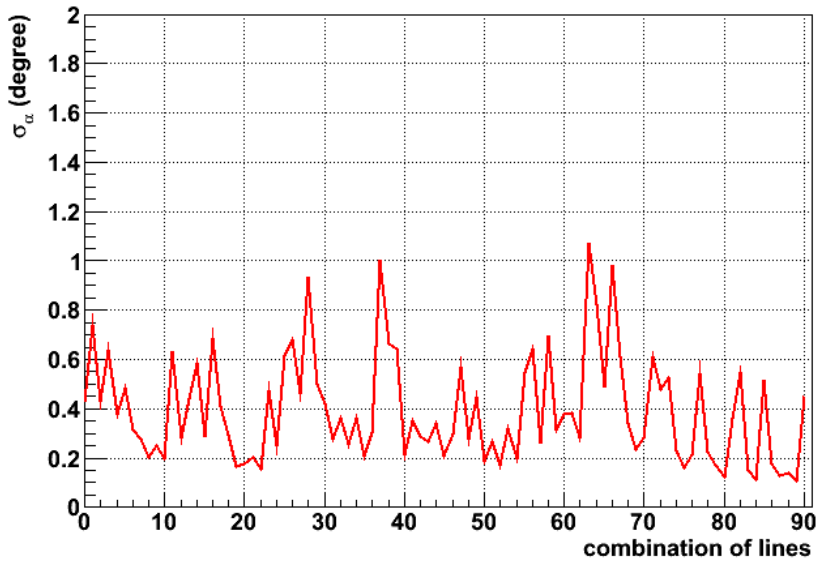

Figure 4.10: The RMSs of the 3D angular distributions of the different combinations of lines.

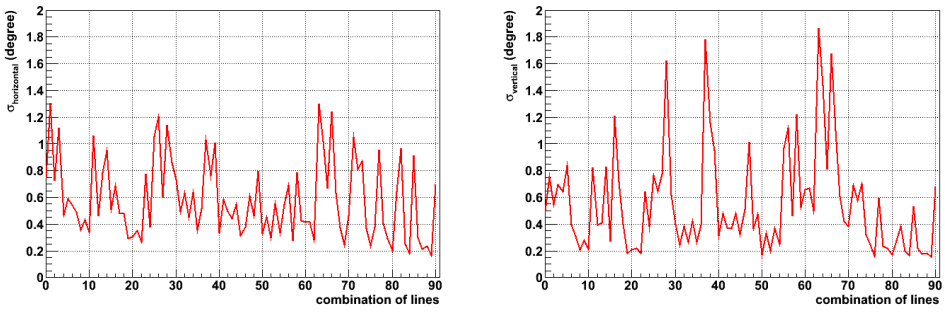

Figure 4.11: The RMSs of the horizontal (left) and the vertical (right) angular distributions of the different combinations of lines.

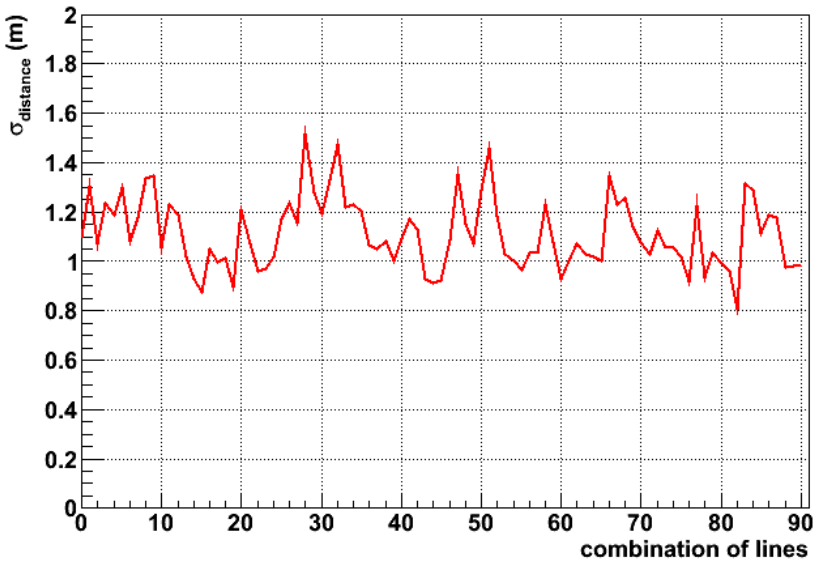

Figure 4.12: The RMS of the distances distributions of the different combinations of lines.

4.6.5 Uncertainty recalculation of the BSS position

This step is an intermediate step between the pointing calculations with the LFLBL and HFLBL systems.

In addition to the LFLBL system, two more independent information are used to decrease the uncertainties on the z coordinates of the transducers and the transponder:

- The pressure measured by the pressure sensor fixed on the submarine at the time of the line connection. It allows to measure the relative depth of the BSSs with an accuracy of $\sim$ 10 cm.
- The triangulated positions of all Rxs of the same line when the sea current velocity is small i.e. the lines are almost vertical. This technique looks to the line inclination obtained by triangulation when changing the depth of few RxTxs.

This additional information does not lead to more accurate absolute depth value. However, it is efficient for the relative depth measurement. In fact, the translational movement does not affect the absolute pointing; only the rotational movement does.

Name	z RxTx by LFLBL (m)	z RxTx by LFLBL + pressure + HF distances (m)	Δz (m)
Line 01	-2474.39	-2474.38	0.01
Line 02	-2473.64	-2474.45	0.81
Line 03	-2474.51	-2474.49	0.02
Line 04	-2474.19	-2474.47	0.28
Line 05	-2473.08	-2474.45	1.37
Line 06	-2473.53	-2474.39	0.86
Line 07	-2474.08	-2474.61	0.53
Line 08	-2474.28	-2474.52	0.24
Line 09	-2474.37	-2474.62	0.25
Line 10	-2473.73	-2474.16	0.43
Line 11	-2474.69	-2474.26	0.43
Line 12	-2474.38	-2474.06	0.32
IL-07	-2474.09	-2474.27	0.18
Pyramid	-2473.13	-2472.84	0.29

Table 4.5: The z coordinates of the RxTxs measured by LFLBL and by LFLBL + pressure data + HF distances. The difference between both values is also shown.

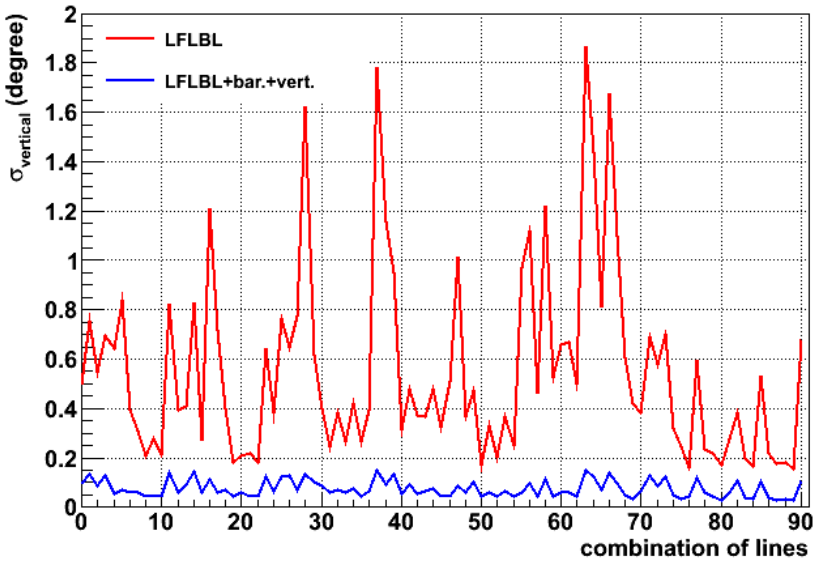

Figure 4.13: The RMSs of the vertical angular distributions of the different combinations of lines.

The new z coordinates of the RxTxs are given in Table 4.5. The uncertainties on the new relative z coordinates are estimated to be ~ 0.1 m.

Figure 4.13 shows the improvement of the pointing in the vertical direction from 1.9° to less than 0.15°.

4.7 Absolute pointing by the HFLBL acoustic positioning system

In this section, the telescope pointing is recalculated by triangulating the HF acoustic distances. The new uncertainty values of the telescope pointing are discussed studying the systematic uncertainties on the HF distances, the BSS positions, the sound velocity and the choice of the Rx hydrophone for the triangulation.

4.7.1 Telescope pointing by the HFLBL system

The positions of the RxTxs, shown in Table 4.3 for x and y and Table 4.5 for z, are now recalculated in Table 4.6 by triangulating the measured HF distances (the real acoustic data). The difference between the coordinates of the positions, before and after triangulation, is around 1 m as it is shown in Table 4.6 which is in a good agreement with the expected precision of the LFLBL system.

Using the new positions of $RxTx$-1, $RxTx$-2 and $RxTx$-3, the new coordinates of π_{1-2} and π_{1-3} are calculated so as the angle between the old and the new π_{1-2} and π_{1-3}. The results are presented in Table 4.7.

The triangulation by the HF acoustic distances shifts π_{1-2} and π_{1-3} by 1.020° and 0.679° respectively. These values agree with the pointing uncertainties calculated by the LFLBL system in Section 4.6.4.

4.7.2 Telescope pointing uncertainty using the HFLBL system

The uncertainty on the telescope pointing, here, is calculated with the same way as in Section 4.6.4 but after triangulating the N_{sim} simulated detectors using HF acoustic distances. To visualize the variation of the simulated positions of the RxTxs and the orientation modification of the simulated detectors, Figure 4.14 represents an example of a detector with three lines. The figure on the left shows the positions of the RxTxs (with the LFLBL system errors) and the simulated three detectors as it is explained in Section 4.6.4 while the figure on the right shows the positions of the RxTxs after the triangulation of the HF acoustic distances. Figure 4.14 shows the decrease of the uncertainty on the RxTx positions using the

RxTx	x RxTx (m) before	y RxTx (m) before	x RxTx (m) after	y RxTx (m) after	Δx (m)	Δy (m)
Line 1	8221.22	2481.33	8222.17	2480.66	0.95	0.67
Line 2	8294.79	2442.20	8295.23	2443.18	0.44	0.98
Line 3	8207.68	2423.42	8208.00	2423.14	0.32	0.28
Line 4	8264.96	2395.56	8264.02	2395.12	0.94	0.44
Line 5	8159.17	2462.50	8159.28	2463.82	0.11	1.32
Line 6	8311.47	2370.37	8311.82	2371.06	0.35	0.69
Line 7	8182.14	2369.41	8181.86	2368.64	0.28	0.77
Line 8	8230.60	2346.77	8230.10	2346.72	0.50	0.05
Line 9	8120.50	2393.56	8119.96	2394.03	0.54	0.47
Line 10	8279.04	2306.05	8279.73	2306.16	0.69	0.11
Line 11	8140.89	2326.98	8141.01	2326.54	0.12	0.44
Line 12	8206.81	2285.66	8206.53	2284.92	0.28	0.74
IL-07	8275.75	2504.21	8276.03	2505.01	0.28	0.80
Pyramid	8331.90	2557.80	8331.19	2556.82	0.71	0.98

Table 4.6: The x and y coordinates of the RxTxs measured by the LFLBL and HFLBL systems and the difference between their positions before and after HF acoustic distances triangulation.

Point	$r.a.$	δ	l	b	$\Delta\Omega$
π_{1-2}	$23^h56'29''$	$-18°17'53''$	$64.974°$	$-74.574°$	$1.020°$
π_{1-3}	$17^h58'04''$	$-45°59'20''$	$346.4°$	$-10.677°$	$0.679°$

Table 4.7: The coordinates of π_{1-2} and π_{1-3} in the Equatorial and the Galactic coordinates in January first, 2007 at $12^h00'00''$ after the triangulation of the HF acoustic distances. The difference between the coordinates before and after triangulation is shown.

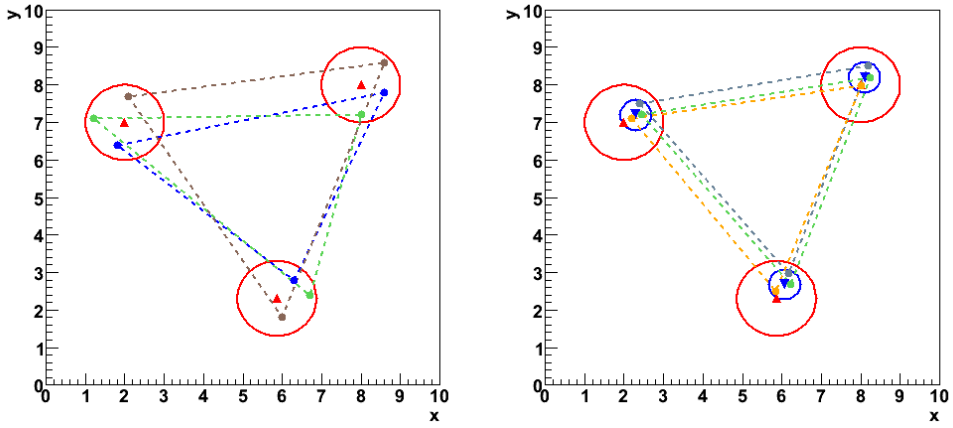

Figure 4.14: An example of three simulated detectors with 3 lines without and with the HF acoustic distances triangulation in the left and in the right plots respectively. The red triangles are the RxTxs positions given by the LFLBL system. The red circles present the errors on the RxTxs positions due to the LFLBL acoustic system. The blue circles are defined by the triangulated positions where the blue triangles are the center of gravity of the triangulated positions distributions.

HFLBL system. The RMSs of the angular distributions of the directions made by the points p_j^m and p_j^n with $m \neq n$ and $j = 1, 2, \cdots, N_{\text{sim}}$ are smaller, too.

For the 12-line detector, the decrease of the RxTxs positions uncertainty is presented by the distributions in the horizontal plane of the simulated points before and after the triangulation shown in figures 4.15 and 4.16 respectively. Figure 4.17 shows, in red, the distributions of the distances between the RxTxs positions measured by the LFLBL system (Gaussian center) and the generated positions before the triangulation of the HF distances. It shows also, in blue, the distributions of the distances between the triangulated positions and their center of gravity. Like the previous plots, these distributions illustrate the decrease of the uncertainties on the RxTxs positions.

The new uncertainties are equal to $\sigma_{\text{horizontal}} = 0.126^\circ$ and $\sigma_{\text{vertical}} = 0.024^\circ \pm 0.004^\circ$. The error $\pm 0.004^\circ$ is due to the rigidity of the detector.

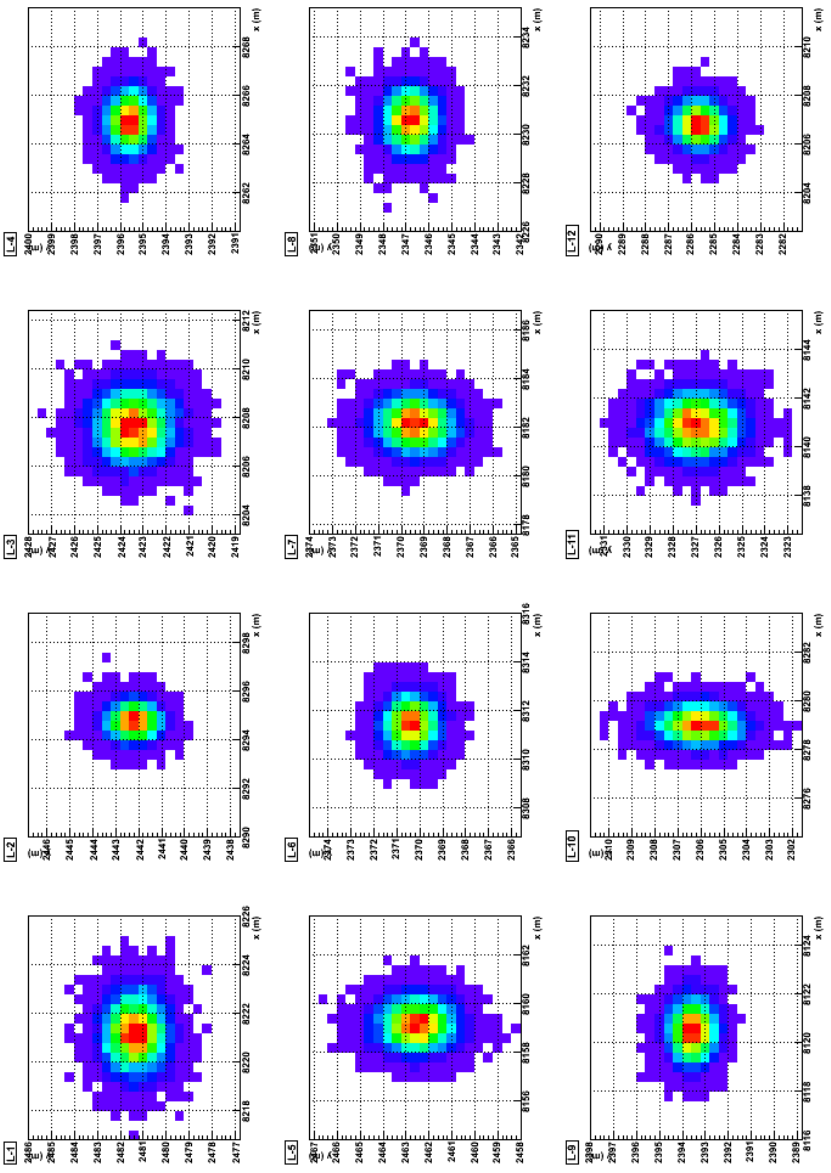

Figure 4.15: The positions distributions of the generated points in the horizontal plane before the HF distances triangulation.

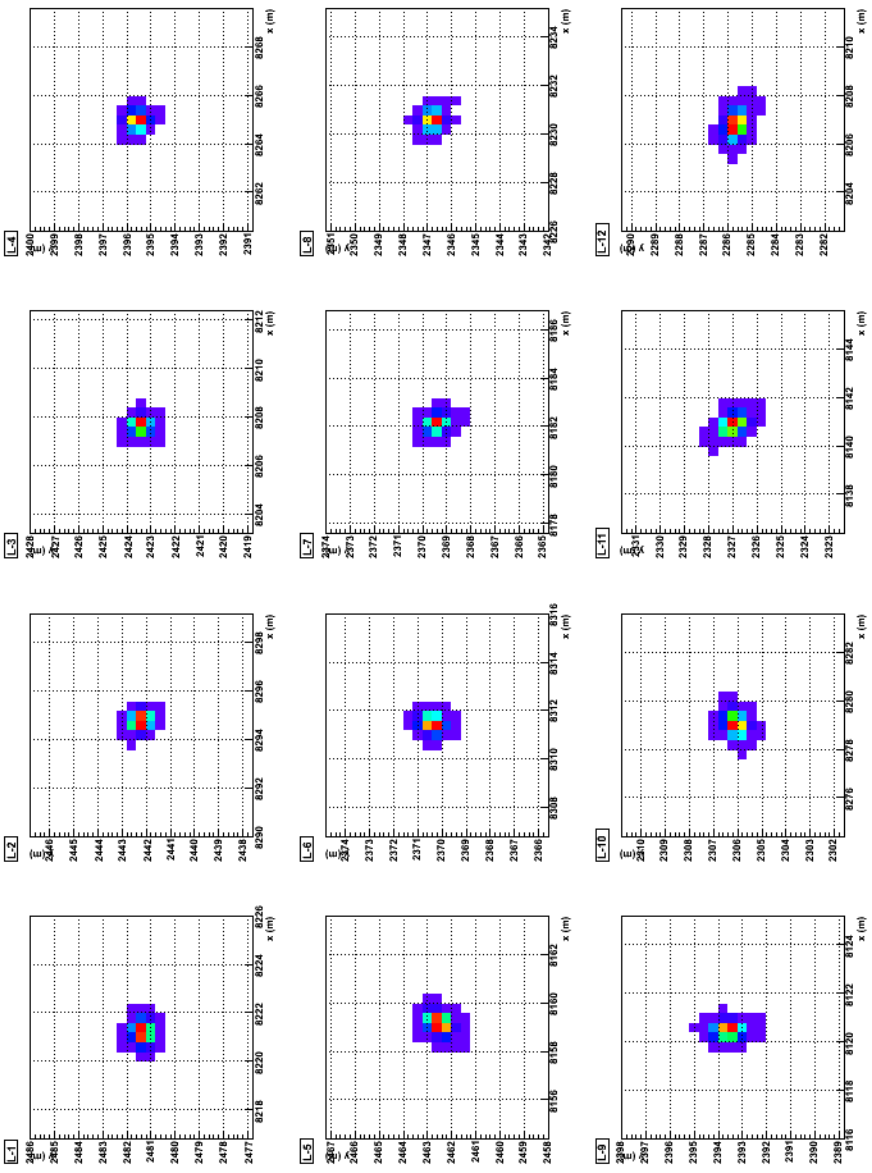

Figure 4.16: The positions distributions of the generated points in the horizontal plane after the HF distances triangulation.

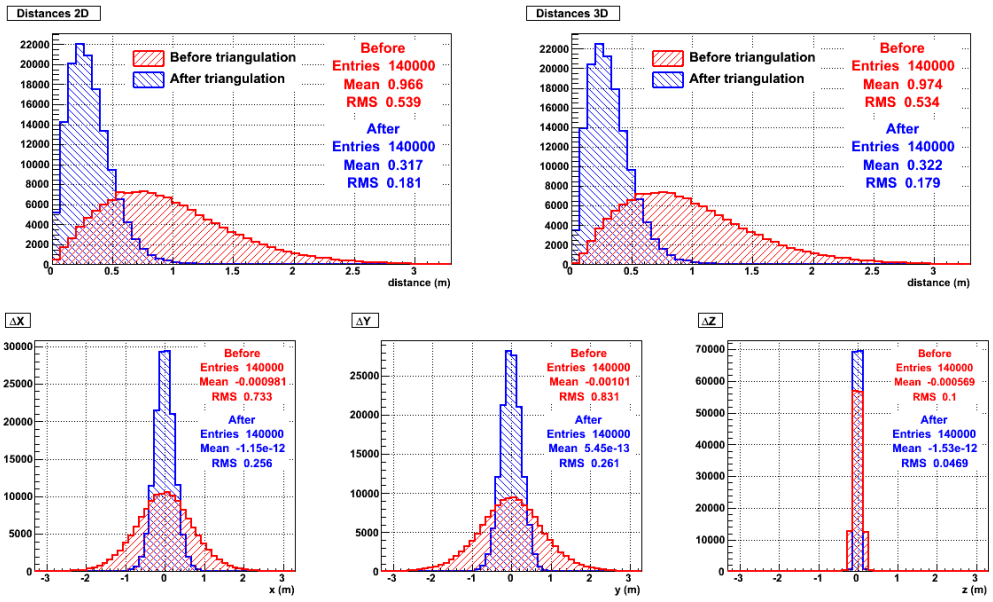

Figure 4.17: The two plots on the top present the distances between the generated points and their gravity center in the horizontal plane (left) and 3D space (right) before and after the HF acoustic distances triangulation. The three bottom plots present the projections of the generated points on the x axis (left), y axis (middle) and z axis (right).

4.7.3 Systematic uncertainties

Four sources of systematic uncertainties are studied: the uncertainty on the measured acoustic distance between the acoustic emitter and receiver, the errors on the RxTxs positions measured by the LFLBL system, the uncertainty on the sound velocity and the choice of the Rx used for the HF distances triangulation.

4.7.3.1 Uncertainty on the measured acoustic distance between the acoustic emitter and receiver

The uncertainty on the measured HF acoustic distance between the emitter and receiver is due to the time error of the emission and the reception of the acoustic wave. This uncertainty is measured in the laboratory by setting the transmitter and the receiver one beside the other in order to have a zero distance. Measuring many times and with different transmitters and receivers, the average time difference between the measured values and the real values, taking in account the intrinsic time delay of the devices, is equivalent to a distance of 3 cm.

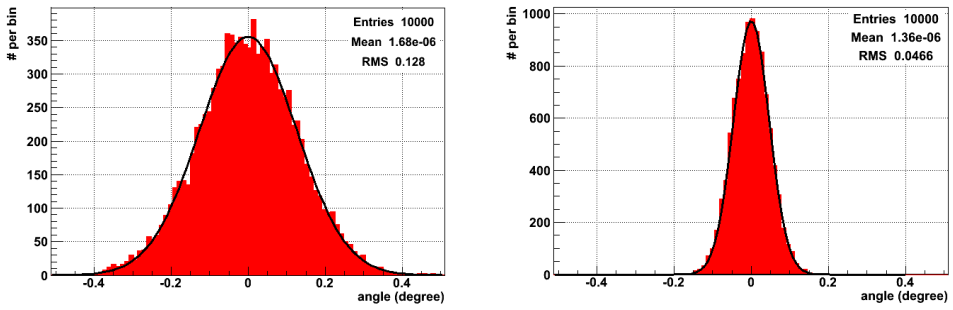

Figure 4.18: The horizontal (left) and the vertical (right) angular distributions for the directions joining N_{sim} positions of Line 1 and Line 3. Both distributions are fitted by Gaussian function.

The effect of the measured HF distances uncertainty on the pointing uncertainty is studied by smearing the HF distances by a Gaussian with RMS value equal to 3 cm before triangulation. The new pointing uncertainty is $\sigma_{\text{horizontal}} = 0.127 \pm 0.002^\circ$ and $\sigma_{\text{vertical}} = 0.035^\circ \pm 0.020^\circ$. The errors on these values are due to the rigidity of the detector. Figure 4.18 shows the distributions of the directions made by the points p_j^m and p_j^n with $m = 1, n = 3$ and $j = 1, 2, \cdots, N_{\text{sim}}$.

The variation of the detector pointing uncertainty is studied increasing the error on the HF acoustic distances from 3 cm to 10 cm. Figure 4.19 shows that this variation is linear.

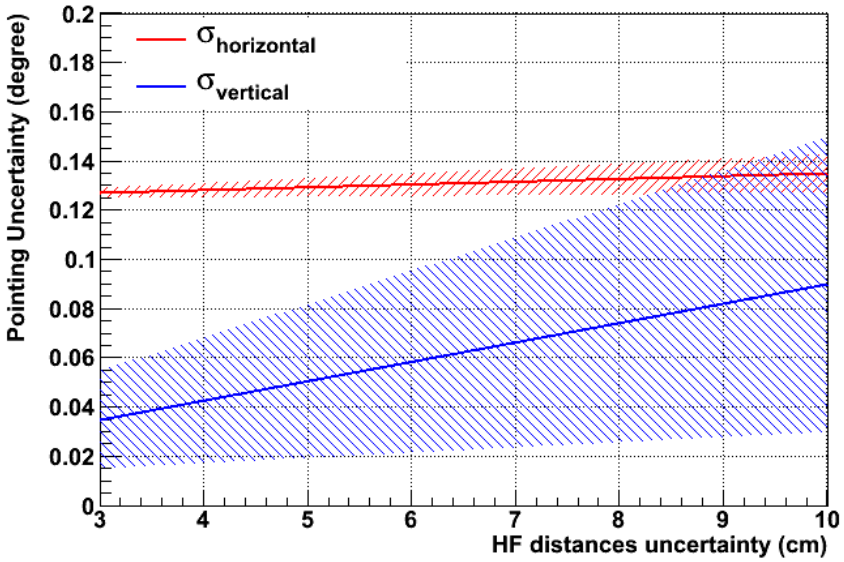

Figure 4.19: The uncertainty on the pointing in the horizontal (red) and vertical (blue) directions as a function of the HF acoustic distances error. The uncertainty on the pointing uncertainty (dashed region in the plot) is due to the rigidity of the detector.

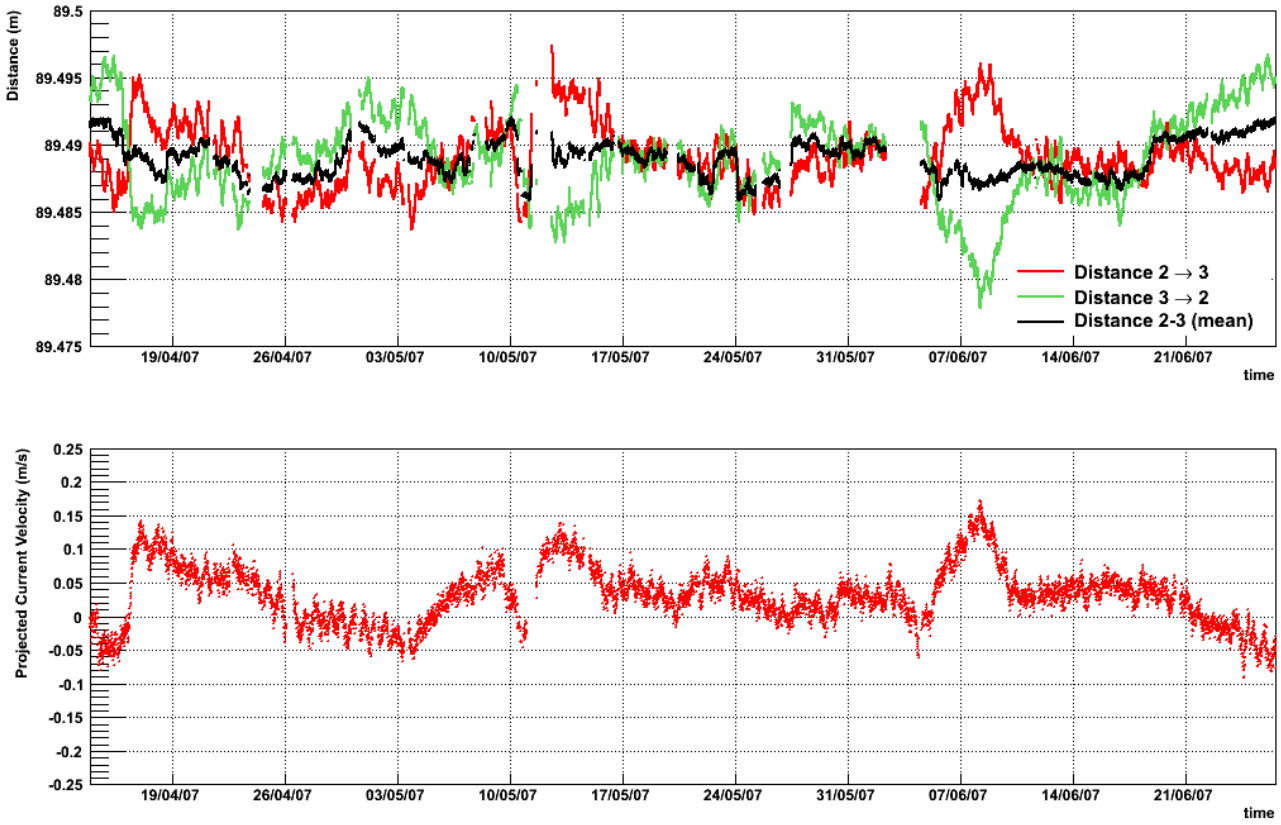

Figure 4.20: Top plot: HF acoustic distances calculated by the emission of *RxTx*-2 and the reception by *RxTx*-3 ($2 \rightarrow 3$) and vice versa ($3 \rightarrow 2$). The black line represents the mean value. The bottom plot: sea current velocity projected in the direction of *RxTx*-2 and *RxTx*-3.

Figure 4.20 is an illustration of the acoustic distance between the RxTxs of Line 2 and Line 3 for a period of time. It is calculated using the emission-reception time of the HF acoustic waves in both directions i.e. the emission by $RxTx$-2 then the reception by $RxTx$-3 ($2 \rightarrow 3$) and vice versa ($3 \rightarrow 2$).

The value of the distances $2 \rightarrow 3$ and $3 \rightarrow 2$, as a function of time, are symmetrical with respect to their mean value. The projection of the sea current velocity on the direction made by both RxTxs, as a function of time, shows clear correlation with one direction and anti-correlation with the other. In fact, when the acoustic wave propagates in the same (inverse) direction as the sea current, it will be faster (slower) than the propagation in a non-moving medium as it is illustrated in Equation 4.17 (4.18).

$$v = v_0 + v_c \tag{4.17}$$

$$v = v_0 - v_c \tag{4.18}$$

where v_c is the sea current velocity and v_0 (v) is the propagation velocity of the acoustic waves in a non-moving (moving) medium. This velocity variation increases / decreases the "real" distance by a factor of $v_c \times \Delta t$, where Δt is the emission-reception time.

In theory, the mean value of the distances of both directions, which does not include the sea current effect, should be equal to $v_0 \times \Delta t$ (constant as a function of time). The mean value in Figure 4.20 shows variations that do not fluctuate by more than 3 cm which is the uncertainty on the HF acoustic distances.

4.7.3.2 Effect of the BSSs positions uncertainties given by the LFLBL system on the pointing

Before the triangulation of the HF distances, the pointing uncertainty is recalculated changing the uncertainties on the BSSs positions given by the LFLBL system. The 3 cm error discussed in the previous section is included. The error on the telescope pointing increases linearly with the change of the BSS position uncertainty in the horizontal and vertical directions (Figure 4.21).

The average uncertainty on the BSSs positions given by the LFLBL system is equal to ~ 0.8 m (bottom-left and bottom-center plots of Figure 4.17). The corresponding pointing uncertainty agrees well, especially in the horizontal direction, with the value estimated in the previous section. The small difference (within the errors) in the vertical direction is due to the fact that in the previous section the uncertainties on the x and y values of the BSSs are the real errors given in Table 4.3 but Figure 4.21 uses the average values.

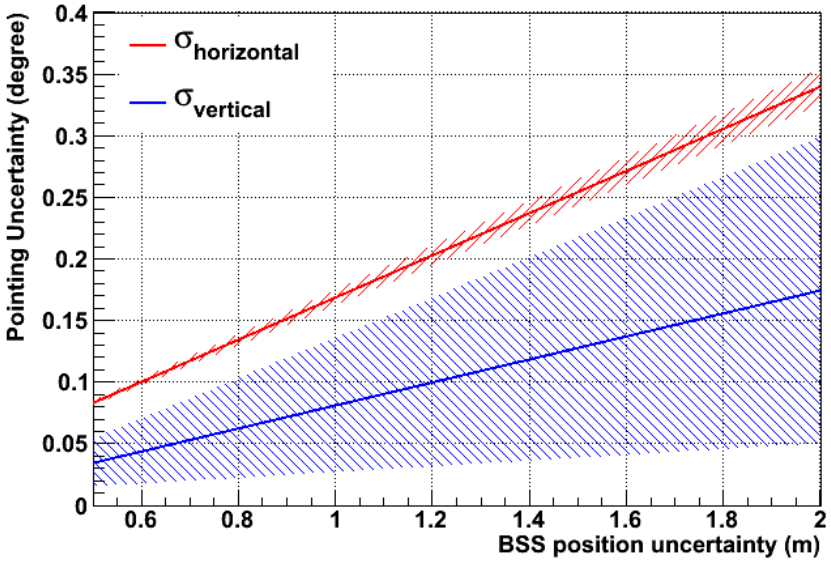

Figure 4.21: The pointing uncertainty as a function of the BSS position uncertainty in the horizontal and the vertical directions. The uncertainty region in the plot presents the error on the values due to the rigidity of the detector.

4.7.3.3 Uncertainty on the sound velocity

After the deployment of the ANTARES lines in the sea, the uncertainty on the sound velocity is computed by measuring the emission of acoustic waves from the RxTxs and their reception by the Rxs using the constraints on the length of the cables. The length stretch by the tension from one side and the contraction from the other side can result a variation estimated to be less than $\sim$ 6 cm, therefore, the sound velocity uncertainty is estimated to be less than 0.2 m/s. This value is equal to the error on the Chen-Millero equation.

The uncertainty on the sound velocity is taken into account by adding / removing an offset on the distances equivalent to $\pm$ 0.2 m/s. The pointing of the telescope is not affected by this offset ($\Delta\Omega < 0.001^{\circ}$) and that is due to the fact that the volume of the telescope increases /decreases without significant rotational movements.

4.7.3.4 Check on the choice of the hydrophone

Being out of the RxTxs horizontal plane, the use of an Rx hydrophone for the HF acoustic distances triangulation is mandatory to decrease the numerical error on the algorithm output. For the analysis discussed above, the hydrophone *Rx*-5

of Line 8 is used. The Line 8 being one of the four inner lines of the detector (Figure 4.6), the study is repeated with the hydrophone *Rx*-5 of Line 10 (outer line). Then, it is repeated again using the hydrophone *Rx*-2 of Line 8 to check the altitude influence. For both changes, the variation of the pointing is negligible ($\Delta\Omega < 0.001^\circ$).

4.8 Relative uncertainty on the hydrophone position

In this section, the uncertainty on the Rx position in the relative referential is studied. In addition to the compass and the tiltmeter data, the positions of the Rxs are used to find the positions of the optical modules used in the reconstruction algorithm of the muon tracks.

Monte-Carlo simulations are developed to generate 10000 detectors with fixed positions of RxTxs. Including the uncertainty on the HF acoustic distances (Section 4.7.3.1), the uncertainty on the relative positions of the Rx hydrophones is estimated to be 6 cm in the horizontal plane and 1 cm in the vertical direction. As shown in Section 4.7.3.3, the influence of the sound velocity systematic error is estimated adding an offset of 0.2 m/s on the HF acoustic distances. The simulations show that the uncertainty remains the same, however, the position of the Rx is shifted vertically by a maximum of 6 cm.

4.9 Conclusion

In this chapter, the absolute pointing of the ANTARES telescope and its uncertainty are studied using the LFLBL and the HFLBL acoustic positioning systems. Two directions, π_{1-2} and π_{1-3}, are defined by the positions of $RxTx1$, $RxTx2$ and $RxTx3$. These directions point to $r.a. = 23^h56'29''$, $\delta = -18^\circ17'53''$ and $r.a. = 17^h58'04''$, $\delta = -45^\circ59'20''$ respectively in January the first of 2007 at $12^h00'00''$. The uncertainty on the absolute pointing is estimated using Monte-Carlo simulations evaluating the systematic errors (on the sound velocity, on the acoustic time measurements, ...). This uncertainty is estimated to be a Gaussian with $\sigma_{\text{horizontal}} = 0.127^\circ \pm 0.002^\circ$ and $\sigma_{\text{vertical}} = 0.035^\circ \pm 0.020^\circ$ in the horizontal and vertical directions respectively. The uncertainty on the positions of the acoustic receivers in the relative referential is studied as well. The error on the positions of Rx hydrophones is about 6 cm.

Chapter 5

Search for neutrino point sources in the 2007 data using BBfit

In this chapter, the search of neutrino point sources in the ANTARES 2007 data, with the 5-line detector configuration, using the BBfit reconstruction strategy is presented. The search algorithm is based on an unbinned maximum-likelihood ratio method.

In Section 5.1, the selected data and the Monte-Carlo simulations are described. In Section 5.2, comparisons of data and Monte-Carlo distributions for relevant parameters and for various cuts are performed. In sections 5.3 and 5.4, the impact of these cuts on the effective area and the angular resolution is discussed. In Section 5.5, the unbinned maximum-likelihood ratio method used in this analysis is presented. In Section 5.6, the candidate sources list and the all sky search strategies are discussed. In Section 5.7, the preferred cuts which yield to the best discovery potential and sensitivity are extracted. The study of the systematic uncertainties are discussed in Section 5.8. In Section 5.9, Monte-Carlo skymaps resulting from the all sky search strategy are shown. Finally, in Section 5.10, the data results are presented.

5.1 Data and Monte-Carlo

The runs where the counting rate baseline (Section 3.2.7.2) is lower than 120 kHz and where the burst fraction[1] is lower than 0.4 are classified as silver runs. The data sample is the 2007 silver runs (939 runs). The total livetime of the selected runs is 167.7 active days (47.2 days for HighThreshold = 10 p.e. and 120.5 days for HighThreshold = 3 p.e.) (Section 3.2.5). The events are triggered with the 3N

[1]The burst fraction is the fraction of the run period where the counting rate is 20% higher than the baseline.

filter. Due to a dead time present in the online trigger at that time, this is equivalent to 139.7 active days (39.3 days for 10 p.e. and 100.4 days for 3 p.e.) [124]. The Monte-Carlo simulations used in this study are described in Section 3.3.

All Monte-Carlo files are processed by TriggerEfficiency with the 3N trigger. The non-Gaussian tails in the charge distribution of the background hits are included. The ARS dependent L0 thresholds are also applied. The summary-of-summaries files[2], for 10 p.e. and 3 p.e., are used to simulate the background single rates on the optical modules for the 10 p.e. and 3 p.e. periods respectively. The neutrino and the muon events are reconstructed with BBfit v3r5.

5.2 Data and Monte-Carlo comparisons

The selection cuts are optimized to have the best discovery potential based on the Monte-Carlo simulations assuming an E^{-2} energy spectrum for the signal (Section 5.7). The definition of the discovery potential is given in Section 5.5.1. The optimization is a trade-off between the effective area, the angular resolution and the background rejection.

A minimum set of basic cuts is defined:

- more than five hits used in the BBfit track fit ($nhit > 5$).
- at least two lines used in the BBfit track fit ($nline \geq 2$).
- the zenith[3], z, less than 90° (reconstructed as an up-going muon).

The following quantities are considered in the cut optimization:

- the $tchi2$, BBfit muon track fit quality parameter (the optimized value: $tchi2 \leq 1.8$ when $z \leq 80°$ and $tchi2 \leq 1.4$ when $80° < z \leq 90°$).
- the $bchi2$, BBfit bright point fit quality parameter (the optimized value: $bchi2 \geq 2.2$).
- the zenith z (the optimized value: $z \leq 80°$ when $tchi2 \leq 1.8$ and $80° < z \leq 90°$ when $tchi2 \leq 1.4$).

Figure 5.1 compares the data and Monte-Carlo distributions of $tchi2$ for $bchi2 \geq 2.2$ and $z \leq 90°$. The atmospheric neutrino flux (Monte-Carlo) is 10% higher than the data flux in the range of $tchi2 \leq 1.4$.

[2]The summary-of-summaries files are extracted from the data to summarize the information on the optical background and the dead channels.

[3]The zenith is the angle made by the reconstructed muon and the up-going vertical direction.

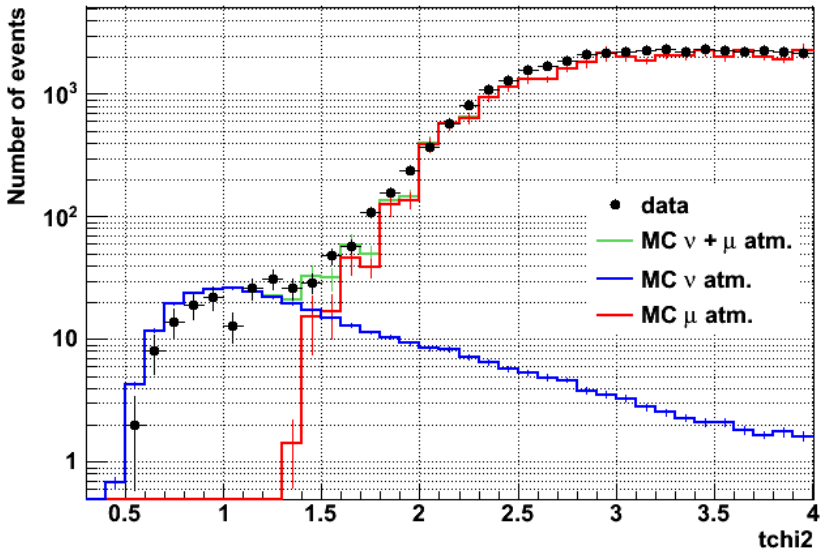

Figure 5.1: *tchi*2 distribution for the data and Monte-Carlo (*bchi*2 ≥ 2.2 and $z \leq 90°$).

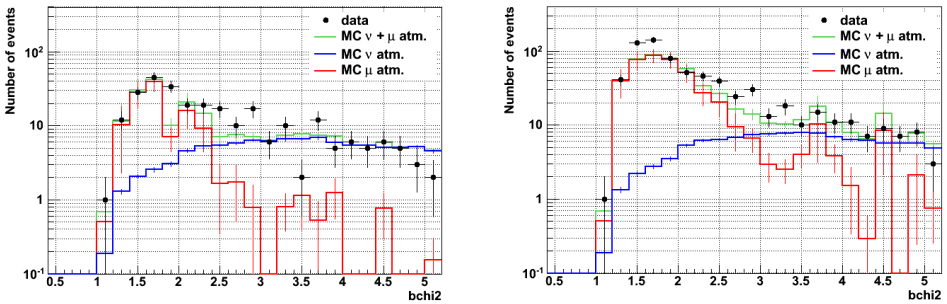

Figure 5.2: *bchi*2 distribution for *tchi*2 ≤ 1.8 and $z \leq 80°$ (left), $z \leq 90°$ (right).

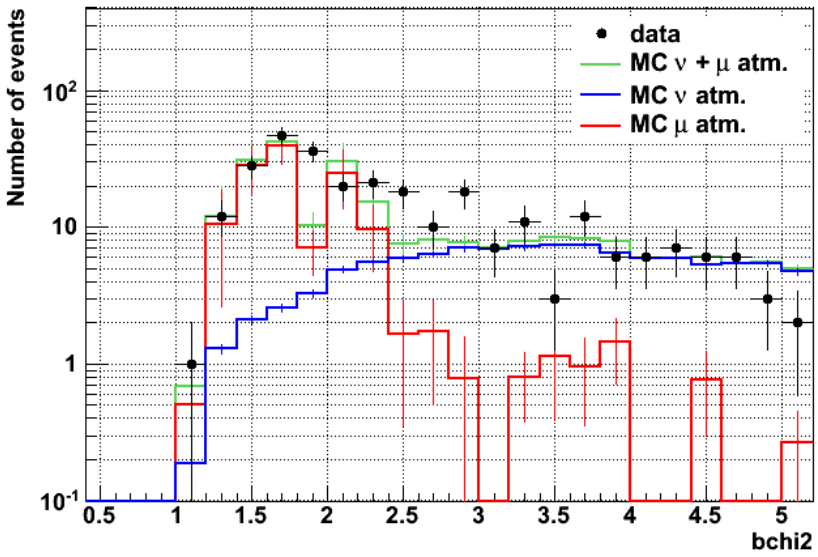

Figure 5.3: *bchi*2 distribution for the optimized cuts (except *bchi*2).

Figures 5.2 and 5.3 compare the data and Monte-Carlo distributions of *bchi*2. The motivation to cut on *bchi*2 is the rejection of the atmospheric muons at low *bchi*2 values.

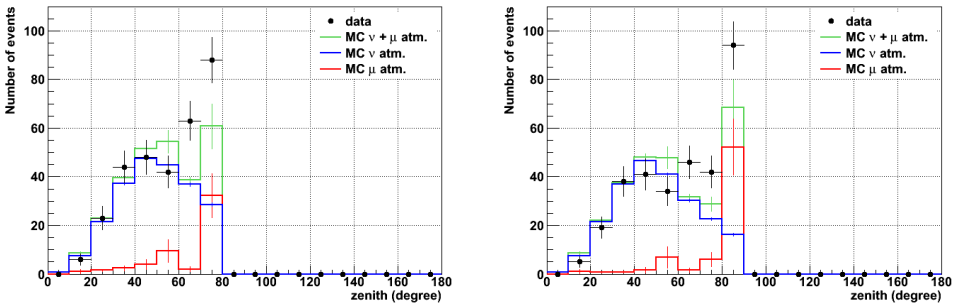

Figure 5.4: z distribution for $z \leq 80^\circ$ and *bchi*2 ≥ 1.8 (left), $z \leq 90^\circ$ and *bchi*2 ≥ 2.6 (right). *tchi*2 ≤ 1.8 for both.

Figures 5.4, 5.5, 5.6, 5.7 and 5.8 compare the data and Monte-Carlo distributions of the zenith and the declination angles of the reconstructed tracks. In the right plot of Figure 5.4, the zenith bin $80^\circ < z \leq 90^\circ$ suffers from a large contamination of badly reconstructed down-going muons. Consequently, for events

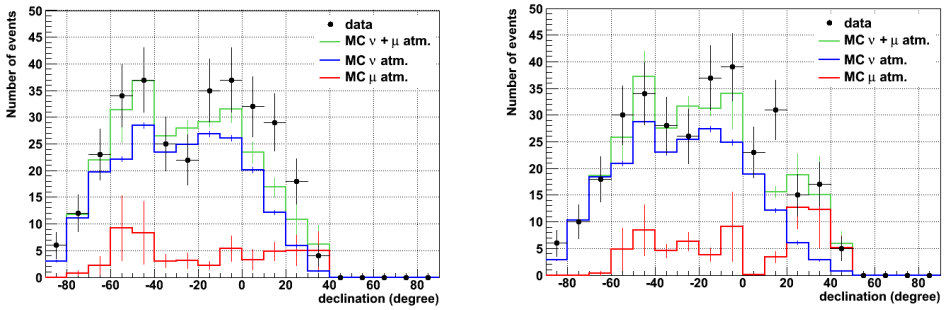

Figure 5.5: Declination distribution for $z \leq 80°$ and $bchi2 \geq 1.8$ (left), $z \leq 90°$ and $bchi2 \geq 2.6$ (right). $tchi2 \leq 1.8$ for both.

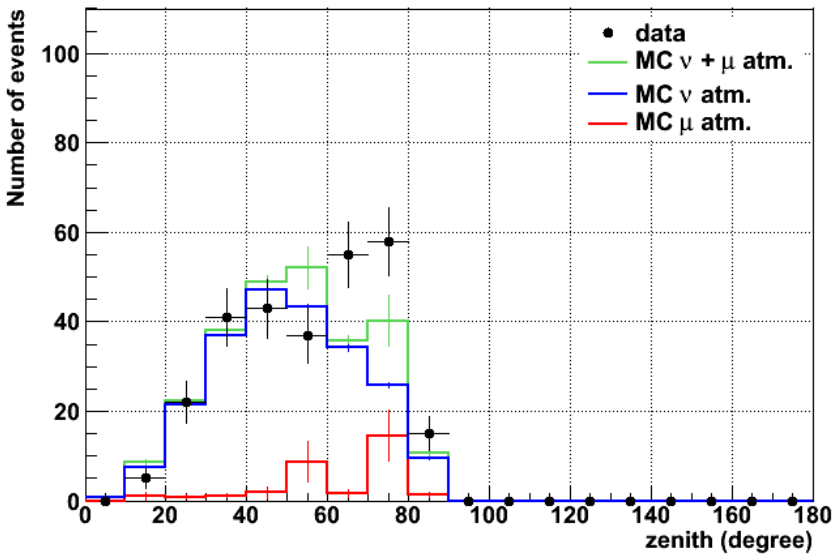

Figure 5.6: z distribution for the optimized cuts.

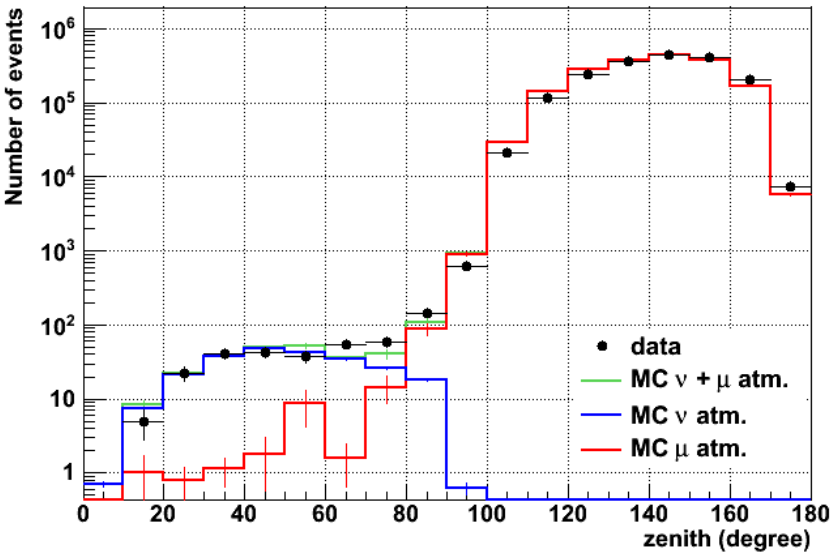

Figure 5.7: z distribution for $tchi2 \leq 1.8$ and $bchi2 \geq 2.2$.

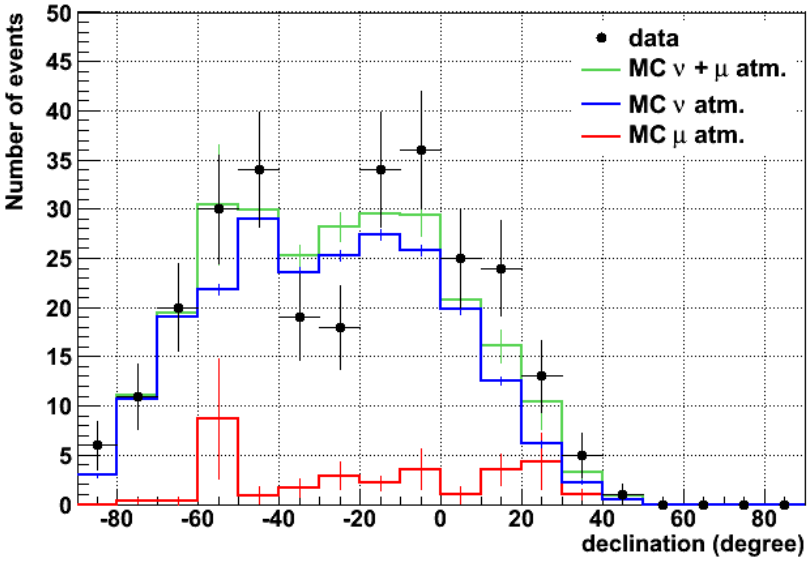

Figure 5.8: Declination distribution for the optimized cuts.

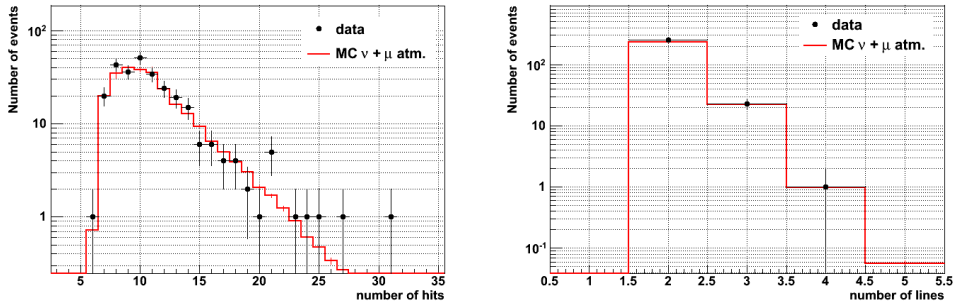

Figure 5.9: Number of hits (left) and lines (right) used in the reconstruction for the optimized cuts.

in this bin a harder cut on *tchi*2 is applied. The excess of muons in the zenith bin $70^\circ < z \leq 80^\circ$, in the left plot of Figure 5.4, decreases applying a harder *bchi*2 cut (Figure 5.6). The absence of the events at high declinations in figures 5.5 and 5.8 is due to the telescope visibility (Section 5.3).

Figure 5.9 compares the data and Monte-Carlo distributions of the number of hits and the number of lines used in the track fit after cuts optimizations. Good agreement is observed.

5.3 Effective area and visibility

The calculation of the effective area for ν and $\overline{\nu}$ is presented in Appendix C and the visibility in Appendix D. The ANTARES neutrino telescope does not recognize the difference between the neutrinos and the anti-neutrinos. In the following, the word neutrino is used to indicate both neutrino and anti-neutrino.

Figure 5.10 shows the effective area as a function of the true neutrino declination, averaged with an energy spectrum E^{-2}, for the zenith cuts at 80° and 90°. The looser zenith cut increases the effective area after $\delta = -57^\circ$ and increases the declination range covered by the detector from 37° to 47°. This is due to the ANTARES visibility as it is illustrated in Figure 5.11 which shows the visibility for both cuts. Figures 5.12 and 5.13 illustrate the visibility of ANTARES in the Equatorial and the Galactic coordinates systems respectively.

Figure 5.14 shows the effective area as a function of the true neutrino energy for various cuts on *tchi*2 and both zenith.

Figure 5.15 shows the effective area as a function of the true neutrino declination and the true neutrino energy for various cuts on *bchi*2. The effective area is less sensitive to the *bchi*2 cut than to the *tchi*2 cut.

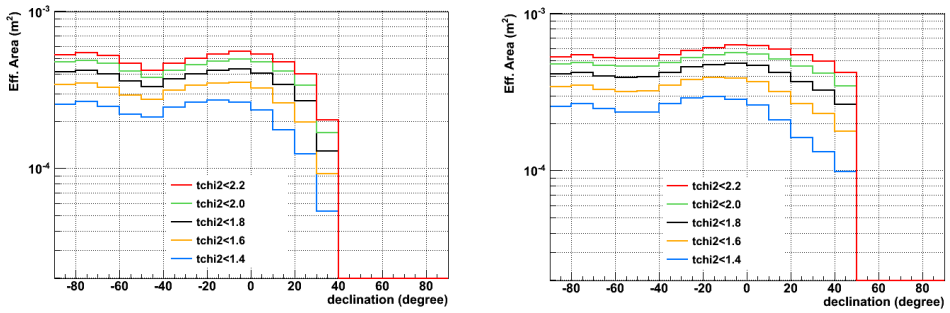

Figure 5.10: Effective area as a function of the true neutrino declination for $bchi2 \geq 1.8$ and $z \leq 80°$ (left), $z \leq 90°$ (right).

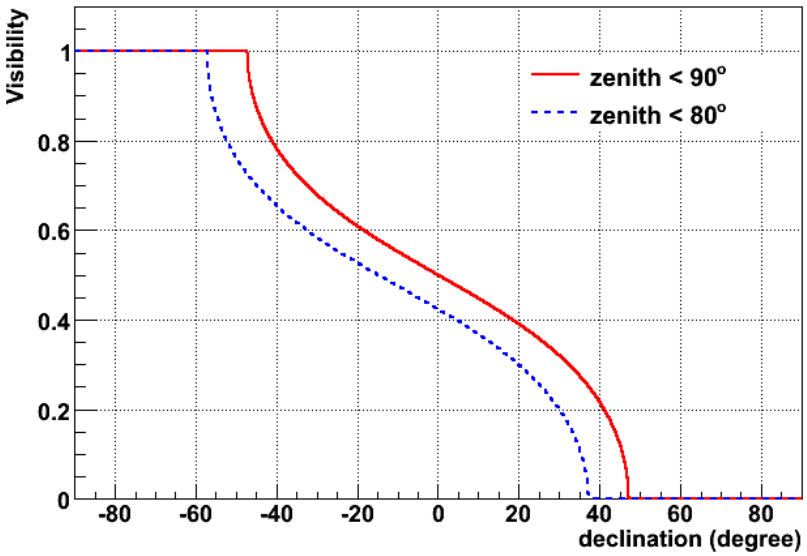

Figure 5.11: Visibility of the ANTARES telescope.

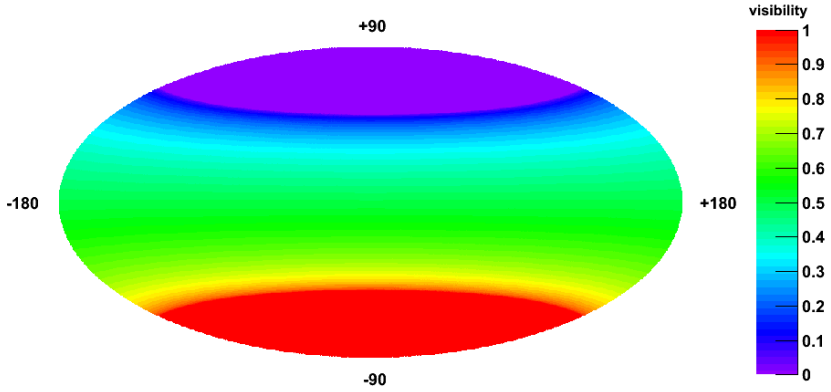

Figure 5.12: Visibility in the Equatorial coordinates ($z \leq 90^\circ$).

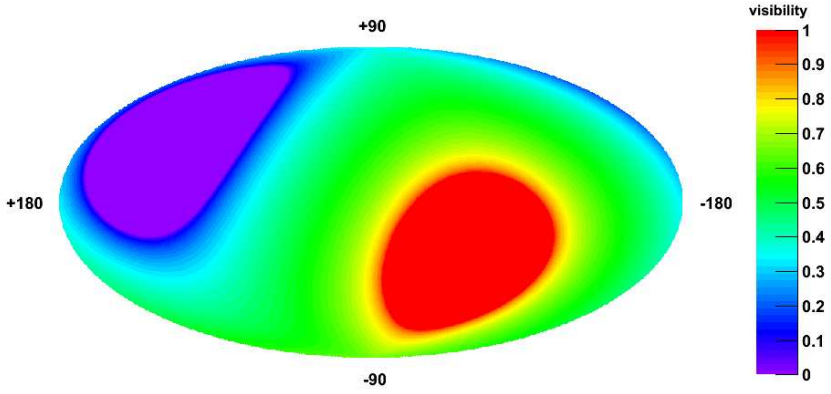

Figure 5.13: Visibility in the Galactic coordinates ($z \leq 90^\circ$).

In Figure 5.16, the effective area as a function of the true neutrino declination and the true neutrino energy for the optimized cuts is presented.

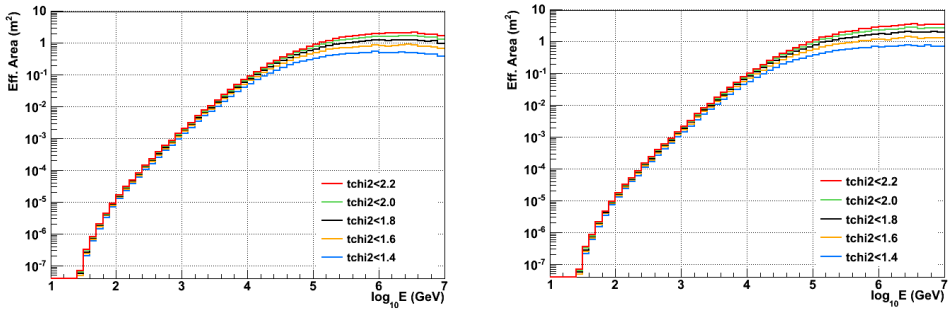

Figure 5.14: Effective area as a function of the true neutrino energy for $bchi2 \geq 1.8$ and $z \leq 80^\circ$ (left), $z \leq 90^\circ$ (right).

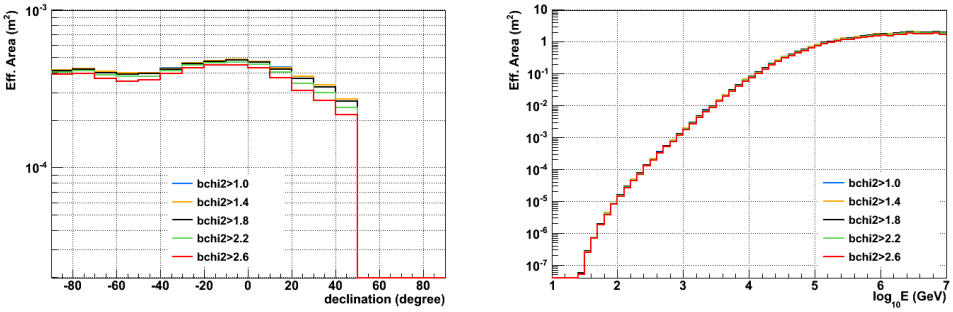

Figure 5.15: Effective area as a function of the true neutrino declination (left) and true neutrino energy (right) for $tchi2 \leq 1.8$ and $z \leq 90^\circ$.

5.4 Angular resolution

Figure 5.17 shows the difference of the angle between the true neutrino direction and the reconstructed muon direction for a point source simulated at declination of -25° and weighted with E^{-2}. This distribution represents the Point Spread Function (PSF) for this declination. In the following, the angular resolution is defined as the median of the angular difference distribution. Figure 5.18 presents the cumulative event fraction of the angular difference distribution.

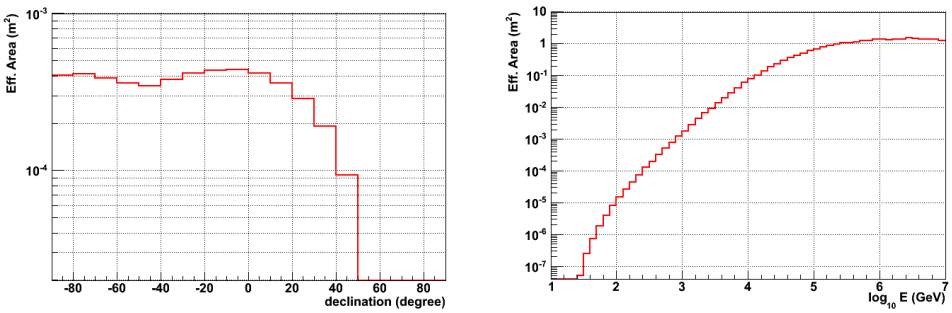

Figure 5.16: Effective area as a function of the true neutrino declination (left) and true neutrino energy (right) for the optimal cuts.

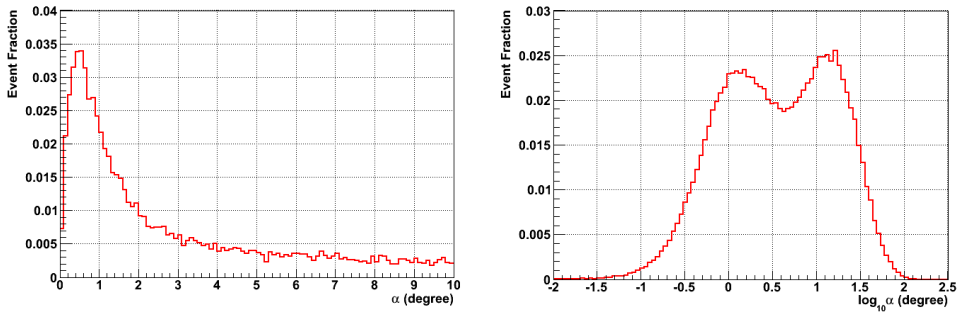

Figure 5.17: PSF of a point source at declination of $-25°$.

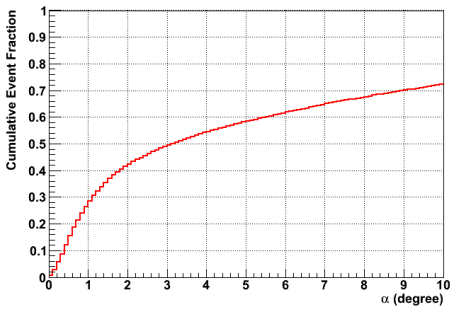

Figure 5.18: Cumulative event fraction of a point source at declination of $-25°$.

Figure 5.19 shows the angular resolution as a function of the true neutrino zenith and azimuth. The resolution is not uniform in azimuth due to the asymmetry in the detector layout. The resolution is the best for vertical tracks.

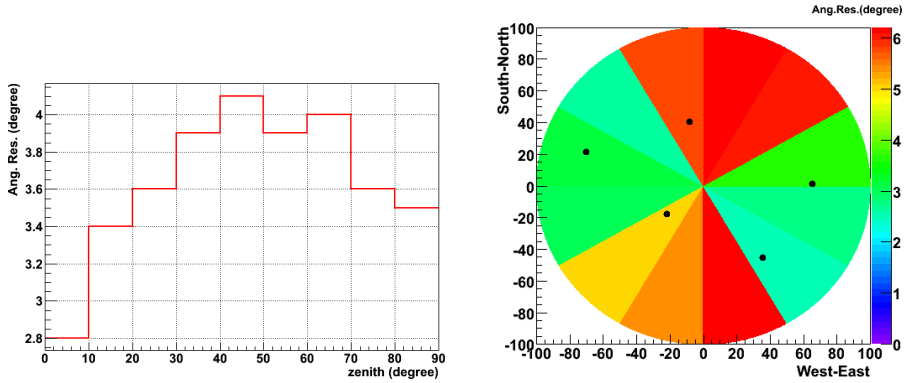

Figure 5.19: Angular resolution as a function of the true neutrino zenith (left) and azimuth (right). The points in the right plot present the relative positions of the 5 lines in the horizontal plane and the colors indicate the angular resolution (degree).

Figure 5.20 shows the angular resolution as a function of the true neutrino declination for the reconstructed zenith cuts at 80° and 90°. The looser zenith cut improves the angular resolution above the equator.

Figure 5.21 shows the angular resolution as a function of the true neutrino energy. A harder cut on *tchi*2 leads to a better angular resolution for energies less than 100 TeV, but worse for energies above 100 TeV.

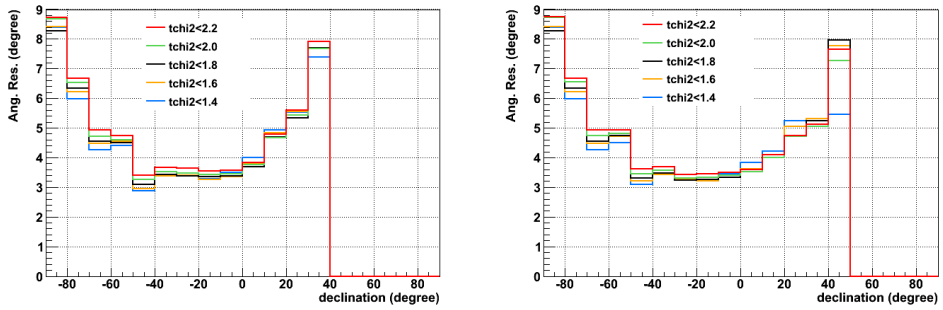

Figure 5.20: Angular resolution as a function of the true neutrino declination for $bchi2 \geq 1.8$ and $z \leq 80°$ (left), $z \leq 90°$ (right).

Figure 5.22 shows the angular resolution as a function of the true declination and energy for different *bchi*2 cuts. Comparing with figures 5.20 and 5.21, the

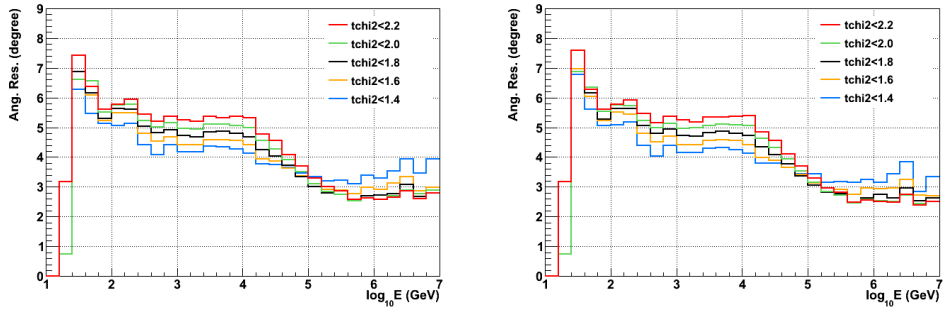

Figure 5.21: Angular resolution as a function of the true neutrino energy for $bchi2 \geq 1.8$ and $z \leq 80^\circ$ (left), $z \leq 90^\circ$ (right).

*bchi*2 cuts have uniform effect over all declination and energy ranges contrary to the $tchi2$ cuts.

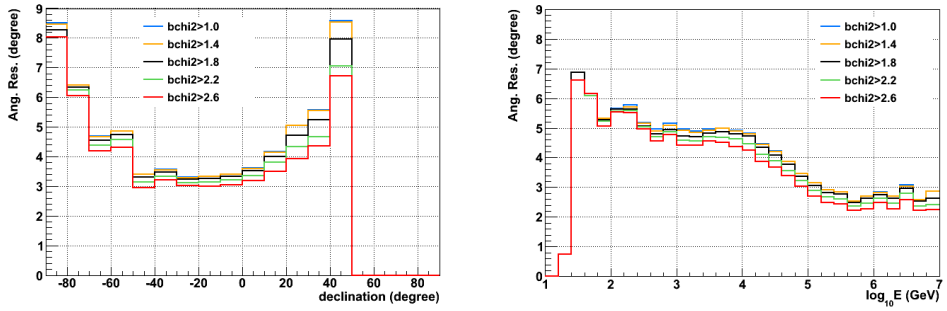

Figure 5.22: Angular resolution as a function of the true neutrino declination (left) and the true neutrino energy (right) for $tchi2 \leq 1.8$ and $z \leq 90^\circ$.

In Figure 5.23, the angular resolution as a function of the true neutrino declination and the true neutrino energy for the optimized cuts is presented.

5.5 Point source unbinned search method

In this analysis, the point sources are searched with an unbinned method based on a likelihood ratio maximization. The goal is to test, at a given point (defined as a "search-point" in the following), the probability to have a signal for a given background model. The Probability Density Functions (PDF)s of the signal and the background are one-dimensional PDFs extracted from the Monte-Carlo simulations. This method is robust, rapid and has a single free parameter. There are no

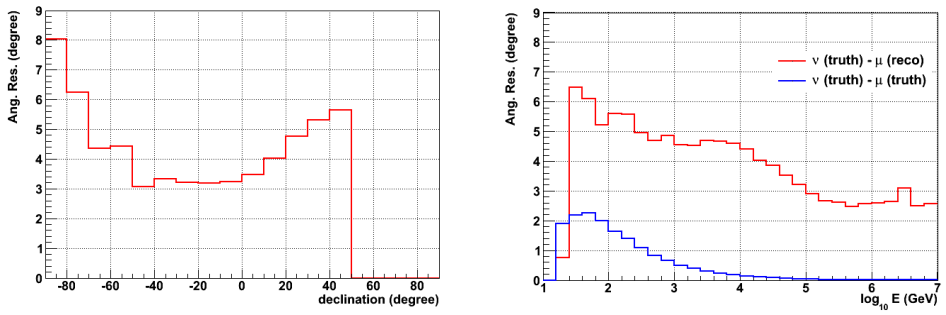

Figure 5.23: Angular resolution as a function of the true neutrino declination (left) and the true neutrino energy (right) for the optimized cuts.

singularities because the calculations are performed in spherical space (Equatorial coordinates).

This method consists of two steps. The first step is to calculate the angular distance $\alpha \in [0°, 180°]$ between the search-point and the position of all selected events in the sky. The second step is to fit the angular distance distribution with the signal and background PDFs using the likelihood ratio maximization technique.

The likelihood ratio λ, defined in Equation 5.1, is the probability ratio of $H_{\text{sig+bg}}$ (the hypothesis of mixed signal and background models) over the H_{bg} (the hypothesis of only background model).

$$\lambda = \log \frac{\prod_{i=1}^{n} P(x_i|H_{\text{sig+bg}})}{\prod_{i=1}^{n} P(x_i|H_{\text{bg}})} = \sum_{i=1}^{n} \log \frac{P(x_i|H_{\text{sig+bg}})}{P(x_i|H_{\text{bg}})} \tag{5.1}$$

where n is the total number of events (x_i) in the sky. $P(x_i|H_{\text{sig+bg}})$ and $P(x_i|H_{\text{bg}})$ are given by:

$$P(x_i|H_{\text{sig+bg}}) = \frac{n_{\text{sig}}}{n} \times P_{\text{sig}}(\alpha_i) + (1 - \frac{n_{\text{sig}}}{n}) \times P_{\text{bg}}(\alpha_i) \tag{5.2}$$

$$P(x_i|H_{\text{bg}}) = P_{\text{bg}}(\alpha_i) \tag{5.3}$$

where:

- n_{sig} is the number of signal events, therefore $\frac{n_{\text{sig}}}{n}$ and $1 - \frac{n_{\text{sig}}}{n}$ are the fractions of signal and background events respectively.
- $P_{\text{sig}}(\alpha_i)$ and $P_{\text{bg}}(\alpha_i)$ are the PDFs of the signal and the background respectively. They are a function of the angular distance α_i.

Replacing expressions 5.2 and 5.3 in Equation 5.1 yields:

$$\lambda = \sum_{i=1}^{n} \log \frac{\frac{n_{\text{sig}}}{n} \times P_{\text{sig}}(\alpha_i) + (1 - \frac{n_{\text{sig}}}{n}) \times P_{\text{bg}}(\alpha_i)}{P_{\text{bg}}(\alpha_i)} \tag{5.4}$$

The only unknown parameter is n_{sig} which is estimated by maximizing λ. The output of the algorithm at a given search-point is the maximized λ value and the corresponding fitted n_{sig} value.

In order to speed up the algorithm, for a given search-point, the event sample is divided into two sets; the events within the search window[4] and the events outside the search window. For the events outside the search window, the signal PDF is equal to zero. The size of the search window is a trade-off between including the maximum number of the signal events and decreasing the algorithm calculation time. For this analysis, a search window of $\alpha \in [0^\circ, 10^\circ]$ is considered.

Let n_{in} be the number of events within the search window, Equation 5.4 can be written as:

$$\lambda = (n - n_{\text{in}}) \times \log(1 - \frac{n_{\text{sig}}}{n}) + \sum_{i=1}^{n_{\text{in}}} \log \frac{\frac{n_{\text{sig}}}{n} \times P_{\text{sig}}(\alpha_i) + (1 - \frac{n_{\text{sig}}}{n}) \times P_{\text{bg}}(\alpha_i)}{P_{\text{bg}}(\alpha_i)} \tag{5.5}$$

The signal PDF is the PSF which is calculated using the Monte-Carlo. The distribution is fitted by Equation 5.6 inside the search window (Figure 5.24) and it is null outside. It is normalized to 1.

$$f(x) = \frac{Ax}{1 + ax^2 + bx^4} + c \tag{5.6}$$

This PDF is also used to generate the signal events in the toy Monte-Carlo taking in consideration the probability that the signal events are generated inside the search window or outside. In case they are outside, they are generated as background events.

The PDF of the background is calculated using the declination distribution of the selected data events (Figure 5.8). This distribution is fitted by a numerical fit. This fit is used to simulate a large number of skymaps with background only hypothesis. For each simulation, the angular distances between a given search-point and the simulated events are calculated. The background PDF is the normalized distribution of all angular distances at this search-point. Figure 5.25 shows the background PDFs of the search-points at a variety of declinations. For two search-points, symmetric with respect to the equator, their background PDFs are symmetric, too. Note that when the search-point is at the South Pole, the background PDF is exactly the fitted distribution of the declination.

[4]The search window is a circle on the celestial sphere where the center is the search-point.

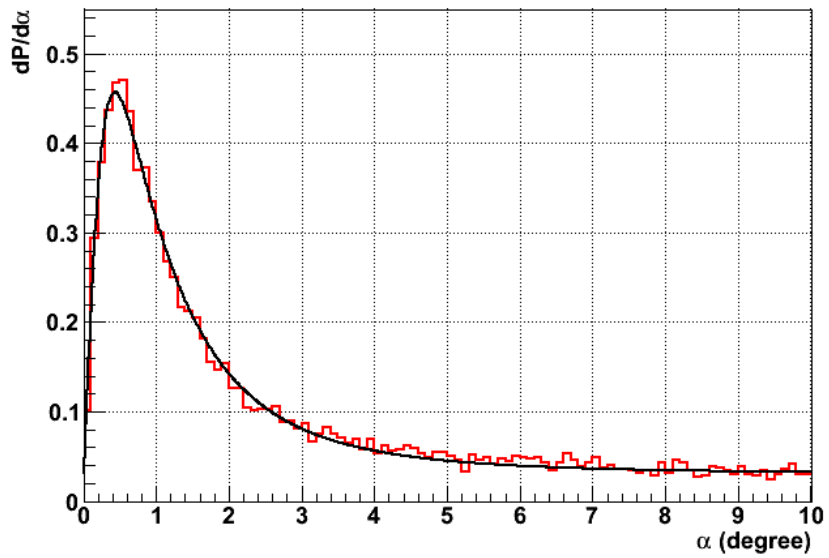

Figure 5.24: Signal PDF at declination $= -25°$.

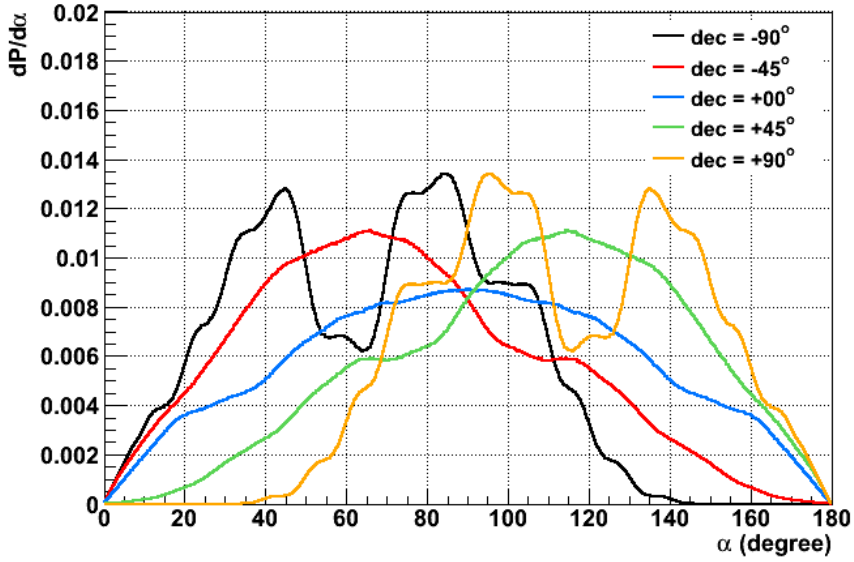

Figure 5.25: Background PDFs for different declinations.

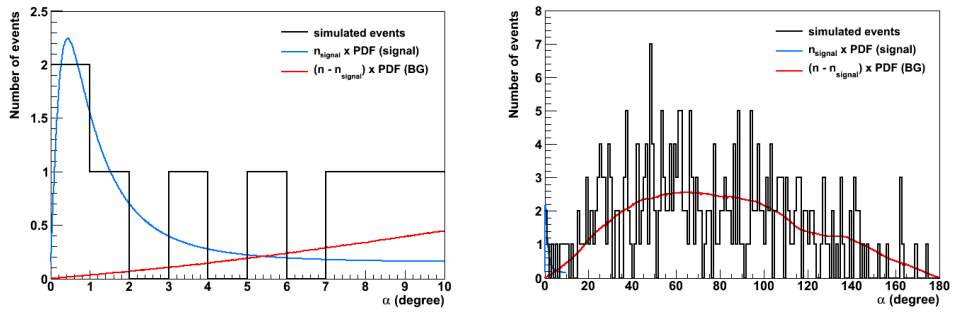

Figure 5.26: Angular distance distribution fitted by the PDFs.

Figure 5.26 shows an example of a single toy Monte-Carlo experiment. The generated number of signal events is 5 (inside the search window) emitted by a point source at ($r.a. = 90^\circ$ and $\delta = -25^\circ$) and the number of generated background events is 271 to have in total 276 events. In this example, the algorithm finds $\lambda = 8.509$ and $n_{\rm sig} = 4.91$.

5.5.1 Sensitivity and discovery potential

To calculate the sensitivity and the discovery potential, λ is used as the test statistic. The median value $\lambda_{0.5}$ and the $\lambda_{n\sigma}$ values (for a given number of σ, e.g. 3σ for observation, 5σ for discovery, ...) are needed, as well as, the λ distributions of many toy experiments for various quantities of signal ($n_{\rm sig}$ = 0, 1, 2, 3, ...). For a given $n_{\rm sig}$, the λ distribution is denoted by $\Lambda(\lambda|n_{\rm sig})$ and it is normalized to 1.

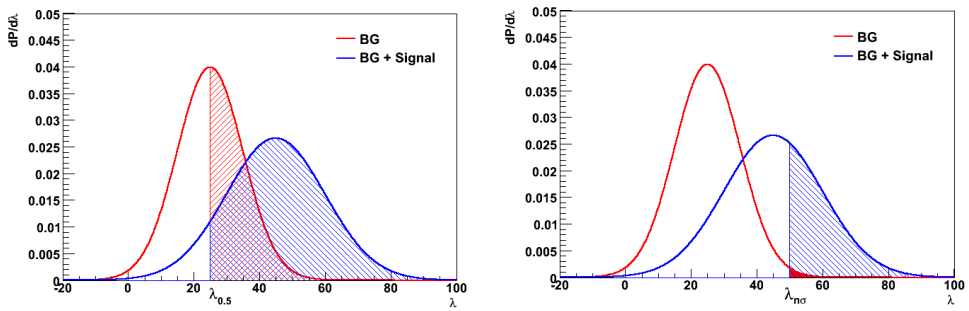

Figure 5.27: Example of λ distributions for only background and background + signal models. In the left plot, the dash area represents the probability $\pi(\lambda \geq \lambda_{0.5}|n_{\rm sig})$ defined in Equation 5.7 and used in the calculation of the sensitivity. In the right, it represents the probability $\pi(\lambda \geq \lambda_{n\sigma}|n_{\rm sig})$ used to compute the discovery potential.

The probability to have a λ value bigger than $\lambda_{0.5}$ is given by (Figure 5.27 left):

$$\pi(\lambda \geq \lambda_{0.5}|n_{\rm sig}) = \int_{\lambda_{0.5}}^{+\infty} \Lambda(\lambda|n_{\rm sig})d\lambda \tag{5.7}$$

The probability to have a λ value bigger than $\lambda_{0.5}$ for a given expected signal events number $\langle n_{\rm sig}\rangle$ is given by:

$$p(\lambda \geq \lambda_{0.5}|\langle n_{\rm sig}\rangle) = \sum_{n_{\rm sig}=0}^{+\infty} \pi(\lambda \geq \lambda_{0.5}|n_{\rm sig}) \frac{\langle n_{\rm sig}\rangle^{n_{\rm sig}} \exp(-\langle n_{\rm sig}\rangle)}{n_{\rm sig}!} \tag{5.8}$$

In this analysis, the sensitivity is calculated for a Confidence Level $CL = 90\%$, i.e. the sensitivity is the flux value corresponding to $\langle n_{\rm sig}\rangle$ when $p(\lambda \geq \lambda_{0.5}|\langle n_{\rm sig}\rangle) = 0.9$.

The discovery potential is calculated in the same way as the sensitivity, but replacing $\lambda_{0.5}$ by $\lambda_{5\sigma}$ (Figure 5.27 right). The discovery potentials shown in this study are calculated for $p(\lambda \geq \lambda_{5\sigma}|\langle n_{\rm sig}\rangle) = 0.5$. The probability $p(\lambda \geq \lambda_{5\sigma}|\langle n_{\rm sig}\rangle)$ as a function of $\langle n_{\rm sig}\rangle$ is defined as the discovery power (Figure 5.30).

The sensitivity and the discovery potential, for a point source at declination δ, are calculated by:

$$E^{\gamma}\frac{d\Phi(\delta)}{dE} = \frac{\langle n_{\rm sig}\rangle(\delta)}{A_{eff}(\delta) \times t \times V(\delta) \times \int_{E_{\rm min}}^{E_{\rm max}} E^{-\gamma} dE} \tag{5.9}$$

where:

- $\langle n_{\rm sig}\rangle(\delta)$ is the expected signal events number.
- $A_{eff}(\delta)$ is the effective area shown in Figure 5.16 (left).
- t is the livetime of the selected runs. In this analysis $t = 1.20701 \times 10^7$ s.
- $V(\delta)$ is the visibility shown in Figure 5.11 ($z \leq 90^{\circ}$).
- $[E_{\rm min}, E_{\rm max}]$ is the simulated events energy range. [10 GeV, 10^7 GeV] for this analysis.
- γ is the signal neutrino energy spectrum. In this analysis $\gamma = 2$.

5.6 Search strategies

Two different search strategies are used in this thesis. In the first approach, neutrinos are searched at the positions of a pre-defined list of known astrophysical sources - "candidate sources list search strategy". The adopted list of the candidate point sources is presented in Table 5.2 [125]. In the second approach, the full sky is searched for sources of neutrinos at any position - "all sky search strategy". Although the latter approach suffers from a larger trial factor, there is no risk to miss an "unexpected" point source of neutrinos.

5.6.1 Candidate sources list search strategy

Figure 5.28 shows the λ distributions obtained for many toy Monte-Carlo experiments containing only background and no signal. Examples are given for search-points located at declinations of -25° and -45°. The tails of the distributions are fitted with an exponential function.

In the candidate sources list search strategy, more than 50% of λ values of background only model are equal to zero which is the possible minimum value for λ (Figure 5.28). Hence, $\lambda_{0.5}$, the median value, is zero. To avoid unphysical solutions (probability equal to 1), a conservative solution is to use $\pi(\lambda > \lambda_{0.5}|n_{\rm sig})$ instead of $\pi(\lambda \geq \lambda_{0.5}|n_{\rm sig})$ and $p(\lambda > \lambda_{0.5}|\langle n_{\rm sig}\rangle)$ instead of $p(\lambda \geq \lambda_{0.5}|\langle n_{\rm sig}\rangle)$ in equations 5.7 and 5.8 respectively.

Figure 5.29 shows the λ distributions obtained from many toy Monte-Carlo experiments for different background + signal models of a source at declination of -25°. Also, it shows the corresponding number of fitted signal events. This algorithm converges to the correct number of events in the search window. In this case, due to the large PSF, only 65% to 75% (depending on the declination) of the signal events are contained within the 10 degrees search window (Figure 5.18), thus the mean of the fitted number of signal events is lower than the number of generated signal events (Figure 5.29 right).

Figure 5.30 shows the discovery power of the candidate sources list search strategy for a source at declination of -25°.

5.6.2 All sky search strategy

For the all sky search strategy, the sky is scanned with an angular step of 0.1°, an angular step which is much smaller than the angular resolution. A total of 4,126,182 search-points are considered, each of which yields a value of λ. The largest value of λ from all the search-points is taken as the λ of that particular toy Monte-Carlo experiment. The complete process is then repeated for a large number of toy Monte-Carlo experiments.

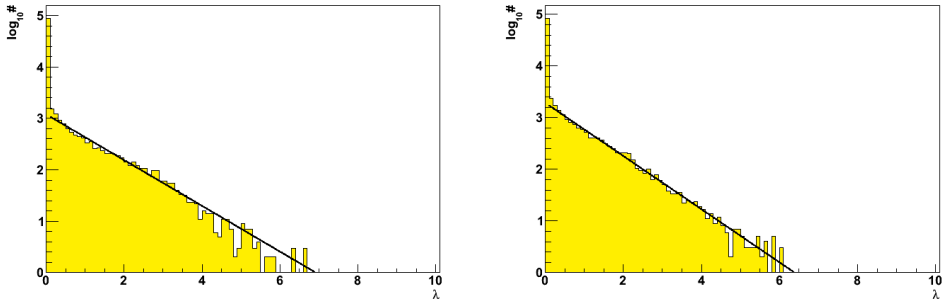

Figure 5.28: λ distributions for just background model at declinations of $-25°$ (left) and $-45°$ (right) using the optimal cuts.

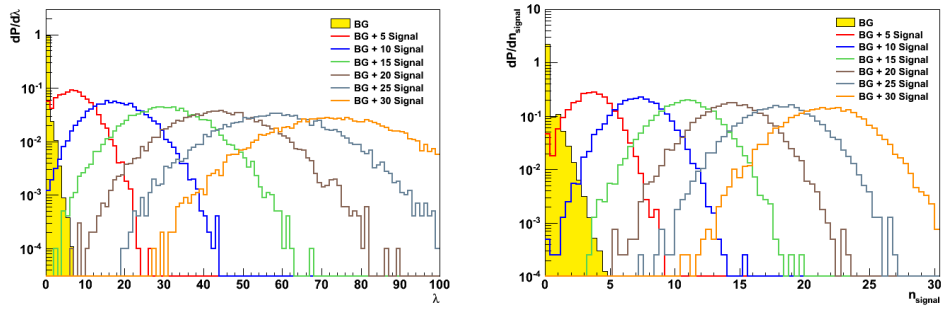

Figure 5.29: λ value distributions (left) and fitted numbers of events (right) of a source at declination $= -25°$.

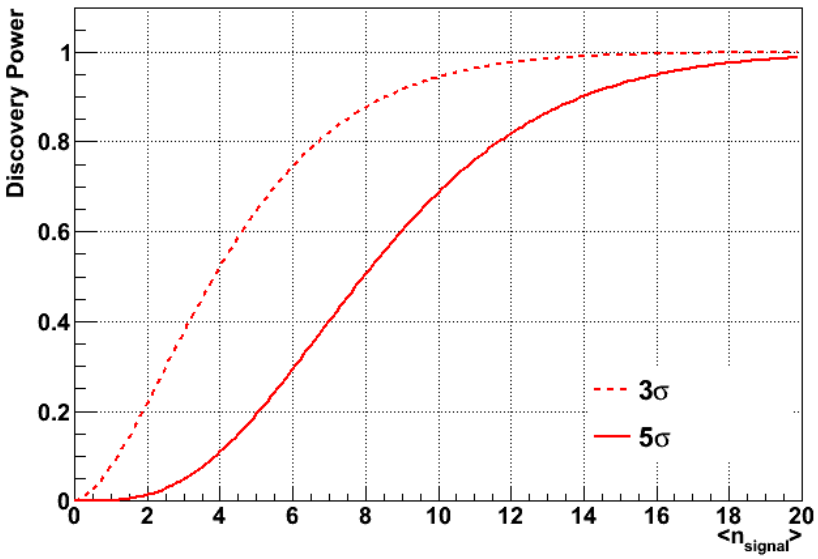

Figure 5.30: Discovery power of the candidate sources list search strategy for a source at declination $= -25°$ as a function of expected signal events number.

Figure 5.31 shows the outputs of the all sky search strategy for different background + signal models for a source at declination of $-25°$.

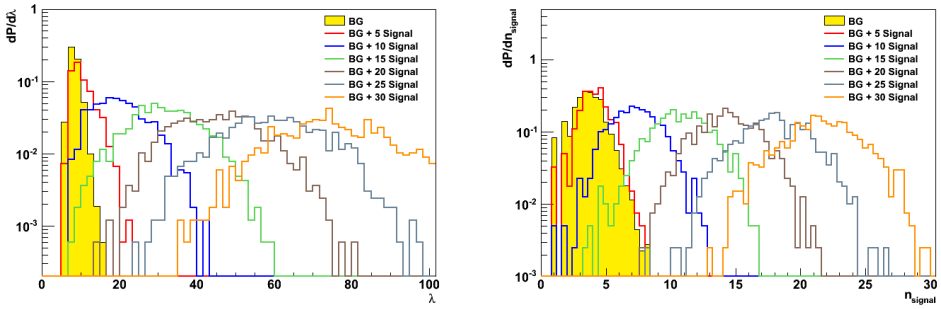

Figure 5.31: λ value distributions (left) and fitted numbers of events (right) of a source at declination $= -25°$.

Figure 5.32 shows the integral of the normalized λ distribution of the background only model fitted with an exponential. This distribution is used to calculate the sensitivity, the discovery potential, the discovery power and the significance in the all sky search strategy.

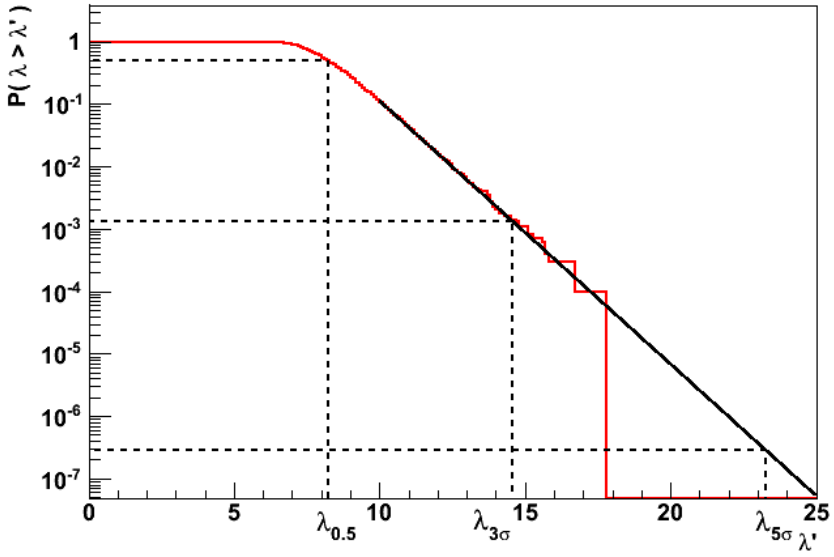

Figure 5.32: Integral of the background statistic test distribution fitted with an exponential.

Figure 5.33 shows the discovery power of the all sky search strategy for a source at declination of $-25°$. Compared to the discovery power of the candidate sources list search (Figure 5.30), a larger number of signal events are required to make a discovery. This is due to the larger trial factor in the all sky search strategy. This is also reflected in the shift of the λ distribution for the background only (and low signal) experiments to higher values (figures 5.29 and 5.31). Therefore, the sensitivity and the discovery potential are better for the candidate sources list search strategy than the all sky search strategy.

5.7 Cut optimization

As mentioned at the end of Section 5.6.2, the discovery potential and the sensitivity are better for the candidate sources list strategy than for the all sky search strategy. Therefore, the cuts are optimized for the former and then applied on both strategies.

Different values of *tchi*2 (1.4, 1.6, 1.8, 2.0, 2.2, 2.4, 2.6), *bchi*2 (1.0, 1.4, 1.8, 2.2, 2.6) and z ($80°$, $90°$) are considered for the sensitivity and discovery potential optimizations. This results 70 possible combinations, only very few are presented here to justify the optimal choice.

Figures 5.34 and 5.35 show the sensitivity and discovery potential for a variety

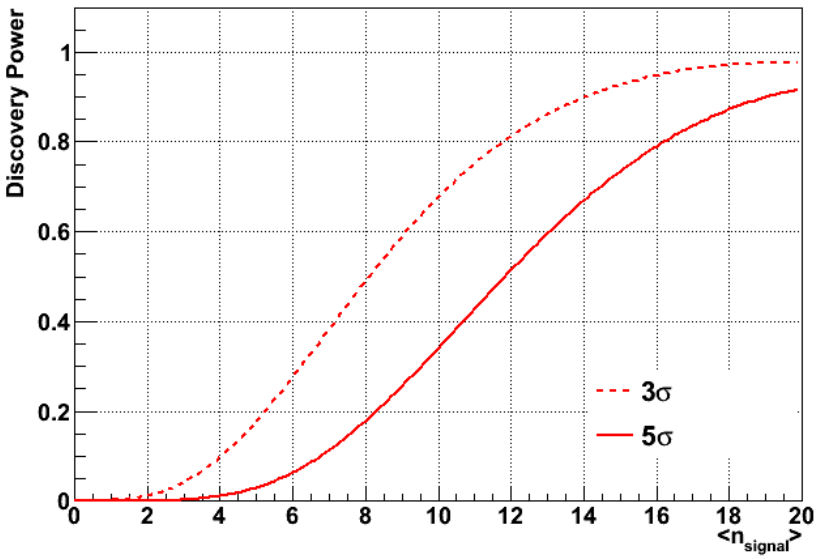

Figure 5.33: Discovery power of a source at declination of -25° for the all sky search strategy.

of cuts on *tchi*2 and for two zenith cuts (80°, 90°). As noted previously, the cut $z \leq 90^\circ$ is better for declinations above -57°. This is also true for other choices of the *bchi*2 cut.

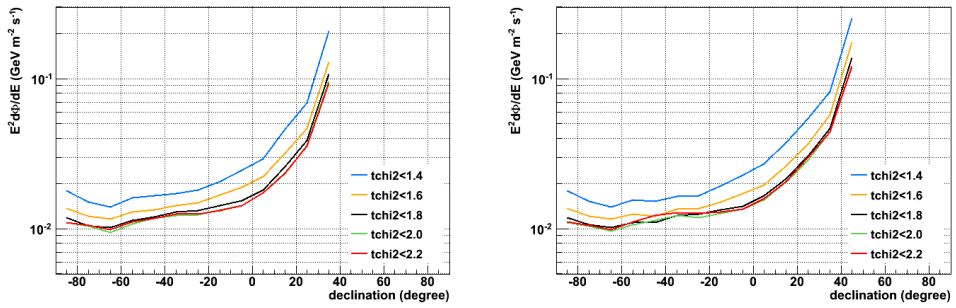

Figure 5.34: Sensitivity for $bchi2 \geq 1.8$ and $z \leq 80^\circ$ (left), $z \leq 90^\circ$ (right).

In Figure 5.37 shows that the discovery potential for $bchi2 \geq 2.6$ is better than the looser cuts on *bchi*2, this is related to the improvement of the angular resolution (Figure 5.22). This is also true for the sensitivity (Figure 5.36).

Amongst the different sets of cuts, $tchi2 \leq 1.8$ is the optimal cut. Therefore, at this stage, the optimal cuts are $tchi2 \leq 1.8$, $bchi2 \geq 2.6$ and $z \leq 90^\circ$. However, this

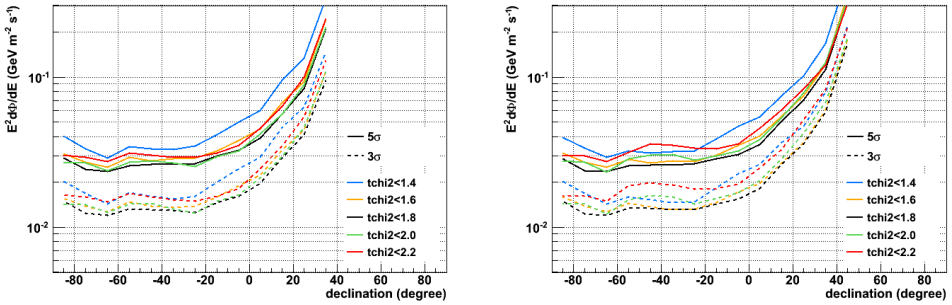

Figure 5.35: Discovery potential for $bchi2 \geq 1.8$ and $z \leq 80°$ (left), $z \leq 90°$ (right).

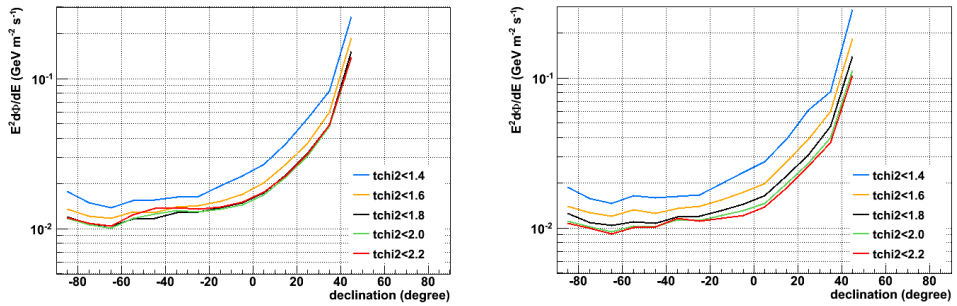

Figure 5.36: Sensitivity for $z \leq 90°$ and $bchi2 \geq 1.0$ (left), $bchi2 \geq 2.6$ (right).

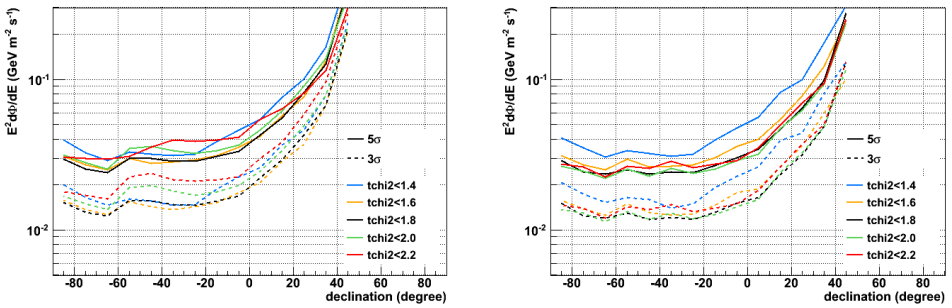

Figure 5.37: Discovery potential for $z \leq 90°$ and $bchi2 \geq 1.0$ (left), $bchi2 \geq 2.6$ (right).

choice yields a relatively high fraction of atmospheric muons contamination close to the horizon ($80^\circ < z \leq 90^\circ$ in Figure 5.4). Therefore, it is decided to apply a tighter *tchi*2 cut just for this zenith bin, this allowed to relax the *bchi*2 from ≥ 2.6 to ≥ 2.2 over the full range of zenith. Finally, the used cuts are $bchi2 \geq 2.2$, $tchi2 \leq 1.8$ when $z \leq 80^\circ$ and $tchi2 \leq 1.4$ when $80^\circ < z \leq 90^\circ$.

Figure 5.38 shows, for the optimal cuts, the average number of signal neutrino events corresponding to a sensitivity of $CL = 90\%$ and discovery of 50% probability.

Figure 5.39 presents the sensitivity ($CL = 90\%$) and discovery potential (50% probability) for the optimal cuts.

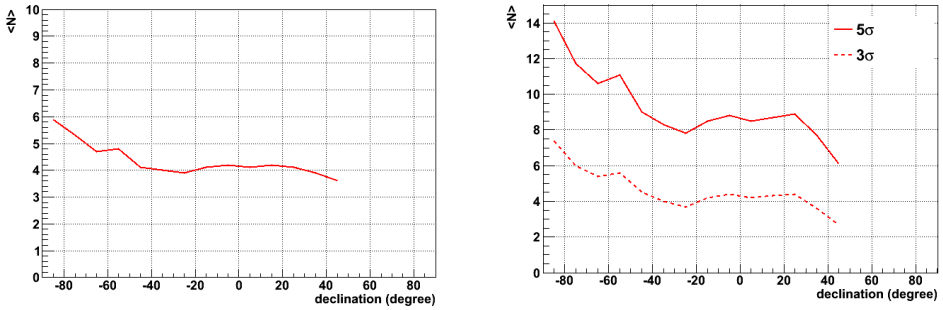

Figure 5.38: Average number of signal neutrino events corresponding to a sensitivity of $CL = 90\%$ (left) and discovery potential of 50% probability (right).

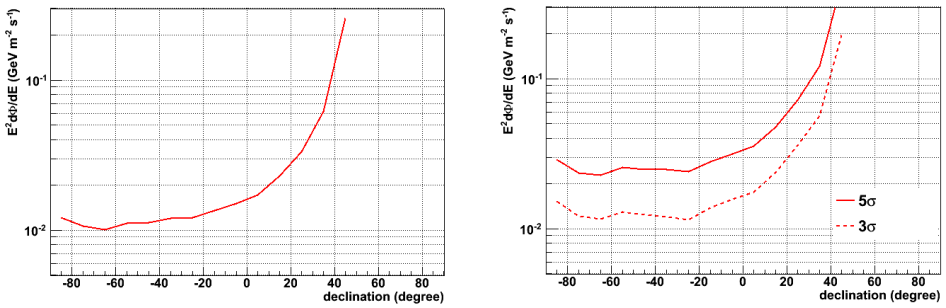

Figure 5.39: Sensitivity of $CL = 90\%$ (left) and discovery potential of 50% probability (right).

5.7.1 Selected events

After applying all cuts, 276 data events and 257 Monte-Carlo events are selected. Table 5.1 shows the number of selected data and Monte-Carlo events. It also shows the number of selected atmospheric neutrinos and atmospheric muons separately.

Cuts	Data	$\nu + \mu$	ν	μ
$tchi2 \leq 1.8$ and $z \leq 80$	261 ± 16	247 ± 8	217 ± 2	30 ± 8
$tchi2 \leq 1.4$ and $80 < z \leq 90$	15 ± 4	11 ± 1	10 ± 1	1 ± 1
Both	276 ± 17	257 ± 8	227 ± 2	31 ± 8

Table 5.1: Selected number of events in this analysis with the statistical uncertainties ($bchi2 \geq 2.2$).

5.8 Systematic uncertainties

For the systematic uncertainties two contributions are considered:
1. The angular resolution may be degraded compared to that assumed in the simulation.
2. The efficiency of the detector may be different than that assumed by the simulation.

The uncertainty on the absolute pointing, calculated in Chapter 4, is negligible relatively to the angular resolution (Section 5.4).

5.8.1 Systematic uncertainty on the angular resolution

Systematic uncertainties on the angular resolution can arise from positioning misalignment or time calibration uncertainties. As the BBfit algorithm assumes that the optical modules are located on the axis of the detector line, there are no systematic uncertainties due to the storeys rotations. For the silver runs selection, the mean sea current is 4.6 cm/s, leading to a displacement of the top of the line by less than one metre. This induces a maximum uncertainty of 0.15° over the 350 m height of a line, negligible compared to the angular resolution.

A conservative degradation of the angular resolution by 10% is assumed. The discovery potential, the discovery power and the sensitivity are reduced by less than 5% (figures 5.40 and 5.41).

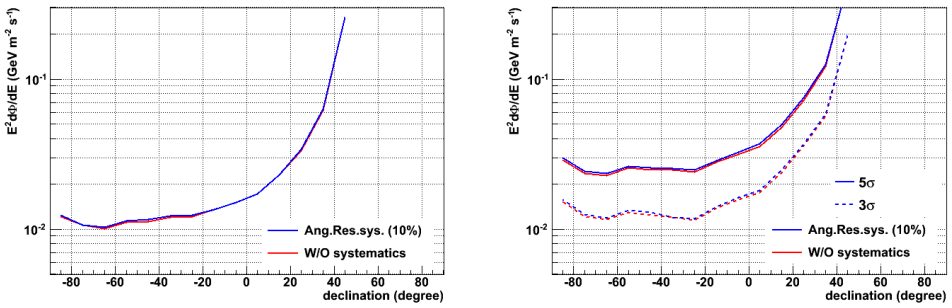

Figure 5.40: Sensitivity (left) and discovery potential (right) with 10% systematic error on the angular resolution.

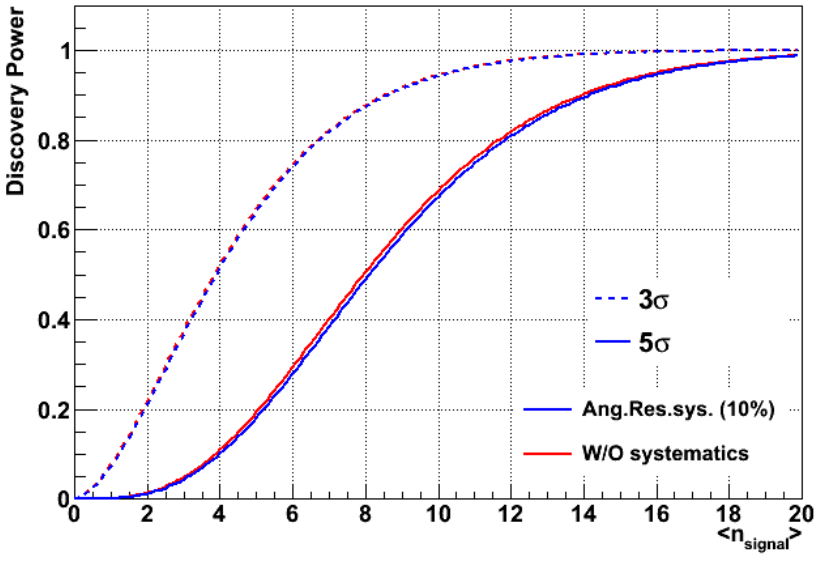

Figure 5.41: Discovery power of the candidate sources list search strategy for a source at declination of -25° as a function of expected signal events number.

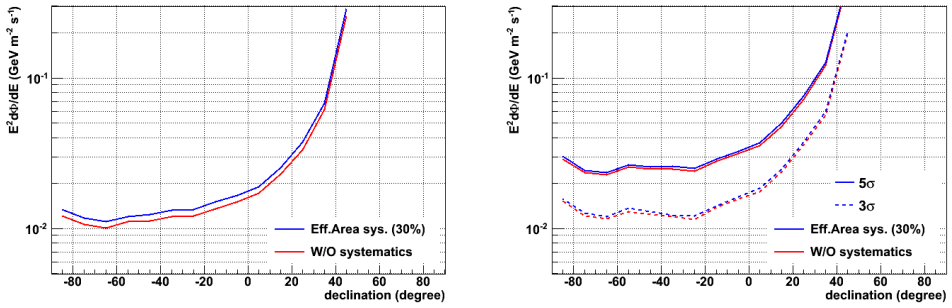

Figure 5.42: Sensitivity (left) and discovery potential (right) with the systematic error on the effective area.

5.8.2 Systematic uncertainty on the detector efficiency

As the amount of background and its declination distribution are measured in the data itself, there is no systematic uncertainty on the level of the background estimation. The statistical uncertainties in the parameterization of the declination distribution are negligible.

For the signal, systematic uncertainties on the detection efficiency affect the assumed effective area and therefore the estimated neutrino flux. A correct estimation of the absolute detector efficiency relies on knowledge of many parameters, for example, the absorption length in the sea water, the quantum efficiency, area and collection efficiency of the PMTs, the thresholds applied to the front-end electronics etc.

The method of Cousins and Highland [126] with $\sigma = \pm 30\%$ (conservative) is used to estimate the impact of the systematic uncertainty on the sensitivity and the discovery potential.

Figure 5.42 shows the effect of the effective area systematic uncertainty on the sensitivity and discovery potential.

Finally, figures 5.43 and 5.44 show the final results with the total systematic uncertainty (angular resolution and effective area).

5.9 Skymaps

The algorithm of the all sky search strategy provides several skymaps in the Equatorial and the Galactic coordinates.

Figures 5.45 and 5.46 show 276 simulated events where 271 are background events over all the sky and 5 are signal events inside the search window emitted by a source at ($r.a. = 90^\circ$, $\delta = -25^\circ$).

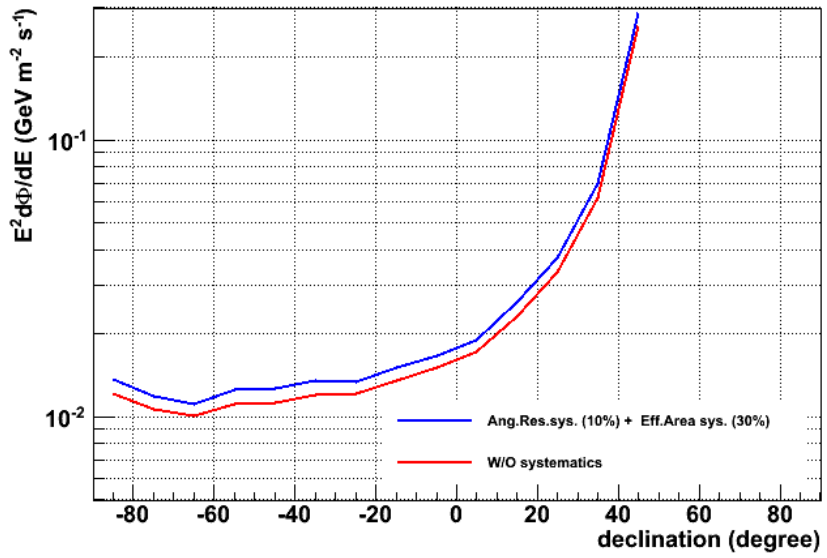

Figure 5.43: Sensitivity with the combined systematic uncertainties (on the angular resolution and the effective area).

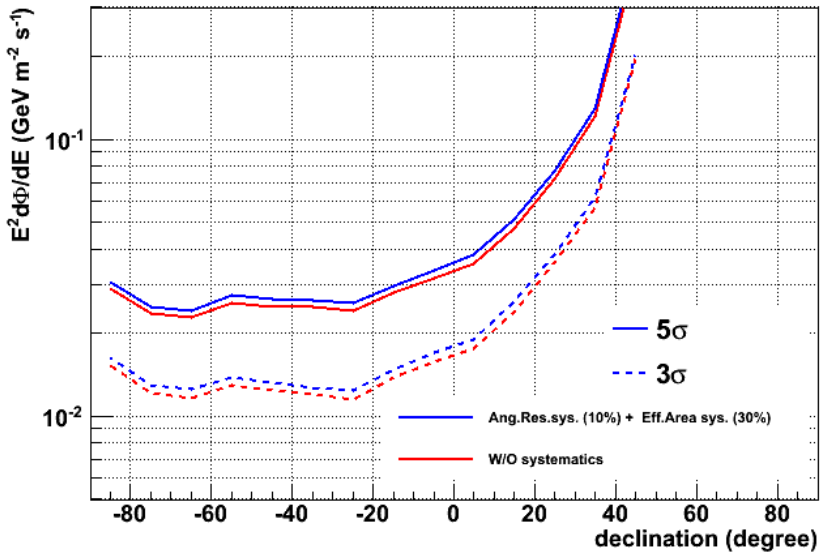

Figure 5.44: Discovery potential with the combined systematic uncertainties (on the angular resolution and the effective area).

The fitted number of signal events and the maximized value of λ at each search-point are presented in the skymaps of figures 5.47, 5.48, 5.49 and 5.50. The 10% systematic uncertainty on the angular resolution is taken into account.

The hottest point (the search-point corresponding to the biggest λ value) is found at $r.a. = 5^h55'18.264''$ and $\delta = -26°12'00''$ with $\lambda = 12.819$ and $n_{\text{sig}} = 4.9$.

The simulated background events in figures 5.45 and 5.46 are correlated with the angular acceptance skymaps of figures 5.51 and 5.52.

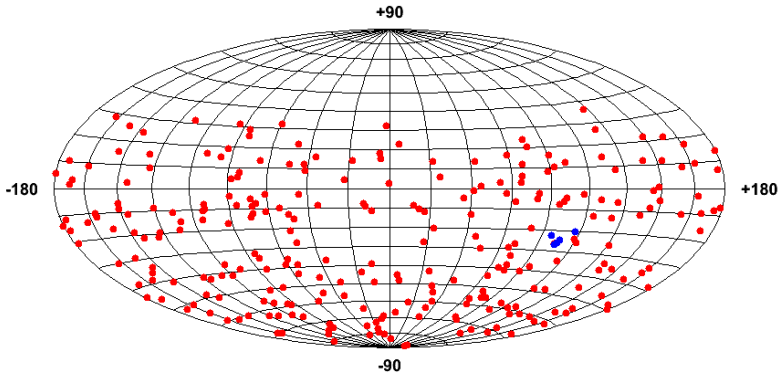

Figure 5.45: Simulated events in the Equatorial coordinates. The blue points present the signal events and the red ones the background events.

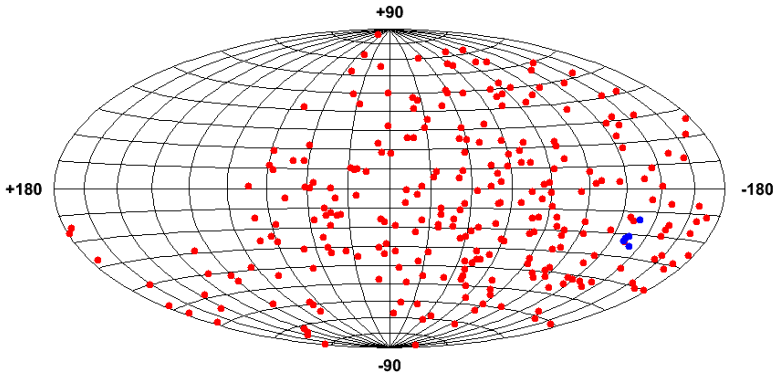

Figure 5.46: Simulated events in the Galactic coordinates. The blue points present the signal events and the red ones the background events.

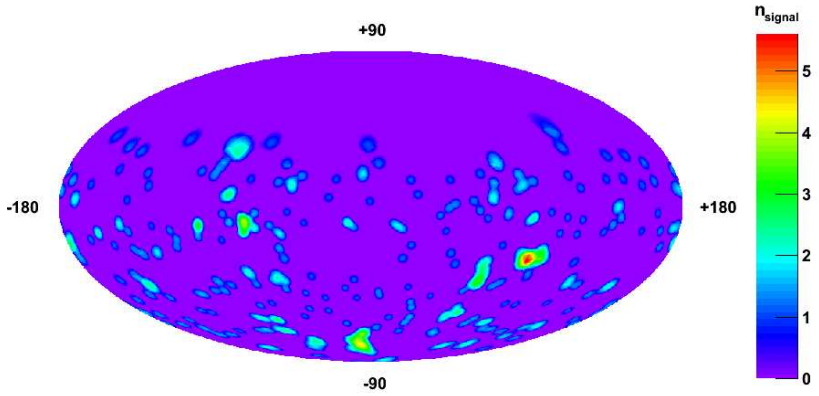

Figure 5.47: Fitted number of events in the Equatorial coordinates.

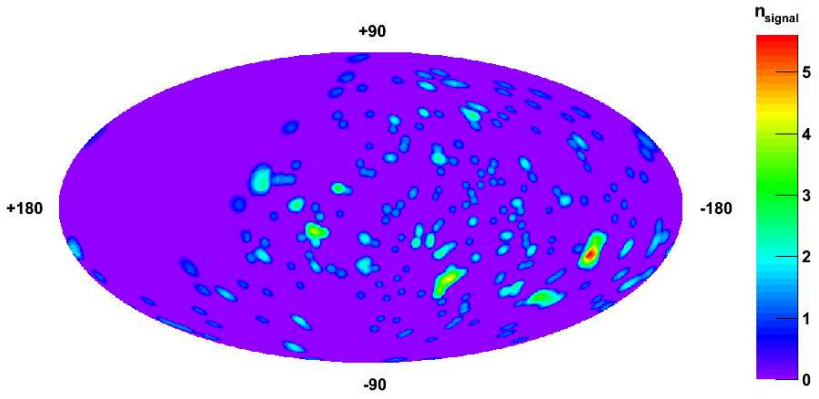

Figure 5.48: Fitted number of events in the Galactic coordinates.

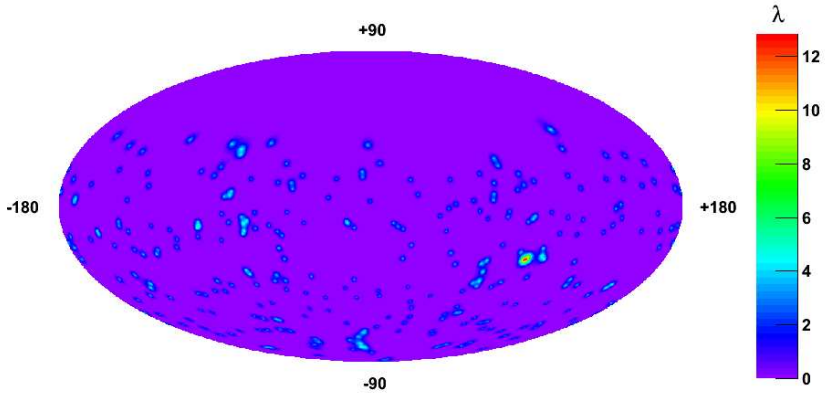

Figure 5.49: λ value in the Equatorial coordinates.

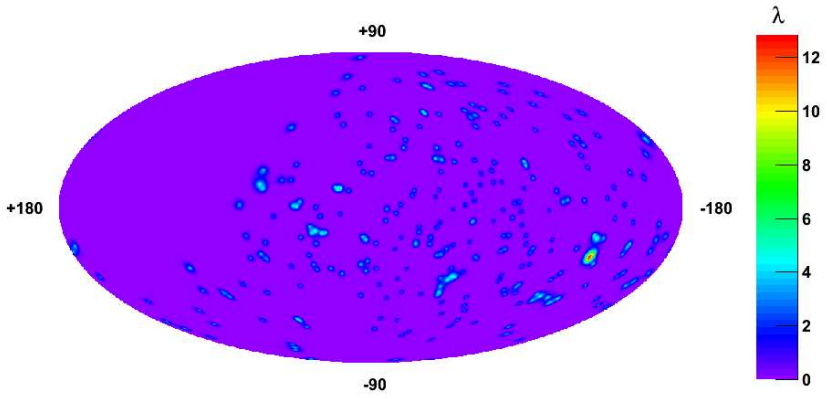

Figure 5.50: λ value in the Galactic coordinates.

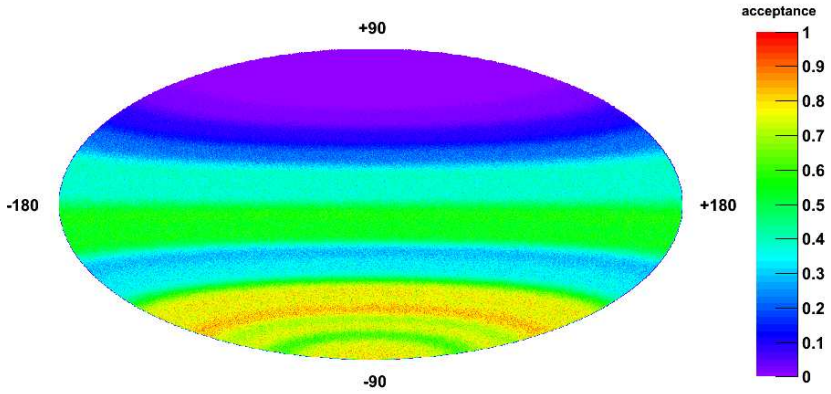

Figure 5.51: Angular acceptance (relative scale) in the Equatorial coordinates.

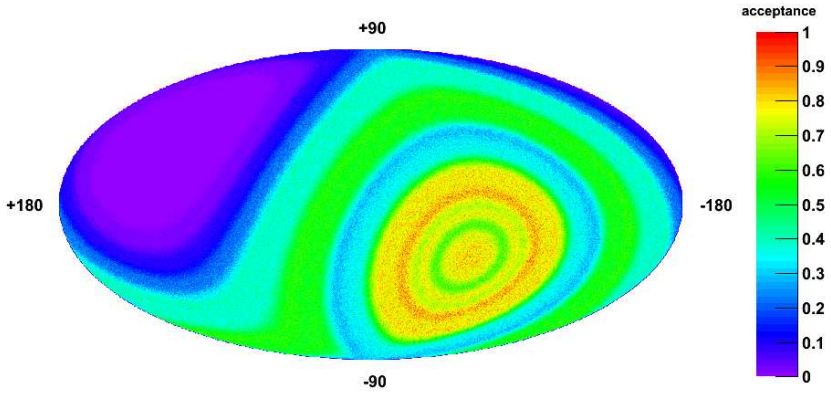

Figure 5.52: Angular acceptance (relative scale) in the Galactic coordinates.

5.10 Results

In the previous sections, the optimization of the cuts is discussed. They are chosen to provide the best discovery potential using Monte-Carlo simulations with 5-line ANTARES detector and the BBfit reconstruction algorithm.

The application of these cuts on the data sample leads to 276 reconstructed as up-going candidate neutrino events. In this section, the results of the 2 search strategies (Section 5.6) are illustrated for the 2007 5-line data. No discovery is made for both search strategies, therefore, an upper limit is derived.

In figures 5.53 and 5.54, the selected data events are presented in the Equatorial and the Galactic coordinates systems respectively. The positions of the 24 candidate sources, mentioned in Table 5.2, chosen for the candidate sources list search strategy are also shown in both skymaps.

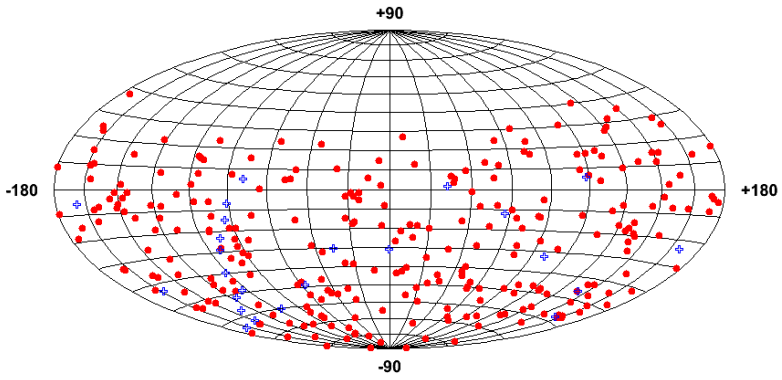

Figure 5.53: In the Equatorial coordinates system, the selected data events (red points) and the 24 candidate sources (blue crosses).

5.10.1 Candidate sources list strategy

In the candidate sources list strategy search, 24 candidate sources are selected containing galactic and extragalactic sources (Table 5.2). The choice of the number of these sources is a trade-off between the trial factor[5] and the number of astrophysical bodies (Galactic Center, supernovae, blazar, ...) which are likely to be high energy neutrino sources.

[5]Increasing the number of candidate sources, the trial factor increases because of statistical fluctuations.

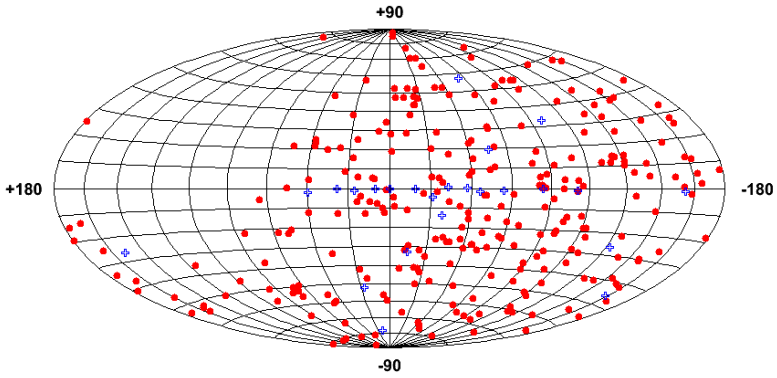

Figure 5.54: In the Galactic coordinates system, the selected data events (red points) and the 24 candidate sources (blue crosses).

The results of the candidate sources list strategy is presented as pre-trial and post-trial results. For the first, the unbinned search method, described in Section 5.5, is applied on each source separately. For the post-trial, the 24 sources are included together in the study and the final results are illustrated.

5.10.1.1 Pre-trial results

As it is mentioned above, the search strategy considers one source at a time ignoring the 23 other sources. Before applying the unbinned search strategy on the data, the λ distributions of the different models (background + 0 signal, background + 1 signal, background + 2 signals, ...) are computed as it is explained in Section 5.6. The only difference, here, is that the positions of the sources are the true positions of the candidate sources. These distributions are indispensable to calculate the *p-value*, the sensitivity and the discovery potential. The signal and background PDFs are computed with the optimized cuts to have the best discovery potential (Section 5.7). The 10% systematic error on the angular resolution, discussed in Section 5.8.1, is included to generate the signal events.

For the λ distributions, 10^5 sky simulations are made for background only model and 10^4 simulations for the other models. Each time the unbinned search algorithm is applied on the search-point which is, in this case, the true position of the candidate source position.

The application of the algorithm on the data, at a given source position, leads to one single λ, denoted by λ_{data}. At this search-point, the *p-value* of just back-

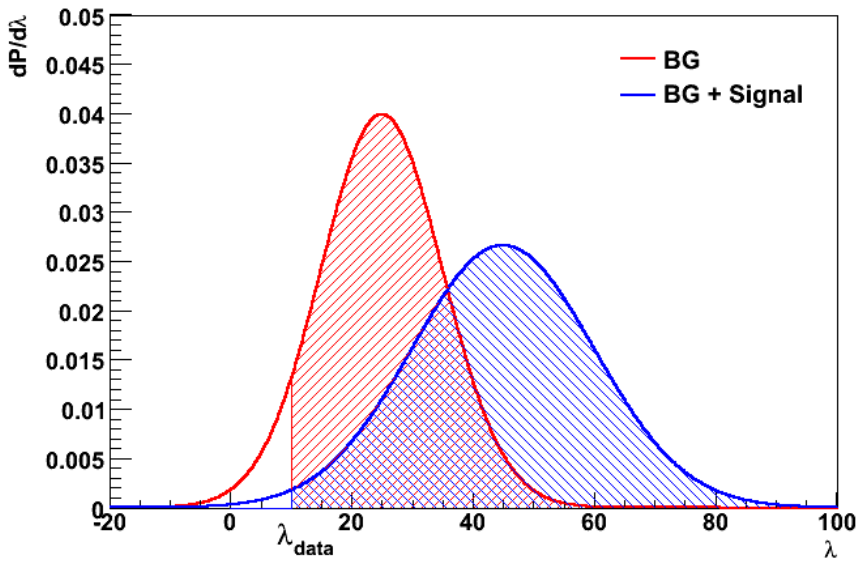

Figure 5.55: Example of λ distributions for background only and background + signal models.

ground like model is given in Equation 5.10 (Figure 5.55).

$$p\text{-}value = \int_{\lambda_{\text{data}}}^{+\infty} \Lambda(\lambda | n_{\text{sig}} = 0) \mathrm{d}\lambda \tag{5.10}$$

where $\Lambda(\lambda | n_{\text{sig}} = 0)$ is normalized to 1. The tail of the λ distribution, for the background only model, is fitted by an exponential.

The corresponding σ value with 1 side Gaussian convention is given by:

$$n_\sigma(p\text{-}value) = \sqrt{2} \times \text{erfc}^{-1}(2 \times p\text{-}value) \tag{5.11}$$

$$\text{erfc}(x) = \frac{2}{\sqrt{\pi}} \int_x^{+\infty} \exp(-t^2) \mathrm{d}t \tag{5.12}$$

For the candidate sources list strategy, the λ_{data}, the corresponding fitted number of signal, the *p-value* and the pre-trial number of σ are presented in Table 5.2.

Source	*r.a.*	δ	l	b	Visibility	λ_{data}	n_{signal}	Pre-trial *p-value*	Pre-trial σ (1 side)	ϕ_{90}
HESS J0632+057	$6^h32'58''$	$5°48'20''$	205.66	-1.44	0.47	0.517	1.0	0.081	1.4	5.8
RX J0852.0-4622	$8^h52'00''$	$-46°22'00''$	266.28	-1.24	0.92	2.643	1.6	0.007	2.5	9.7
HESS J1023-575	$10^h23'18''$	$-57°45'50''$	284.19	-0.39	1.00	4.019	4.1	0.0014	3.0	13.9
PSR B1259-63	$13^h02'49''$	$-63°50'02''$	304.19	-0.99	1.00	0	0	-	-	5.2
RCW 86	$14^h42'43''$	$-62°29'00''$	315.79	-1.46	1.00	0.046	0.4	0.182	0.9	5.8
Cir X-1	$15^h20'41''$	$-57°10'00.26''$	322.12	0.04	1.00	0	0	-	-	5.4
HESS J1614-518	$16^h14'19''$	$-51°49'12''$	331.52	0.58	1.00	0	0	-	-	5.4
GX 339	$17^h02'49''$	$-48°47'23''$	338.94	-4.33	1.00	0	0	-	-	4.6
RX J1713.7-3946	$17^h13'00''$	$-39°45'00''$	347.28	-0.38	0.78	0	0	-	-	4.7
Galactic Center	$17^h45'41''$	$-29°00'22''$	359.95	-0.05	0.67	0.895	1.6	0.048	1.7	5.9
W28	$18^h01'42''$	$-23°20'06''$	6.66	-0.27	0.63	0	0	-	-	4.4
LS 5039	$18^h26'15''$	$-14°49'30''$	16.90	-1.28	0.58	0	0	-	-	4.6
HESS J1837-069	$18^h37'38''$	$-6°57'00''$	25.18	-0.12	0.54	0	0	-	-	4.6
SS 433	$19^h11'50''$	$4°58'58''$	39.69	-2.24	0.47	0	0	-	-	4.6
RGB J0152+017	$1^h52'40''$	$1°47'19''$	152.38	-26.61	0.49	0	0	-	-	4.6
1ES 0347-121	$3^h49'23''$	$-11°59'27''$	201.93	-45.71	0.56	0	0	-	-	4.6
PKS 0548-322	$5^h50'40.6''$	$-32°16'16.4''$	237.56	-26.14	0.70	0	0	-	-	4.4
1ES 1101-232	$11^h03'38''$	$-23°29'31''$	273.19	33.08	0.63	0	0	-	-	4.4
3C 279	$12^h56'11''$	$-5°47'21''$	305.10	57.06	0.53	0	0	-	-	4.7
Centaurus A	$13^h25'27.6''$	$-43°01'08.8''$	309.52	19.46	0.83	0	0	-	-	4.5
ESO 139-G12	$17^h37'39.5''$	$-59°56'29''$	334.04	-13.77	1.00	0	0	-	-	5.3
PKS 2005-489	$20^h09'29''$	$-48°49'19''$	350.39	-32.61	1.00	0.413	1.1	0.100	1.3	6.0
PKS 2155-304	$21^h58'53''$	$-30°13'18''$	17.74	-52.25	0.68	0	0	-	-	4.4
H 2356-309	$23^h59'08''$	$-30°37'39''$	12.84	-78.04	0.68	0	0	-	-	4.4

Table 5.2: Pre-trial results of the candidate sources list search strategy.

Amongst the 24 sources, the most significant source is HESS J1023-575 with *p-value* equals to 0.0014 which corresponds to 3σ pre-trial using one side Gaussian convention. Four events are found close to this source. They are detected in February 28th, May 26th, June 21th and October 3rd. The time window between their detection is high enough to reject a transit source scenario. The event display[6] of four neutrinos found close to the candidate source HESS J1023-575 are shown in figures 5.56, 5.57, 5.58 and 5.59.

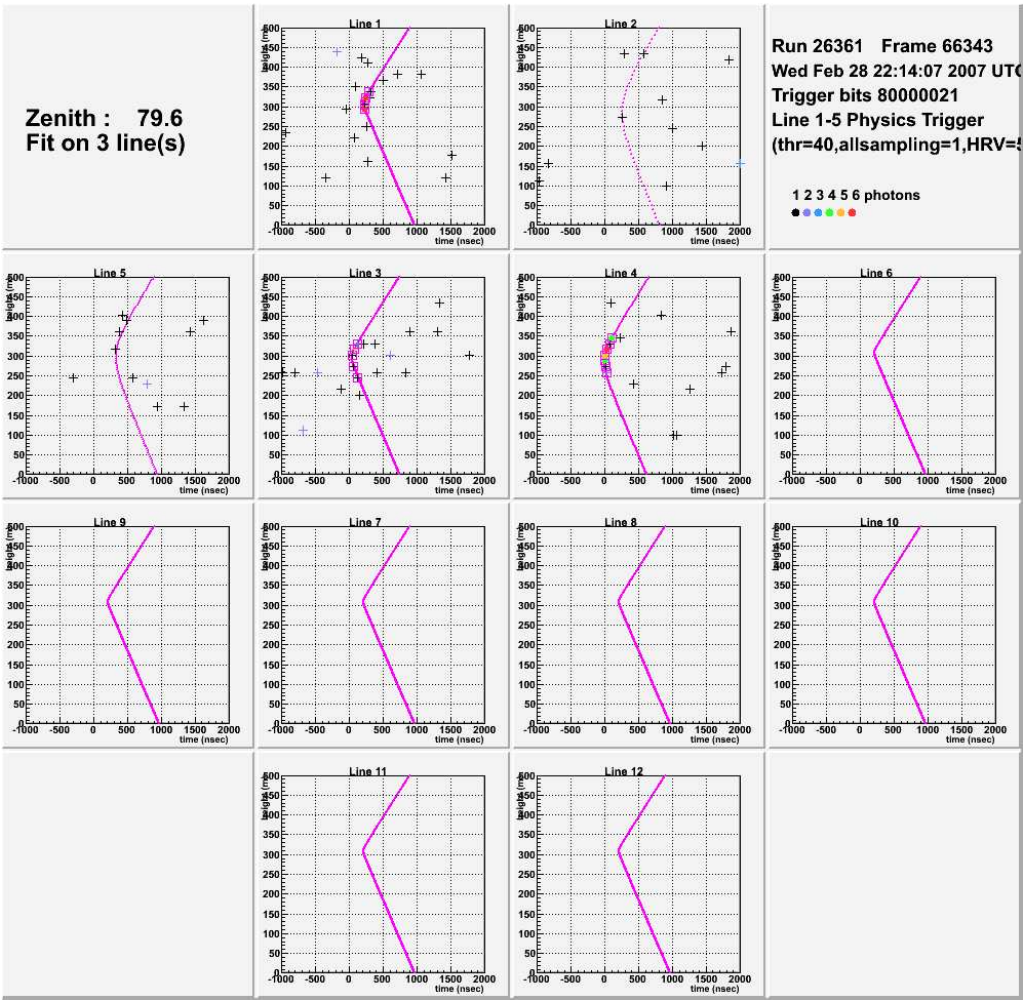

Figure 5.56: The event display of the first neutrino event close to HESS J1023-575.

[6]The event display shows the hits altitude from the sea bed as a function of time. The twelve plots represent the twelve lines and the magenta lines represent the reconstructed wave front of Cherekov photons.

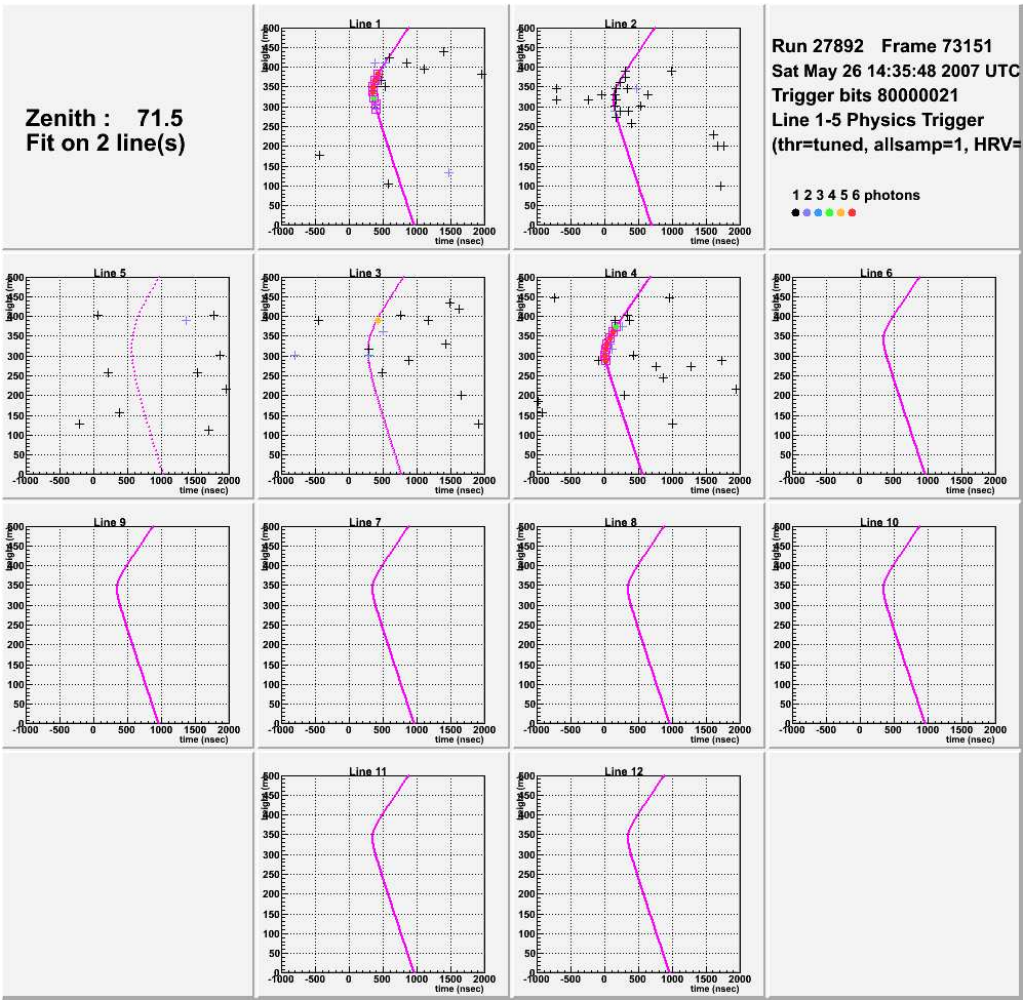

Figure 5.57: The event display of the second neutrino event close to HESS J1023-575.

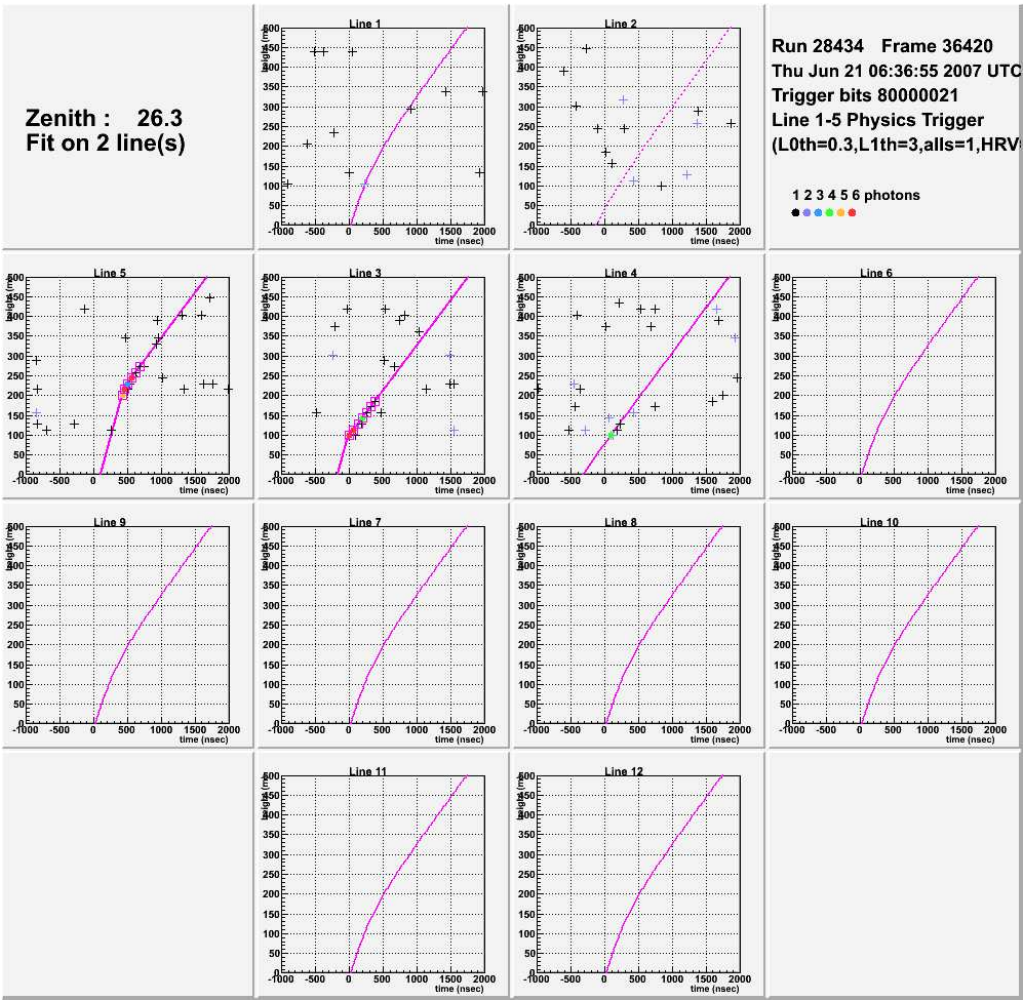

Figure 5.58: The event display of the third neutrino event close to HESS J1023-575.

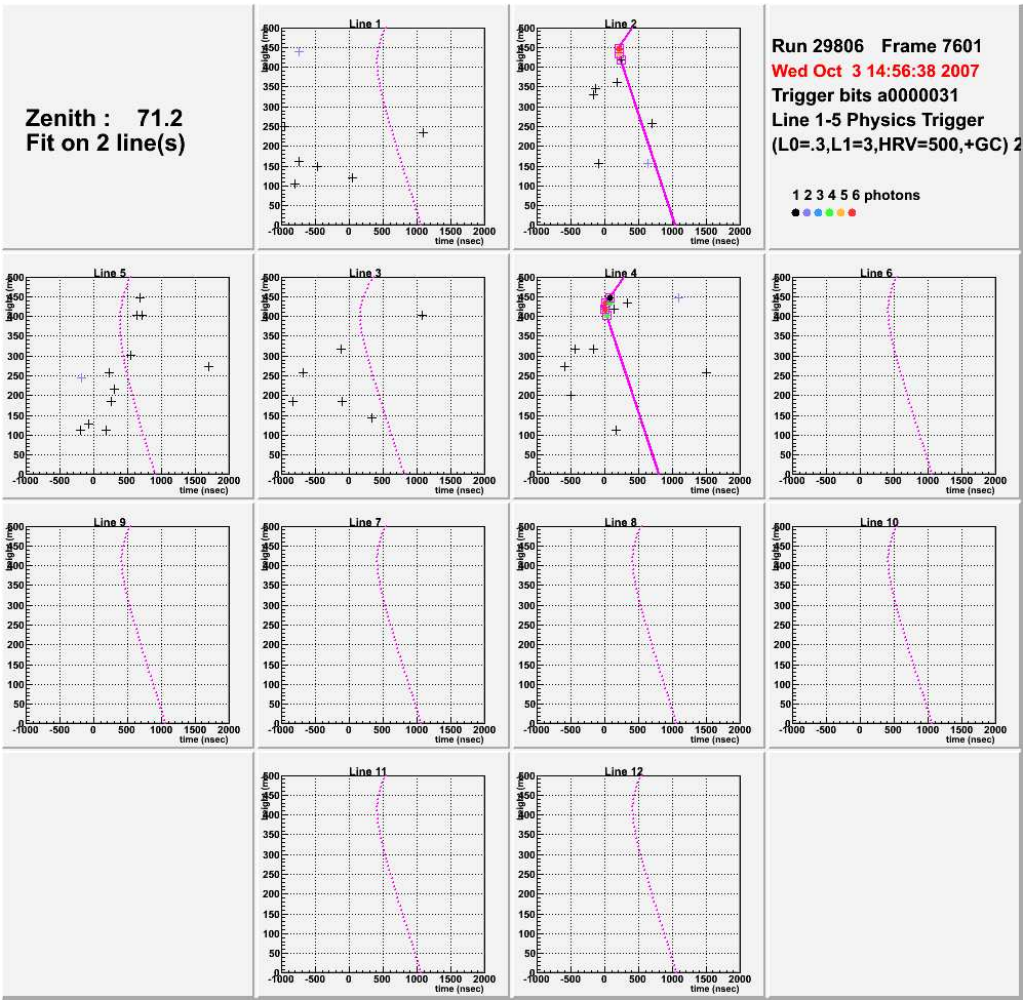

Figure 5.59: The event display of the fourth neutrino event close to HESS J1023-575.

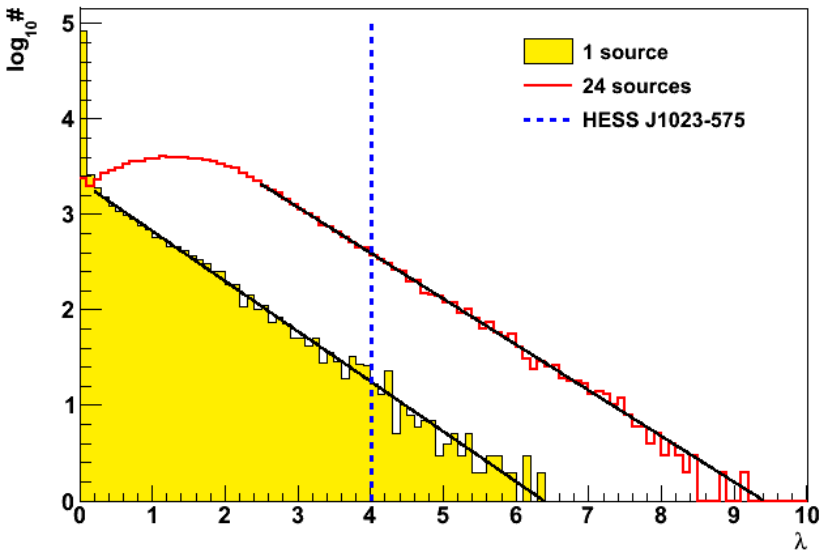

Figure 5.60: The background λ distributions for one and 24 candidate sources. λ_{data} is shown in dashed line.

5.10.1.2 Post-trial results

To compute the post-trial *p-value* for the brightest source HESS J1023-575, the 24 sources are simulated in the same time (10^5 simulations). For each simulated sky, the unbinned search algorithm is applied on each source and 24 λ values are calculated. Between these λ values, the biggest λ value is chosen to be the λ value of the experiment and the entry for the post-trial λ distribution.

Figure 5.60 shows the λ distributions of the background only model for one source at HESS J1023-575 position (yellow histogram) and for 24 candidate sources (red histogram). The λ_{data} for HESS J1023-575 is also presented (blue line).

The post-trial *p-value* is computed using λ_{data}, Equation 5.10 and the post-trial λ distribution for background only model. For HESS J1023-575, the post-trial *p-value* is 0.036 which corresponds to 1.8σ. The trial factor defined as the ratio between the post-trial and the pre-trial *p-value* is 24.8, close to the number of candidate sources.

5.10.1.3 Upper limit

The upper limits on the neutrino flux of the 24 candidate sources are derived. The upper limit is computed using the pre-trial λ distributions and equations 5.7 and 5.8, but replacing $\lambda_{0.5}$ by λ_{data}. These upper limits are illustrated in Figure 5.61

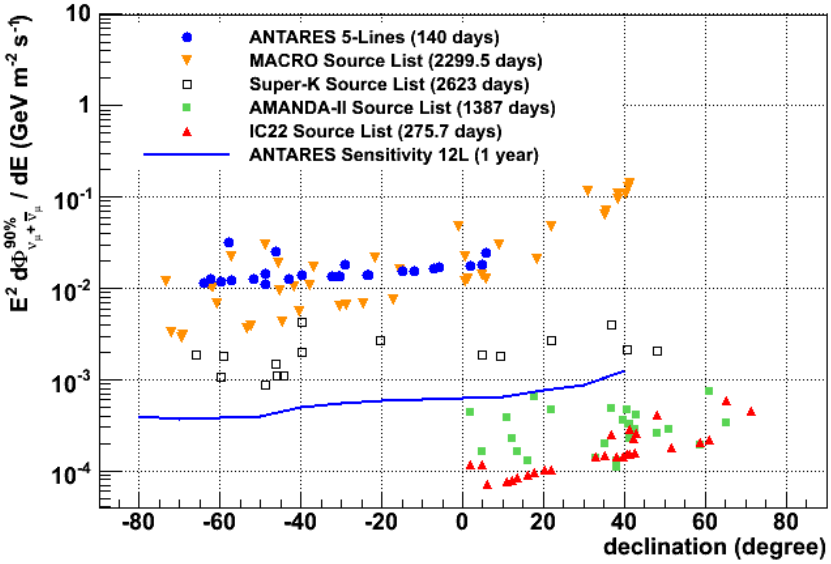

Figure 5.61: Neutrino flux upper limit at 90% *CL* for the 5-line 2007 ANTARES data, compared with the results from other experiments (IceCube [128], AMANDA [129], SuperKamiokande [130] and [131] and MACRO [132]). The sensitivity of ANTARES for one year with 12-line configuration [127] is also shown. The assumed source spectrum is E^{-2}, except for MACRO, for which an $E^{-2.1}$ spectrum was used.

and are compared to results from other experiments. The sensitivity of ANTARES for one year with 12-line configuration [127] is also shown. The upper limits on the neutrino events number, ϕ_{90}, are presented in Table 5.2 with $CL = 90\%$.

5.10.2 All sky search strategy

The all sky search strategy is also applied on the data. The hottest point (the search-point corresponding to the biggest λ value) is found at $r.a. = 14^h48'35.28''$ and $\delta = -9°30'00''$. The four brightest clusters are shown in Table 5.3 (figures 5.62, 5.63, 5.64, and 5.65).

The λ_{data} corresponding to this point is 8.834. The *p-value* of this point is equal to 0.309 and the significance is 0.5σ (1 side Gaussian convention) calculated with Equation 5.11. The *p-value* for the all sky search is already post-trial value since the unbinned search algorithm is applied over 4,126,182 search-points and only the biggest λ value is registered.

Cluster rank (brightness)	λ value	n_{signal}	*r.a.*	δ
1	8.834	4.3	$14^h48'35.28''$	$-9°30'00''$
2	7.390	4.4	$10^h36'32.16''$	$-56°36'00''$
3	6.886	3.9	$8^h47'39.36''$	$-20°12'00''$
4	6.876	3.5	$19^h31'41.04''$	$-78°24'00''$

Table 5.3: The four brightest clusters in the all sky search strategy.

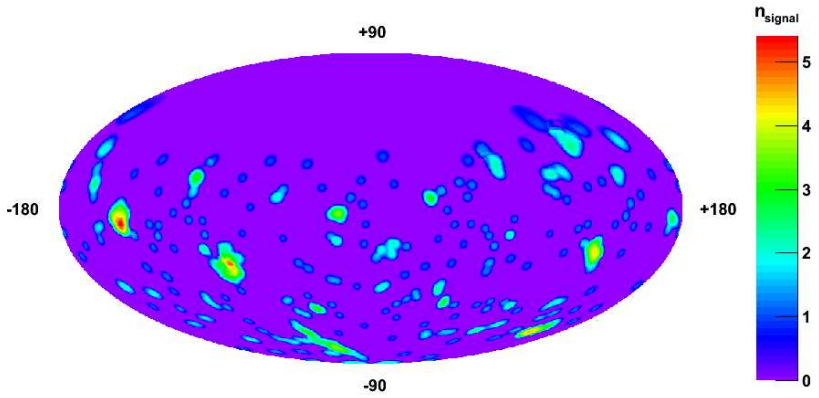

Figure 5.62: Fitted number of events in the Equatorial coordinates system for the data sample.

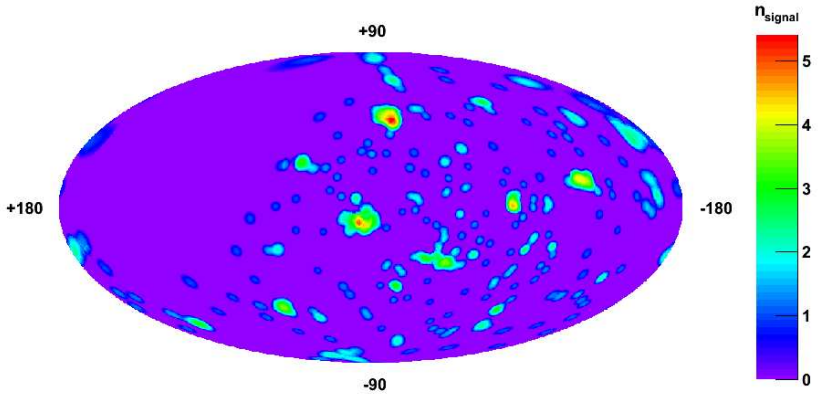

Figure 5.63: Fitted number of events in the Galactic coordinates system for the data sample.

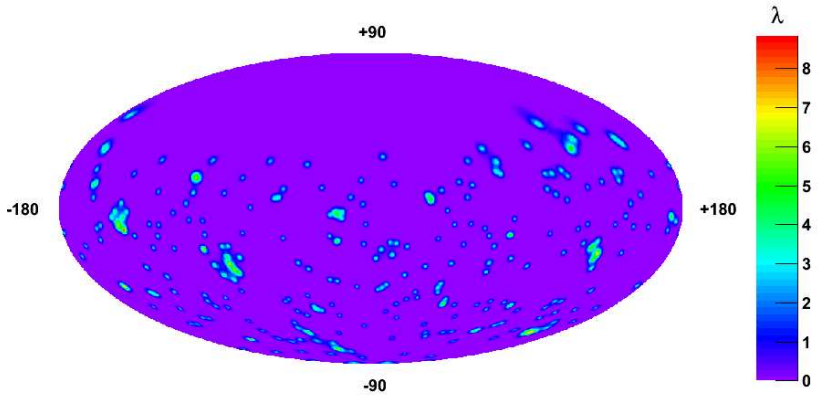

Figure 5.64: λ value in the Equatorial coordinates system for the data sample.

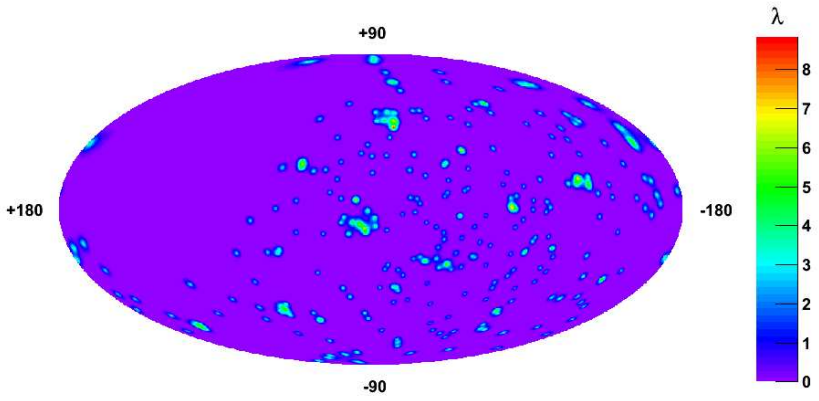

Figure 5.65: λ value in the Galactic coordinates system for the data sample.

5.11 Conclusion

The event selection cuts are optimized to have the best discovery potential ($nhit > 5$, $nline \geq 2$, $tchi2 \leq 1.8$ when $z \leq 80^\circ$ and $tchi2 \leq 1.4$ when $80^\circ < z \leq 90^\circ$, $bchi2 \geq 2.2$). The 2007 5-line ANTARES data is analysed using an unbinned method based on a maximum-likelihood ratio method. Two search strategies "the candidate sources list search strategy" and "the all sky search strategy" are applied. 24 astrophysical bodies are used as candidate neutrino sources. The most significant source with the candidate sources list search strategy is HESS J1023-575 with 1.8σ. The lowest upper limit computed is $E^2 \mathrm{d}\Phi^{90\%}_{\nu_\mu+\bar{\nu}_\mu}/\mathrm{d}E = 1.09 \times 10^{-2}$ GeV m^{-2} s^{-1} at $\delta = -48^\circ 47' 23''$. The brightest cluster found with the all sky search strategy is at $r.a. = 14^h 48' 35.28''$ and $\delta = -9^\circ 30' 00''$ with 0.5σ.

Chapter 6

Search for neutrino point sources in 2007 + 2008 data using AAfit

In this chapter, the analysis of the 2007+2008 data is presented. For this analysis the AAfit reconstruction algorithm, rather than the BBfit algorithm, is adopted. During the 2007 data analysis reported in Chapter 5, the AAfit algorithm was under development and suffered from discrepancies when comparing various data and Monte-Carlo distributions, thus the BBfit algorithm was chosen. Quite recently, these discrepancies have been understood as due to an over simplification in the simulation of the charge distribution of the background noise hits. Once this is corrected in the simulation, a reasonable data versus Monte-Carlo agreement is obtained.

As discussed in Section 3.4.2, the AAfit algorithm is based on a PDF approach and makes full use of the acoustic positioning and compass information. Its performance in terms of angular resolution and effective area is significantly better than the BBfit algorithm.

6.1 Data and Monte-Carlo

The data used in this chapter is taken from the beginning of 2007 until the end of 2008 by different detector configurations (5-9-10-12-line). The total livetime is 295 active days, 144 for the 5-line configuration and 151 for 9-10-12-line combined configuration. The data runs are processed by 3N and/or T3 triggers.

The data events used in this analysis are selected by the following quality cuts adopted from Reference [133]:

- Λ_{reco}: it is the track reconstruction quality cut (equal to the likelihood divided by the number of degrees of freedom). The well reconstructed muon tracks have Λ_{reco} higher than the badly reconstructed tracks. The Λ_{reco} value

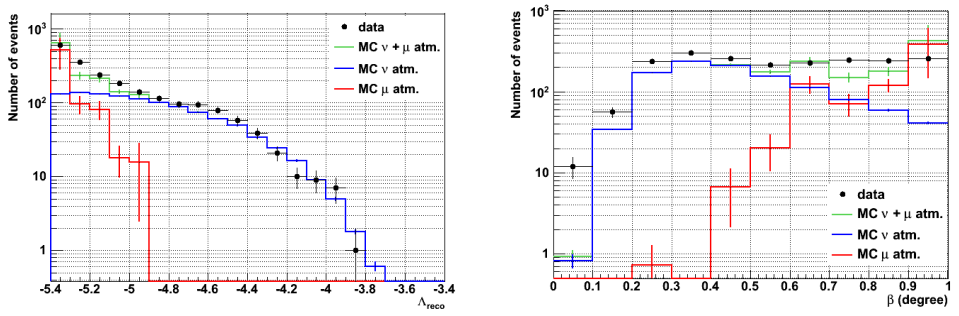

Figure 6.1: Distributions of Λ_{reco} (left) and β (right) of the data and Monte-Carlo for the optimized cuts.

used to select the data set is $\Lambda_{reco} >$ -5.4 and it is optimized to have the best sensitivity and discovery potential. Figure 6.1 (left) shows the Λ_{reco} distribution of the data and Monte-Carlo. A good agreement is seen for the selected region.

- β: it is the error on the reconstructed angle calculated by the reconstruction algorithm. Figure 6.1 (right) shows a comparison between the data and Monte-Carlo distributions. The value used to select the data set is $\beta < 1^\circ$. This cut selects well reconstructed tracks and rejects a large fraction of the atmospheric muons.

- z: it is the zenith of the reconstructed track. Figure 6.2 shows the zenith and the declination distributions of the data and Monte-Carlo for $\Lambda_{reco} >$ -5.4, $\beta < 1^\circ$ and $z < 90^\circ$. Very high number of atmospheric muons is rejected by the zenith cut $z < 90^\circ$.

With these three cuts ($\Lambda_{reco} >$ -5.4, $\beta < 1^\circ$ and $z < 90^\circ$), the number of selected data and Monte-Carlo events are presented in Table 6.1. Figures 6.2 represents the zenith (left) and the declination (right) distributions of the selected data events compared with the Monte-Carlo simulations.

Data	$\nu + \mu$	ν	μ
2040 ± 45	1820 ± 28	1096 ± 8	724 ± 27

Table 6.1: Number of selected events in this analysis with the statistical uncertainties.

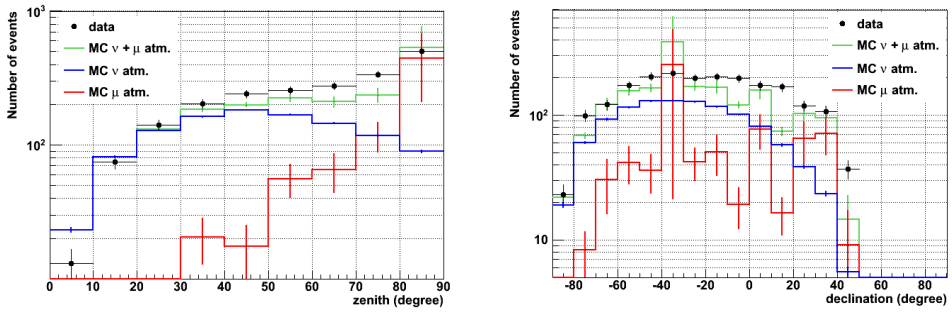

Figure 6.2: Zenith (left) and declination (right) distributions of the data and the Monte-Carlo for the optimized cuts.

6.2 Effective area and angular resolution

The effective area and the angular resolution are calculated with the same way as in Chapter 5. Figures 6.3 and 6.4 show the effective area and the angular resolution, respectively, as a function of the point source declination and the true neutrino energy. Comparing with the previous analysis (5-line BBfit), the effective area increases by at least a factor of 2.5 whereas the angular resolution is improved by a factor of six (minimum) for the neutrinos with energies higher than 10 TeV. The improvement of both, effective area and angular resolution, is not due only to the increase of the detector size. The use of the likelihood maximization method in the reconstruction algorithm and the acoustic positioning data in the alignment (including the compasses and the tiltmeters) gives AAfit an advance on BBfit algorithm.

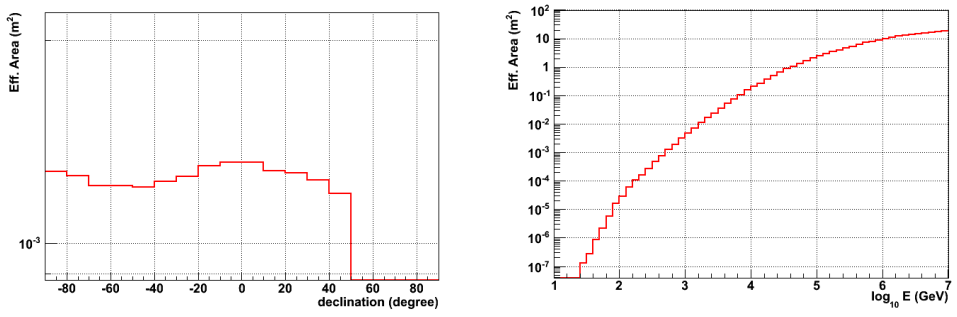

Figure 6.3: The effective area as a function of the true neutrino declination (left) and the true neutrino energy (right).

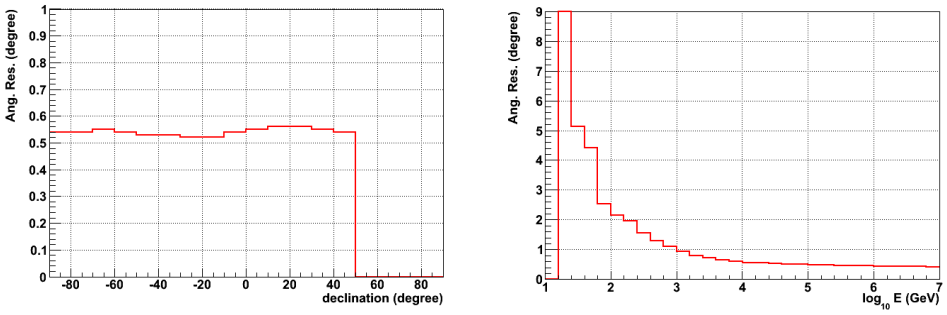

Figure 6.4: The angular resolution as a function of the true neutrino declination (left) and the true neutrino energy (right).

Figures 6.5 and 6.6 show the PSF (the difference between the true neutrino direction and the reconstructed muon direction) for a point source at $\delta = -25^{\circ}$. The improvement of the angular resolution, for this analysis, can be seen by the PSFs comparison in the right plot of Figure 6.5. The cumulative event fraction plot of this analysis (Figure 6.6), compared to Figure 5.18 of the previous analysis, shows the decrease of the number of events falling outside the search window from 30% to 5%.

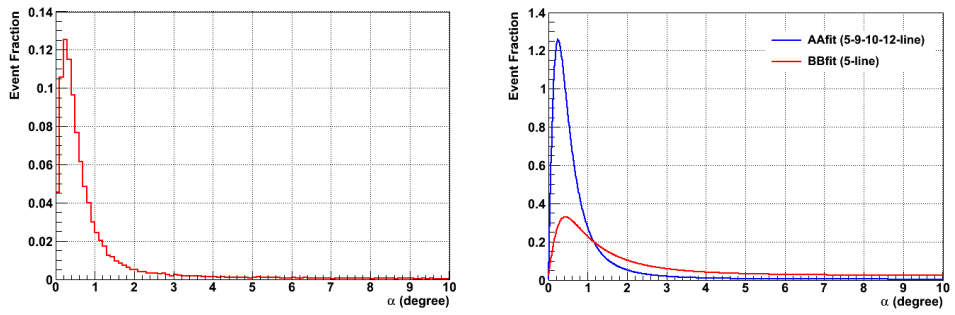

Figure 6.5: PSF of a point source at declination of -25°. In the right plot, the comparison between the PSFs for the BBfit (5-line) and AAfit (5-9-10-12-line) are shown.

6.3 Sensitivity and discovery potential

The unbinned method explained in Section 5.5 is used in the sensitivity and the discovery potential calculations. The systematic uncertainty on the absolute pointing calculated in Chapter 4 is included. For each simulated skymap, two ran-

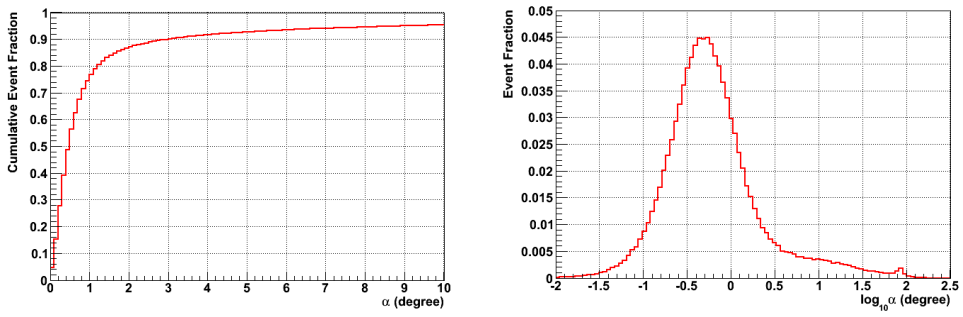

Figure 6.6: Cumulative event fraction of a point source at declination of -25° (left) and the PSF in logarithmic scale (right).

dom values are generated with a Gaussian distribution where $\sigma_{\text{zenith}} = 0.13^\circ$ and $\sigma_{\text{azimuth}} = 0.06^\circ$. These values are applied as an offset over all the events of the same skymap. The systematic uncertainties on the angular resolution and the detector acceptance are adopted from Reference [133] and they are equal to 15%.

The λ and the fitted number of signal distributions are shown in Figure 6.7. The λ distributions are better separated in this analysis than in the previous analysis (Figure 5.29) due to the improvement of the angular resolution. As it is explained in Section 5.6.1, the fitted number of signal events is 95% of the number of simulated events because of the 5% of events are outside the 10° search window (Figure 6.6).

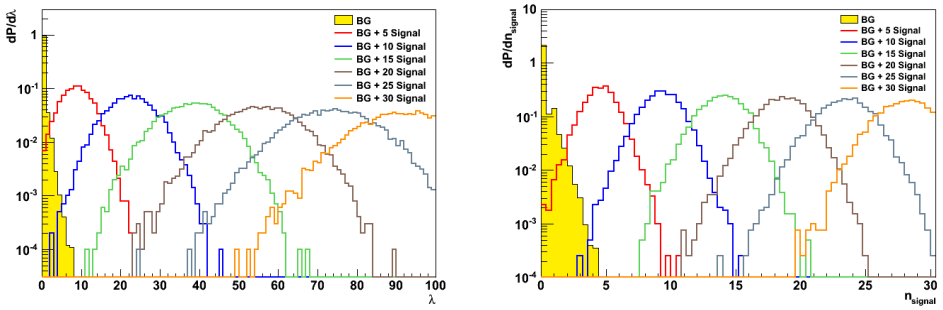

Figure 6.7: Distributions of λ values (left) and fitted numbers of events (right).

Figure 6.8 shows the average number of signal neutrino events corresponding to a sensitivity of $CL = 90\%$ and a discovery potential of 50% probability including the systematic uncertainties.

Figure 6.9 presents the sensitivity ($CL = 90\%$) and the discovery potential

(50% probability) for this analysis. it is improved by one order of magnitude compared to the previous analysis.

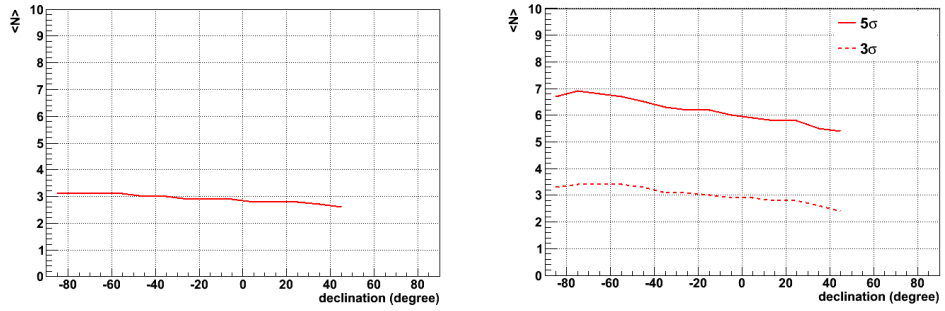

Figure 6.8: Average number of signal neutrino events corresponding to a sensitivity of $CL = 90\%$ (left) and a discovery potential with 50% probability (right). The systematic uncertainties are included.

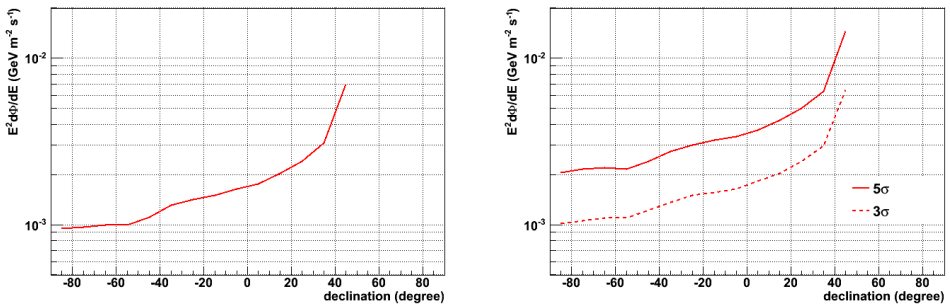

Figure 6.9: The sensitivity of $CL = 90\%$ (left) and the discovery potential with 50% probability (right) for the optimized cuts. The systematic uncertainties are included.

6.4 Results

Using the candidate sources list search strategy, no discovery is made in the 2007+2008 data. The best upper limits on the high energy cosmic neutrinos from various sources in the Southern sky are obtained. Figure 6.10 shows the upper limits given by the 2007 data analysis discussed in Chapter 5 and the 2007+2008 data analysis presented in this chapter. The results from other experiments are shown, too. The upper limits calculated in this chapter using 2007+2008 data

with AAfit reconstruction algorithm are improved by an order of magnitude compared to 2007 data with BBfit.

Table 6.2 shows the fitted number of signal events, the λ value, the pre-trial *p-value* and the significance of the 24 candidate sources. The most significant source is GX 339 with *p-value* equals to 0.0024 corresponding to 2.8σ (pre-trial) where the post-trial *p-value* is 0.067 which corresponds to 1.5σ. The lowest upper limit is $E^2 \mathrm{d}\Phi^{90\%}_{\nu_\mu+\bar{\nu}_\mu}/\mathrm{d}E = 9.7 \times 10^{-4}$ GeV m^{-2} s^{-1}.

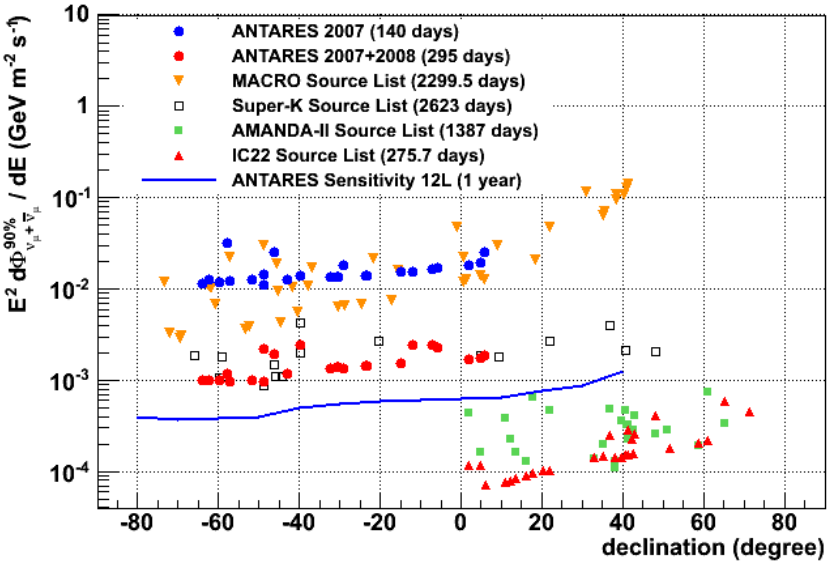

Figure 6.10: Neutrino flux upper limit at 90% *CL* for the 5-line 2007 (BBfit) and 5-9-10-12-line 2007 + 2008 (AAfit) ANTARES data, compared with the results from other experiments (IceCube [128], AMANDA [129], SuperKamiokande [130] and [131] and MACRO [132]). The sensitivity of ANTARES for one year with 12-line configuration [127] is also shown. The assumed source spectrum is E^{-2}, except for MACRO, for which an $E^{-2.1}$ spectrum was used.

Source	*r.a.*	δ	l	b	Visibility	λ_{data}	n_{signal}	Pre-trial $p-value$	Pre-trial σ (1 side)	ϕ_{90}
HESS J0632+057	$6^h32'58''$	$5°48'20''$	205.66	-1.44	0.47	0	0	-	-	2.9
RX J0852.0-4622	$8^h52'00''$	$-46°22'00''$	266.28	-1.24	0.92	1.856	1.2	0.018	2.1	5.4
HESS J1023-575	$10^h23'18''$	$-57°45'50''$	284.19	-0.39	1.00	0.203	1.0	0.132	1.1	3.6
PSR B1259-63	$13^h02'49''$	$-63°50'02''$	304.19	-0.99	1.00	0	0	-	-	3.1
RCW 86	$14^h42'43''$	$-62°29'00''$	315.79	-1.46	1.00	0	0	-	-	3.1
Cir X-1	$15^h20'41''$	$-57°10'00.26''$	322.12	0.04	1.00	0	0	-	-	3.0
HESS J1614-518	$16^h14'19''$	$-51°49'12''$	331.52	0.58	1.00	0	0	-	-	3.1
GX 339	$17^h02'49''$	$-48°47'23''$	338.94	-4.33	1.00	3.425	2.2	0.0024	2.8	6.8
RX J1713.7-3946	$17^h13'00''$	$-39°45'00''$	347.28	-0.38	0.78	2.337	1.1	0.0098	2.3	5.8
Galactic Center	$17^h45'41''$	$-29°00'22''$	359.95	-0.05	0.67	0	0	-	-	2.9
W28	$18^h01'42''$	$-23°20'06''$	6.66	-0.27	0.63	0	0	-	-	2.9
LS 5039	$18^h26'15''$	$-14°49'30''$	16.90	-1.28	0.58	0	0	-	-	2.9
HESS J1837-069	$18^h37'38''$	$-6°57'00''$	25.18	-0.12	0.54	1.161	1.0	0.039	1.8	4.3
SS 433	$19^h11'50''$	$4°58'58''$	39.69	-2.24	0.47	0	0	-	-	2.8
RGB J0152+017	$1^h52'40''$	$1°47'19''$	152.38	-26.61	0.49	0	0	-	-	2.8
1ES 0347-121	$3^h49'23''$	$-11°59'27''$	201.93	-45.71	0.56	1.508	1.5	0.025	2.0	4.6
PKS 0548-322	$5^h50'40.6''$	$-32°16'16.4''$	237.56	-26.14	0.70	0	0	-	-	3.0
1ES 1101-232	$11^h03'38''$	$-23°29'31''$	273.19	33.08	0.63	0	0	-	-	2.9
3C 279	$12^h56'11''$	$-5°47'21''$	305.10	57.06	0.53	1.051	1.0	0.044	1.7	4.1
Centaurus A	$13^h25'27.6''$	$-43°01'08.8''$	309.52	19.46	0.83	0	0	-	-	3.0
ESO 139-G12	$17^h37'39.5''$	$-59°56'29''$	334.04	-13.77	1.00	0	0	-	-	3.1
PKS 2005-489	$20^h09'29''$	$-48°49'19''$	350.39	-32.61	1.00	0	0	-	-	3.0
PKS 2155-304	$21^h58'53''$	$-30°13'18''$	17.74	-52.25	0.68	0	0	-	-	3.0
H 2356-309	$23^h59'08''$	$-30°37'39''$	12.84	-78.04	0.68	0	0	-	-	3.0

Table 6.2: Pre-trial results of the candidate sources list search strategy.

The all sky search strategy is applied on the selected data events (figures 6.11 and 6.12). The most significant cluster is found at $r.a. = 8^h58'26.4''$ and $\delta = 13°18'00''$ ($\lambda = 12.978$ and $n_{\text{sig}} = 5.5$) with $p\text{-}value = 0.024$ corresponding to 2.0σ. Figures 6.13, 6.14, 6.15 and 6.16 show the skymaps of the fitted number of events and the λ value for both Equatorial and Galactic coordinates systems.

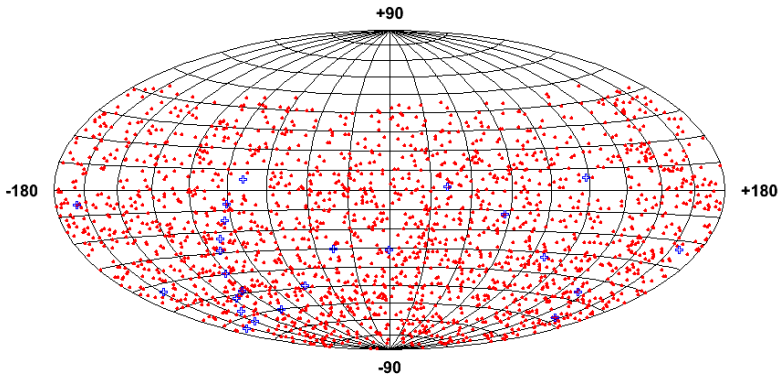

Figure 6.11: In the Equatorial coordinates system, the selected data events (red points) and the 24 candidate sources (blue crosses).

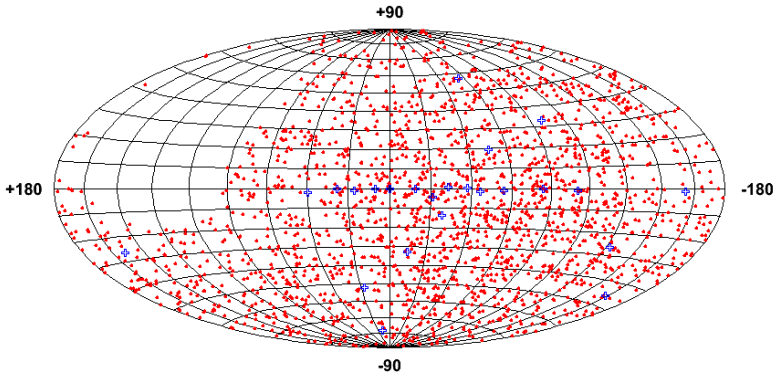

Figure 6.12: In the Galactic coordinates system, the selected data events (red points) and the 24 candidate sources (blue crosses).

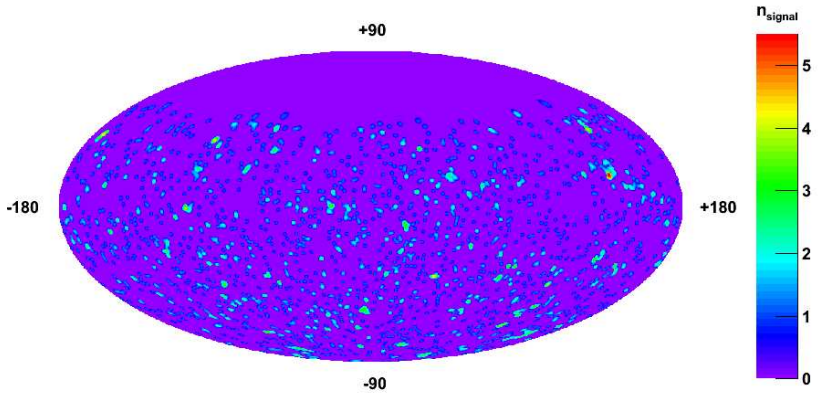

Figure 6.13: Fitted number of events in the Equatorial coordinates system for the data sample.

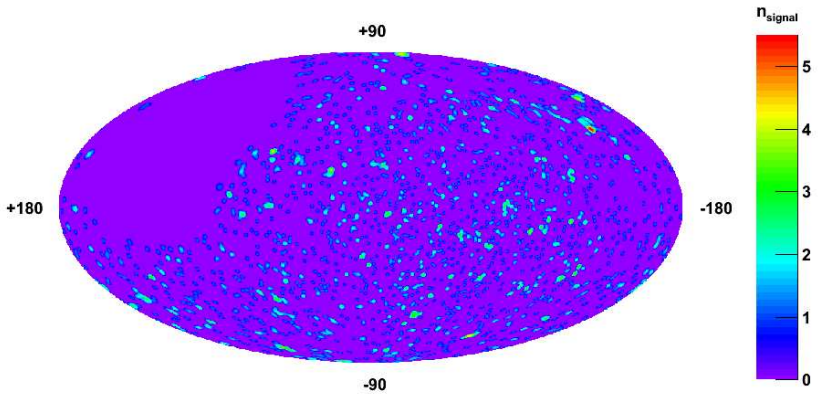

Figure 6.14: Fitted number of events in the Galactic coordinates system for the data sample.

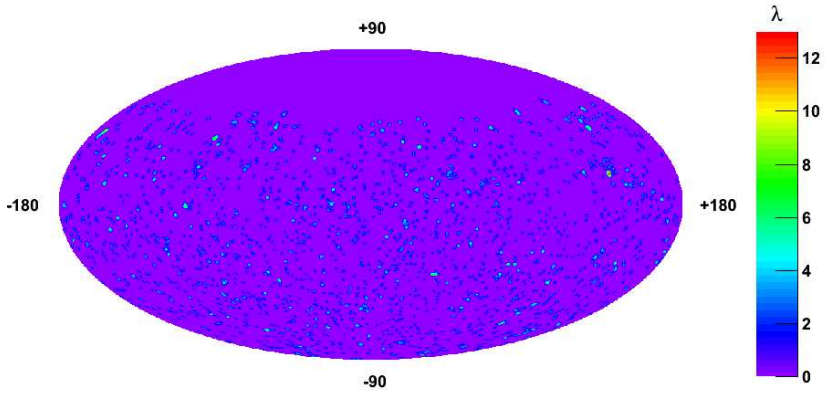

Figure 6.15: λ value in the Equatorial coordinates system for the data sample.

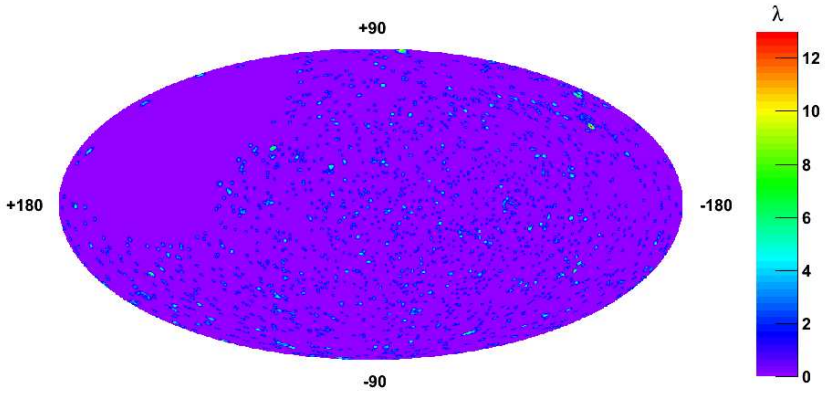

Figure 6.16: λ value in the Galactic coordinates system for the data sample.

Conclusion

In Chapter 1, the Ultra High Energy Cosmic Rays (UHECR)s and the mystery of their origin are discussed. The most recent results published by the UHECR detectors such the Pierre Auger Observatory (PAO) do not indicate a strong correlation between the UHECRs and potential sources. The chemical composition of the primary cosmic rays remains an open question with the contradiction between the PAO and HiRes results. For the γ-ray astronomy, the story is different. Many γ-ray sources, galactic and extragalactic, are detected and the energy spectrum for each source is measured. However, with the present γ-ray astronomy results published by HESS, FERMI, and other telescopes, the emission processes are still unclear and the sources of the UHECRs remain unidentified. Neutrino astronomy can offer an answer to these questions. The detection of very high energy cosmic neutrinos from a source is a signature of the existence of hadronic processes leading to the clarification of the UHECRs origin. Neutrino particles, being neutral and having a low cross-section with matter, offer the possibility of detection over the full energy spectrum and for a farther horizon. Finally, different potential sources of cosmic neutrinos, galactic and extragalactic, are discussed.

In Chapter 2, the flux of high energy cosmic neutrinos at the Earth and the number of events that can be observed by the ANTARES detector are estimated. In this study, the hypotheses of the neutrino production are based completely on hadronic scenarios. The γ-ray astronomy data is used to define the neutrino energy spectrum at the source, then at the Earth after taking into consideration neutrino oscillations. For the extragalactic sources, the optical depth of the Very High Energy (VHE) γ-rays are calculated. The flux of these γ-rays is attenuated because of their interactions with the Extragalactic Background Light (EBL) producing electrons and positrons. The number of events corresponding to the estimated flux is found using the effective area of 5-9-10-12-line combined detector configuration. All the numbers are calculated for 295 days which is the active period of 2007 + 2008. The results indicate a potential discovery of cosmic neutrinos after few years of data taking with ANTARES.

The ANTARES neutrino telescope, discussed in Chapter 3, started taking data in 2007 with a 5-line configuration. Since then, additional lines were added reaching its final configuration of 12 lines in June 2008. First, the neutrino detection principle and the main detector components are described. Then, the data acquisition, the trigger, the time calibration, and the various backgrounds are discussed. The Monte-Carlo simulations and the muon track reconstruction algorithms, BBfit and AAfit, used in the cosmic neutrino point sources analysis are presented. Finally, the characteristics and the performances of two future telescopes, IceCube and KM3NeT, are indicated.

Chapter 4 discusses a study of the ANTARES telescope absolute pointing and its uncertainty using the acoustic positioning system. In the first step, the absolute pointing is calculated by the Low Frequency Low Base Line (LFLBL) system with an uncertainty higher than one degree in some directions. In the second step, using the High Frequency Low Base Line (HFLBL) system in addition to the LFLBL system, the High Frequency (HF) acoustic distances are triangulated and the absolute pointing of the telescope is recalculated improving the results by one order of magnitude. The systematic errors due to the HF acoustic distances, the uncertainties on the RxTx transducers positions, the sound velocity, and the choice of the Rx hydrophone for the triangulation are studied. Finally, the uncertainty on the absolute pointing of the ANTARES telescope is estimated to be a Gaussian distribution with $\sigma_{\text{horizontal}} = 0.127^\circ \pm 0.002^\circ$ and $\sigma_{\text{vertical}} = 0.035^\circ \pm 0.020^\circ$.

Chapters 5 and 6 present the high energy cosmic neutrino point sources search with both reconstruction strategies, BBfit and AAfit, respectively. For the former, the 2007 data with 5-line configuration is analysed. For the latter, the analysis is done using both 2007 and 2008 data with 5-9-10-12-line combined detector configuration. The search algorithm is an unbinned algorithm based on the likelihood ratio method using 1D PDFs for the signal and the background. This algorithm is chosen after testing other algorithms (binned and unbinned). A Monte-Carlo study of this algorithm demonstrates robustness, rapidity, and absence of singularities. Two search strategies are applied: "the candidate sources list search" and "the all sky search". The most significant source in the candidate sources list search strategy is HESS J1023-575 with 1.8σ for BBfit 5-line analysis and GX 339 with 1.5σ for AAfit 5-9-10-12-line analysis (post-trial and 1 side Gaussian). Therefore, no discovery is made and the world's best upper limits on neutrino fluxes from various sources in the Southern sky are established. The lowest upper limit is $E^2 \mathrm{d}\Phi^{90\%}_{\nu_\mu+\overline{\nu}_\mu}/\mathrm{d}E = 9.7 \times 10^{-4}$ GeV m^{-2} s^{-1}. The all sky search strategy did not find any significant source. The most significant one is found at *r.a.* $= 14^h48'35.28''$ and $\delta = -9^\circ30'00''$ with 0.5σ for BBfit 5-line analysis and at

r.a. $= 8^h58'26.4''$ and $\delta = 13^\circ18'00''$ with 2.0σ for AAfit 5-9-10-12-line analysis. Finally, several neutrino skymaps are produced.

Appendix A

Cosmic rays acceleration

An explanation to the mechanism of the acceleration process of cosmic rays was given by Enrico Fermi in 1949 [9]. The charged particles gain kinetic energy by interacting with shock waves due to moving magnetic fields. This process can be explained by defining two referential frames R and R'. R is fixed relatively to the stars and R' is the referential frame of moving magnetic field.

Using Lorentz transformations, the energy of the incident particle in R' is given as a function of its energy in R and the velocity v between the both referential frames:

$$E'_{\text{in}} = \gamma E_{\text{in}} \left(1 - \beta \cos \theta_{\text{in}}\right) \tag{A.1}$$

where

$$\gamma = \frac{1}{\sqrt{1-\beta^2}} \quad \text{with} \quad \beta = \frac{v}{c} \tag{A.2}$$

Due to the magnetic field, the particles can follow a semi-circular trajectory. The energy of emerging particles in R is given by:

$$E_{\text{out}} = \gamma E'_{\text{out}} \left(1 + \beta \cos \theta'_{\text{out}}\right) \tag{A.3}$$

The fact that $E'_{\text{in}} = E'_{\text{out}}$, the energy of the emerging particle can be written as:

$$E_{\text{out}} = \gamma^2 E_{\text{in}} \left(1 - \beta \cos \theta_{\text{in}}\right) \left(1 + \beta \cos \theta'_{\text{out}}\right) \tag{A.4}$$

The energy of the particle is increased by a gain of ε defined as:

$$\varepsilon = \frac{\Delta E}{E} = \frac{E_{\text{out}} - E_{\text{in}}}{E_{\text{in}}} = \frac{\beta \left(\cos \theta'_{\text{out}} - \cos \theta_{\text{in}}\right) + \beta^2 \left(1 - \cos \theta_{\text{in}} \cos \theta'_{\text{out}}\right)}{1 - \beta^2} \tag{A.5}$$

If this process is repeated n times, the energy of the particle as a function of its initial energy will be given by the following equation:

$$E_n = E_0 \left(1 + \varepsilon\right)^n \tag{A.6}$$

Equation A.6 enables to compute the number n as a function of energies as shown below:

$$n = \frac{\log\left(\frac{E_n}{E_0}\right)}{\log(1+\varepsilon)} \tag{A.7}$$

The probability for a particle to escape from the region is P_{esc} and to return to it is P_{ret}. They are related by $P_{\text{esc}} + P_{\text{ret}} = 1$. The number of accelerating particles is:

$$N_n = N_0 P_{\text{ret}}^n = N_0 (1 - P_{\text{esc}})^n \tag{A.8}$$

where N_0 is the initial number of particles with energies E_0. The number of particles carrying energies higher than E_n, $N(\geq E_n)$, is given by:

$$N(\geq E_n) = \sum_{i=n}^{\infty} (1 - P_{\text{esc}})^i = \frac{(1 - P_{\text{esc}})^n}{P_{\text{esc}}} \tag{A.9}$$

Replacing Relation A.7 in Equation A.9 gives:

$$N(\geq E_n) = \frac{(1 - P_{\text{esc}})^{\frac{\log\left(\frac{E_n}{E_0}\right)}{\log(1+\varepsilon)}}}{P_{\text{esc}}} \tag{A.10}$$

Using the mathematical property $a^{\log b} = \mathrm{e}^{\log a \log b} = b^{\log a}$, Equation A.10 becomes:

$$N(\geq E_n) = \frac{1}{P_{\text{esc}}} \left(\frac{E_n}{E_0}\right)^{\frac{\log(1-P_{\text{esc}})}{\log(1+\varepsilon)}} \tag{A.11}$$

The number of particles after n iterations with energy E_n is equal to:

$$N(E_n) = \frac{\mathrm{d}N(\geq E_n)}{\mathrm{d}E_n} = \frac{1}{P_{\text{esc}} E_0} \frac{\log(1 - P_{\text{esc}})}{\log(1+\varepsilon)} \left(\frac{E_n}{E_0}\right)^{\frac{\log(1-P_{\text{esc}})}{\log(1+\varepsilon)} - 1} \tag{A.12}$$

$$N(E_n) = \frac{1}{P_{\text{esc}} E_0} (1 - x) \left(\frac{E_n}{E_0}\right)^{-x} \tag{A.13}$$

where

$$x = 1 - \frac{\log(1 - P_{\text{esc}})}{\log(1+\varepsilon)} \tag{A.14}$$

Equation A.13 shows a power low spectrum which is the case of cosmic rays energy spectrum (Figure 1.1).

Appendix B

UNESCO parameterizations for salinity and sound velocity equations

B.1 Conversion from electrical conductivity ratio to salinity

The electrical conductivity ratio is defined by [119]:

$$R = \frac{C(S,t,p)}{C(35,15,0)} \tag{B.1}$$

where $C(S,t,p)$ is the electrical conductivity for salinity S (PSS-78), temperature t (IPTS-68) and pressure p (dbar) and $C(35,15,0)$ is the reference value for $S = 35$, $t = 15°\text{C}$ and the atmospheric pressure.

The electrical conductivity ratio is factorized into three parts as it is shown in the following equation:

$$R = R_p \times R_t \times r_t \tag{B.2}$$

r_t and R_p are calculated by equations B.3 and B.4. However, R_t is deduced from Equation B.2 and it is given by Equation B.5.

$$r_t = c_0 + c_1 \times t + c_2 \times t^2 + c_3 \times t^3 + c_4 \times t^4 \tag{B.3}$$

$$R_p = 1 + \frac{p \times (e_1 + e_2 \times p + e_3 \times p^2)}{1 + d_1 \times t + d2 \times t^2 + (d_3 + d_4 \times t) \times R} \tag{B.4}$$

$$R_t = \frac{R}{R_p \times r_t} \tag{B.5}$$

The salinity is given by:

$$S = a_0 + a_1 \times R_t^{1/2} + a_2 \times R_t + a_3 \times R_t^{3/2} + a_4 \times R_t^2 + a_5 \times R_t^{5/2} + \Delta S \tag{B.6}$$

with

$$\Delta S = \frac{t-15}{1+k\times(t-15)} \times (b_0 + b_1 \times R_t^{1/2} + b_2 \times R_t + b_3 \times R_t^{3/2} + b_4 \times R_t^2 + b_5 \times R_t^{5/2}) \tag{B.7}$$

B.2 Chen-Millero parameterization

The speed of sound in seawater, denoted by U, is parameterized by Chen-Millero parameterization in 1977 and it is presented by the following equation [119]:

$$U = C_W + A \times S + B \times S^{3/2} + D \times S^2 \tag{B.8}$$

where C_W, A, B and D are given by equations B.9, B.10, B.11 and B.12 respectively and S is the salinity.

$$\begin{aligned} C_W &= C_{00} + C_{01} \times t + C_{02} \times t^2 + C_{03} \times t^3 + C_{04} \times t^4 + C_{05} \times t^5 \\ &+ (C_{10} + C_{11} \times t + C_{12} \times t^2 + C_{13} \times t^3 + C_{14} \times t^4) \times p \\ &+ (C_{20} + C_{21} \times t + C_{22} \times t^2 + C_{23} \times t^3 + C_{24} \times t^4) \times p^2 \\ &+ (C_{30} + C_{31} \times t + C_{32} \times t^2) \times p^3 \end{aligned} \tag{B.9}$$

$$\begin{aligned} \mathrm{A} &= A_{00} + A_{01} \times t + A_{02} \times t^2 + A_{03} \times t^3 + A_{04} \times t^4 \\ &+ (A_{10} + A_{11} \times t + A_{12} \times t^2 + A_{13} \times t^3 + A_{14} \times t^4) \times p \\ &+ (A_{20} + A_{21} \times t + A_{22} \times t^2 + A_{23} \times t^3) \times p^2 \\ &+ (A_{30} + A_{31} \times t + A_{32} \times t^2) \times p^3 \end{aligned} \tag{B.10}$$

$$B = B_{00} + B_{01} \times t + (B_{10} + B_{11} \times t) \times p \tag{B.11}$$

$$D = D_{00} + D_{10} \times p \tag{B.12}$$

Coefficient	Value
a_0	$+0.0080$
a_1	-0.1692
a_2	$+25.3851$
a_3	$+14.0941$
a_4	-7.0261
a_5	$+2.7081$
b_0	$+0.0005$
b_1	-0.0056
b_2	-0.0066
b_3	-0.0375
b_4	$+0.0636$
b_5	-0.0144
c_0	$+6.766097 \times 10^{-01}$
c_1	$+2.005640 \times 10^{-02}$
c_2	$+1.104259 \times 10^{-04}$
c_3	$-6.969800 \times 10^{-07}$
c_4	$+1.003100 \times 10^{-09}$
d_1	$+3.426 \times 10^{-02}$
d_2	$+4.464 \times 10^{-04}$
d_3	$+4.215 \times 10^{-01}$
d_4	-3.107×10^{-03}
e_1	$+2.070 \times 10^{-05}$
e_2	-6.370×10^{-10}
e_3	$+3.989 \times 10^{-15}$
k	$+0.0162$

Table B.1: Coefficients of equations B.3, B.4, B.6 and B.7.

Coefficient	Value
C_{00}	$+1402.388 \times 10^{+00}$
C_{01}	$+5.037110 \times 10^{+00}$
C_{02}	$-5.808520 \times 10^{-02}$
C_{03}	$+3.342000 \times 10^{-04}$
C_{04}	$-1.478000 \times 10^{-06}$
C_{05}	$+3.146400 \times 10^{-09}$
C_{10}	$+1.535630 \times 10^{-01}$
C_{11}	$+6.898200 \times 10^{-04}$
C_{12}	$-8.178800 \times 10^{-06}$
C_{13}	$+1.362100 \times 10^{-07}$
C_{14}	$-6.118500 \times 10^{-10}$
C_{20}	$+3.126000 \times 10^{-05}$
C_{21}	$-1.710700 \times 10^{-06}$
C_{22}	$+2.597400 \times 10^{-08}$
C_{23}	$-2.533500 \times 10^{-10}$
C_{24}	$+1.040500 \times 10^{-12}$
C_{30}	$-9.772900 \times 10^{-09}$
C_{31}	$+3.850400 \times 10^{-10}$
C_{32}	$-2.364300 \times 10^{-12}$

Table B.2: Coefficients of Equation B.9.

Coefficient	Value
A_{00}	$+1.3890 \times 10^{+00}$
A_{01}	-1.2620×10^{-02}
A_{02}	$+7.1640 \times 10^{-05}$
A_{03}	$+2.0060 \times 10^{-06}$
A_{04}	-3.2100×10^{-08}
A_{10}	$+9.4742 \times 10^{-05}$
A_{11}	-1.2580×10^{-05}
A_{12}	-6.4885×10^{-08}
A_{13}	$+1.0507 \times 10^{-08}$
A_{14}	-2.0122×10^{-10}
A_{20}	-3.9064×10^{-07}
A_{21}	$+9.1041 \times 10^{-09}$
A_{22}	-1.6002×10^{-10}
A_{23}	$+7.9880 \times 10^{-12}$
A_{30}	$+1.1000 \times 10^{-10}$
A_{31}	$+6.6490 \times 10^{-12}$
A_{32}	-3.3890×10^{-13}
B_{00}	-1.9220×10^{-02}
B_{01}	-4.4200×10^{-05}
B_{10}	$+7.3637 \times 10^{-05}$
B_{11}	$+1.7945 \times 10^{-07}$
D_{00}	$+1.7270 \times 10^{-03}$
D_{10}	-7.9836×10^{-06}

Table B.3: Coefficients of equations B.10, B.11 and B.12.

Appendix C

Effective area

The effective area of the telescope can be calculated, from an isotropic neutrino flux simulation, using the following equation:

$$A^{\nu}_{eff} = \sum_{i=1}^{n} \frac{w2_i}{N \times I_\theta \times I_E \times E_i^{\Gamma} \times t} \tag{C.1}$$

where:

- $w2_i = \frac{w3_i}{\mathrm{d}\Phi/\mathrm{d}E}$ (GeV.m^2.sr.s.yr^{-1}). The $w3_i$ (yr^{-1}) is the weight of the event i per one year and $\mathrm{d}\Phi/\mathrm{d}E$ is the signal neutrino differential flux (GeV^{-1}.m^{-2}. sr^{-1}.s^{-1}.yr^{-1}) [134].
- n is the number of the reconstructed events which pass the quality cuts.
- N is the total number of simulated events[1].
- Γ is the generated energy spectrum index (1.4 in GENHEN).
- t is the time window of the simulation (1 year in GENHEN).
- $I_\theta = 2\pi \times [\cos(\theta_{\mathrm{max}}) - \cos(\theta_{\mathrm{min}})]$ is the angular phase space factor (2π srad in GENHEN).
- I_E is the energy phase space factor given by Equation C.2. (E_{min} = 10 GeV and E_{max} = 10^7 GeV in GENHEN)

$$I_E = \int_{E_{\mathrm{min}}}^{E_{\mathrm{max}}} E^{-\Gamma} dE = \frac{E_{\mathrm{max}}^{1-\Gamma} - E_{\mathrm{min}}^{1-\Gamma}}{1-\Gamma} \tag{C.2}$$

[1] In the BBfit output files, the $w2_i$ is already divided by N.

The effective area for neutrinos in a given energy bin ΔE is given by:

$$A_{eff}^{\nu,\Delta E} = \sum_{i=1}^{n_{\Delta E}} \frac{w2_i}{F_{\Delta E} \times N \times I_\theta \times I_E \times E_i^\Gamma \times t} \tag{C.3}$$

with

$$F_{\Delta E} = \frac{\int_{\Delta E} E^{-\Gamma} dE}{\int_{E_{\min}}^{E_{\max}} E^{-\Gamma} dE} \tag{C.4}$$

where:

- $n_{\Delta E}$ is the number of the reconstructed events in ΔE (true neutrino energy bin) which pass the quality cuts.
- $F_{\Delta E}$ is the fraction of simulated events in ΔE.

C.1 Effective area as a function of the true neutrino declination

The effective area of the telescope for neutrinos for a given true neutrino energy bin ΔE and true neutrino declination bin $\Delta\theta$ averaged with energy spectrum E^{-2} is given by:

$$A_{eff}^{\nu,\Delta\theta} = \sum_{i=1}^{n_{\Delta\theta}} \frac{w2_i}{F_{\Delta\theta} \times F_{\Delta E_i} \times N \times I_\theta \times I_E \times E_i^\Gamma \times t} \times \frac{\int_{\Delta E_i} E^{-\gamma} dE}{\int_{E_{\min}}^{E_{\max}} E^{-\gamma} dE} \tag{C.5}$$

where:

- $n_{\Delta\theta}$ is the number of the reconstructed events in $\Delta\theta$ bin which pass the quality cuts.
- γ is the signal neutrinos energy spectrum (2 in this analysis).
- $F_{\Delta\theta}$ is the fraction of events generated as up-going in the $\Delta\theta$ bin. This last is calculated numerically by a Monte-Carlo simulation of high number of neutrinos (10^7 neutrinos) with the zenith between 0° and 90° (up-going) (Figure C.1).

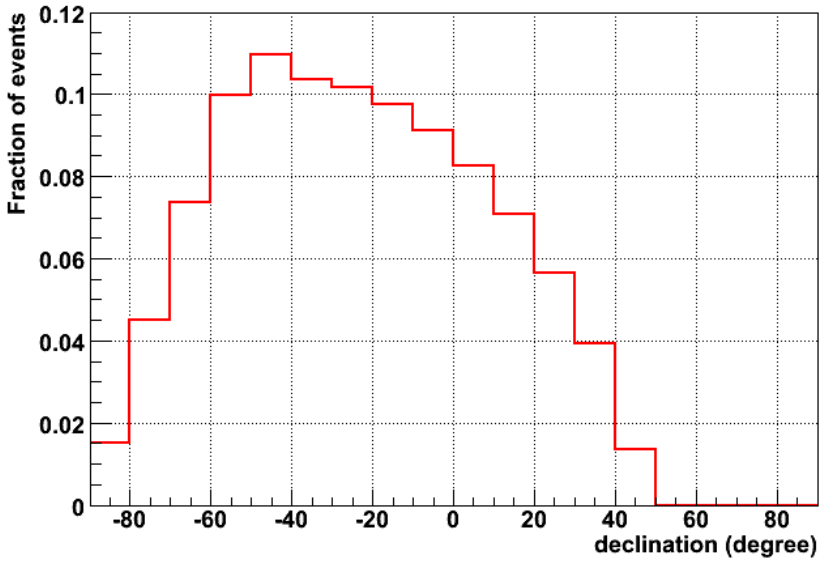

Figure C.1: Fraction of events in each declination bin for isotropically generated up-going neutrinos.

C.2 Total effective area for ν and $\overline{\nu}$

The neutrino and anti-neutrino fluxes for the astrophysical sources, in this thesis, are assumed to be equal (Equation C.6).

$$\phi_{\nu} = \phi_{\overline{\nu}} \tag{C.6}$$

The total number n of ν and $\overline{\nu}$ (Equation C.7), the total flux ϕ (Equation C.8), the effective area A_{eff} for ν and $\overline{\nu}$ and the time of the data taking are related by Equation C.9.

$$n = n_{\nu} + n_{\overline{\nu}} \tag{C.7}$$

$$\phi = \phi_{\nu} + \phi_{\overline{\nu}} \tag{C.8}$$

$$n = \phi \times A_{eff} \times t \tag{C.9}$$

Equation C.9 is correct also for only neutrino or anti-neutrino (Equation C.10).

$$n_{\nu,\overline{\nu}} = \phi_{\nu,\overline{\nu}} \times A_{eff}^{\nu,\overline{\nu}} \times t \tag{C.10}$$

Replacing Equation C.10 in Equation C.7, n is given by:

$$n = (\phi_{\nu} \times A_{eff}^{\nu} + \phi_{\overline{\nu}} \times A_{eff}^{\overline{\nu}}) \times t \tag{C.11}$$

Using equations C.6, C.8 and C.11, n is presented by:

$$n = \frac{\phi}{2} \times (A^{\nu}_{eff} + A^{\overline{\nu}}_{eff}) \times t \tag{C.12}$$

Comparing Equation C.9 and C.12, the total effective area is given by:

$$A_{eff} = \frac{A^{\nu}_{eff} + A^{\overline{\nu}}_{eff}}{2} \tag{C.13}$$

Appendix D

Visibility

In the point source analysis, the sources in question are at more important distances than the radius of Earth's orbit around the Sun. In this case, only the proper rotational motion of the Earth relative to the stars[1] is considered. The period of this rotation is one sidereal day which is less than the solar day[2] by 4 minutes on average (Figure D.1).

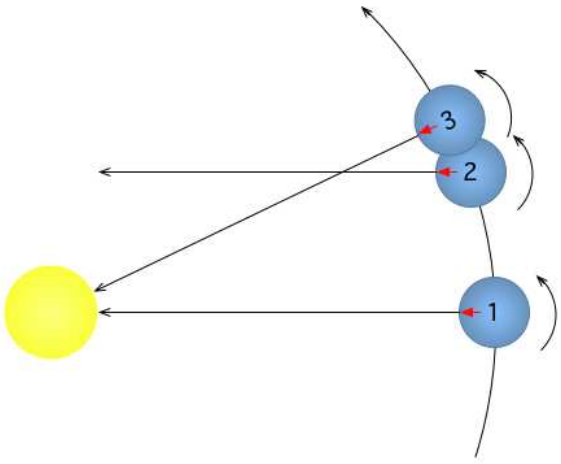

Figure D.1: The Earth spends one sidereal day to reach position 2 from position 1, and one solar day to reach position 3.

The visibility, v, is defined as the fraction of one sidereal day where the source is in the field of view of the telescope. This field of view is represented by a cone the axis of which is oriented towards the center of the Earth and the opening angle of the cone γ (Figure D.2). For up-going neutrinos, γ is equal to 90°.

[1]The stars are considered fix relative to each other for the ANTARES detector lifetime.
[2]The solar day is the period between two consecutive noons.

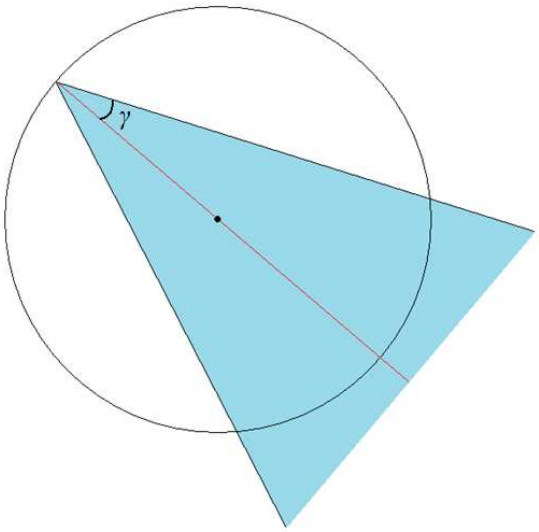

Figure D.2: The field of view of the telescope is represented by the blue region.

To compute the visibility for a given source, let's consider the reference frame R (Figure D.3) where the z axis coincides with the Earth's axis, and the Northern direction is taken as the positive direction. The x axis is chosen to have the telescope in the xOz plane $(y = 0)$. Therefore, the Earth is stationary and the source rotates around the z axis. Let **a** and **s** be the unity vectors of ANTARES and the source respectively. The cosine of α, the angle between **a** and **s**, is given by:

$$\cos\alpha = \mathbf{a}.\mathbf{s} = \cos l \cos\delta \cos\beta + \sin l \sin\delta \tag{D.1}$$

where:

- l is ANTARES latitude. $l = 42°47'56.1''$
- δ is the declination of the source in the Equatorial coordinates system.
- β is the angle between the projection of **a** and **s** on xOy plane.

During one sidereal day, the source will make a uniform rotation of 360° around the z axis. From the point of view of visibility, the point sources can be classified in three categories:

1. sources with $v = 1$ (100% visible).
2. sources with $v = 0$ (0% visible).

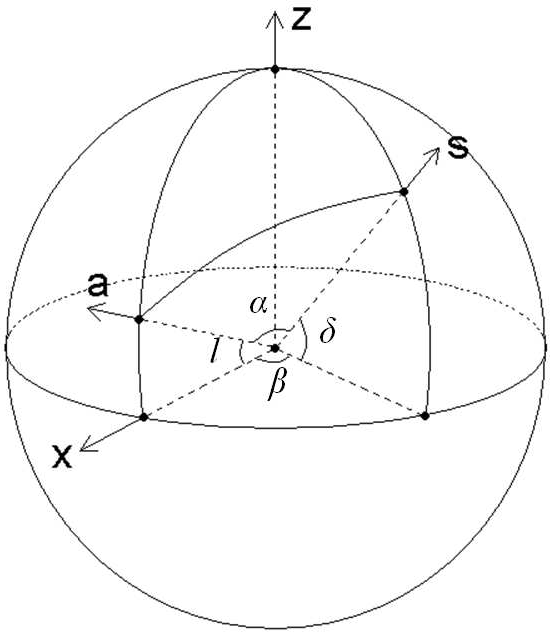

Figure D.3: The reference frame *R*.

3. sources with partial visibility.

For the third category, the sources touch the borders of the cone representing the field of view twice per sidereal day. At these two particular moments, the relation between α and γ angles is given by $\gamma = 180^\circ - \alpha$. Therefore, Equation D.1 can be written as the following:

$$\cos\beta = \frac{\cos(180^\circ - \gamma) - \sin l \sin\delta}{\cos l \cos\delta} \tag{D.2}$$

For this category of sources, the visibility v is given by:

$$v = \frac{\pi - \beta}{\pi} \tag{D.3}$$

For the first and second categories, the sources do not touch the borders of the cone that represent the field of view. Based on Equation D.2, the factor b is defined as:

$$b = \frac{\cos(180^\circ - \gamma) - \sin l \sin\delta}{\cos l \cos\delta} \tag{D.4}$$

The visibility will be 100% ($v = 1$) when $b > 1$ and $v = 0$ when $b < -1$.

Equations D.2, D.3 and D.4 show that the visibility of a given source depends only on its declination.

Bibliography

[1] J. Paul, Une brève histoire des rayons cosmiques, Physique et astrophysique du rayonnement cosmique, Ecole CNRS de Goutelas XXVI (2003).

[2] http://www.auger.org/.

[3] P. Abreu *et al.*, Update on the correlation of the highest energy cosmic rays with nearby extragalactic matter, (2010), arXiv:1009.1855.

[4] http://www.mpi-hd.mpg.de/hfm/HESS/.

[5] http://fermi.gsfc.nasa.gov/.

[6] J. N. Bahcall, Solar Models and Solar Neutrinos: Current Status, Phys. Scripta T121 (2005), hep-ph/0412068.

[7] G. G. Raffelt, Supernova Neutrino Oscillations, Phys. Scripta T121 (2005), hep-ph/0501049.

[8] E. Parizot, Accélération des particules : les mécanisme de Fermi, Physique et astrophysique du rayonnement cosmique, Ecole CNRS de Goutelas XXVI (2003).

[9] E. Fermi, On the origin of the cosmic radiation, Physical Review **75** (1949).

[10] X. Bertou, M. Boratav, and A. Letessier-Selvon, Physics of Extremely High Energy Cosmic Rays, Int. J. Mod. Phys. **A15** (2000), arXiv:astro-ph/0001516.

[11] J. R. Horandel, Cosmic rays from the knee to the second knee: 10^{14} eV to 10^{18} eV, Mod. Phys. Lett. **A22** (2007).

[12] J. Abraham *et al.*, Measurement of the energy spectrum of cosmic rays above 10^{18} eV using the Pierre Auger Observatory, Phys. Lett. B **685** (2010), arXiv:1002.1975.

[13] K. Greisen, End to the Cosmic-Ray Spectrum?, Physical Review Letters **16** (1966).

[14] G. T. Zatsepin and V. A. Kuz'min, Upper Limit of the Spectrum of Cosmic Rays, Journal of Experimental and Theoretical Physics Letters **4** (1966).

[15] J. Rich, Principes de la cosmologie, (2004).

[16] J. L. Puget, F. W. Stecker, and J. H. Bredekamp, Photonuclear interactions of ultrahigh energy cosmic rays and their astrophysical consequences, The Asrophysical Journal **205** (1976).

[17] F. W. Stecker and M. H. Salamon, Photodisintegration of Ultra-High-Energy Cosmic Rays: A New Determination, The Asrophysical Journal **512** (1999), arXiv:astro-ph/9808110.

[18] C. D. Dermer, On Gamma Ray Burst and Blazar AGN Origins of the Ultra-High Energy Cosmic Rays in Light of First Results from Auger, 30th International Cosmic Ray Conference (2007), arXiv:0711.2804v2.

[19] J. Abraham *et al.*, Properties and performance of the prototype instrument for the Pierre Auger Observatory, Nucl. Instrum. Meth. A **523** (2004).

[20] I. Allekotte *et al.*, The Surface Detector System of the Pierre Auger Observatory, Nucl. Instrum. Meth. A **586** (2008), arXiv:0712.2832 [astro-ph].

[21] J. Abraham *et al.*, The Fluorescence Detector of the Pierre Auger Observatory, Nucl. Insrum. Meth. **620** (2010), arXiv:0907.4282 [astro-ph.IM].

[22] J. Linsley, Evidence for a Primary Cosmic-Ray Particle with Energy 10^{20} eV, Physical Review Letters **10** (1963).

[23] C. Bonifazi, Angular Resolution of the Pierre Auger Observatory, 29th ICRC (2005).

[24] http://www.cosmic-ray.org/.

[25] R. U. Abbasi *et al.*, A Study of the Composition of Ultra High Energy Cosmic Rays Using the High Resolution Fly's Eye, The astrophysical journal **622** (2005), arXiv:astro-ph/0407622v3.

[26] D. R. Bergman, Latest Results from HiRes, (2008), arXiv:0807.2814v1.

[27] R. U. Abbasi *et al.*, Study of small-scale anisotropy of ultrahigh energy cosmic rays observed in stereo by HiRes, The astrophysical journal **610** (2004), arXiv:astro-ph/0404137v2.

[28] A. M. Hillas, The origin of ultra-high-energy cosmic rays, Annual Review of Astronomy and Asrophysics **22** (1984).

[29] M. P. Véron-Cetty and P. Véron, A catalogue of quasars and active nuclei: 12th edition, Astron. Astrophys. **455** (2006).

[30] W. Heitler, The Quantum Theory of Radiation, Oxford University Press (1954).

[31] J. Matthews, A Heitler model of extensive air showers, Astroparticle Physics **22** (2005).

[32] J. Abraham *et al.*, Measurement of the Depth of Maximum of Extensive Air Showers above 10^{18} eV, Physical Review Letters **104** (2010), arXiv:1002.0699v1.

[33] R. U. Abbasi *et al.*, Indications of Proton-Dominated Cosmic Ray Composition above 1.6 EeV, Physical Review Letters **104** (2010), arXiv:0910.4184v2.

[34] http://www.mpi-hd.mpg.de/hfm/HESS/.

[35] M. Punch, Results from Observations of AGNs with the HESS Telescope System and Future Plans, (2007), arXiv:astro-ph/0501155v1.

[36] P. M. Saz Parkinson, Fermi: Gamma-ray Space Telescope Observations of Gamma-ray Pulsars, (2009), arXiv:0901.3405v1.

[37] J. Knodlseder, Studies of Gamma Ray Sources with the Fermi Large Area Telescope, (2010), arXiv:1006.2635v1.

[38] A. P. Marscher and W. K. Gear, Models for high-frequency radio outbursts in extragalactic sources, with application to the early 1983 millimeter-to-infrared flare of 3C 273, The Astrophysical Journal **298** (1985).

[39] L. Maraschi, G. Ghisellini, and A. Celotti, A jet model for the gamma-ray emitting blazar 3C 279, The Astrophysical Journal **397** (1992).

[40] S. D. Bloom and A. P. Marscher, An Analysis of the Synchrotron Self-Compton Model for the Multi-Wave Band Spectra of Blazars, The Astrophysical Journal **461** (1996).

[41] C. D. Dermer and R. Schlickeiser, Model for the High-Energy Emission from Blazars, The Astrophysical Journal **416** (1993).

[42] M. Sikora, M. C. Begelman, and M. J. Rees, Comptonization of diffuse ambient radiation by a relativistic jet: The source of gamma rays from blazars?, The Astrophysical Journal **421** (1994).

[43] C. D. Dermer, S. J. Sturner, and R. Schlickeiser, Nonthermal Compton and Synchrotron Processes in the Jets of Active Galactic Nuclei, The Astrophysical Journal Supplement **109** (1997).

[44] G. Ghisellini and P. Madau, On the origin of the gamma-ray emission in blazars, MNRAS **280** (1996).

[45] M. Blazejowski *et al.*, Comptonization of Infrared Radiation from Hot Dust by Relativistic Jets in Quasars, The Astrophysical Journal **545** (2000).

[46] C. Arbeiter, M. Pohl, and R. Schlickeiser, The influence of dust on the inverse Compton emission from jets in Active Galactic Nuclei, A&A **386** (2002).

[47] K. Mannheim and P. L. Biermann, Gamma-ray flaring of 3C 279: A proton-initiated cascade in the jet?, A&A **253** (1992).

[48] K. Mannheim, The proton blazar, A&A **269** (1993).

[49] F. Aharonian, TeV gamma rays from BL Lac objects due to synchrotron radiation of extremely high energy protons, New Astronomy **5, 377** (2000).

[50] A. Mucke and R. J. Protheroe, Modeling the April 1997 flare of Mkn 501, AIP Conf. Proc. **515, 149** (2000).

[51] J. Rachen and P. Mészáros, Photohadronic neutrinos from transients in astrophysical sources, Physical Review D **58** (1998).

[52] A. Mucke and R. J. Protheroe, A proton synchrotron blazar model for flaring in Markarian 501, Astroparticle Physics **15, 121** (2001).

[53] A. Mucke *et al.*, BL Lac objects in the synchrotron proton blazar model, Astroparticle Physics **18, 593** (2003).

[54] T. K. Gaisser, Cosmic Rays and Particle Physics, Cambridge University Press (1990).

[55] C. Picq, Détermination du flux de muons atmosphériques avec le télescope à neutrinos ANTARES, Ph.D. thesis .

[56] F. Halzen and D. Hooper, High-energy Neutrino Astronomy: The Cosmic Ray Connection, Reports on Progress in Physics **65** (2002), arXiv:astro-ph/0204527.

[57] W. Bednarek, G. F. Burgio, and T. Montaruli, Galactic discrete sources of high energy neutrinos, New Astronomy Reviews **49** (2005), arxiv:astro-ph/0404534.

[58] F. W. Stecker, Note on high-energy neutrinos from active galactic nuclei cores, Physical Review D **72** (2005).

[59] C. Hazard *et al.*, Investigation of the Radio Source 3C 273 By The Method of Lunar Occultations, Nature **197** (1963).

[60] J. Krolik, Active Galactic Nuclei From the Central Black Hole to the Galactic Environment, Princeton Series in Astrophysics (1999).

[61] C. K. Seyfert, Nuclear Emission in Spiral Nebulae, Astrophysical Journal **97** (1943).

[62] L. S. Sparke and J. S. Gallagher, Galaxies in the Universe: An Introduction, Cambridge University Press (2000), ISBN 0-521-67186-6.

[63] R. W. Klebesadel, I. B. Strong, and R. A. Olson, Observations of Gamma-Ray Bursts of Cosmic Origin, Astrophysical Journal (Letters) **182, L85** (1973).

[64] A. Loeb and E. Waxman, The Cumulative Background of High-Energy Neutrinos from Starburst Galaxies, JCAP 0605 (2006), astro-ph/0601695.

[65] F. L. Villante and F. Vissani, How precisely can neutrino emission form supernova remnants be constrained by gamma ray observations?, Physical Review D **78** (2008), arXiv:astro-ph/0807.4151.

[66] A. Kappes *et al.*, Potential Neutrino Signals from Galactic γ-Ray Sources, The astrophysical journal **656** (2007), arXiv:astro-ph/0607286v3.

[67] M. Meyer *et al.*, The Crab Nebula as a standard candle in very high-energy astrophysics, Astronomy & Astrophysics (2010), arXiv:astro-ph/1008.4524v1.

[68] D. Horns *et al.*, Nucleonic gamma-ray production in Vela X, Astronomy and Astrophysics **451** (2006).

[69] S. Migliari *et al.*, Iron Emission Lines from Extended X-ray Jets in SS 433: Reheating of Atomic Nuclei, Science **297** (2002).

[70] S. Karkar, Détection de microquasars et calibration en temps du télescope a neutrinos ANTARES, Ph.D. thesis, Université de la Méditerranée (2004).

[71] F. Aharonian *et al.*, Discovery of very-high-energy γ-rays from the Galactic Centre ridge, Nature **439** (2005), arXiv:astro-ph/0603021v1.

[72] F. Aharonian *et al.*, Very high energy gamma rays from the direction of Sagittarius A *, Astronomy & Astrophysics **425** (2004), arXiv:astro-ph/0408145v2.

[73] S. Meng, R. S. Tracy, and P. F. Douglas, Giant Gamma-Ray Bubbles from Fermi-LAT: AGN Activity or Bipolar Galactic Wind?, (2010), arXiv:1005.5480v3.

[74] R. M. Crocker and F. Aharonian, The Fermi Bubbles: Giant, Multi-Billion-Year-Old Reservoirs of Galactic Center Cosmic Rays, (2010), arXiv:1008.2658v3.

[75] E. Waxman and J. Bahcall, High energy neutrinos from astrophysical sources: An upper bound, Physical Review D **59** (1998).

[76] A. Kouchner, Antares : étalonnage de l'électronique frontale, étude de muons atmosphériques, et recherche de neutrinos cosmiques, HDR .

[77] A. Domínguez *et al.*, Extragalactic Background Light Inferred from AEGIS Galaxy SED-type Fractions, (2010), arXiv:1007.1459v4.

[78] J. M. Jauch and F. Rohrlich, The Theory of Photons and Electrons: The Relativistic Quantum Field Theory of Charged Particles with Spin One-half, Hardcover (1955).

[79] E. Dwek and F. Krennrich, Simultaneous constraints on the spectrum of the extragalactic background light and the intrinsic TeV spectra of Mrk 421, Mrk 501, and H1426+428, The Astrophysical Journal **618** (2005), arXiv:astro-ph/0406565v2.

[80] J. Alvarez-Muniz and F. Halzen, Possible High-Energy Neutrinos from the Cosmic Accelerator RX J1713.7-3946, The Astrophysical Journal Letters **576** (2002), arXiv:astro-ph/0205408 v3.

[81] G. Giunti, Neutrino flavour states and the quantum theory of neutrino oscillations, Journal of Physics G **34** (2007).

[82] F. Aharonian *et al.*, Detection of VHE gamma-ray emission from the distant blazar 1ES 1101-232 with H.E.S.S. and broadband characterisation, Astronomy and Astrophysics **470** (2007), arXiv:0705.2946v2.

[83] The ANTARES Collaboration, A Deep Sea Telescope for High Energy Neutrinos, (1999), arXiv:astro-ph/9907432.

[84] The ANTARES Collaboration, Technical design report of the ANTARES telescope, http://antares.in2p3.fr/Publications/index.html.

[85] C. Quigg, M. H. Reno, and T. P. Walker, Interactions of ultra high energy neutrino, Physical Review Letters **57** (1986).

[86] C. Quigg and M. H. Reno, On the detection of ultrahigh-energy neutrinos, Physical Review D **37** (1988).

[87] C. Amsler *et al.*, Particle Physics Booklet, (2008).

[88] W. M. Yao *et al.*, Review of Particle Physics, J. Phys. G **33** (2006).

[89] A. Oppelt, Étude de la résolution angulaire du télescope à neutrinos ANTARES, Thèse de doctorat, Université de la Méditerranée Aix-Marseille II (2001).

[90] J. D. Jackson, Classical Electrodynamics, John Wiley and Sons, Inc (1998).

[91] M. A. Markov, Proceedings of the Rochester Conference, New-York (1960).

[92] http://www.google.fr/maps.

[93] The ANTARES Collaboration, Transmission of light in deep sea water at the site of the Antares neutrino telescope, Astroparticle Physics **23** (2005).

[94] http://antares.in2p3.fr/index.html.

[95] J. A. Aguilar *et al.*, First results of the Instrumentation Line for the deep-sea ANTARES neutrino telescope, Astroparticle Physics **26** (2006), astro-ph/0606229.

[96] The ANTARES Collaboration, Study of large hemispherical photomultiplier tubes for the ANTARES neutrino telescope, Nucl. Instr. Meth. **A555** (2005).

[97] J. P. Gómez-González, Timing Calibration of the ANTARES Neutrino Telescope, Proceedings of the 31^{st} ICRC (2009).

[98] The ANTARES Collaboration, Measurement of the atmospheric muons flux with a 4 GeV threshold in the ANTARES neutrino telescope, Astroparticle Physics **33** (2010).

[99] D. Bailey, Genhen v5r1 : Software Documentation, (2002), ANTARES-SOFT-2002-004.

[100] S. Ricciardi, Università Ferrara, Ph.D. Thesis (1996).

[101] G. Ingelman, A. Edin, and J. Rathsman, LEPTO 6.5, Comput. Phys. Commun. **101** (1997).

[102] J. Pumplin *et al.*, New generation of parton distributions with uncertainties from global QCD analysis, JHEP 07, 012 (2002), arxiv:hep-ph/0201195.

[103] K. Kuzmin, T. Montaruli, and I. A. Sokalski, GENHEN v6r3: implementation of the Glashow resonance and of MUSIC transport code, (2004), ANTARES-SOFT-2004-012.

[104] E. V. Korolkova and L. Thompson, Monte Carlo Simulation of Cosmic Ray Muons at Sea Level with CORSIKA, (2003), ANTARES-SOFT-2003-002.

[105] D. Bailey, KM3 v2r1 : User Guide, (2002), ANTARES-SOFT-2002-006.

[106] J. Brunner, The BBfit Reconstruction algorithm, (2009), ANTARES-SOFT-2009-003.

[107] A. Heijboer, Track Reconstruction and Point Source Searches with ANTARES, Ph.D. thesis (2004).

[108] http://icecube.wisc.edu/.

[109] A. Karle, IceCube, Proceedings of 31st ICRC (2009), arXiv:1003.5715.

[110] http://www.km3net.org/.

[111] R. Abbasi *et al.*, First Neutrino Point-Source Results From the 22-String IceCube Detector, The Astrophyscal Journal Letters **701** (2009), arXiv:astro-ph/0905.2253.

[112] F. Aharonian *et al.*, High energy astrophysics with ground-based gamma ray detectors, Reports on Progress in Physics **71** (2008).

[113] A. Achterberg *et al.*, Multiyear search for a diffuse flux of muon neutrinos with AMANDA-II, Physical Review D **76** (2007).

[114] M. Ackermann *et al.*, Search for Ultra-High-Energy Neutrinos with AMANDA-II, The Astrophysical Journal **675** (2008).

[115] J. Zornoza, Sensitivity to diffuse fluxes and energy spectrum reconstruction in the Antares neutrino telescope, Universitat de Valéncia (2005).

[116] J. Ahrens *et al.*, Sensitivity of the Icecube detector to astrophysical sources of high energy muon neutrinos, Astroparticle physics (2009).

[117] NASA, The EGM96 Geoid Undulation with Respect to the WGS84 Ellipsoid.

[118] V. Bertin, Determination of the new BSS position for the 10+1 lines detector, ANTARES collaboration meeting in Pisa (2008).

[119] Unesco / SCOR / ICES / IAPSO Joint Panel on Oceanographic Tables and Standards and SCOR Wroking Group 51. Algorithms for computation of fundamental properties of seawater.

[120] V. Niess, Rapport de stage sur le système de positionnement acoustique Base Longue moyenne fréquence GENISEA du détecteur ANTARES.

[121] V. Niess, GENISEA acoustic positioning: Description and data base storage, ANTARES-Cali/2007-006.

[122] Numerical Recipes in C: The art of scientific computing, Cambridge University Press .

[123] V. Bertin, Opération VICTOR sur site ANTARES, version C, (2009).

[124] J. Brunner, Analysis of 2007 and 2008 data with BBfit, (2009), ANTARES-PHYS-2009-006.

[125] S. Toscano, Golden-list for a point source search in ANTARES, (2009), ANTARES-PHYS-2009-002.

[126] R. D. Cousins and V. L. Highland, Incorporating systematic uncertainties into an upper limit, Nucl. Instrum. Meth. A **320, 331** (1992).

[127] J. A. Aguilar, Analysis of the Optical Beacon system and search for point-like sources in the ANTARES neutrino telescope, Ph.D. thesis .

[128] R. Abbasi *et al.*, First Neutrino Point-Source Results from the 22 String Icecube Detector, Astrop. J. Lett. **701** (2009), arXiv:0905.2253.

[129] R. Abbasi *et al.*, Search for point sources of high energy neutrinos with final data from AMANDA-II, Phys. Rev. D **79** (2009), arXiv:0809.1646.

[130] S. Desai *et al.*, Study of TeV neutrinos with upward showering muons in Super-Kamiokande, Astrop. Phys. **29** (2008).

[131] E. Thrane *et al.*, Search for Astrophysical Neutrino Point Sources at Super-Kamiokande, Astrophys. J. **704** (2009), arXiv:0907.1594v1.

[132] M. Ambrosio *et al.*, Neutrino Astronomy with the MACRO Detector, Astrophys. J. **546** (2001).

[133] C. Bogazzi, J. Hartman, and A. Heijboer, Point Source Search with 2007 and 2008 data, ANTARES-PHYS-2010-008 version 2 .

[134] J. Brunner, Updated tag list for the new ANTARES event format, (1999), ANTARES-SOFT-1999-003.

Abstract

English Title: Search for high energy cosmic neutrino point sources with ANTARES.

The aim of this thesis is the search for high energy cosmic neutrinos emitted by point sources with the ANTARES neutrino telescope. The detection of high energy cosmic neutrinos can bring answers to important questions such as the origin of cosmic rays and the γ-rays emission processes. In the first part of the thesis, the neutrino flux emitted by galactic and extragalactic sources and the number of events which can be detected by ANTARES are estimated. This study uses the measured γ-ray spectra of known sources taking into account the γ-ray absorption by the extragalactic background light. In the second part of the thesis, the absolute pointing of the ANTARES telescope is evaluated. Being located at a depth of 2475 m in sea water, the orientation of the detector is determined by an acoustic positioning system which relies on low and high frequency acoustic waves measurements between the sea surface and the bottom. The third part of the thesis is a search for neutrino point sources in the ANTARES data. The search algorithm is based on a likelihood ratio maximization method. It is used in two search strategies; "the candidate sources list strategy" and "the all sky search strategy". Analysing 2007+2008 data, no discovery is made and the world's best upper limits on neutrino fluxes from various sources in the Southern sky are established.

Key Words: Neutrino, ANTARES, point source, astroparticle.

Résumé

L'objectif de cette thèse est la recherche des neutrinos cosmiques de haute énergie émis par des sources ponctuelles avec le télescope à neutrino ANTARES. La détection des neutrinos cosmiques de haute énergie peut apporter des réponses à des problèmes importants comme l'origine des rayons cosmiques et les procédures d'émission des rayons γ. Dans la première partie de la thèse, le flux des neutrinos émis par des sources galactiques et extragalactiques et le nombre des événements qui peut être détecté par ANTARES sont estimés. Cette étude utilise les spectres des rayons γ des sources connues en tenant compte de l'absorption de ces rayons par la lumière extragalactique diffuse. Dans la deuxième partie de la thèse, le pointage absolu du télescope ANTARES est étudié. Étant situé à une profondeur de 2475 m dans l'eau de mer, l'orientation du détecteur est déterminée par un système de positionnement acoustique qui utilise des ondes de basse et haute fréquences entre la surface de la mer et le fond. La troisième partie de la thèse est la recherche des sources ponctuelles de neutrinos avec les données d'ANTARES. L'algorithme de recherche est basé sur une méthode de maximisation du rapport de vraisemblance. Il est utilisé dans deux stratégies de recherche; "la stratégie de recherche avec des sources candidates" et "la stratégie de recherche dans tout le ciel". L'analyse des données de 2007+2008 n'a pas marqué une découverte. Les meilleures limites supérieures au monde sur les flux de neutrinos provenant des différentes sources dans l'Hémisphère Sud sont établies.

Mots Clés: Neutrino, ANTARES, source ponctuelle, astroparticule.